

**A MODELING PERSPECTIVE ON DEVELOPING
NATURALISTIC NEUROPROSTHETICS USING ELECTRICAL
STIMULATION**

by
Cynthia R. Steinhardt

A dissertation submitted to Johns Hopkins University in
conformity with the requirements of the degree for Doctor of
Philosophy

Baltimore, Maryland
February 2022

Abstract

Direct electrical stimulation of neurons has been an important tool for understanding the brain and neurons, since the field of neuroscience began. Electrical stimulation was used to first understand sensation, the mapping of the brain, and more recently function, and, as our understanding of neurological disorders has advanced, it has become an increasingly important tool for interacting with neurons to design and carry out treatments. The hardware for electrical stimulation has greatly improved during the last century, allowing smaller scale, implantable treatments for a variety of disorders, from loss of sensations (hearing, vision, balance) to Parkinson's disease and depression. Due to the clinical success of these treatments for a variety of impairments today, there are millions of neural implant users around the globe, and interest in medical implants and implants for human-enhancement are only growing. However, present neural implant treatments restore only limited function compared to natural systems.

A limiting factor in the advancement of electrical stimulation-based treatments has been the restriction of using charge-balanced and typically short sub-millisecond pulses in order to safely interact with the brain, due to a reliance on durable, metal electrodes. Material science developments have led to more flexible electrodes that are capable of delivering more charge safely, but a focus has been on density of electrodes implanted over changing the waveform of electrical stimulation delivery. Recently, the Fridman lab at Johns Hopkins University developed the Freeform Stimulation (FS)—an implantable device that uses a microfluidic H-bridge architecture to safely deliver current for prolonged periods of time and that is not restricted to charge-balanced waveforms. In this work, we refer to these non-restricted waveforms as galvanic stimulation, which is used as an umbrella term that encompasses direct current, sinusoidal current, or alternative forms of non-charge-balanced current. The invention of the FS has opened the door to usage of galvanic stimulation in neural implants, begging an exploration of the effects of local galvanic stimulation on neural function.

Galvanic stimulation has been used in the field of neuroscience, prior to concerns about safe long-term interaction with neurons. Unlike many systems, it had been historically used in the vestibular system internally and in the form of transcutaneous stimulation to this day. Historic and recent studies confirm that galvanic stimulation of the vestibular system has more naturalistic effects on neural spike timing and on

induced behavior (eye velocities) than pulsatile stimulation, the standard in neural implants now. Recent vestibular stimulation studies with pulses also show evidence of suboptimal responses of neurons to pulsatile stimulation in which suprathreshold pulses only induce about half as many action potentials as pulses. This combination of results prompted an investigation of differences between galvanic and pulsatile electrical stimulation in the vestibular system.

The research in this dissertation uses detailed biophysical modeling of single vestibular neurons to investigate the differences in the biophysical mechanism of galvanic and pulsatile stimulation. In Chapter 2, a more accurate model of a vestibular afferent is constructed from an existing model, and it is used to provide a theory for how galvanic stimulation produces a number of known effects on vestibular afferents. In Chapter 3, the same model is used to explain why pulsatile stimulation produces fewer action potentials than expected, and the results show that pulse amplitude, pulse rate, and the spontaneous activity of neurons at the axon have a number of interactions that lead to several non-monotonic relationships between pulse parameters and induced firing rate. Equations are created to correct for these non-monotonic relationships and produce intended firing rates. Chapter 4 focuses on how to create a neural implant that induces more naturalistic firing using the scientific understanding from Chapters 2 and 3 and machine learning. The work concludes by describing the implications of these findings for interacting with neurons and population and network scales and how this may make electrical stimulation increasingly more suited for treating complex network-level and psychiatric disorders.

Primary reader: Gene Y. Fridman, PhD

Secondary reader: Charles C. Della Santina, MD, PhD

Acknowledgements

I whole-heartedly thank my Ph.D. advisor Prof. Gene Fridman for sharing his passion for exploring the edge of what is known with me, supporting me when even I did not believe in myself and taking on every type of challenge with me to make it possible to pursue these questions – questions that I only dreamed of working on during my career. For me, he truly embodies an ideal academic and mentor. Thank you for being the one *yes* that I needed in a sea of *no*'s and for everything you have taught me.

I am very grateful to my thesis committee - Profs. Kathleen Cullen, Charles Della Santina, and Elisabeth Glowatzki - for their sincere commitment to making me a better scientist by challenging me to grow my depth of knowledge, communication and understanding of my field. I was fortunate to have so many role models and mentors who truly wanted to better my research and my career.

I am also so grateful to my friends and family who showed up for me through so many ups and downs to encourage me to keep going when things seemed impossible, commiserate with me, and celebrate the life events and victories along the way.

Thank you all for the person you collectively helped me to become and inspire me to continue to strive to be. In many ways, the work discussed here is the product of strong friendships, love, and supportive communities - of people who are truly passionate about contributing through their job and their actions to improving the world.

Table of Contents

Abstract	ii
Acknowledgements	iv
List of Tables	viii
List of Figures	ix
Chapter 1 : Introduction	1
1.1 Significance.....	1
1.2 Background	2
1.2.1 <i>The Role of Electrical Stimulation in Neuroscience Research and Treatments</i>	2
1.2.2 <i>Limitations of the Existing Electrical Stimulation Paradigm</i>	3
1.2.3 <i>The Re-emergence of Galvanic Stimulation as an Alternative to Pulses</i>	4
1.2.4 <i>Using the Vestibular System as a Window into Effects of Electrical Stimulation</i>	5
Chapter 2 : A Cohesive Theory of Galvanic Electrical Stimulation	8
2.1 Introduction.....	8
2.1.1 <i>A Brief Introduction to Vestibular Afferents</i>	8
2.1.2 <i>History of Galvanic Stimulation in the Vestibular System</i>	12
2.2 Methods.....	15
2.2.1 <i>Vestibular Axon Model</i>	15
2.2.2 <i>Other Channels Added into the Model:</i>	19
2.2.3 <i>Hair Cell Adaptation Effect</i>	21
2.2.4 <i>Simulating Effects of GVS on Firing Regularity</i>	23
2.2.5 <i>Simulating Adaptation Observed in Response to GVS</i>	23
2.2.6 <i>Simulating Baseline Current Step Experiments</i>	24
2.2.7 <i>Simulating Sinusoidal Waveform Experiments</i>	24
2.2.8 <i>Statistical Comparison to Experimental Results</i>	25
2.3 Results	25
2.3.1 <i>Unmodified HK Model Is Insufficient to Reproduce GVS-Evoked Responses</i>	27
2.3.2 <i>EPSC Arrival Rate Increases Firing Rate without Affecting CV*</i>	28
2.3.3 <i>Channel Conductances Determine Maximum Firing Rate and Firing Regularity in Response to GVS</i>	29
2.3.4 <i>GVS Stimulation Maintains CV* by Changing Sampling Variance of EPSCs</i>	31
2.3.5 <i>Hypothesis for Similarity between Preservation of CV* with GVS and Naturally</i>	32
2.3.6 <i>Axonal Response to GVS Alone is Insufficient to Explain Firing Rate Adaptation and Rapid Onset Response</i>	33
2.3.7 <i>Simulating GVS Effects on the Hair Cell</i>	35
2.3.8 <i>Filtering Effects of Hair Cell-Afferent Model Explain Frequency Responses</i>	38
2.3.9 <i>The Complete In Vivo Vestibular Afferent Model Behavior Predicts Experimental Outcomes</i>	40
2.4 Discussion and Future Directions.....	42
2.4.1 <i>Afferent and hair cell properties implicated in GVS-modulated responses</i>	43
2.4.2 <i>Implications of targets of GVS stimulation for integration in prostheses</i>	48
2.5 Findings in the Context of Vestibular and GVS Research	49
2.5.1 <i>A Cohesive Theory of Natural Vestibular Firing and Regularity</i>	50
2.5.2 <i>Possible Sources of Conflicting Results of Galvanic Vestibular Stimulation</i>	54
2.5.3 <i>Possible Alternative Vestibular Afferents Mechanisms that May be Engaged in GVS</i>	57
2.5.4 <i>Conclusions</i>	60
2.6 Appendix	61
Chapter 3 : Rules of Pulsatile Stimulation	63
3.1 Introduction.....	63
3.2 Methods.....	64
3.2.1 <i>Vestibular Afferent Experimental Paradigm</i>	64

3.2.2 Data Fitting with Equation $F = \phi(R, I, S)$	66
3.2.3 Biophysical Modeling of Vestibular Afferents.....	67
3.2.4 Simulated Pulsatile Stimulation Experiments.....	69
3.2.5 Predictive Equation.....	70
3.2.6 Pulse-Pulse Interactions.....	70
3.2.7 Pulse-Spontaneous Interactions.....	73
3.3 Results.....	76
3.3.1 Effects of Pulses on Neurons with No Spontaneous Activity.....	79
3.3.2 Effects of Pulses on Spontaneously Firing Neurons.....	82
3.3.3 Predictability of Single Neuron Responses.....	85
3.3.4 Implications for Current Usages of Pulsatile Stimulation.....	87
3.4 Discussion.....	91
3.5 Further Support for the Effects of Pulsatile Stimulation on Neurons Across Neural Systems.....	94
3.5.1 Support for Non-linearities observed in Steinhardt et al. (2021).....	97
3.6 Appendix.....	100
Chapter 4 : Using Electrical Stimulation to Create More Naturalistic Neural Implants.....	102
4.1 A General Approach for a Novel Neural Implant Algorithm.....	102
4.2 A Novel Neural Implant Front-end Focusing on Cochlear Implant Usages.....	105
4.2 Methods.....	108
4.2.1 Generation of Training and Test Waveforms.....	108
4.2.2 Modeling Cochlear Neuron Response.....	110
4.2.3 Recurrent Neural Network (RNN) Model.....	110
4.2.4 Performance Metrics.....	111
4.3 Results.....	112
4.3.1 Performance on Synthetic Sounds.....	114
4.3.2 Performance on Natural Sounds.....	114
4.3.3 Real-time Applicability.....	115
4.4 Utilizing Electrical Stimulation for a Better Neural Implant Back-End.....	118
4.5 Discussion.....	119
Chapter 5 : From Single Neurons to Population-Level Effects.....	121
5.1 Introduction.....	121
5.1.1 Viewing the Brain as a Network of Neurons.....	121
5.1.2 The Role of Electrical Stimulation in Network Neuroscience.....	122
5.1.3 Studying Differences between Pulsatile and Electrical Stimulation in a Decision-Making Network.....	124
5.2 Materials and Methods.....	126
5.2.1 Perceptual Decision-making Task.....	126
5.2.2 Biophysical Attractor Model.....	126
5.2.3 Realistic Intracortical Microstimulation.....	127
5.2.4 Simulating Distinct Virtual Subjects.....	128
5.2.5 Decision Data Analyses.....	128
5.3 Results.....	129
5.3.1 Behavioral Differences.....	129
5.3.2 Differences in Spatial Spread of Neuronal Activation during Pulsatile and Galvanic Stimulation.....	131
5.3.3 Differences in Spike-timing.....	132
5.3.4 Population-level Differences.....	134
5.4 Discussion.....	135
5.4.1 Future Directions.....	136
Chapter 6 : Conclusions.....	138
6.1 Limitations of Biophysical Modeling.....	138
6.2 Future Directions.....	139
6.3 Implications and Impact.....	140

References.....	143
Curriculum Vitae	154

List of Tables

<i>Table 2-1. State Transitions for Nav 1.5 Channel</i>	19
<i>Table 2-2. Summary of findings about Galvanic stimulation</i>	42
<i>Table 2-3. Variables used throughout Equations for Modeling Biophysical Effects of Galvanic Stimulation</i>	61
<i>Table 3-1. RMS across simulations of vestibular afferents with different spontaneous rates and normal conductance levels</i>	85
<i>Table 3-2. RMS Values and Percent Error Per Afferent</i>	87
<i>Table 3-3. Variables used in Equations for Modeling Pulsatile Interactions.</i>	100
<i>Table 4-1. Parameters for Sinusoidal Input Generation</i>	109
<i>Table 4-2. Parameters for Step Input Generation</i>	109

List of Figures

Figure 1. Hair cell-Afferent Morphology.....	9
Figure 2. Spatial Location and diversity of Afferent Terminals.	12
Figure 3. The Six Distinctive Effects of GVS Stimulation	14
Figure 4. Diagram of the axonal model based on Hight and Kalluri (2016)	26
Figure 5. Role of afferent axon in GVS response.....	28
Figure 6. Effect of Conductances on Maximum Firing Rate	30
Figure 7. Distortion of CV-ISI with Axonal GVS only.	32
Figure 8. Effect of Nav 1.5 Channels on Observed Transients	34
Figure 9. Adaptation in GVS modulated afferent response	35
Figure 10. Responses to sinusoidal GVS modulation can be accounted for by the hair cell adaptation response.	38
Figure 11. The complete effects of GVS in the in vivo model including hair cell adaptation.....	40
Figure 12. Effect of EPSC Arrival Rate on Phase	42
Figure 13. A theory for CV* naturally and in response to GVS.....	53
Figure 14. Physical Factors that Affect Frequency Response.....	55
Figure 15. Cross-species comparison of Vestibular Filtering Effects to Galvanic Electrical and Mechanical Stimulation	57
Figure 16. Contributing factors to Vestibular Processing Differences	60
Figure 17. Paradigm for Studying Pulsatile Stimulation	77
Figure 18. Map of firing rate changes in response to pulse rate trains given spontaneous activity (S) and pulse amplitude (I)	79
Figure 19. Effects of Pulse on a Silent Neuron	82
Figure 20. Interactions of Pulses with Spontaneous Firing	83
Figure 21. Prediction of Experimental Vestibular Afferent Responses	85
Figure 22. Effect of Conductance on Response with Current	87
Figure 23. Effect of Regularity on Pulsatile Stimulation.....	89
Figure 24. Using Rules to Achieve Desired Spike Rates in Single Neurons	91
Figure 25. Evidence of Non-linear mapping of Output with Pulse Parameters.....	97
Figure 26. Evidence of Predicted Non-Monotonicities Across Systems	100
Figure 27. General Architecture of Neural Implant	105
Figure 28. Front-end Processor Experiment Design	106
Figure 29. Comparison of CIS to Natural Sound Encoding in Cochlea	107
Figure 30. Network architecture for this study	111
Figure 31. Loss/Performance with Epochs.....	113
Figure 32. Relative Performance on Sine and Step Waveforms	113
Figure 33. Performance on Natural Sounds.....	116
Figure 34. Run-time Evaluation of RNN	117
Figure 35. Uses of Electrical Stimulation to interact with Networks of Neurons	122
Figure 36. Predicted Effects of Electrical Stimulation on a Population of Neurons.....	123
Figure 37. Decision Making Experiment Design and Simulated Implementation	127
Figure 38. Effects of Pulsatile and Galvanic Stimulation on Decision Making and Decision Time	130
Figure 39. Effects of Pulsatile and Galvanic Stimulation in Connected Network.....	131
Figure 40. Differences in Induced Spike Timing between Pulsatile and Galvanic Stimulation	133
Figure 41. Effects of Pulsatile and Galvanic Stimulation on P1 Firing Rate during Wins and Loses	135
Figure 42. Raster Plots across Different Stimulus Coherences and Stimulation Paradigms.....	136

Chapter 1 : Introduction

1.1 Significance

Neural implant and electrical stimulation-based treatments are becoming increasingly common due to the clinical success they have demonstrated, particularly for treating neurological issues such as sensory loss (hearing, vision, and balance) ^{1,2} that have no alternative pharmacological treatment and medically resistant epilepsy or Parkinson's disease^{3,4}. They have also become more promising for treatments for issues, such as chronic pain, due to their system specificity, removability, and lack of addictive effects⁵. According to the U.S. Department of Health and Human Services, over 20 million people suffer from peripheral nerve damage; 1.7 million U.S. citizens suffer from traumatic brain injuries; 12,000-20,000 new spinal cord injuries occur every year; and millions of people remain limited by neurogenerative disorders, such as Parkinson's disease^{6,7}; all of these disorders having treatments in the form of neural implants. In addition to these possible uses, as neural implants improve, they are becoming of more interest in the commercial and human-enhancement spaces. At the same time, the number of people with neural implants remains limited, because the level of restored function across use cases is substantially below the normal level ^{1-3,8,9}, and these devices require major surgery for implantation; this has caused neural implants to remain a last resort for most treatments^{4,10}.

Over the last fifty years, there have been concerted efforts across neural systems to understand the limitations of neural implants and to improve them. Much of this work has focused on improving the electrode materials for safer implantation and ability to deliver stronger current amplitudes¹¹⁻¹³. An important finding was that delivering electrical current for a prolonged duration from a metal electrode in implanted tissue produces toxic electrochemical reactions; this led to a reliance on short, biphasic pulses of electrical stimulation in scientific and clinical use cases¹⁴. As a result, neural implants presently all contain implanted pulse generators (IPGs) and rely on pulse amplitude or pulse rate modulation strategies to encode information or interfere with neural firing^{4,15-17}. Even as prosthetics developed with higher density electrodes and improved strategies for preventing current spread^{18,19} to more accurately target desired populations, plateaus in functional restoration have remained²⁰. In this work, we focus on understanding the effects of

what we term “galvanic stimulation,” delivering non-pulsatile waveforms without constraining signals to keep delivered waveforms charge-balanced. Recent work in non-invasive galvanic stimulation has shown additional effects on plasticity and cognition, which has revived interest in non-pulsatile stimulation²¹. Additional development of a microfluidic-based implantable stimulator that is capable of delivering direct current, sinusoidal current, or arbitrary waveforms without producing detrimental electrochemical effects²²⁻²⁴ at the point of stimulation opens an avenue of invasive research: how non-pulsatile stimulation can improve neural interfaces²⁵⁻²⁷.

This work aims to address this question by first using biophysical modeling of the effects of galvanic (non-pulsatile) and pulsatile stimulation on vestibular afferents – a target of vestibular prostheses – to understanding existing evidence for why galvanic stimulation produces more natural responses at the single cell and behavioral level than pulsatile stimulation²⁷⁻²⁹. It then takes a more universal perspective on how these findings will apply to other neural systems, based on the biophysical understanding gained of the single cell interactions observed at the vestibular afferent hair cell, and this understanding of electrical stimulation and machine learning techniques is used to put forward a novel neural implant algorithm architecture that could be used to induce more naturalistic firing and improve neural prosthetic performance across systems and neurological disorders.

1.2 Background

1.2.1 The Role of Electrical Stimulation in Neuroscience Research and Treatments

The possibilities of coherently driving the brain using electrical stimulation has been a fascination of the field of neuroscience and the public alike, since the first experiments of Luigi Galvani inspired Mary Shelley’s *Frankenstein*³⁰. Very quickly, electrical stimulation became the main tool for advancing neuroscientific understanding. In the late nineteenth century, Fritsch and Hitzig first used it to establish a functional association between different parts of the nervous system and evoke movements from the brain³¹. In the early twentieth century, Krause³² and Cushing³³ began to perform electrical stimulation of the human brain to elicit motor responses, and Foerster stimulates the human brain while recording from neurons³⁴. His student Penfield then performed studies on sensory, motor, and cognitive effects of electrical stimulation in humans³⁵. A parallel history deriving from Galvani’s first experiments in muscles was a study of conduction

velocity in the peripheral nervous system, which leads to the development of the first technology for recording an action potential and the understanding of the resting potential and electrical action potential produced by neurons³⁶. By the mid-twentieth century, Hodgkin and Huxley had uncovered voltage-gated channels that drive action potentials and created differential equations to model their effects^{37,38}, and electrical properties of dendrites were under investigation as well³⁹. From there, the field continued to use electrical stimulation for understanding of complexity cognition, such as decision making and object identification^{40,41}. Electrical stimulation experiments are presently common, particularly in epilepsy clinics as a tool for understanding the human brain, because powerful genetic tools, such as optogenetics, are not viable for study of human subjects. Thus, electrical stimulation continues to be an essential tool for investigating functional and anatomical connectivity in the human brain⁴²⁻⁴⁴ in addition to finding uses in the study of electrical effects on glia and nerve regeneration among other newer usages⁷.

Just as the underpinnings of the action potential were being understood, the first implantable cardiac pacemakers were invented and used to successfully extend lives⁴⁵. Due to similarities between the electrical cardiac cells and neurons, this quickly brought on a new era in which electrical stimulation had many potential uses in the form of neural implants. Since the invention of the pacemaker, the architecture of neural implants has not greatly deviated from an implanted pulse generator (IPG), a device for sending short pulses of current through tissue, and metal electrodes delivering current to target tissue; using this technology, there is now a neural implant for nearly every function of the nervous system⁴. In addition to neural implants for sensory replacement (cochlear implants, retinal prosthetics, and vestibular implants), there are devices for disrupting pathological function, such as deep brain stimulators (DBS) for Parkinson's disease, or spinal cord stimulators (SCS) for chronic pain, and emerging treatments for psychiatric disorders^{4,10}. Additionally, electrical stimulation is important for assessing neurological function⁵⁰, and pre-resection mapping is highly important to minimizing inadvertent, negative effects of epilepsy resection surgeries^{46,47}.

1.2.2 Limitations of the Existing Electrical Stimulation Paradigm

Although there are substantial clinical successes with neural implants, such as the cochlear implant that has restored speech perception and improved language acquisition for children around the world ², neural implant users experience significant reduction in function for implanted neural systems, compared to healthy

subjects. For example, cochlear implants users understand non-tonal language very well, but they struggle with hearing in noise, which likely involves engagement of top-down circuits, and pitch perception, which is encoding with complex spike-timing in healthy subjects^{2,48,49}. In vestibular prosthetics, induced eye velocities are significantly slower than healthy subjects, and central regions shows adaptation to stimulation inputs that have been implicated in this reduced response²⁹. Other implants, like SCS, may not be able to alleviate pain consistently across patients and over time⁵⁰.

A number of solutions have been enacted to improve neural interfaces. Based on the early success of the cochlear implant, a large focus of the field of neuromodulation has been on increasing the density of electrodes that can be implanted in a small area to improve control of neurons; however, cochlear implant studies show that there are additional problems that are not resolved with higher electrode concentration^{20,51}. Changes to the electrode material to minimize immune responses and increase safe charge injection capacity have also been heavily studied^{12,52,53}. Improvements to stimulation algorithms have also been investigated. The waveform shape of current delivery has been investigated to some extent⁵⁴; however, exploration has been primarily restricted to biphasic, charge-balanced electrodes because delivery of charge from metal electrodes for even a few milliseconds causes toxic electrochemical reactions that damage neural tissue¹⁴. So, investigations have typically taken place in the context of delivery of biphasic, charge-balanced electrodes. Initially, the choice of stimulation parameters was empirically determined⁴. Innovations included improvements of perception with high-rate pulsatile stimulation^{55,56}, rapid delivery of thousands of short pulses of current per second, and high rate blocking⁵⁵⁻⁵⁸, as pulses traditionally are used to induce action potentials. A more recent focus has been on developing algorithms capable of inducing more naturalistic function^{59,60}. Optimization approaches have become popular, in which stimulation parameters are optimized to produce a target behavioral or neural response; alternatively control-loops are used to improve device responses to on-going neural activity^{4,61,62}. Additionally, there has been some work on model-based approaches, using complex models of neural function to determine stimulation patterns, but these algorithms have had mixed success and often suffer from being too computationally intensive. Thus, pulse rate and pulse amplitude modulation paradigms are still the norm in neural implants^{4,60,63,64}.

1.2.3 The Re-emergence of Galvanic Stimulation as an Alternative to Pulses

Prior to a focus on creating implantable neurostimulation devices, galvanic stimulation (GS), stimulation with non-charge balanced waveforms capable of producing irreversible electrochemical reactions in metal electrodes, including direct current, sinusoids, or arbitrary waveforms, was common in electrical stimulation studies^{28,30,36,65}. Due to restrictions for safe charge delivery in neural implants, the focus of the field turned to pulsatile stimulation-based algorithms and studies of neural function. However, galvanic stimulation has returned to use in clinical studies in several forms. GS is used externally, as transcranial direct stimulation (tDCS) for a number of different uses, particularly for psychiatric treatments⁶⁶⁻⁶⁹. It is also used in the vestibular field for testing vestibular function, particularly while using sinusoidal stimulation^{70,71}. While both these effects involve GS, because of the external current delivery mechanism currents are of very small magnitudes and affect large populations of neurons, which effects local function and networks of neurons differently than localized pulsatile stimulation^{72,73}.

Drawing upon a bridge rectifier stimulation concept described in 2001 by Spelman et al.⁷⁴, the Fridman lab at Johns Hopkins University has recently developed technology to safely deliver GS in an implantable device. The device, formerly known as the Safe Direct Current Stimulator and now renamed the Freeform Stimulator, uses a microfluidic H-bridge architecture and electrodes comprised of an ionic gel, as opposed to a metal electrode to deliver current^{22,24,75,76}. This construction prevents toxic reactions from affecting neurons and allows the device to locally deliver galvanic current of any waveform for seconds or more without having toxic effects. With the development of this device, current delivery with the spatial specificity of present neural implants is now possible⁷⁵. *In vitro* studies of GS have already shown the GS has effects on neural regeneration and plasticity, which are not observed with pulsatile stimulation^{7,76,77}. Using this novel technology, localized GS has been shown to have more naturalistic effects on firing pattern and behavior, as well, further supporting investigations into uses for GS in implantable devices.

1.2.4 Using the Vestibular System as a Window into Effects of Electrical Stimulation

The vestibular system is ideal for this study because vestibular afferents have several characteristics that make them helpful for understanding the effects of electrical stimulation on neurons more generally, and the vestibular system is one of the few in which the effects of galvanic stimulation and pulsatile stimulation have been systematically investigated at the level of single neurons.

Vestibular afferents have multiple characteristics that would be informative about electrical interactions with other neuron types. Vestibular afferents encode head velocity by modulating firing rate compared to a spontaneous firing rate that averages 100 spikes per second (sps) in healthy humans and squirrel monkeys (the animal model used in the main galvanic stimulation studied discussed below (Goldberg et al., 1984). Firing modulates with a well-characterized natural firing regularity, which is measured with a CV* value, a corrected measure of the coefficient of variation of firing^{28,78}. Additionally, vestibular afferents have an axon that produces action potentials using standard voltage-gated sodium and potassium channels, as opposed to calcium-channels^{79,80}, gap junctions⁸¹, or other more atypical mechanism in periphery cells. Finally, vestibular afferents also receive inputs from hair cells, sensory endings of smaller size and different geometry than an axon⁸²⁻⁸⁵, so the effects of GS could be compared with pulsatile stimulation on axons and end organs to draw conclusions about differences between the two forms of ES.

Vestibular afferents are also one of the few neuron types that have been targeted with galvanic and pulsatile stimulation and studied in detailed on the single neuron level. Studies have shown that direct current GS has can modulate vestibular afferent firing up or down from baseline proportional to the current amplitude while maintaining CV*^{27,28}. The effects on induced eye velocity using GS versus pulsatile stimulation of the semicircular canals has also been compared. GS has been shown to induce larger eye velocity responses than pulsatile stimulation that approach natural excitation and create up to three-fold larger eye movements to inhibitory inputs. These results suggest that GS more naturally interacts with the vestibular pathway overall. Investigations of the effects of pulsatile stimulation on vestibular afferents show that only about half of pulses expected to produce action potentials do so when vestibular afferents are stimulated; additionally, central vestibular neurons adapt to pulsatile stimulation in the absence of natural input, and restoration of natural input recover neural responsiveness^{29,86}. These finds suggest that the firing patterns produced by stimulated vestibular afferents are detrimentally different than natural inputs. Within these papers, speculations are made that the issue may be the with unnatural, synchronous spike-timing produced with pulsatile stimulation^{29,86}. These existing results in the vestibular system motivate using the vestibular system to investigate the reason for differences between the effects of galvanic and pulsatile stimulation from the single neuron level upward.

This work therefore starts by using detailed biophysical modeling of vestibular afferents to understand the difference between galvanic and pulsatile stimulation. An existing biophysical model of the vestibular afferent was shown to produce firing with specific regularities observed naturally and to be excited and inhibited by simulated galvanic stimulation⁸⁷. Chapters 2 and 3 directly simulate the experiments in the vestibular system highlighted above and do a detailed investigation of the biophysical underpinnings of the observed responses to ES. Chapter 4 shows how these findings can be built into improving biomimetic algorithms, using a model-based approach, and Chapter 5 discusses the implications of these results for scientific uses of electrical stimulation, such as functional mapping and driving behavior from a network perspective.

Chapter 2 : A Cohesive Theory of Galvanic Electrical Stimulation

2.1 Introduction

In contrast to conventional pulsatile neural prostheses used to excite neural targets⁴, galvanic electrical stimulation (GS), and, particularly, direct current (DC) neuromodulation emerged as having potential for use in a variety of new medical treatments due to its unique ability to evoke a broad range of beneficial clinical effects on target neurons⁷⁵. These have been shown in its ability to achieve peripheral nerve block for pain suppression^{88,89} modulate cortical activity and synaptic connectivity for psychiatric treatments^{21,66,90}, and excite and inhibit vestibular afferent activity to treat balance disorders^{27,75}. Recent innovations with DC stimulation technology have also led to the development of safe direct current stimulation (SDCS)^{22,75,91,92}, which makes it possible to chronically deliver localized direct ionic current. This innovation has taken the form of a biocompatible technology that is of a scale that it will soon be translatable to implantable devices. Preliminary behavioral testing of the Freeform Stimulation (FS) for vestibular balance disorders (in the form of vestibular occur reflex tests) as well as for the treatment of pain suppression revealed that DC neuromodulation has multiple beneficial effects on targeted neural populations that cannot all be produced with pulsatile stimulation, including inhibiting, exciting, and sensitizing neural targets in a natural, desynchronized manner^{25,75,93}. While these behavioral results are encouraging, the cellular mechanisms that respond to electric fields are not well understood. In this work, we study the effects of GS in the vestibular system, where there is a relatively long history of using it to generate an explanation of the effects of GS not only in the vestibular system but on other neurons based on similarity in physiology between vestibular afferents and other neuron types. To be consistent with the terminology used in the field of vestibular neuromodulation that is addressed here specifically, we refer to this non-pulsatile current delivery as “galvanic vestibular stimulation”, or GVS throughout the following sections.

2.1.1 A Brief Introduction to Vestibular Afferents

The vestibular pathway is highly specialized to allow rapid, highly sensitive responses to head motions. Unlike many neural pathways, the pathways from the semicircular canals to eye movement only contains two synapses, and a significant amount of complexity is built into the point of sensation, the vestibular

afferent. As a result, there is abundant morphological diversity observed at the vestibular hair cell, synapse, and afferent. Despite this diversity, vestibular afferents share a unique set of firing properties that have been central to vestibular research for the last several decades: a rapid response to head rotations, a high spontaneous firing rate, and a neuron-specific inter-spike timing distribution that is characterized with the CV* statistic; vestibular firing modulates up and down around a baseline rate proportional to head velocity changes while preserving these firing statistics^{94,95}.

Much is known about hair cell and afferent signaling, although the contribution of each of the points of morphological diversity is still under investigation. This study focuses on the responses of vestibular afferents to electrical and natural stimulation. Generally, when a vestibular afferent responds to natural stimulation - a head movement - it deflects stereocilia of the hair, causing the hair cell to modulate transmitter release onto afferent neuron terminal via a ribbon synapse, a specialized glutamate synapse that allows rapid release of pools of vesicles⁹⁶.

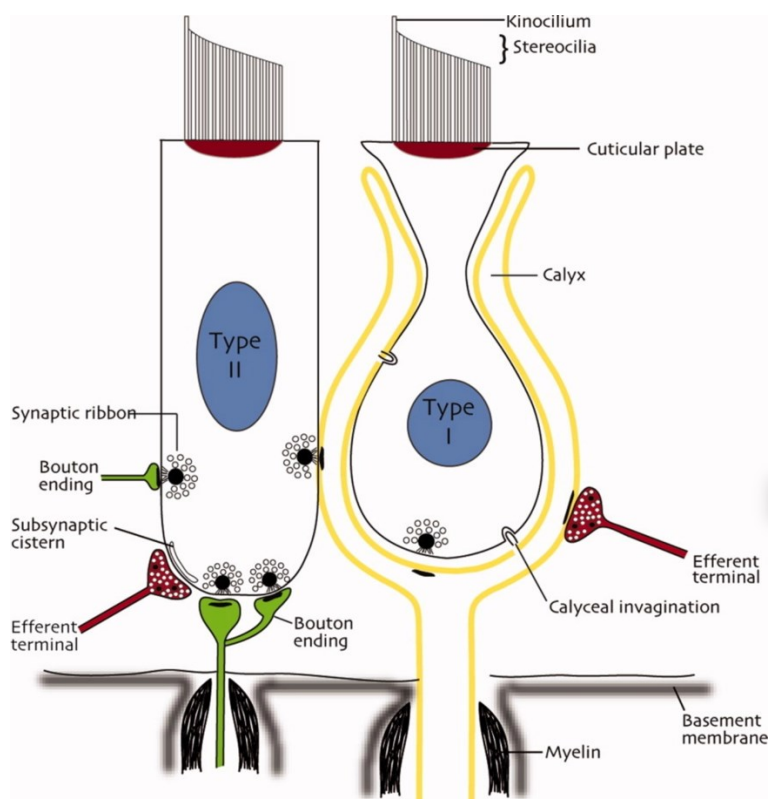


Figure 1. Hair cell-Afferent Morphology

Type II hair cells (rectangular) connect to bouton endings. Type I hair cells (flask shaped) are surrounded by calyces. Both are mechanically activated by deflection of stereocilia. Efferent terminals input at the Type II hair cell and the calyx of the afferents below Type I hair cells. Adapted from Highstein and Holstein (2012).

There is morphological diversity at each level of this pathway. Type I hair cells tend to have a flask-shape, and Type II hair cells tend to have a cylindrical shape (Figure 1)⁹⁵. Afferent terminals have three distinct morphologies: a small bouton connection to the hair cell, a calyx connection, which surrounds the hair cell, and a dimorph, which has a mixture of calyces and boutons (Figure 1). While hair cells are illustrated with one-to-one connections, calyces surround 1-5 Type I hair cells⁹⁵, and estimates have been made that afferents average 10-100 boutons contacting one or more hair cells⁹⁷ over distances of 25 to 75 μm ⁹⁴. Dimorphic fibers provide a mixed innervation of 1-4 calyx endings (that surround Type I hair cells) to 1-50 bouton endings to Type II hair cells⁹⁴. Localization studies reveal that both the utricle and the cristae of the semicircular canal have a region, like the macula of the eye, of higher sensitivity to input. For the cristae, the central region is primarily filled with calyces and dimorph terminals and the periphery with boutons (Figure 2)^{98,99}. This has been observed across turtles, chinchillas, and mammals. The functional differences appear to be that terminations with calyces tend to have higher spike timing irregularity than afferents with only boutons. Regularity has come to be defined as neurons of CV* value less than 0.1, although vestibular afferents smoothly take regularities between 0 and 1. However, channels within the afferent have also been implicated as the main reason for differences in spike regularity⁸⁷. Which physiological attributes contribute to differences in regularity and the reason that CV changes with firing rate but with a fixed range of CV values per neuron (CV*) has yet to be explained.

Additionally, there are two other synaptic effects of vestibular afferents that have become a topic of deep investigation in the last decade: the non-quantal effect and efferent inputs to the vestibular hair cell and afferent. How these features play a role in natural vestibular processing as well as how they may interact with GS is important to this work. The non-quantal effect is specific to the Type I fibers and known to occur at calyces but not at bouton connections^{100,101}. Quantal transmission at the hair cell-afferent complex refers to release of neurotransmitters, while non-quantal (NQ) transmission or the NQ effect refers to ephaptic coupling and potassium accumulation in the synaptic cleft^{101,102}. The importance of the NQ effect remains unclear, partially because it is difficult to experimentally measure differences in potential and ion concentrations at the hair afferent and hair cell. A leading theory is that the NQ effect evolved to allow faster input to reflex pathways to ensure stable locomotion¹⁰⁰. The current understanding is that the NQ effect causes an increased sensitivity to incoming EPSC inputs and other depolarizations at the afferent, which

averages around a 4-fold increase in the turtle¹⁰³. One related observation may be that low voltage potassium channels (KL), which are prevalent within the calyx, open more with depolarization and result in reduced input resistance⁸³. This channel opening may trigger increased afferent sensitivity during the NQ effect. Additionally, elevated potassium near the hair cell is thought to depolarize the hair cell such that significantly lower currents are sufficient to trigger synaptic vesicle fusion¹⁰⁴. Together these effects would lead to increased firing by direct depolarization of the axon¹⁰⁵. Additionally, they could increase the frequency of quantal release and increased sensitivity of the axon to EPSPs.

Unlike the NQ effect, efferent transmission affects neurons of all firing regularities via inputs to Type I calyces and Type II hair cells¹⁰⁶. Efferents importantly exist in all vertebrates with relatively conserved location within the vestibular system and brain stem nuclei. They have thus been suggested to perform a similar function of modulating vestibular afferent sensitivity based on context or some other top-down signal^{106,107}. However, there are fewer clustered groups of efferents in non-mammalian vestibular systems, and efferents more often project unilaterally with larger dendritic arborizations as opposed to bilaterally, implying differences in information processing across vertebrates¹⁰⁸. A majority of non-mammalian and all mammalian efferents seem to cause an increase in background afferent discharge, and these effects are more pronounced in irregular afferents¹⁰⁹⁻¹¹¹. However, inhibitory responses have also been observed. Additionally, efferents have commonly been found to have inhibitory effects on hair cells that have been related to differences in acetylcholine receptors at the hair cell and afferent^{109,112}. The mammalian efferent system is still in the process of being investigated, but current hypotheses point to efferents having a long-term effect on processing in vestibular afferents. Efferents are significantly smaller than afferents, so they are not thought to be excited by pulsatile stimulation, but GS has been shown to depolarize dendrites and thus may interact with efferents⁷⁶,

In this chapter, as the effects of GVS are explored, the question is raised why firing rates induced using GVS take on naturalistic firing regularities and other characteristics observed in response to mechanical perturbation¹¹³. Although the NQ effect and efferent contributions had not been modeled in detail at the time of this study, this section considered how channels of the afferent, hair cell vesicle release, the non-quantal effect, and efferent-induced effects may also be influenced by GVS.

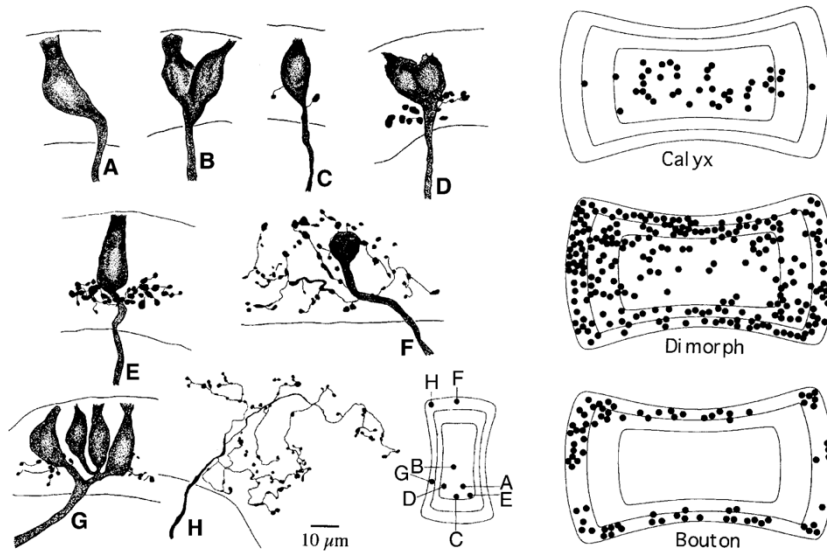


Figure 2. Spatial Location and diversity of Afferent Terminals.

a-h) show different combinations of **a-b)** calyx-bearing **c-g)** dimorphic and **h)** bouton-ending fibers. (right) spatial distribution of each type of fiber and (lower right) locations of afferents **a-h)**. Adapted from Goldberg (2000)

2.1.2 History of Galvanic Stimulation in the Vestibular System

GVS modulation in the vestibular system has revealed a number of effects of galvanic stimulation on neurons that require explanation summarized in Figure 3: (I) low amplitude GVS can both increase and decrease firing rate depending on the polarity^{27,28}; (II) cathodic GVS can cause dramatic increases in firing rate of up to 2.5 spikes per second (sps) per μA^{28} ; (III) vestibular afferents fire with specific spiking regularity or coefficient of variance (CV) profile termed CV*, and GVS can maintain this regularity while changing firing rate²⁸; (IV) long duration GVS step induces an immediate change in firing rate that adapts back to a new baseline firing rate on the scale of seconds^{27,28}; (V) after a baseline of GVS, the afferent appears to sensitize, showing a weaker inhibitory response after an inhibitory (anodic) baseline and weaker excitatory response after an excitatory baseline²⁷; (VI) sinusoidal GVS leads to increased/decreased firing rate in the cathodic/anodic half of a cycle with increased frequency of sine wave, and the neuronal response shows a phase lead for frequencies above 4 Hz that decreases to zero around 4-8 Hz^{27,71}. Although other studies of the effects of galvanic stimulation on single neurons exist^{71,114}, we focus on modeling data from the Goldberg, Smith, Fernandez (1984) and Manca *et al.* (2019) studies because the stimulation protocol (electrode placement, invasive approach, etc.) for both experiments was made as similar as possible. Thus, both experiments could be simulated with no changes to the experimental protocol but only to vestibular afferent

properties. Together these results create a set of vestibular afferent response characteristics to GVS that are informative about vestibular function and targets of galvanic stimuli.

Based on the range of the galvanic-affected response characteristics that appear to match natural mechanically-evoked firing behavior of the afferents¹¹³ as well as mechanically-evoked vestibulo-ocular reflex (VOR) response^{25,114}, we hypothesize that GVS must be activating natural cellular mechanisms in both the afferent and the hair cell.

To test this hypothesis, we systematically modified a computational model of a GVS-stimulated irregular axon-hair cell complex until it could completely reproduce all natural and GVS-induced responses from the experimental studies being simulated. Irregular afferents primarily innervate the center of the striola and are highly sensitive to motion detection. Although Type II hair cells and bouton endings may connect to some of the recorded afferents, making them dimorphs, for simplicity, in this study, a one-to-one Type I hair cell to afferent connection was assumed for modeling. Irregular afferents provide a useful case study for how GVS could affect afferents at their inputs as they have particularly tight connectivity to Type I hair cells via large calyceal synapses^{82,104}. Additionally, they fire at a high spontaneous rate which allows both excitatory and inhibitory effects of stimulation to be analyzed. These properties can be used to make predictions about effects on Type II hair cells, less regular afferents and bouton inputs, as well.

We began this procedure by implementing the Hight and Kalluri (HK) model, the most recent and detailed mechanistic model of the vestibular afferent⁸⁷ and subjecting it to electric fields induced by locally applied GVS (within 1mm). We first modified model parameters to simulate afferents with firing ranges and statistics of what we consider a typical *in vivo* (data that we will refer to as the Goldberg data or neurons). We found this model was unable to reproduce all observed effects of GVS stimulation. Then, we added simulations of physiologically relevant hair cell and synaptic behaviors not previously present in the model, based on our hypothesis. We additionally include data from an *in vitro* study of rat neurons that we will refer to as the Manca data or neurons. We conclude that all experimentally observed behaviors can be replicated when the hair cell and synaptic modulation by GVS are introduced into the model. The results section describes these systematic modeling results and modifications to the HK model that led to the mechanistic theory we put

forth. The paper concludes with (Table 2-2) of the necessary axonal and hair cell mechanisms implicated in GVS neuromodulation in order to produce Effects I-VI described in Figure 3.

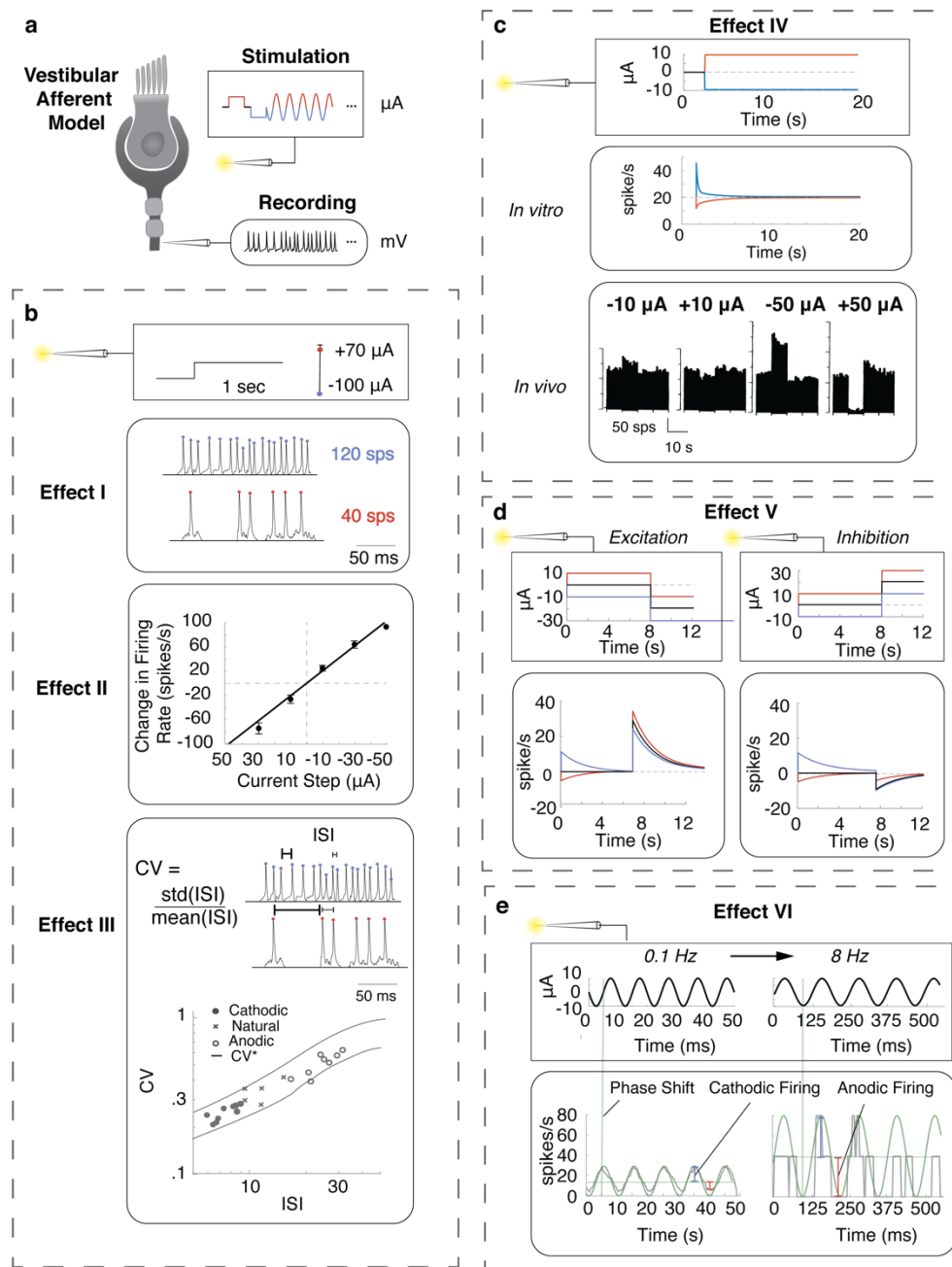


Figure 3. The Six Distinctive Effects of GVS Stimulation

Experimental studies of GVS have revealed six effects on vestibular afferents. They were investigated in irregular afferent responses with the hope of understanding hair cell, calyx, and afferent contribution. **a)** Square boxes indicate the GVS stimulus, and rounded boxes represent the corresponding neural responses from the vestibular afferent. **b)** Transient response patterns. Effect I. Low amplitude GVS stimulation increases and decreases firing rate with cathodic (blue) and anodic (red) current. Effect II. Cathodic GVS stimulation can cause dramatic increases in firing rate of up to 2.5 spikes per second (sps) per μA. Effect III. GVS stimulation can maintain firing regularity (CV*) while changing firing rate; **c)** Long duration adaptation. Effect IV. Long term GVS stimulation induces an immediate change in firing rate that adapts to a new baseline firing rate on the scale of seconds. In vivo (black) adaptation occurs with baseline offset in firing rate. **d)** Adaptation from different GVS-evoked baselines. Effect V. After adaptation to a baseline of GVS

stimulation, the afferent shows a smaller inhibitory response after an inhibitory (anodic) baseline and smaller excitatory response after an excitatory baseline. **e)** Responses to sinusoidal modulation. Effect VI. Sinusoidal GVS modulation leads to increased/decreased firing rate in the cathodic/anodic half of a cycle with increased frequency of sine wave. Measures of firing rate were taken on average during each phase (e.g. cathodic firing), and the neuronal response shows a phase shift compared to stimulation sine functions that showed a consistent phase lead for frequencies above 4 Hz that decreases to zero around 4-8 Hz. In vivo data in b,c is adapted from Goldberg, Smith, Fernandez (1984). In vitro data in c,d,e is adapted from Manca et al. (2019).

2.2 Methods

2.2.1 Vestibular Axon Model

Although vestibular afferents take on a range of irregularities in firing, vestibular afferents can be broken into the dichotomy of irregular and regular neurons. Both types of afferents differ in physiology, synaptic inputs, and channel expression. However, the Hight & Kalluri model showed that vestibular firing can be simulated accurately by assuming cells have the same shape and size. Irregular and regular neurons are modeled as differing only in channel expression and EPSC magnitude (K), and interval (μ). The model also uses a set of non-linear differential equations to simulate channel dynamics for a number of channels specific to vestibular afferents, finding only a sodium (Na), high-voltage gated potassium (KH), and low-voltage gated potassium (KL) channel as well as a leak term are necessary to reproduce firing dynamics. The membrane potential (V) varies as:

$$\frac{dV_m}{dt} = 1/(C_m S)(I_{Na} + I_{KL} + I_{KH} + I_{leak} + I_{epsc} + I_{stim}) \quad (2-1)$$

where in addition to the current from each channel, membrane potential is influenced by the EPSCs arriving at the hair cell (I_{epsc}) and the injected current (I_{stim}). The system of equations in ⁸⁷ represents each cell as a single node with overall surface area, $S_m = 1.1 \cdot 10^{-5} \text{ cm}^2$ and capacitance $C_m = 0.9 \text{ mF/cm}^2$ EPSC functions and channel modeling derives from a number of biophysical studies described in full in the methods of the HK paper⁸⁷.

For this study, we use a modified version of the Hight & Kalluri (HK) model to simulate an irregular neuron axon on which to test the response to GVS stimulation (Supplemental Methods). The purpose of the study was to use comparison between two experiments studies performed under similar stimulation conditions but that resulted in difference axonal firing rates to understand how GVS may affect vestibular afferents. We simulate only irregular neurons, because experimental data existed across both studies for long-term and short-term experiments on only irregular neurons. The experimental data came from two studies^{27,28} in which the neurons have different spontaneous firing rates (100 sps and 20 sps) and different firing ranges (0-250

sps and 0-60 sps). To goal was to address the contribution of hair cells, calyces, and afferents to these response and extend our predictions to regular afferents based on our results. Thus, the data focuses on shown data from the Goldberg study Figs. 3, 5, and 7 from units #382-24H, #381-11H and the average irregular afferent data from the Manca study Figs. 2b,d, 3c-e, 4c-f, and 5 (Table 2-2).

In ⁸⁷, a range of biophysically realistic conductance values for mammalian hair cells were given: $g_{Na} = 1.7-75 \text{ mS/cm}^2$, $g_{KL} = 0-1.7 \text{ mS/cm}^2$, and $g_{KH} = 1.8-11 \text{ mS/cm}^2$ based on *in vivo* rodent studies^{115,116}; these values were explored for each channel, and they found irregular firing could be imitated with conductance values: $g_{Na} = 13 \text{ mS/cm}^2$, $g_{KH} = 2.8 \text{ mS/cm}^2$, and $g_{KL} = 1.1 \text{ mS/cm}^2$. Data across studies was combines to make an afferent that could replicate the change in firing regularity (CV^*) observed in the Goldberg *et al.* 1984 study that we model in our simulations, as well. In our simulations, we found g_{Na} and g_{KH} could significantly change the induced firing range of neurons, and g_{Na} had the stronger effect on firing range. Induced firing range similar to regular irregular afferents ($fr = 188 \text{ sps}$) could be simulated with $g_{Na} = 6 \cdot 13 = 78 \text{ mS/cm}^2$, $g_{KH} = 4 \cdot 2.8 = 11.2 \text{ mS/cm}^2$, and $g_{KL} = 1.1 \text{ mS/cm}^2$ (Figure 6). We construct a model *in vitro* axon by lowering conductances such that the induced firing range matched that observed in the study²⁷. There are multiple ways to model a lower conductance axon with lower firing range. To minimize changes in parameters we only decrease g_{Na} to 7.8 mS/cm^2 , and we decreased μ_o to 8-15 ms, to produce lower spontaneous rate, fr_o of 15-20 sps.

In the HK model⁸⁷, hair cells are simulated with a stochastic function that releases vesicles such that EPSCs arrive at a certain inter-EPSC interval with distribution around mean value (μ_o) and with certain measured range of quanta sizes that they scaled by some magnitude (K) for the whole simulation that drives the spontaneous firing rate; the authors find that a number of combinations of K and μ can produce naturalistic firing properties and select $K = 1$ and $\mu = 3 \text{ ms}$ as the settings for simulating a typical irregularly firing neuron. They also tested several EPSC shapes, noting shape did not have a significant effect on the range of K and m_o used to obtain the correct firing properties. We use the EPSC shape that was measured from synaptic current recordings from calyx terminals^{87,117}, with $\alpha = 0.4$ for all studies. To simulation neurons with spontaneous rates that matched of the studies, we assume the quanta size ($K = 1$) is maintained across studies and set the spontaneous rates by changing the mean EPSC arrival rate. For a spontaneous rate of

100-120 sps, $\mu_o = 0.55-0.75$ ms was used. For a spontaneous rate of 15-20 spikes per second (sps) (with the lower firing range conductance values), $\mu_o = 8-15$ ms was used.

The HK study only models intracellular current injection into the axon of a vestibular afferent at a point source of a unmyelinated fiber in perilymph. We also simulate extracellular GVS as a point source, assuming that if this represents the first node of the afferent that received incoming EPSCs it can predict whether action potentials will propagate; the current experienced at the axon is reduced by the distance of the axon to the point source, r , which for an object x vertical and y horizontal distance from the point source is: $r = \sqrt{(x^2 + y^2)}$. Then, the current change of the axon would be the surface area of the axon (S_m) times the current per surface area at a distance r . The increase in firing rate with I_{stim} in the simulation with the HK model is significantly lower than reported in ²⁸. We hypothesized that one reason for this is that the original HK model does not include NQ effects without which the axon would have a lower sensitivity to incoming currents. The internal stimulation current was modeled as

$$I_{stim} = -S_m \frac{I_{electrode}}{4\pi r^2} \quad (2-2)$$

The model of the Manca study only included this positional conversion, because we found evidence that the experimental preparation reduced axonal sensitivity, leading to features of firing such as a low spontaneous rate and firing rate. To achieve the sensitivity observed in the Goldberg study to GVS, we find that the model required including NQ effects in Eq. 2-11. We use specific parameters to match the change in firing rate observed in the sample data from the Goldberg study Fig. 5. We hypothesize for each individual neuron there should be some change in effect size, but we assume that the example relationships shown in the Goldberg study are representative of the population of neurons and, if properly fit in a single model, could simulate the average irregular afferent response or be tuned to closely match other observed firing statistics only by slightly altering parameters.

The channel equations used in the original model can be found below.

$$\frac{dV_m}{dt} = \left(\frac{1}{C_m S_m} \right) (-I_{KL} - I_{Na} - I_{KH} - I_{leak}) \quad (2-3)$$

For every state:

$$\frac{dx}{dt} = (x_\infty - x) / \tau_x \quad (2-4)$$

Sodium Channels

I_{Na}

$$E_{Na} = 82 \text{ mV}$$

$$I_{Na} = g_{Na} m^3 h S_m (V_m - E_{Na}) \quad (2-5)$$

$$m_{\infty} = \left(1 + e^{\frac{-V+38}{7}}\right)^{-1}$$

$$h_{\infty} = \left(1 + e^{\frac{V_m+65}{6}}\right)^{-1}$$

$$\tau_m = 10 \left[5e^{\frac{V_m+60}{18}} + 36e^{\frac{-V+60}{25}} \right]^{-1} + 0.04$$

$$\tau_h = 100 \left[7e^{\frac{V_m+60}{11}} + 10e^{\frac{-V+60}{25}} \right]^{-1} + 0.6$$

Potassium Channels

$$E_K = -81 \text{ mV}$$

I_{KH}

$$\phi = 0.85$$

$$I_{KH} = g_{KH} S_m (\phi n^2 + (1 - \phi)p(V_m - E_K)) \quad (2-6)$$

$$n_{\infty} = \left(1 + e^{\frac{-V_m+15}{5}}\right)^{-0.5}$$

$$p_{\infty} = \left(1 + e^{(-V_m+23)/6}\right)^{-1}$$

$$\tau_n = 100 \left[11e^{(V_m+60)/24} + 21e^{-(V_m+60)/23} \right]^{-1} + 0.7$$

$$\tau_p = 100 \left[4e^{(V_m+60)/32} + 5e^{-(V_m+60)/22} \right]^{-1} + 5$$

I_{KL}

$$I_{KL} = g_{KL} S_m w^4 z (V_m - E_K) \quad (2-7)$$

$$w_{\infty} = \left(1 + e^{\frac{-V_m+44}{8.4}}\right)^{-\frac{1}{4}}$$

$$z_{\infty} = (1 - \gamma) \left(1 + e^{\frac{V_m+71}{10}}\right)^{-1} + \gamma, \gamma = .5$$

$$\tau_w = 100 \left(6e^{\frac{V_m+60}{6}} + 16 \left(e^{\frac{-V_m+60}{45}} \right) \right)^{-1} + 1.5$$

$$\tau_z = 1000 \left(e^{\frac{V_m+60}{20}} + 16e^{\frac{-V_m+60}{8}} \right)^{-1} + 50$$

I_{leak}

$$E_{leak} = -65 \text{ mV}$$

$$I_{leak} = g_{leak} S_m (V_m - E_{leak}) \quad (2-8)$$

Additionally, in supplemental work, we assessed the contribution of other axonal channels to firing to determine whether the axon alone could produce the transient effect. The equations used for this analysis can be found below.

2.2.2 Other Channels Added into the Model:

I_h

$$I_h = g_h(1 - r^3)S(V_m - E_h) \quad (2-9)$$

$$r_\infty = \left(1 + e^{\frac{-V_m + 100}{7}}\right)^{-1}$$

$$\tau_r = 10^5 \left(237e^{\frac{V_m + 60}{12}} + 17e^{\frac{-V_m + 60}{14}}\right)^{-1} + 25$$

$I_{Nav1.5}$

A Markov model implementation of a Nav1.5 channel opening and closing was modified into an efficient matrix multiplication in MATLAB. The original code as individual equations can be found here¹¹⁸. This model relies on capturing changes between two closed states, two open states, and two inactivated states. The rows of the matrix were in the order B (magnitude), v (hemiactivation voltage), k (slope factor). This matrix Y was 12 x 6. The transitions were separated into a hyperpolarizing and a depolarizing component with the same three variables:

Table 2-1. State Transitions for Nav 1.5 Channel

State Transitions	B _{hyp}	V _{hyp}	k _{hyp}	B _{dep}	V _{dep}	k _{dep}
C1C2	0	0	0	10	-13	10
C2C1	1	-43	8	10	-13	-10
C2O1	0	0	0	10	-23	-10
O1C2	1	-53	8	10	-23	-10
C2O2	0	0	0	0.05	-10	-10
O2C2	2	-50	10	0.05	-10	-10
O1I1	7	-44	13	10	-19	-13
I1O1	0.00001	-20	10	0	0	0
I1C1	0.19	-100	7	0	0	0
C1I1	0	0	0	0.016	-92	-6
I1I2	0	0	0	0.00022	-50	-5
I2I1	0.0018	-90	30	0	0	0

The parameters for the equations described in ¹¹⁸ for calculating each state transition for opening (O) and closing (C), and inactivation (I) probabilities for Nav1.5 channel.

The states were a vector in the order:

A, the transition rates, were calculated as follows for all state transitions simultaneously, producing a 12x1 vector:

$$A = Y_1 \left(1 + e^{\frac{V-Y_2}{Y_3}} \right)^{-1} + Y_4 \left(1 + e^{\frac{V-Y_5}{Y_6}} \right)^{-1} \quad (2-10)$$

A then needed to be multiplied by the current states to get the correct transition probabilities over time.

The states were arranged in the vector x in the order (O1, O2, C1, C2, I1, I2).

The transitions in and out of state were then calculated in a matrix form with the following equation M :

$$\begin{vmatrix} -(A4 + A7) & 0 & 0 & A3 & A8 & 0 \\ 0 & -A6 & 0 & A5 & 0 & 0 \\ 0 & 0 & -(A1 + A10) & A2 & A9 & 0 \\ A4 & A6 & A1 & -(A2 + A3 + A5) & 0 & 0 \\ A7 & 0 & A10 & 0 & -(A9 + A11 + A8) & A12 \\ 0 & 0 & 0 & 0 & A11 & -A12 \end{vmatrix}$$

$$x(t + 1) = dtM + x(t)$$

$$I_{Na} = g_{Na}S(x_1 + x_2)(V - V_{Na})$$

Where $x_1 + x_2$ is the total probability of being in the open state. S is the same surface area of the axon used above. dt was the same as for the rest of the study (1e-3 ms).

Dynamic NQ effect

There was not existing data that could be used to model the mechanism of K⁺ concentration change in the cleft and the resulting effect on the axon and hair cell. Instead, we created a more realistic phenomenological model of the non-quantal effect based on trajectories of the non-quantal effect in response to current and voltage steps¹⁰⁴.

$\tau_{NQ} = 100 \text{ ms}$, $g_{NQ} = 0.025$ to get the correct trajectory and the change in current necessary to produce the size of non-quantal effect needed to replicate the slope of change in firing rate with DC stimulation in the *in vivo* axon model. These equations include the non-quantal effect to current at the axon I_{stim} while immitating the slow rise with current amplitude observed previously (I_{stim}^G).

$$\frac{dI_{stim}^G}{dt}(t) = g_{NQ}I_{stim}(t) - \frac{1}{\tau_{NQ}}I_{stim}^G(t - 1) \quad (2-11)$$

$$I_{stim}^G(t) = I_{stim}^G(t - 1) + \frac{dI_{stim}^G}{dt}(t)$$

Then, I_{stim}^G can be directly added to received EPSC inputs to produce the change in internal current over time at the axon. This gave a final scaling of about 3.5 times in the model of the Goldberg data. This value was used in place of I_{stim} in Eq. 2-1.

2.2.3 Hair Cell Adaptation Effect

In the Manca experiments²⁷, an adaptation effect to GVS current stimulation for ten seconds was found that decayed with a time constants of as high as 8.5 s. In the literature, for a toadfish in water around 20°C, an adaptation in firing rate was found to natural, mechanical stimulation that moved the stereocilia of the hair cell to a fixed position for an extended period of time of up to 13 s¹¹³. We hypothesize that GVS stimulation is able to activate this natural adaptation mechanism in the hair cell, resulting in the observed adaptation in Manca *et al.* (2019). In Rabbitt *et al.* (2005)¹¹³, the adaptation could have up to k components but was shown to be closely replication if two were used, represented as two hidden states, a slow state (s) and a fast state (f). Both states have the same state evolution equations

$$\frac{d\eta_k}{dt} = g_k \frac{di}{dt} + \frac{g_{\infty k}}{\tau_k} i - \frac{1}{\tau_k} \eta_k \quad (2-12)$$

, where i is the inputted stimulus signal (originally mechanical but adapted for electrical stimulation in our study), g_k is the instantaneous gain to a change in the signal, and $g_{\infty k}$ is the steady state gain to which the signal will adapt¹¹⁹. We hypothesize that the $g_{\infty k}$ term, a baseline shift in firing rate is negligible compared to larger axonal effects which are of the same magnitude as the offsets observed in the Goldberg dataset. So, we set $g_{\infty k} = 0$, such that $\frac{d\eta_k}{dt} = g_k \frac{di}{dt} - \frac{1}{\tau_k} \eta_k$ for both adaptation states.

Adaptation was modeled as an additive effect on top of the natural firing rate, so that $F(t) = F_{axon} + F_{adapt}(t)$, due to evidence of a separable hair cell adaptation pathway and axonal responsiveness to GVS stimulation. In this absence of stimulation F_{axon} would just be F_o . The contribution of adaptation to firing rate (F_{adapt}) is a sum of the two states we call s and f , where the response to excitatory mechanical stimulation has a larger fast component than the response to inhibitory stimulation:

$$F_{adapt} = \eta_s + r\eta_f, \quad r = \begin{cases} \alpha & \eta_f < 0 \\ 1 & \eta_f \geq 0 \end{cases} \quad (2-13)$$

The choice of α was not carefully measured in Rabbitt *et al.* (2005); we set $\alpha = 0.1$ based on their choice. For a different choice of α , g_s and g_f would have to be adjusted to fit the data.

The hair cell affects firing rate in the HK model through the stochastic process that generates EPSCs with a magnitude scale factor (K) and inter-EPSC interval (μ). We theorize $\mu(t)$ is a stochastic function of F_{adapt} ,

because hair cells do not typically modify the packing of vesicles we assume that the magnitude of the EPSCs (K) arriving remains fixed but vesicle release rates have been shown to change in response to stimuli¹²⁰. We assume firing rate and EPSC arrival rate are approximately linearly related, such that $F_o = \frac{k_F}{\mu_o}$, where k_F is a scaling. Then, the firing rate relation can be solved in terms $\mu(t)$:

$$\begin{aligned} \frac{k_F}{\mu(t)} &= \frac{k_F}{\mu_o} + F_{adapt}(t) \\ \mu(t) &= \frac{\mu_o}{1 + \frac{\mu_o}{k_F} F_{adapt}} = \frac{\mu_o}{1 + \frac{F_{adapt}}{F_o}} \end{aligned} \quad (2-14)$$

$F_{adapt}(t)$ is a continuous function, but EPSC delivery is a discretized process related to quantal release from the hair cell and therefore changes in release rate would not be immediate. So, we divided the trial into windows of length $t_{d\mu} = \mu_o$ ms, and in each window the stochastic EPSC generation equation was used to generate μ_o ms of EPSC trains which were concatenated to create the final EPSC train used during simulation experiments. μ_o ms was chosen because with $\mu(t)$ updating every μ_o ms which on average allowed several EPSCs to sum before a new value of $\mu(t)$ was used to generate the next window of EPSCs. This value could affect phase shift and firing rates as discussed in the results section. At this value, phase shift and firing rate results replicate the sine wave experiment results, but likely it varies depending on the neurons spontaneous firing properties.

Next, we tuned the equation to the observations from Manca *et al.* (2019) to select values of g_s and g_f . We model GVS stimulation by setting $i = -I_{electrode}$ with the current amplitude in μA , because negative/positive current causes an excitatory/inhibitory effect on firing. We fit the initial change in firing rate to the current step in ²⁷ such that

$$F_{adapt} = \begin{cases} (g_s + 0.1g_f) \frac{di}{dt} & \eta_f < 0 \\ (g_s + g_f) \frac{di}{dt} & \eta_f \geq 0 \end{cases} \quad (2-15)$$

We find that $g_s = 0.75$, $g_f = 4.5$, $\tau_s = 2$ s, and $\tau_f = 0.15$ s replicates the time course and gain of the the experimentally observed adaptation results well for the Goldberg or Manca data. These values also still fall well with-in the biophysical range measured in the Rabbitt et al. paper¹¹³, so we found them biologically plausible.

2.2.4 Simulating Effects of GVS on Firing Regularity

The firing rate and range were set in a simulation such that neurons had a high induced firing range and high spontaneous firing rate. The change in firing rate with GVS stimulation amplitude was measured by applying one-second GVS stimulation fields at each current amplitude between $-100\ \mu\text{A}$ to $70\ \mu\text{A}$. In each trial, stimulation steps were preceded with a 50 ms window without stimulation to assure the membrane potential was at rest. APs in this time window were excluded. A trial with 1050 ms of stimulation at each current amplitude was simulated nineteen times with different random seeds to replicate experimental results²⁸; the CV versus ISI comparison, the change in slope, and the maximum firing rate across neurons were found across the population. The action potentials were detected from the voltage trace by finding points where the voltage was above $-35\ \text{mV}$ and greater than the voltage 0.01 ms before and after. The CV and ISI were calculated from the detected times of action potential peaks. The slope of increase in the Goldberg data with cathodic current was fit linearly. The trend of increase in the simulated data was fit with a fifth-order polynomial, and the last current for which the curve had positive slope was the lowest current amplitude point included.

2.2.5 Simulating Adaptation Observed in Response to GVS

Adaptation was captured in both replicated experiments but had a different responses. We hypothesized that there are two components to the responses to GVS stimulation, an axonal response that produces an overall change in firing rate while current is being driven through the axon and a hair cell response that is responsible for the adaptation shape. In Manca *et al.* (2019), we believed the *in vitro* prep left afferents significantly less responsive to GVS than the *in vivo* afferents from the Goldberg study, leading to the lower spontaneous range and smaller induced firing range. We fit the adaptation function to these data (see above). We then tested whether adaptation was properly captured by assuring that the response to a 10-second GVS field of $+10\ \mu\text{A}$ and $-10\ \mu\text{A}$ produced the same initial change in firing rate with a current step and decayed back to baseline after 10 seconds.

In the *in vivo* axon model with higher conductance values and a larger NQ effect, both the NQ and adaptation effect need to be slightly reduced to replicate experimental results. We used $k_{\text{NQ}} = 3.5$ and scale adaptation parameters down to $g_s = 0.49$ and $g_f = 2.9$, so the ratio of g_s and g_f remain fixed. This is due to

the axon being more responsive to inputs when conductances are larger. With these parameters, we confirmed that adaptation to a five-second GVS step followed by five-seconds after the current stepped down produced a change in baseline firing rate with an adaptation effect on top during the step and adaptation in the opposite direction after it stepped down. The experiment was simulated to steps of GVS current of -50, -30, -10, 10, 30, 50, and 70 μA . The response to -70 μA in the Goldberg dataset could not be replicated because at -70 μA the simulated neuron underwent cathodic block.

2.2.6 Simulating Baseline Current Step Experiments

In the Manca study²⁷, a baseline of -10 mA, 0 μA or +10 μA GVS current was delivered for ten seconds then current step of ± 20 , ± 15 , ± 10 , ± 7.5 , ± 5 , ± 2.5 , and 0 μA away from this baseline were delivered for an additional two seconds. Changing in firing rate was compared between the baseline firing rate in the last one second of baseline and the first 50-500 ms after the current step. We repeated this simulation on ten model neurons *in silico* to match the size of the study in the experimental data being replicated²⁷.

2.2.7 Simulating Sinusoidal Waveform Experiments

In the Manca study²⁷, the response to fifteen cycles of sinusoidal waves of height ± 10 μA at frequencies of 0.1, 0.2, 0.5, 1, 2, 4, and 8 Hz was recorded across ten neurons. As in the study, we needed to determine the phase shift of the response to each signal. For each simulated neuron, the phase shift was determined by fitting a sinewave at the stimulation frequency to all cycles of response to the sinewave. For lower frequencies, fewer cycles are required to capture the phase shift, so, for frequencies less than 1 Hz, we simulate five cycles and, for frequencies of 1 or more Hz, seventeen cycles, excluding the first and last cycle from analyses. We then measure the firing rate in windows centered around the cathodic half of the response and anodic half of the response in each cycle and take the average to measure the gain in firing rate. We report the firing rates per cathodic and anodic half of the response and phase shift across neurons. We extend the study to see the responses to frequencies from 0.005 Hz to 150 Hz to capture the full frequency response of the neurons. We analyze the results on $F_{adapt}(t)$, which represents the change that hair cell adaptation contributes to the neural response without the noise of axonal response, and on the full axon model.

2.2.8 Statistical Comparison to Experimental Results

To compare slope of increase with cathodic current across models, we fit the original data from Fig. 5a²⁸ with a line of best fit with intercept zero. We compare this slope and 95% confidence interval of fit to the slope and 95% confidence interval of fit of each of our models. If the experimental slope is within the bounds of the model, we declare the experimental data replicated.

To compare CV-ISI relationships between the experimental study and the simulated results, we use the equation for CV* with values that match the 95% confidence interval observed in the study. We then count the number of points between 5 ms and 50 ms that fall within these bounds (Figure 5f), checking whether over 95% fall within experimentally observed boundaries.

To compare the change in firing rate with current steps from three baseline conditions (control, anodic baseline, or cathodic baseline) in the Manca study to our simulation results we perform a non-parametric cluster statistic at the level of $p < 0.05$ on the traces of change in firing rate and phase with sinewave frequency. In each comparison, the neuronal firing rate relationships to current amplitude is compared to one other condition. We permute condition identity for each neuron tested between the groups 500 times and find clusters of values that significantly differ from permutation results and reality. The t-value of the cluster needed to exceed 3 to be significant. We used this test for comparisons within experimental²⁷ and simulated data between baseline conditions. We also compare results of the sinewave experiment with and without adaptation.

2.3 Results

Our approach was to uncover the neural targets of GVS stimulation by determining the necessary features and parameters for a mechanistic vestibular afferent model to produce the known responses to GVS stimulation discovered through electrophysiology experiments on two vestibular afferents reported by Goldberg et al 1984 (specifically, 381-11H in Figure 3 of and unit 328-24H in Figure 7 of that paper) and ten neurons empirically studied by Manca et al 2019 (details in Table 2-2). We compared how well our model produces GVS effects with experimental results from two studies. These studies use different preparations which result in afferents with distinct firing properties. The Goldberg study²⁸ was performed on squirrel monkey afferents with a broad firing range (0-300 sps) and high spontaneous rate (100-120 sps) using

extracellular electrodes 2 mm from afferents in the perilymphatic space of the vestibular. The second study was recently performed in our laboratory²⁷. It used an *in vitro* preparation in which afferents respond with a low spontaneous rate (15-20 sps) and a narrow firing range (0-60 sps). These experiments applied GVS through micropipettes to an explanted mouse vestibular crista, while acquiring action potentials using an extracellular loose-patch pipette technique. For all simulations we used the same number of simulated neurons as the neurons from each experiment with the same firing rates and ranges.

Extracellular electric fields are typically assumed to affect axons at substantially lower amplitudes than smaller cell volumes and cell bodies due to geometry and size differences¹²¹⁻¹²³. Therefore, we first start by testing whether GVS could produce all the firing effects we aim to model solely through interactions with the biophysically modeled features of the axon.

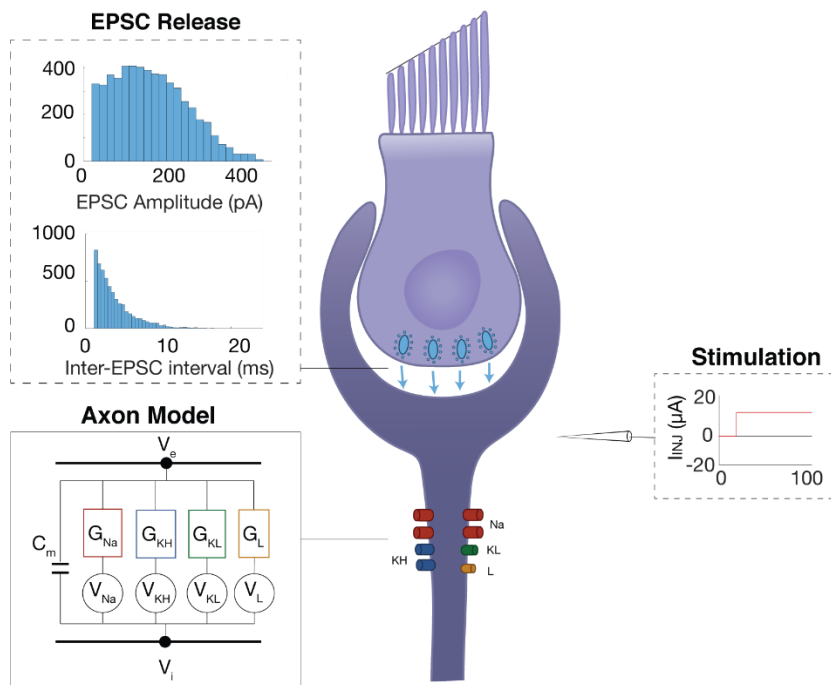


Figure 4. Diagram of the axonal model based on Hight and Kalluri (2016)

The HK model uses three specific voltage gated channels - a sodium (Na), high-voltage gated potassium (KH), and low-voltage gated potassium (KL) channel - as well as a leak channel to reproduce axon firing dynamic, as seen in Figure 4. Spontaneous firing in the axon model is driven by simulated excitatory postsynaptic currents (EPSCs), an axonal manifestation of vesicle release from the hair cell. EPSC arrival is controlled by two stochastic functions: one that determines EPSC amplitude, set with EPSC scaling (K), and

one that determines EPSC release rate by setting the average inter-EPSC interval (μ_o). The HK model suggests that these mechanisms in concert are necessary to generate realistic spontaneous vestibular afferent firing, as seen in Figure 4. We first disentangled how each of these mechanisms is contributing to firing through exposure to GVS stimulation.

2.3.1 Unmodified HK Model Is Insufficient to Reproduce GVS-Evoked Responses

The assays for replicating the firing statistics from the Goldberg dataset (Effects I-III in Figure 3b) are (1) the mean spontaneous firing rate (F_o) of 100-120 sps, (2) change in spike rate in response to GVS steps ($dF/dCurrent \approx -2$ sps/ μA) in response to GVS steps between -100 μA and +100 μA , (3) maximum firing rate ($F_{max} > 200$ sps), and firing regularity that remains within CV* as firing rate changes²⁸. These are all depicted in black in Figure 5c-f.

We first tested the ability of the unmodified HK model to reproduce firing statistics with and without exposure to GVS stimulation. With the original parameters, $F_o = 52.7 \pm 3.3$ sps ($N = 19$), as seen in Figure 5c-f (dark blue), is significantly below the activity recorded experimentally. Figure 5c shows that, when we applied GVS steps at the amplitudes ranging between -100 μA to +100 μA , we observed that while the CV* profile was maintained (dark blue), the maximum firing rate was 70.6 ± 6.2 sps in response to -46 μA , significantly lower than that recorded experimentally (>200sps). The slope of the response to GVS ($dF/dCurrent$) was -0.5 sps/ μA (95% confidence interval (CI) [-0.47, -0.55]) compared to the ~2 sps/ μA seen experimentally, as seen in Figure 5c-f (dark blue). Figure 5d shows that increasing the cathodic stimulus beyond -45 μA decreased the axonal response, suggesting cathodic stimulus interference (“Cathodic Block”) (dark blue). This block was previously observed⁸⁸ and likely is due to GVS inducing exceedingly high membrane potentials at the axon, causing voltage gated sodium channels to be held in the inactivated state and prevented from reopening. Although this was not commented on in the Goldberg study, this is a known effect of GVS or GS generally. Thus, finding this effect also occurs within the biophysical vestibular afferent model suggests that the channel dynamics are being modeled accurately enough to capture essential effects of GS at the axon.

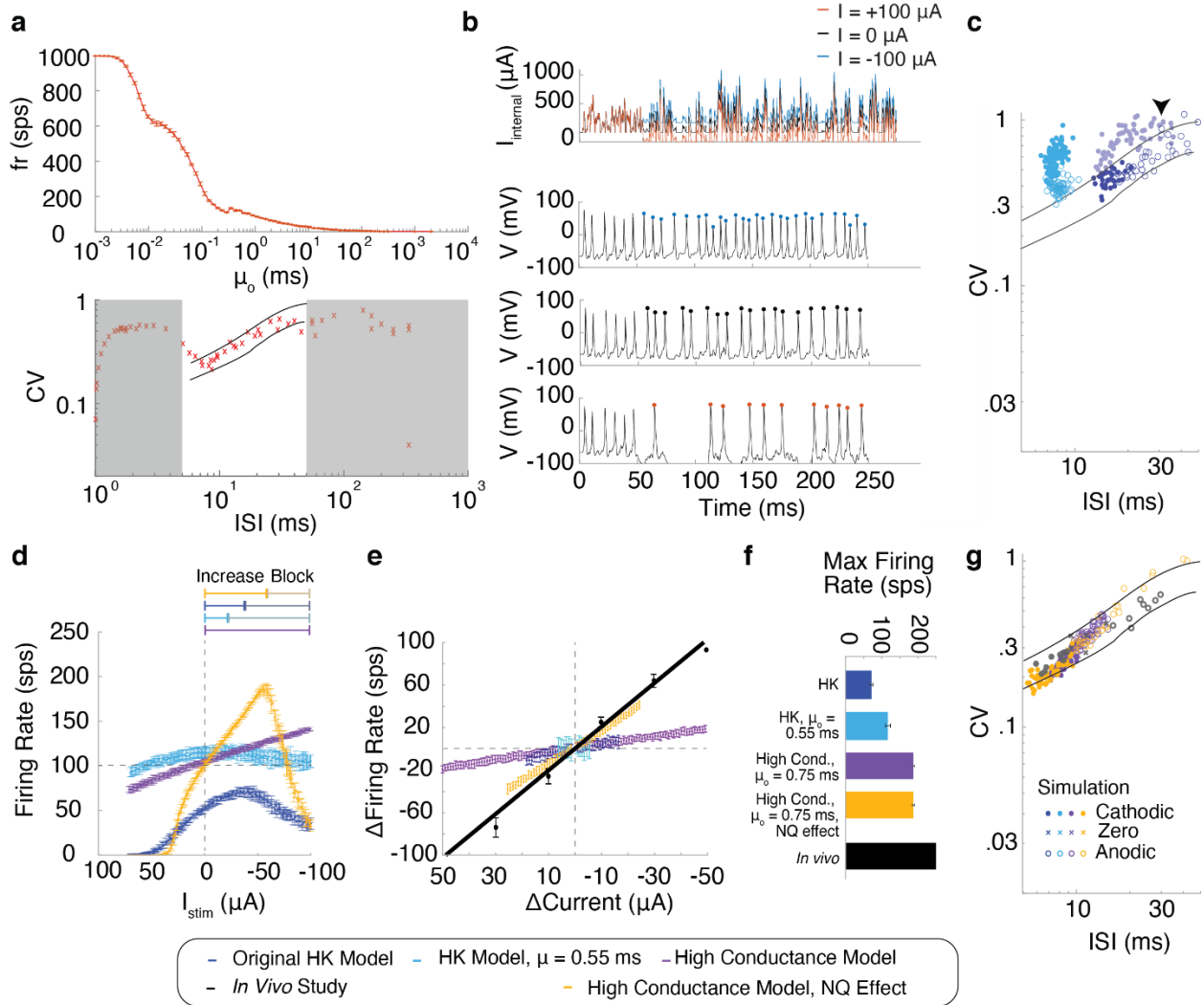


Figure 5. Role of afferent axon in GVS response

a Changes in mean EPSC arrival rate μ_o result in increased firing rate (top) and conformance to CV* (bottom) using original HK model. White region in bottom plot indicates the zone shown in the experimental *in vivo* data with CV* boundaries for the irregular neuron. **b** EPSC (top) and membrane voltage V (lower three). GVS is turned on at 50 ms. (top V) Cathodic current increases EPSC baseline bringing the membrane potential closer to depolarization causing more APs (blue). (middle V) no GVS, (bottom V) Anodic current decreases EPSC baseline bringing it closer to hyperpolarization causing fewer APs (orange). **(c-g)** Dark blue: standard HK model, Light blue: HK model modified with $\mu_o = 0.55$ ms, Purple: HK model with $\mu_o = 0.75$ ms and high conductance, Yellow: HK model with $\mu_o = 0.75$ ms, high conductance, and NQ effect, Black: experimental *in vivo* data. **c** CV* and CV as GVS current is applied (HK model modified with $\mu_o = 0.55$ ms light blue, standard HK with $\mu_o = 3$ ms dark blue) arrow points to the shaded dark blue points that occurred during the Cathodic Block. Open circles are anodic stimulation, filled circles are cathodic stimulation. **d** Firing rate as a function of GVS stimulation amplitude. **e** Change in firing rate as a function of stimulation amplitude. **f** Maximum firing rates of the responses. **g** CV of the responses. Lines indicate experimental CV* from the Goldberg experiment.

2.3.2 EPSC Arrival Rate Increases Firing Rate without Affecting CV*

As spontaneous firing is induced through changes in membrane potential by EPSCs, we first hypothesized that increasing the rate of EPSC arrival will increase F_o and GVS effects on firing rate at the axon. We examined the effect of changing μ_o in absence of GVS stimulation. We targeted this aspect of EPSCs due to the existing evidence that the release rate is modulated as a function of mechanical motion¹²¹,

while the amplitudes of the EPSCs remain nearly constant so the scaling of EPSCS (K) was not changed¹²⁰. This phenomenon is likely due to vestibular afferents having specialized ribbon synapses and multivesicular release that allows up to sub-millisecond inter-EPSC arrival times to changes to hair cell motion^{82,124}. EPSC timing was however modeled as updating after certain time delays to account for likely signaling cascades that underpin adaptation in ribbon synapse dynamics. Varying μ_o from 0.1 ms to 250 ms produced firing rates of up to 1ksps, while maintaining the appropriate CV* behavior, as seen in Figure 5a. This meant the model is capable of producing extremely high firing rates if pushed to unnatural limit, but GVS induced firing within realistic ranges suggesting a reasonable parameterization. We found that faster EPSC-arrival is more likely to generate larger changes in membrane potential more quickly, producing larger firing rates.

To match the spontaneous activity of neurons in the Goldberg dataset, we then decreased μ_o to 0.75 ms to achieve $F_o = 102.8 \pm 3.7$ sps. However, with this change to μ_o , the model produced responses that were significantly different than those observed experimentally in response to GVS stimulation. Figure 5d shows cathodic and anodic stimulation both decreased firing rate within 50 μ A, resulting in a slope of -0.04 sps/ μ A, CI[-0.2,0.29] (light blue); the maximum induced firing rate reached only 120 sps, and the CV* of the spiking activity was no longer maintained. This suggests that the axonal response to GVS stimulation was interfering with the EPSC response as opposed to having strong excitatory effects. Thus, something differs from the experimental conditions to cause a limited respond to GVS.

2.3.3 Channel Conductances Determine Maximum Firing Rate and Firing Regularity in Response to GVS

Figure 5 shows GVS steps create a baseline change in membrane potential that shifts all EPSCs at the membrane uniformly in a depolarizing or hyperpolarizing direction (dark blue and red respectively). The positive shift in EPSC height with cathodic stimulation raise the previously slightly subthreshold EPSCs above the firing threshold, increasing the number of action potentials (APs). The anodic baseline shift lowers the height of EPSCs that would normally raise the membrane potential high enough to reach AP firing threshold, reducing the firing rate. When μ_o was set to 3 ms as indicated by the HK model, in the range of cathodic stimulation that produces cathodic block (-45 μ A to -100 μ A), Na channels had a lower probability of opening in response to increases in membrane potential with EPSCs, as seen in Figure 5d. When μ_o was set to 0.55 ms, CV at all firing rates increased above the CV* boundaries in the same way as those observed

during the Cathodic Block with $\mu_o = 3$ ms (light blue, shaded dark blue with arrow, respectively), as seen in Figure 5c. Based on this similarity to the CV^* relationship we hypothesize that channel density, parameterized as channel conductance, should be larger to generate APs in response to this faster EPSC arrival and comply with CV^* performance.

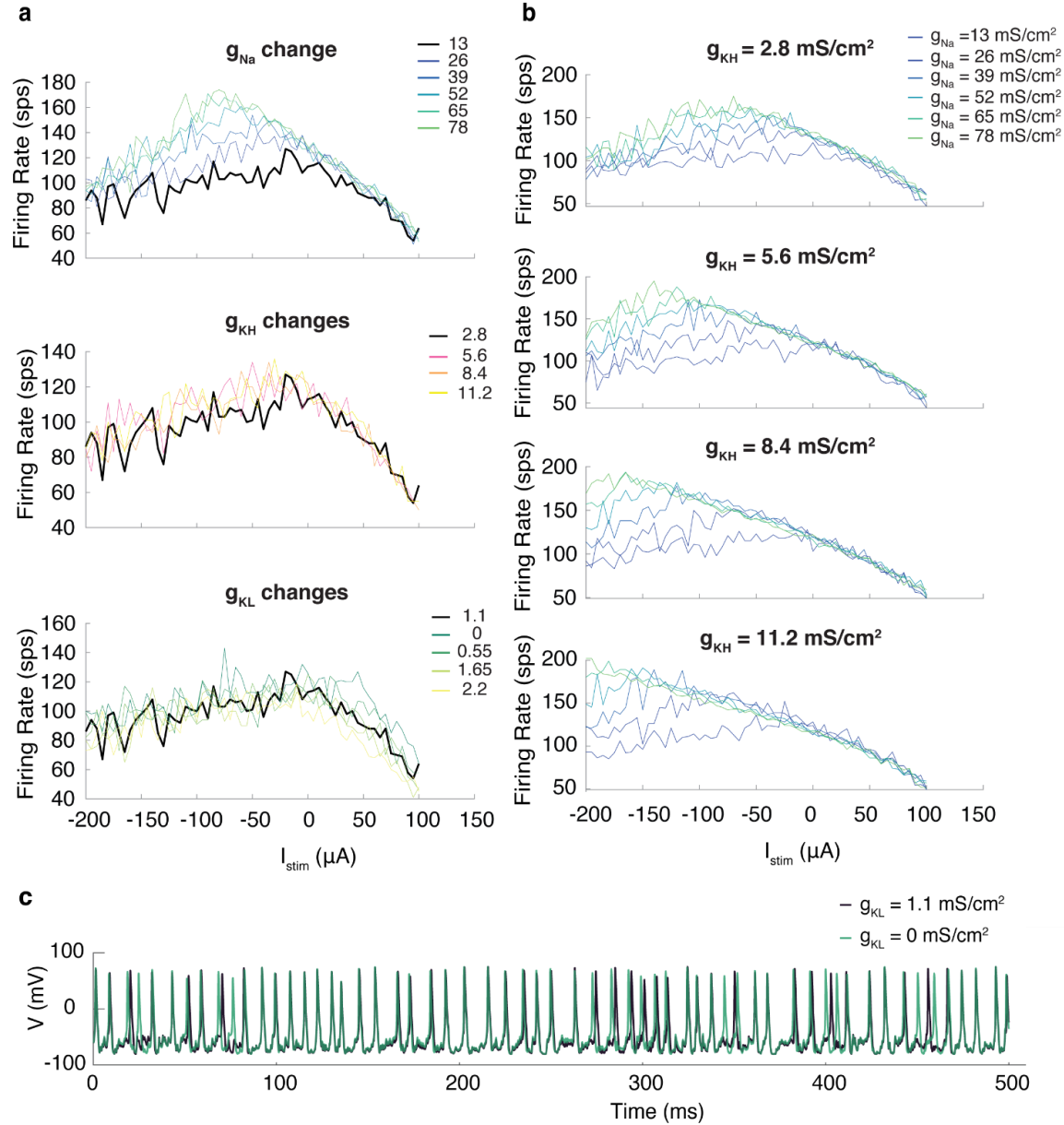


Figure 6. Effect of Conductances on Maximum Firing Rate

a) Increasing g_{Na} , g_{KH} and g_{KL} from initial value to highest value possible within biologically realistic values. Original values (black) compared to increase. b) Result of increasing g_{Na} in combination with each increase in g_{KH} at each tested value of g_{KH} from 2.8 to 11.2 mS/cm². c) g_{KL} effect on action potentials.

As described previously, the membrane conductances affect the sensitivity to electrical stimuli. We found that increasing g_{Na} and g_{KH} together increased the firing range in response to GVS stimulation, as seen in Figure 6a-b. Meanwhile, increasing g_{KL} only increased the irregularity of firing in agreement with previous observations^{85,87,125}. Thus, we kept $g_{KL} = 1.1 \text{ mS/cm}^2$ and scaled the conductance values for g_{Na} and g_{KH} to the upper limit of the biologically realistic conductance values⁸⁷. With higher conductance and with $\mu_o = 0.75 \text{ ms}$, simulated neurons exhibited a GVS-induced firing range of 0-188 sps and $F_o = 100.3 \pm 2.4 \text{ sps}$ (Figure 5d-g purple). Although the maximum induced firing rate observed in the Goldberg study (~250 sps)²⁸ is outside the induced firing range of the neuron model after tuning, these values approach the realistic firing range of a vestibular afferent (Figure 5f purple), with CVs that remained within the CV* boundary (Figure 5g purple). The increase in firing rate however remained low at $-0.32 \text{ sps/}\mu\text{A}$, CI[-0.35, -0.28], about six times smaller than reported values (black) of $-2.01 \text{ sps/}\mu\text{A}$ CI[-2.19,-1.89] (Figure 5e purple). We take these data to represent an average irregular neuron with the assumption that if these data can be replicated in one model similarly other irregular afferent properties could be simulated with minimal changes in parameters as the general mechanism of GVS is being approximately captured.

Previous experiments indicate that irregular afferents with calyces have strong “non-quantal” (NQ) effect that can increase afferent response to external current up to 4.5 times and has been reported to be a modulatory effect that increases response to GVS^{82,126}. K⁺ accumulation in the synapse has been implicated as the source of the effect^{104,127}. Incorporation of the NQ effect into the model boosted the sensitivity in response to GVS presentation ($-1.65 \text{ sps/}\mu\text{A}$ CI[-1.67,-1.63]) (Figure 5d, e yellow). This simulated response more closely matches the experimental slope $-2.01 \text{ sps/}\mu\text{A}$ CI[-2.19,-1.89] (Figure 5e, black) while also adhering to the other experimental observations (Effects I-III) (Figure 5d-g yellow).

2.3.4 GVS Stimulation Maintains CV* by Changing Sampling Variance of EPSCs

To understand how CV* is maintained during GVS stimulation, we examined the model's predictions for how induced current at the axon depends on magnitude of GVS stimulation. In the model, GVS stimulation creates a baseline shift in membrane current that shifts all EPSCs by a current amplitude proportional to stimulation current at the membrane uniformly without changing EPSC timing (Figure 5b blue and orange). All EPSCs arrived with timing and height defined by the hair cell and which can be captured with a set of

stochastic functions with fixed parameters that define a distribution of EPSC amplitudes and inter-EPSC intervals used to simulate the input to the axon ⁸⁷. Therefore, an increase or decrease in the number of EPSCs that become APs can be approximated as sampling this underlying distribution more (cathodic stimulation) or fewer (anodic stimulation) times. With more samples, the variance will decrease, and with fewer samples the variance will increase. In probability theory, this effect is commonly referred to as “sampling variance.” As a result, the standard deviation of firing rate will follow this trend, leading to a decrease in CV with higher induced firing rate. Note, CV values may still show some level of increase and decrease as firing rate goes up due to the statistical properties of sampling from distributions like exponential distributions with low means, but, on average, there should be an observed decrease in variance. Because all EPSCs in the model are drawn from the same distribution, firing regularity should follow the underlying distribution, leading to each neuron having a CV^* that governs the relationship between CV and ISI. We further show that the output from the model hair cell is necessary to maintain the model output’s CV^* during simulated GVS by performing the same simulation for a model afferent without any EPSC arrival. This simulation shows extremely low, CV values far outside the CV^* boundaries (Figure 7).

2.3.5 Hypothesis for Similarity between Preservation of CV^* with GVS and Naturally

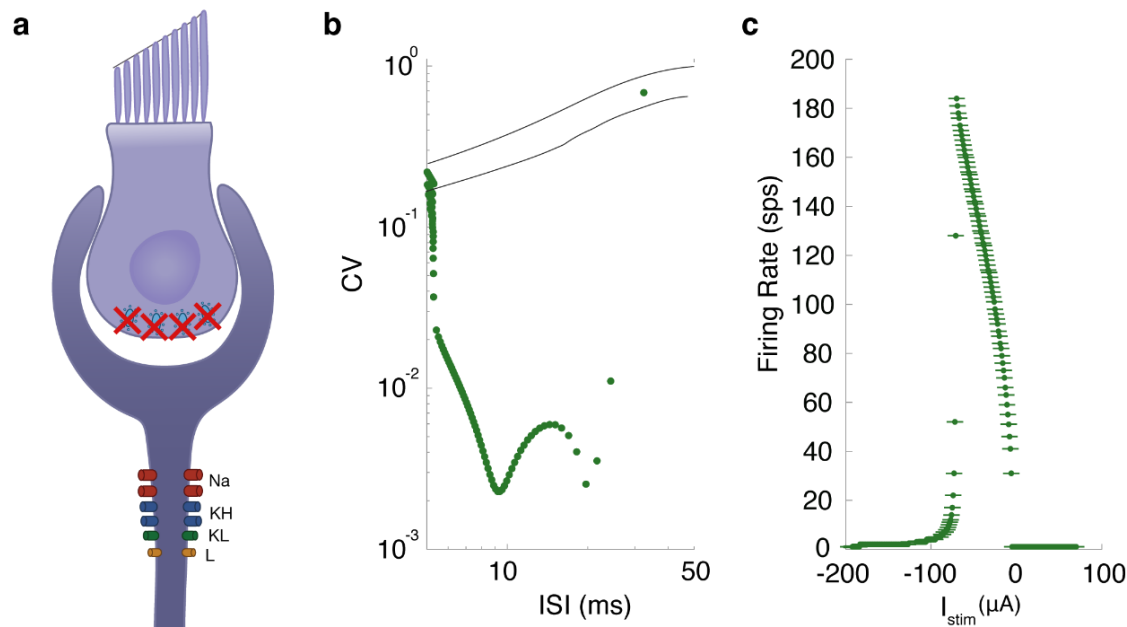


Figure 7. Distortion of CV-ISI with Axonal GVS only.

Support for the idea that the output from the hair cell is necessary to maintain the CV^* relationship when GVS is applied. **a)** Simulated paradigm in which GVS current with amplitudes between +70 μA to -100 μA is introduced to the axon with no EPSCs **b)** The CV vs

ISI relationship in this case produces much lower CVs than the CV* found in experimental data. c) The induced firing range is approximately the same but firing rate increases from 0 sps at 0 μ A of stimulation to the maximum firing rate.

2.3.6 Axonal Response to GVS Alone is Insufficient to Explain Firing Rate Adaptation and Rapid Onset Response

Simulated GVS stimulation of the model axon alone produced did not produce simulated responses with a transient onset that adapts over seconds shown in Effect IV, nor did it produce adaptation-to-baseline Effect V, nor high pass frequency response of Effect VI (Figure 3). The HK model that we modified did not possess any mechanisms with the response characteristics that could account for the adaptation durations seen in Effect IV. Further review of the literature revealed that the afferents and their calyceal endings contain Na_v 1.5 voltage gated sodium channels^{125,128} not originally included in the HK model. These voltage gated channels have long recovery from inactivation that last over seconds¹¹⁸. Additionally, more recent examination of the NQ effect suggests that the permeation of K^+ in the synaptic cleft increases sensitivity to EPSP release from the hair cell as the result of increased afferent activity. The dynamics of the NQ effect due to influx and efflux of K^+ appear to match the long adaptation time course seen in the GVS firing rate response^{104,129}. To investigate the possibility that Effects IV, V, and VI could be attributed to axonal response to GVS, we introduced a more detailed dynamic NQ effect and a Markov model of the Na_v 1.5¹¹⁸ into the axonal model. We then applied steps of -30 μ A cathodic GVS to examine the responses (Figure 8a). While these responses clearly show the increase in firing rate, they fail to demonstrate the rapid increase in onset activity at the time of GVS stimulation and the subsequent adaptation towards spontaneous firing rates described in Effects IV and V in Figure 3.

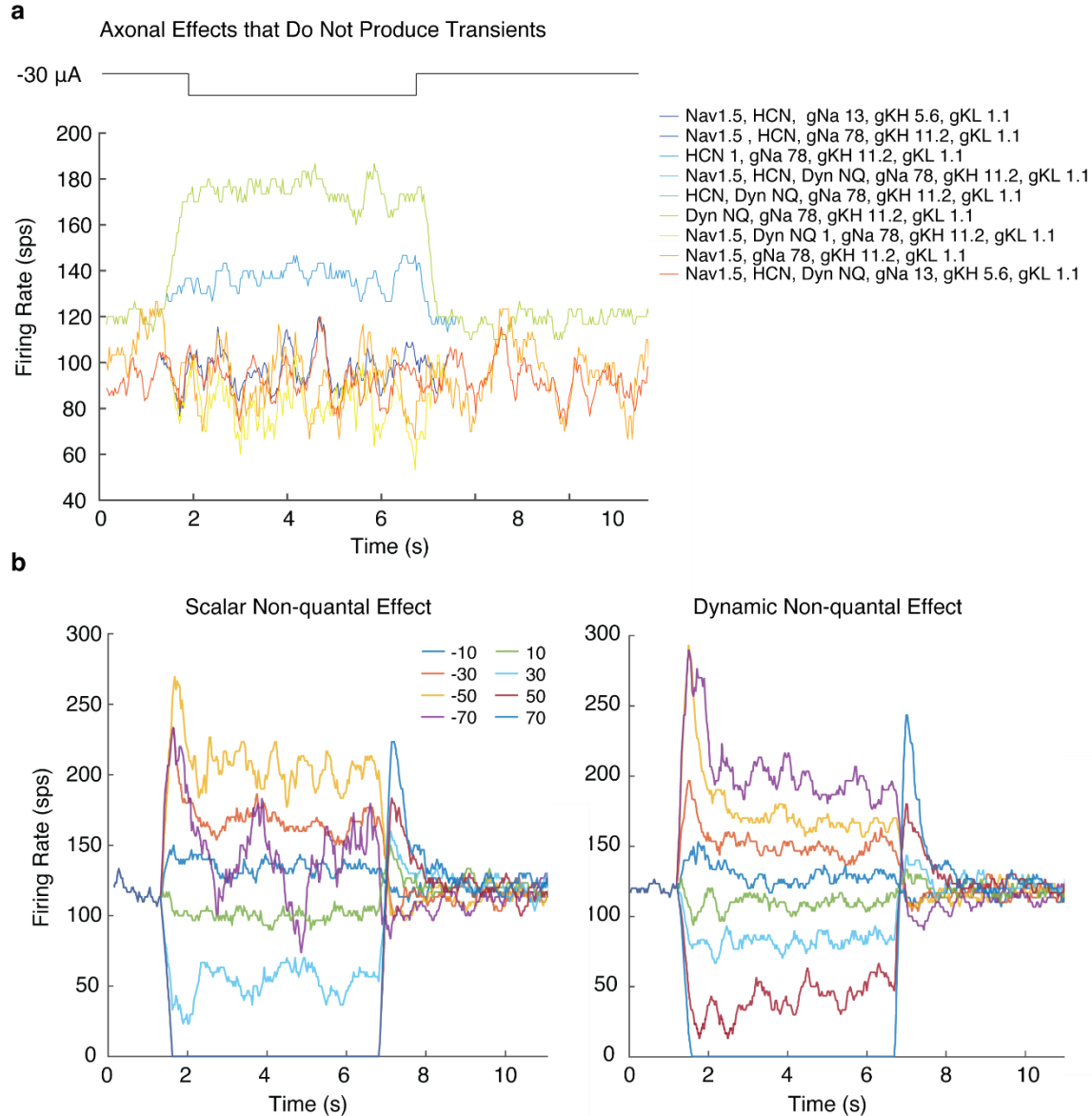


Figure 8. Effect of Nav 1.5 Channels on Observed Transients

Inclusion of Nav 1.5, HCN channels and Dynamic NQ response is insufficient to explain rapid onset and adaptation effects seen experimentally in response to a step GVS. a) Multiple manipulation of conductances and introduction of Nav 1.5, HCN, and Dynamic NQ response without hair cell GVS response fails to show the rapid onset followed by slow adaptation seen in the experimental data. b) For the complete axon with hair cell simulation, Dynamic NQ effect that mimics the dynamics of the influx and efflux of K⁺ into the synaptic cleft has only minor impact on step responses over the constant Scalar NQ effect (colored lines are anodic and cathodic steps in μ A).

Afferents have been shown experimentally to have a natural adaptation pathway that responds to mechanical stimulation of the hair cell, resulting in adaptation in overall firing rate^{71,113,119}. The underlying mechanism is not understood^{83,113}, but the similarity of this adaptation time course and gain to excitatory and inhibitory mechanical stimulation compared to that seen for anodic and cathodic GVS step responses (Effect IV) suggests that GVS stimulation is activating some aspect of the same natural pathway¹¹³. For this reason,

we hypothesized GVS stimulation must simultaneously affect the axon and this natural hair cell adaptation mechanism.

2.3.7 Simulating GVS Effects on the Hair Cell

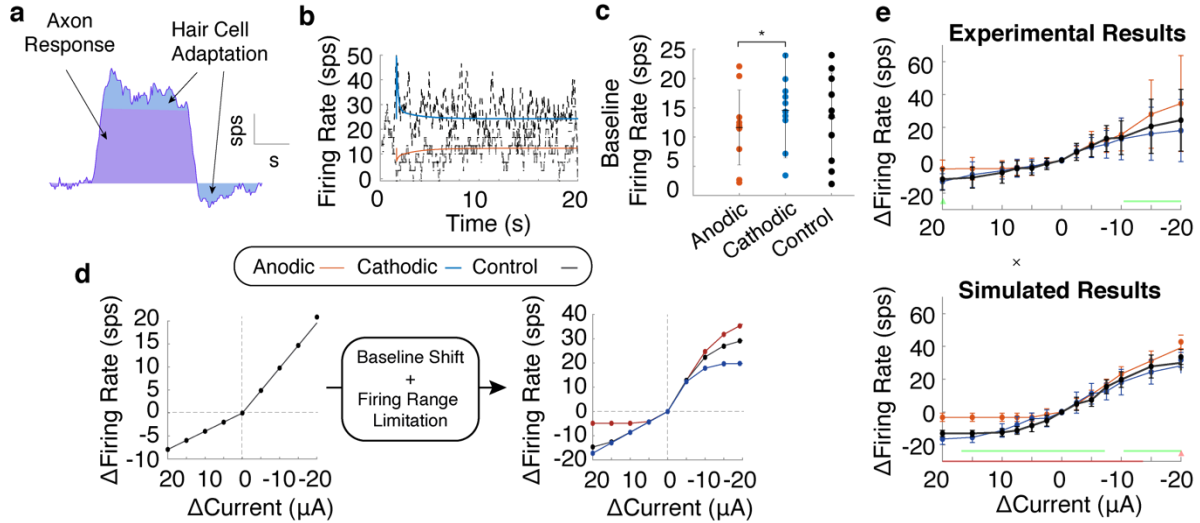


Figure 9. Adaptation in GVS modulated afferent response

a) The full adaptation is composed of a change in firing rate due to axonal response (purple) and hair cell adaptation (blue) which responds to changes in internal current. **b)** We can tune adaptation gains and time constants to get adaptation that resembles experimental *in vitro* results from Manca *et al.* (2019) to -10 μA of cathodic (blue) and anodic (red). **c)** We find a significant baseline shift with anodic and cathodic current in the experimental results in the Manca study ($t(9) = 2.37$, $p = 0.042$). **d)** Without considering baseline shift and the firing range limits ($F_{\text{axon}}=0$, maximum firing rate 55 sps) the spike rate changes to current steps are predicted to be the same after baselines of anodic (red), cathodic (blue), and control or zero baseline (black) using $F(t)$ as they overlap on the plot (left). When $F_{\text{axon}} = F_o$, $F(t)$ resembles experimental results in plot (e). **e)** We use $F_{\text{adapt}}(t)$ to modulate $\mu_o(t)$ in our full model. Traces are in the same colors. A non-parametric cluster statistic is used to compare anodic to cathodic step response (green) within conditions. The Manca experimental data (above) and simulated data (below) was tested for significant differences between conditions with anodic (red), cathodic (blue), and control (black) baselines of GVS followed by steps away from the baseline of +20 to -20 μA using a non-parametric cluster statistic. Significance is shown below each graph with comparisons between anodic and cathodic traces within the experiment or the simulation shown in green. Significance between anodic and control conditions is shown in red and between cathodic and control in blue (none observed). The only point of difference between experiment and simulated results was in the control condition (black x).

We did not find a mechanistic that explained the details of how hair cell adaptation occurs in a biophysical model, so we modify a state-space model¹¹³ that represents the phenomenological hair cell adaptation in firing rate in response to mechanical stimulation (see Methods). The study that introduced this state-space model showed the adaptation response was a summation of a fast (η_f) and a slow (η_s) time constant component. It indicated that the fast component was less present in response to inhibitory stimulation than to excitatory stimuli, but it made no further prediction about the physiological mechanism of adaptation¹¹³.

In both studies we replicated *in silico*, afferents were stimulated for over ten seconds, revealing an adaptation in which cathodic/anodic current initially causes an increase/decrease in firing rate that adapts to a baseline firing rate over the course of about ten seconds. Time courses and ratios of excitatory and inhibitory responses are comparable. In both studies, $\pm 10 \mu\text{A}$ GVS steps were delivered (Figure 3c). Even

at this low amplitude, there is shift in baseline firing rate after the strong initial response to the step is observable in the Goldberg study but not apparent in the Manca study.

We propose that the baseline change in firing rate is the axonal response observed earlier and that the adaptation is attributed entirely to the hair cell, as the baseline activity level increases with current amplitude with height of approximately two times the current amplitude in μA (Figure 9a, Figure 3c black). To test this prediction, we do a brief theoretical prediction of the induced firing rate $F(t)$ with and without axonal firing and determine whether it could explain the data observed in the Manca study. In the Manca study, we observe low overall activity, as indicated by the low spontaneous rate and lower induced firing range. We produced a similar attenuated response by reducing the conductance of the axon in the *in vitro* model such that it became less responsive to EPSCs (low F_o) and GVS stimulation (lower firing range) (e black). However, since the amplitude of the instantaneous response at the onset of the GVS step (excluding the baseline) was comparable to that seen in the Goldberg study, we predicted the hair cell adaptation pathway *in vitro* is separable for axon effects and unaffected by the change in axonal conductance. As a result, the induced firing rate over time could be represented as a function:

$$F(t) = F_{\text{adapt}}(t) + F_{\text{axon}}(t) \quad (2-16)$$

, where $F_{\text{adapt}}(t)$ is the hair cell adaptation function based on¹¹³. F_{axon} is the axonal firing rate. Under the influence of GVS in an *in vivo* axon, F_{axon} would be substantially different than the spontaneous rate. In the Manca experiment, we assumed the axon is approximately unresponsive and $F_{\text{axon}} = F_o$, with a maximum firing rate of 55 sps, based on the Manca experimental data. So, all changes in firing rate could be attributed to hair cell response, $F_{\text{adapt}}(t)$. We used this equation to predict the contribution of the hair cell to firing rate without the influence of stochastic channel dynamics on firing rate.

Because EPSC amplitude has not been shown to vary dramatically¹²⁰, we theorized that the mechanism by which hair cell adaptation affects axonal firing is a change in vesicle release rate by the hair cell. For simplicity, we assumed EPSC arrival rate is inversely proportional to firing rate, so we could transform the relationship between firing rate ($F(t)$) and adaptation ($F_{\text{adapt}}(t)$) into a function for change in EPSC arrival over time ($\mu(t)$) (see Methods). We theorized that some internal hair cell pathways would need to change the rate of vesicle release, here $\mu(t)$, and that this change could not be made instantaneously due to the complexity

of protein dynamics involved in vesicle packing, release, and recycling. So, we modified $\mu(t)$ based on $F_{adapt}(t)$ every $t_{d\mu}$ ms. We initially assumed $t_{d\mu} = \mu_o$ ms. When gains and time constants of the equations for $F_{adapt}(t)$ were fitted to the Manca data responses, the gain of the fast component was substantially larger than that of the slow component, with the time constants $\tau_f = 0.15$ s and $\tau_s = 2$ s. With these parameters, the model produced noisy adaptation similar to the original study (Figure 9b). However, even in the low conductance model, there was a noticeable baseline change in firing rate indicating the axon was still responding to GVS stimulation.

Effect V shown in Figure 3d and described in the original manuscript²⁷ suggests that the Manca study response to anodic and cathodic steps decays back to baseline after a prolonged 10 s step in GVS stimulation. It also shows an apparent sensitization such that after a 10 s anodic/cathodic step of stimulation the firing rate changes less to additional steps of anodic/cathodic stimulation and more to steps of the opposite polarity. We reanalyzed the original data from the Manca study. As described in the publication, we confirmed that the firing rate after 10 s of cathodic or anodic baselines is not significantly different than the firing rate without stimulation (F_o) as was computed in the original manuscript²⁷. However, they are slightly, but significantly different from one another based on our additional statistical analysis (paired $t(9) = 2.37$, $p = 0.042$) (Figure 9c). Additionally, $F_{adapt}(t)$ alone would predict when anodic, cathodic, and control (zero) baseline stimulation is delivered there would be no difference in response (Figure 9d left panel). Because of this we theorized that the lowered membrane conductance of the in vitro axon must be responsible for producing Effect V. A hyperpolarizing (anodic) step creates a new baseline closer to zero firing rate from which additional anodic steps brings the firing rate to the zero firing rate plateau. Similarly, when a depolarizing (cathodic) step is given, it creates a new baseline from which additional cathodic steps bring the axon closer to the cathodic block zone, again causing a plateau at the maximum firing rate. In the Manca this plateau was experimentally observed around 55 sps on average. To simulate this, we limited the firing rate to a maximum of 55 sps (Figure 9d right panel), and, when we added the changes in firing rate from baseline offset, the change in firing rate looked very similar to those seen experimentally (Figure 9e top panel). This theoretical explanation would predict there is no additional axonal effect, but that reduced firing range in the neurons from the Manca dataset produced an artificial offset that was previously considered a separate effect (Effect 5).

When we conducted the full simulation with $\mu(t)$ changing as a function of F_{adapt} and the full biophysical model, the simulated results closely matched those seen experimentally (Figure 9e). These results are consistent with the hypothesis that GVS steps activate the hair cell adaptation response and modify the baseline activity of the axon.

2.3.8 Filtering Effects of Hair Cell-Afferent Model Explain Frequency Responses

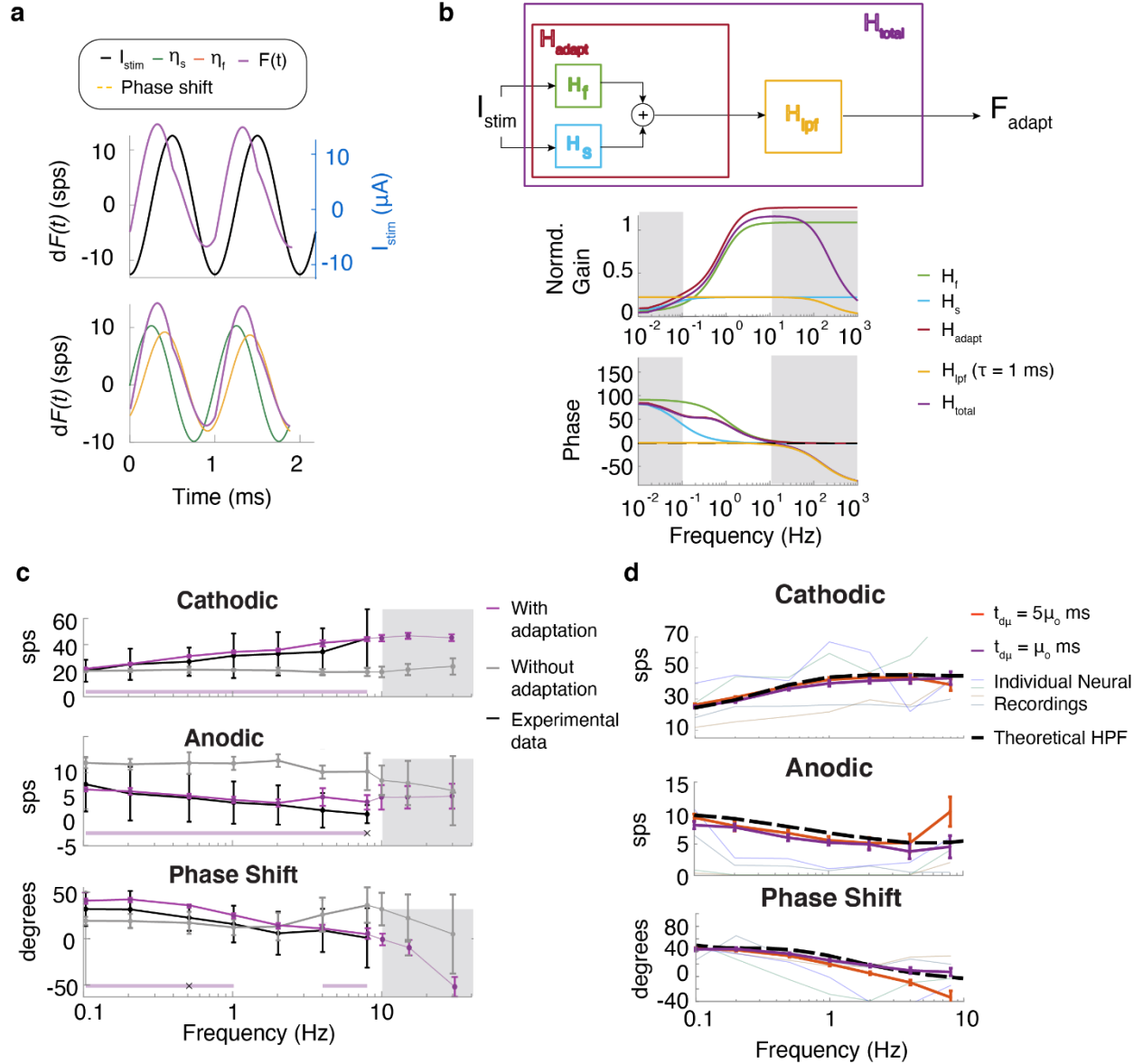


Figure 10. Responses to sinusoidal GVS modulation can be accounted for by the hair cell adaptation response.

a) Response to sinusoidal GVS can be accounted for by the fast and the slow adaptation response of the hair cell. **b)** Frequency response of F_{adapt} comprises the fast and the slow components as well as the hypothesized low pass characteristics associated with the ability to respond to incoming EPSCs. **c)** The firing rate and phase in cathodic and anodic halves of the cycle with the axon modeled with adaptation (purple) without adaptation (grey), and the original data (black). Significance of difference between with and without adaptation cases are indicated in light purple. Significance of differences between the model with adaptation and the original data are marked with x's with matched simulation and afferent recording number. Data outside the original range is shown in grey.

White portion correlated to frequency stimuli used in the *in vitro* experiment. **d)** Examination of the low pass filtering characteristics imposed by changing the rate of EPSC sampling t_{ep} .

If GVS effects on the axon are substantially attenuated in the Manca study as we concluded earlier, the hair cell adaptation mechanism must be primarily responsible for the observed responses to sinusoidal GVS modulation. We investigated whether the hair cell adaptation properties described above could alone be responsible for the firing rate responses to sinusoids (Figure 3e). We observed that $F_{\text{adapt}}(t)$ in response to 0.1 Hz sinusoids shows the phase lead (Figure 10a). On closer inspection, the hair cell adaptation response is the sum of two sinusoidal responses by the fast and slow component, and the phase lead is due to the higher-gain fast component responding more quickly to the maximum change in firing rate that occurs a quarter of a cycle (90 degrees) before the cathodic phase of stimulation. The stochasticity of axonal firing likely smooths this response into the observed sinusoidal firing pattern observed experimentally.

The filtering effects can be broken down by performing linear systems analysis on the equations for $F_{\text{adapt}}(t)$ in frequency domain. The fast and slow components describe two high-pass filters, H_s and H_f with corresponding cutoff frequencies of $1/\tau_s$ and $1/\tau_f$ (Figure 10b). We exposed the *in vitro* model to sinusoidal GVS modulation of 0.1 Hz to 8 Hz, as in the Manca study (Figure 10c white section)²⁷. The simulation with the adaptation effect produced changes in cathodic and anodic firing as well as phase shifts that closely correspond to the experimental data from the Manca study (Figure 10c purple and black traces). When no hair cell adaptation was included, the change in firing rate in each half of the cycle (the gain) and the phase are nearly unaffected (Figure 10c gray traces).

When we extended the analysis to higher frequencies of up to 25 Hz (grey section), the phase decreased below zero in the model including adaptation, which is not a feature of high pass filters. Additionally, the decrease in phase was present at the same frequencies in the axon-only model. Because neuronal firing is limited by the timing of protein and channel dynamics, we must assume that there is a limit to how fast the neuron can respond to stimulation changes. For this reason, we incorporated a hypothetical low-pass filter H_{lp} into the model (Figure 10b) and since we do not know the exact characteristics of this response, we assumed the cutoff to be 1kHz because the HK model could elicit 1kHz firing behavior at small values of μ_0 seen in Figure 5a.

We considered possible mechanisms for this effect. One way to slow response of the axon to hair cell adaptation is if EPSC arrival $\mu(t)$ update with $t_{d\mu}$ substantially slower than the frequency of stimulation. When we slowed down the interval between samples $t_{d\mu}$ from μ_o to $5\mu_o$ ms, there was a decrease in firing rate in the cathodic half of the cycle and an increase in firing rate in the anodic half, consistent with a reduced gain. There is also a dip in phase below zero (Figure 10d red). These are characteristics of a low pass filter. Meanwhile at $t_{d\mu} = \mu_o$ ms, the change in firing rate and phase is like a theoretical high pass filter effect (black dashed line), with phase remaining at zero (Figure 10f purple). This suggests that the update of EPSC arrival rate could be one mechanism behind the low pass filter effect. On re-examining the Manca experimental data, we found trajectories of some isolated neurons (thin colored lines) were consistent with the low pass characteristics predicted by the model. This combination of high and low pass filtering effects creates a bandpass filter effect center around $1/\tau_i$. The centers appear to be offset across recorded neurons, which implies vestibular afferent frequency response may be highly sensitive to small changes in head velocity frequencies in the band-pass filter range. If this theory is accurate, the frequency tuning of the irregular afferents may contribute to head velocity coding propagated to the central nervous system.

2.3.9 The Complete In Vivo Vestibular Afferent Model Behavior Predicts Experimental Outcomes

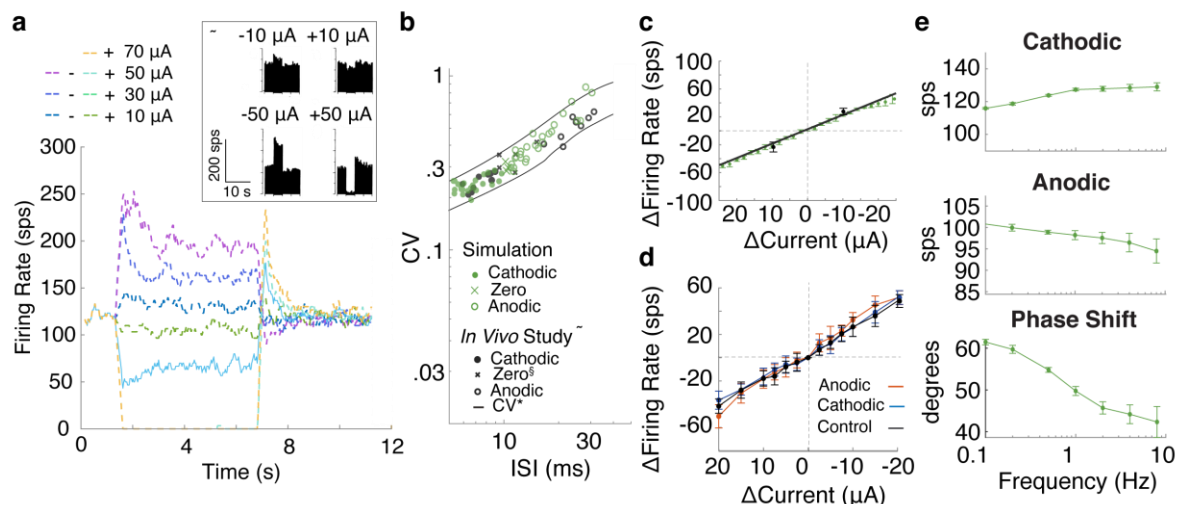


Figure 11. The complete effects of GVS in the in vivo model including hair cell adaptation.

a) Firing range induced with current steps from $-50 \mu\text{A}$ to $70 \mu\text{A}$, showing adaptation and axonal response that matches Goldberg experimental results (box). **b)** The CV vs. ISI associated with GVS stimulation using the model (green) compared to the CV ISI relationship in the original paper (black), which indicates cathodic stimulation (filled circle), anodic stimulation (open circle), and natural head rotation (x's). **c)** The change in firing rate with cathodic current steps at slope of $2.5 \text{ sps}/\mu\text{A}$ (black) as in the experimental results. **d)** The change in firing rate with current steps up to ± 20 from a -10 , $+10$, and $0 \mu\text{A}$ current baseline across 5 repetitions. **e)** The

change in firing rate to cathodic and anodic portions of sinewaves of 10 μ A amplitude and the phase shift to frequencies from 0.1 to 10 Hz.

To create a complete *in vivo* vestibular afferent model, we combined the fitted hair cell adaptation from the Manca study and previously determined *in vivo* axonal parameterization to create a complete *in vivo* afferent model. When we included both effects, the maximum induced firing rate increased to 211 ± 8.7 sps. The adaptation response found in the Goldberg study²⁸ was closely replicated within the firing range, when we set $\mu_o = 0.25$ ms to produce $F_o = 120$ sps (Figure 11a). Additionally, when we included the adaptation effect, the change in CV vs. ISI was more centered in the CV* lines from the Golberg study. The percent of points within the CV* bounds increased from 75% without adaptation to 96.5% when adaptation was included (Figure 11b). The slope of increase in firing rate with cathodic current amplitude also increased such that it replicated the study, with a slope of -1.99 sps/ μ A CI[-2.03, -1.95] (Figure 11c).

We tested whether the responses to steps and sinewaves change in the *in vivo* model by repeating the experiments from the Manca study on that axon. There was however no analogous experiments were performed to compare our simulation results to. We found no significant differences between responses to current steps away from the three baseline conditions (Figure 11d). This finding agrees with our theory that low membrane conductances produce these differences in the Manca study (Effect V) (Figure 3); in the high conductance (*in vivo*) model, there should be no difference between these conditions, because the induced firing rate is well within the possible firing range of the neuron, so the change in amplitude remains approximately linear and not significantly different across the three conditions (Figure 11d). When we repeated the experiments that examine responses to sinusoidal stimuli, the change in firing rate during cathodic and anodic portions of each cycle had the same slope but firing rate changed around a higher starting point (Figure 11e). The phase shift had the same shape but increased by another 20 degrees. The smaller μ_o necessary to produce firing rates like the Goldberg study produced the overall larger phase lead (Figure 12). Together, these axonal and hair cell properties in combination can reproduce GVS effects that were not found to be statistically different from those observed experimentally.

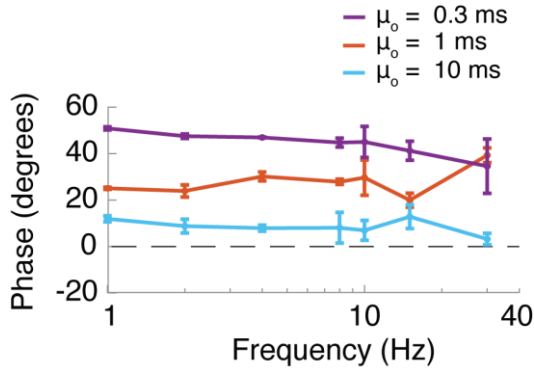


Figure 12. Effect of EPSC Arrival Rate on Phase

The smaller μ_o necessary to produce firing rates as large as the Goldberg study produces the overall larger phase lead.

2.4 Discussion and Future Directions

Table 2-2. Summary of findings about Galvanic stimulation

Effect Number	Dataset Reference	Experimental Paradigm	Experimental Observations	Explanations
I	Goldberg, Smith, Fernandez (1984) Fig. 5b; Manca et al. (2019) Fig. 2, Fig. 5	Squirrel monkey (extracellular stimulation, in vivo); mice (extracellular stimulation, in vitro)	Cathodic GVS increases firing rate. Anodic GVS decreases firing rate.	Axonal effect. GVS stimulation affects the axon by increasing the membrane potential with cathodic stimulation. This makes EPSPs of lower amplitude more likely to become APs. Anodic stimulation decreases the membrane potential so that EPSCs just above threshold become too small to induce an AP.
II	Goldberg, Smith, Fernandez (1984) Fig. 5b	Squirrel monkey (extracellular stimulation, in vivo)	Change in irregular afferent's firing rate to GVS amplitude is ~ 2 spikes/ μ A	Axonal and synaptic NQ effect. This increase and decrease in stimulation is primarily due to GVS stimulation changing axon reactivity to EPSP inputs. However, this effect must be magnified by the non-quantal effect to produce this large of a change in firing rate with respect to current amplitude change.
III	Goldberg, Smith, Fernandez (1984) Fig. 7a #382-24H	Squirrel monkey (extracellular stimulation, in vivo)	CV of GVS-evoked APs follows natural progression of CV*	Axonal effect. GVS stimulation is changing the proportion of EPSPs that become APs. These EPSPs are released at a rate drawn from a single probability distribution as in the normal physiological system in agreement with the concept of sampling variance.
IV	Goldberg, Smith, Fernandez (1984) Fig. 3a-h; Manca et al. (2019) Fig. 4c-d	Squirrel monkey (extracellular stimulation, in vivo); mice (extracellular stimulation, in vitro)	Change in current causes adaptation in firing rate in response to steps in GVS.	Hair cell effect. This effect has a similar time constant and relative magnitude of effect for cathodic and anodic GVS stimulation as for natural excitatory and inhibitory mechanical stimulation of the hair cell. We suggest that this effect is due to GVS stimulation activating the same pathway in the hair cell that is activated with mechanical stimulation either directly or indirectly.
V	Manca et al. (2019) Fig. 5	Mice (extracellular stimulation, in vitro)	Steps of GVS introduced after a baseline GVS presentation result in proportionally different response	Hair cell and axonal effect. This effect was potentially the result of in vitro neurons having a small firing rate such that an anodic baseline lowered baseline firing rate and additional steps of anodic stimulation draw this firing rate towards zero, causing plateau. Similarly,

			amplitudes that depend on the baseline in the in vitro studies but not in the in vivo studies	cathodic stimulation drove baseline firing rate towards the upper limit of the in vitro firing rate.
VI	Manca et al. (2019) Fig. 3	Mice (extracellular stimulation, in vitro)	Sinusoidal GVS modulation suggests a high pass filtering effect.	Hair cell effect. The hair cell pathway that is related to the adaptation effect acts as a high pass filtering effect with a cutoff at around 8 Hz.

Observed effects of GVS stimulation referenced in Figure 3 on vestibular afferents and the physiological explanation predicted by our model. Experimental data either comes from the Manca et al. (2019) study or Goldberg, Smith, Fernandez (1984) study. For some experiments the model was assessed for its ability to fit both models. Final predictions about mechanism are displayed in the last column.

Under the initial hypothesis that GVS stimulation affects only the axon, we started with the simplest biophysically realistic model (only an accepted model of an axon with the minimum number of channels specific to the vestibular afferent to produce naturalistic firing statistics) in the attempt to replicate all experimentally obtained results from the Goldberg and the Manca experiments^{27,28}. When the simplest model was not able to replicate all experimental data, we systematically added more biophysical features to our model until we were able to replicate the displayed irregular afferent experimental data across the two papers compared in this study (Table 2-2). The mechanisms that we found sufficient to simulate those the specific aspects of afferent responses and differences between the two afferents are summarized in Table 2-2.

2.4.1 Afferent and hair cell properties implicated in GVS-modulated responses

The Hight and Kalluri (2016) model depicted vestibular afferent firing as occurring through the afferent fiber acting as a receiver for stochastic hair cell release of vesicles. When subjected to GVS modulation, it produced CV relationships that matched natural firing properties seen in the Goldberg experimental results (Table 2-2). However, to accommodate the natural spontaneous activity and firing range, we had to increase the baseline EPSC arrival rate and membrane channel conductivity (corresponding to the concentration of channel expression), within physiological bounds. We also found that the sensitivity of firing rate to current amplitude was not as high as observed experimentally unless the influence of GVS on the axon was modulated by the NQ effect. This finding is consistent with past results that demonstrate the NQ effect and that it modulates external inputs to the afferent fiber^{83,103}.

The Manca experimental results showed low spontaneous activity and reduced maximal firing rate likely due to preparation effects. We can modify our model of an in vivo afferent to produce an accurate model of

an *in vitro* vestibular afferent. We simulated the reduced axonal sensitivity (lower firing rate and induced firing range) observed in the Manca experiment by reducing the membrane conductance (in our case, g_{Na}) and the magnitude of the NQ effect. It is also possible to reduce sensitivity of the membrane by reducing conductivity of other membrane channels or the NQ effect in different proportions, and we make no claim as to which channels are affected by the preparation. In contrast to the axon, the hair cell appears to be unaffected by the *in vitro* preparations, which would make *in vitro* preparation an excellent paradigm for studies of hair cell properties in isolation from the axon.

The idea that the hair cell pathway could be activated by GVS stimulation has been suggested in several previous studies^{114,130}. The model suggests that EPSC arrival rate and timing are essential to driving the spontaneous rate, inducible firing rates, and adaptation and filtering effects of a vestibular afferent. Without GVS stimulation affecting the axon, even in a low conductance axon that produces a maximum induced firing rate of only 70 sps and are simulated with a fast EPSC arrival rates the simulated neuron could produce firing rates of up to 1000 sps. We believe that this indicates natural head motion is captured by change in EPSC arrival rate. Specific membrane conductances are therefore not necessarily observed in the electrophysiology experiments that are restricted to mechanical stimulation. However, replicating the experimental data from previous studies revealed the importance of specific membrane conductances in a way that had not been previously reported before this study of GVS stimulation^{28,121}. We found that an increase of both g_{Na} and g_{KH} together is required to maximize the induced firing range of a neuron with GVS stimulation, as seen in Figure 6, and we confirm g_{KL} seems to only affect firing regularity without changing induced firing rate^{28,87,125}.

The hypothesis that hair cell adaptation causes the afferent to produce an adapting firing rate over time can be closely simulated through an adaptation in rate of EPSC arrival from the hair cell, suggesting one mechanism of the hair cell adaptation pathway influencing axonal firing. We propose that EPSC rate remains stable without activation of the adaptation pathway and adapts when it is active. A comparison of the Goldberg and Manca response to long-term GVS steps showed that there is both an instantaneous adaptation effect and a baseline change in firing rate that increases with current amplitude. In the example traces in the Manca paper, this effect was nearly unobservable but statistically significant. This suggests the

adaptation pathway in the hair cell is separable from the uniform increase/decrease in firing rate with cathodic/anodic current, which we deduce to be the axonal response to GVS stimulation (*Figure 9a*). An NQ effect is necessary to produce a large enough change in firing rate with GVS stimulation at the axon. However, the mechanism of production of the baseline shift in firing rate and of adaptation does not seem to depend on NQ effect, so we find no evidence that it is anything but modulatory on membrane current influx due to GVS stimulation as previously suggested¹²⁷.

Another important feature of the hair cell adaptation pathway appears to be that it produces a filtering effect on input signals. Our results matched those obtained experimentally in the Manca experiment in which electrodes were positioned directly in the epithelium. Our model assumed no additional filtering due to ionic motion through tissue and could closely match data from the Manca experiments, so we assume that the tissue impedance did not cause a strong effect on the response to GVS. We would, however, expect a frequency-dependent effect in the in vivo application of GVS, especially when the electrode is positioned further away from the target tissue. Tissue impedances at higher frequencies are lower than those at low frequencies due to the inverse capacitive impedance relationship with frequency¹³¹. This effect decreases the sensitivity of cells to electrical stimulation at higher frequencies (>10Hz) as typified in the standard strength duration curves¹³².

Adaptation has been posited to be composed of a fast component and slow component response¹¹³. We show the adding hair cell adaptation that causes an adaptation in the average inter-EPSC arrival interval created a high pass filter effect on firing rate output like that in the Manca data as well as other vestibular afferent studies in response to GVS^{27,71}. We also find evidence of low pass filtering and propose a mechanism that could induce this effect. We theorize that each irregular vestibular afferent has a specific filtering characteristic and phase shift that only equals zero at its center frequency. As observed in a small sample of electrophysiology recordings (*Figure 10d*), they may have a slightly different tuning to a specific frequency of head velocity response. In this way, the irregular vestibular afferents may transfer more information about velocity through the population response than previously suggested¹³³.

We did not have enough data on regular afferent firing to make a thorough characterization of the response to GVS stimulation. However, because regular afferents accept inputs from hair cells, they also

likely have adaptation that leads to frequency-specific tuning. Similarly, axonal effects observed here should occur, but regular neurons have many fewer calyceal synapses in favor of bouton endings and therefore have a substantially reduced NQ effect, which is only seen in calyces. This likely results in the substantially lower slope of increase in firing rate with GVS current amplitude for the regular afferents as compared with irregular afferents, as previously reported²⁸. Adaptation in regular afferents has also been shown to be present but with lower amplitude than in the irregularly firing neurons, also consistent with fewer calyceal inputs in the regular afferents¹³⁰. We would therefore predict that regular neurons would not have as dramatic of a frequency-dependent phase shift in signaling observed in irregular neurons.

The mechanism of single cell firing and response to GVS stimulation has only been modeled previously by Smith and Goldberg (SG model)¹²¹ in an attempt to explain the results obtained in the same Goldberg study. This model can approximately produce Effects I, II, and III with the assumption that galvanic stimulation only affects the axon, but the authors note the change in firing rate does not follow the shape observed experimentally. This model predates the discovery of KL channels and the NQ effect, although the authors hypothesize differences in potassium conductances underly differences in regularity as well as that there must be a ~4 times larger sensitivity of irregular afferents to GVS stimulation. The authors ultimately use larger magnitude EPSCs to drive irregular firing, whereas the higher density of KL channel alone can lead to dynamics that produce irregularity. In addition, we found no evidence of significant difference in EPSC amplitude between afferent types suggested by the SG model and show that only EPSC arrival rate changes are necessary to match experimental data. We note that either larger amplitude EPSCs or faster EPSC delivery would lead to more frequent summations of EPSCs as the axon would often produce a similar change in firing rate. However, our model seems to produce the effects of GVS more accurately, given our current understanding of vestibular afferent and hair cell physiology. In addition, a major contribution of this model is our ability to provide an explanation that addresses Effects IV, V, and VI, which were not explained in the SG model.

Our findings indicate that natural modulation of hair cell vesicle release rate is sufficient to explain the rapid onset followed by a slow, seconds long decay in firing rate in response to a step GVS. There are other possible mechanisms that could be involved in this response profile. (1) We investigated if axonal mechanisms alone could produce this effect, including implementing a dynamic synaptic NQ effect,

hyperpolarization-activated cyclic nucleotide (HCN) channel K⁺ currents, and Nav1.5 channel, not present in our original implementation of the HK model^{104,125}. The dynamic NQ effect and both channels have long time constants on the order of the adaptation terms observed in experimental data. These effects alone could not produce transient changes in firing (Figure 8). It is worth noting that HCN channels are weakly selective to K⁺ compared to most voltage-gated potassium channels¹³⁴, so there may be additional effects unexplored here. (2) Given the presence of the dynamic NQ effect in the hair cell—afferent synapse, it may be possible that instead of GVS affecting the hair cell and producing changes in vesicle release directly, it could change the axonal firing rate, which then in turn would change the K⁺ concentration in the synaptic cleft, causing the hair cell to modulate its vesicle release rate with its natural inherent dynamics following the NQ mechanisms described by Contini et al.^{104,129}. There was insufficient data on calyceal K⁺ concentrations to model this effect directly. (3) Efferents have been shown to cause rapid increase in sensitivity of the afferent that decays over time¹³⁵. It is not clear, however, how this effect could explain the rapid firing rate decrease in response to the hyperpolarizing anodic step. A validated computational model of the efferent activity is not available at this time, and we could not introduce it into the model. (4) Our model replicates experimental cell dynamics in the form of a single afferent receiving input from a single hair cell input (the diversity of EPSC amplitudes and statistics are of variability recorded at an afferent such that it may represent a typical irregular afferent that is dimorphic and receives input from several hair cells though). Rabbitt et al.¹¹³ results, used to develop this aspect of the model, show that a step cupula displacement leads to a rapid onset and subsequent decay of afferent firing rate, potentially somewhat relate to tip link attachment movement. We do not have data to indicate if a single hair cell alone or combinations of hair cells could produce the EPSC pattern that generates the transient response from the afferent, although we suspect it is dimorphic.

The focus of our investigation was on understanding the axonal and hair cell components involved in GVS stimulation. To do this we modeled the axon as a single point model with equations modulating axon inputs and dynamics to account for properties of a hair cell and an afferent. This approach was established by Hight and Kalluri to successfully understand the role of channel dynamics in firing regularity. Because the anatomic features are not included in this model, it is not possible to determine the influence of electric current on the hair cell versus the axon directly. However, our models can predict the magnitude with which GVS affects membrane potential and EPSC arrival. Adding morphologic details to this model might provide

further insight into the effects of electric fields on the hair cell and the axon. We also do not exclude the possibility that these effects may reveal alternate explanations to the observed phenomena.

2.4.2 Implications of targets of GVS stimulation for integration in prostheses

A limitation to producing naturalistic firing would be if the neuron has a reduced firing rate due to low EPSC arrival rate, in contrast to the low firing rate due to reduced membrane conductance implicated in the Manca experiment. This effect is likely to be seen in the gentamicin treated animals^{136,137} and are likely to occur in patients in need of the vestibular prosthesis¹³⁸. Then, GVS stimulation would only be able to elicit APs due to direct depolarization and would produce more unnatural firing statistics. Even when EPSC input was removed from the model, GVS stimulation can induce firing rates of up to 220 sps in our simulated neurons, which approaches the maximum firing rates observed in vestibular afferents, so this limitation appears to be minimal. However, it still requires testing to determine whether the naturalistic rate and statistics of firing produced by GVS at the vestibular afferent are received by downstream targets the stimulated neurons. Past experiments in which hair cells were impaired due to gentamicin exposure on one side of the vestibular system and replaced with GVS stimulation produced VORs closer to the full range of velocities typical in a chinchilla than using pulsatile stimulation^{25,93}. This appears to indicate that the GVS-evoked afferent firing patterns are well received by downstream targets and therefore useful in connecting damaged neuron in neural circuitry.

The finding that GVS stimulation affects both the axon and the hair cell in the vestibular system suggests that similar effects could in principle be advantageous in prosthetic replication of other sensory functions. (1) GVS affects end organs and smaller receptor cells rather than just axons as is the case with pulsatile stimulation. This means that in principle one could affect inputs that are further upstream in neural processing, allowing for potentially more natural responses that could engage the same molecular and cellular machinery as in the normally behaving physiological system. For example, for retinal implants, it means that bipolar or photoreceptor cells could be targeted rather than the retinal ganglion cells and therefore using the natural significant processing capability of the retina. (2) GVS can induce graded amounts of excitation or inhibition through membrane potential changes that can match the natural system firing rates rather than relying on the more artificial activation of the axons with pulsatile stimulation. Meanwhile, pulsatile

stimulation will have limitations on maximum firing rates that are dependent on pulse amplitude¹²³. (3) GVS can capture natural stochastic firing patterns that could be important to the system. We already know for example that in the vestibular system, pulsatile stimulation causes substantial attenuation in the central nuclei in response to concerted firing evoked by pulse trains⁸⁶ possibly due to repeated synchronous afferent activation¹³⁹. Similar realization in cochlear implants has led to the development of high-rate stimulation paradigms⁵⁶, which can desynchronize pulse-evoked activity, but there is no evidence this produces firing that matches the natural stochastic patterns. GVS may be able to evoke the hair cell and axonal responses that maintain natural firing statistics.

2.5 Findings in the Context of Vestibular and GVS Research

This work takes a novel approach to addressing problems that have been central to vestibular research for the last several decades: how do the vestibular afferent and hair cell complex work together to process information, and what aspects of these system are activated by GVS to produce relatively naturalistic firing responses? Instead of simulating and analyzing experimental findings of vestibular afferents under natural head rotations or channel block, we use responses to step and sinusoidal GVS as an assay of vestibular function. Our model starts with the afferent and voltage-gated channels (Na, KL, and KH) considered essential to producing irregular and regular firing⁸⁷. Parameters were modified and additional known properties of vestibular afferents were added only until all GVS responses were observed. Using this method, we produce a theory for how GVS could produce naturalistic firing rate modulation given how natural vestibular processing is suggested to function in the semicircular canals. Our findings suggest that GVS preserves regularity by modifying the statistics of EPSPs at the axon, and the known channel dynamics cause this effect to produce firing with regularity natural to the stimulated neuron. Additionally, the double-exponential effects (Effect IV) and triggering of the non-quantal effect (Effect II) by GVS bear a number of similarities with the current understanding of how efferent signals affect hair cell and afferents. Thus, we hypothesize that GVS is tapping into the set of natural pathways designed for efferents either by directly activating efferents or depolarizing channels central to those same pathways. We also note the caveat that the properties of vestibular afferents and hair cells are distinct in different organisms which complicates our ability to tie these conclusions in with existing studies and make arguments about how our findings may

apply to GVS of the human vestibular system. Below, we review how we came to these conclusions in further detail.

2.5.1 A Cohesive Theory of Natural Vestibular Firing and Regularity

The vestibular mechanisms that underpin firing regularity were first explored using electrical stimulation. The first observation was that irregular afferents recovered from pulsatile stimulation more quickly than regular afferents^{28,94}; this finding led to the theory that there were different potassium channels in the irregular afferent, which allowed a faster afterhyperpolarization recovery. GVS was also used on regular and irregular afferents, revealing a correlation between CV* and sensitivity to galvanic stimulation. It is worth noting that irregular fibers tend to have a larger diameter, which may contribute to easier electrical excitability and this observed effect. However, these findings led to the popular Smith-Goldberg theory that irregular neurons having an alternative potassium channel that allows for faster afterhyperpolarization and increased “synaptic noise” that can lead to more variability and higher sensitivity to EPSC inputs¹²¹.

More recent studies provide several alternative explanations for these phenomena. Smith and Goldberg originally infer a potassium channel is involved, based on similar potassium channels in motor neurons which allow for rapid response¹²¹. The KL, low-voltage activated potassium channel, has been found to be expressed more within irregular afferents, and, if blocked, causes irregularly firing afferents to fire with more regularity^{85,115}. The combination of sodium and potassium channels have dynamics that have been shown to cause periods of irregularity in response to inputs⁸⁷. Presence of KL channels has also been shown to increase resting membrane potential, leading to increased sensitivity to inputs⁸⁷. Another channel implicated in irregularity is the HCN channel, which is shown to be expressed in the calyx^{140,141}. In past simulations, HCN channels were not found to significantly change spike timing^{26,87}. However, more recently, HCN channels were shown to activate KL channels, amplifying effects on irregularity¹⁴². Potentially, this effect was captured by increasing the simulated channel density of KL channels within our model. Within a detailed model of reconstructed bouton and calyx terminating afferents, twelve different ionic channels in boutons and calyces of measured sizes were simulated⁹⁷. These findings, further support the primary importance of KL channels in irregularly. Meanwhile, peripheral terminal structure was not implicated to be a major

determinant of spike train regularity. Within the bouton, SK channels were implicated as being involved in promoting regularity of firing⁹⁷. Addition SK channels to modeling may further complicate our findings.

Another major point of the Smith-Goldberg model, which has driven thinking on vestibular function for some time, is that irregular neurons have larger synaptic variability. While Smith and Goldberg modeled the synaptic noise as differences in quantal sizes, they also noted that synaptic release rate could be a source of variability in EPSP size¹²¹. Support for both possibilities have been found. The specialized ribbon synapses have the capability of releasing quanta quickly and modulating release rate with head motion. Ribbon synapse expression was found to be different across afferents. Differential expression of ribbon synapses could cause a difference in summed postsynaptic depolarization (which are being modeled in the HK model as EPSP size of a single distribution) due to rate of vesicle release. There is other evidence for variance in EPSP size. One-to-one bouton to hair cell connections led to similarly sized EPSPs summing in time, but connections, particularly to increased numbers of calyces led to a subset of higher amplitude EPSPs and higher irregularity of firing⁹⁷. Connectivity to multiple structures more generally was also shown to causes increased irregularity⁹⁷. Understanding as a combination of distributions, even regular distributions, that may have phase offsets, this finding should hold for both regular and irregular firing neurons. Within bouton-ending afferents, EPSP amplitudes were also shown to vary substantially, and EPSP size correlated to bouton size; however, more variance is observed in EPSP size in irregular afferents. Thus, both these sources of “synaptic noise” or EPSP variability are possible.

Another relevant conclusion of the Smith and Goldberg paper is that, if inputs to calyces are from distributed sources, as opposed to the 14x increase in sensitivity for calyx bearing afferents they use in their model, only a 4x increase would be required to produce the observed sensitivity of irregular afferents¹²¹. A later discovery in the vestibular system is that calyx has a NQ effect that amplifies incoming currents to the afferent about four-fold¹⁰³. In this case, significant differences in glutamate release would not be required to make the high sensitivity observed in irregular afferents, and the NQ effect could explain increased sensitivity of irregular afferents. It is additionally worth noting that temporal summation of EPSPs of fixed amplitude occurring at different rates could produce similar action potentials to EPSPs arriving at the same rate but with varying amplitude. Evidence suggests that variance in EPSPs is amplified with calyx bearing afferents, leading to the diverse heights of EPSPs recorded at afferents, but some combination of both effects could

produce EPSPs that are observed naturally. Together, these findings indicate that simulating synaptic transmission that produces natural regularity requires at a minimum experimentally observed variance in EPSP amplitude and rate and differences in KL channel density to replicate differences in firing.

A previously unanswered question about regularity is why it varies within a fixed range with firing rate (CV^*). Smith and Goldberg explain that naturally firing rate changes by modulation of vesicle release, so, if quantal release was not affected by GVS, it would be unclear how CV^* could be preserved. No further publications were found in the literature that addressed how CV^* remains within a certain variance as firing rate changes. Steinhardt and Fridman²⁶ uses biophysical modeling and statistics to suggest that in fact CV^* could be preserved if GVS only affected the axon, and it would statistically mimic natural quantal release modulation. When the simulated axon was exposed to GVS while receiving the same EPSC input, EPSC height was shown to increase and decrease with excitatory and inhibitory galvanic current (blue and red) compared to baseline (black) (Figure 13a). In the simulations, action potential (AP) formation time was within milliseconds of some EPSC time given the EPSC fit a certain set of conditions, so AP time was considered to be a sampling of EPSC arrival time, when EPSCs summed to some threshold level that allowed depolarization. EPSCs were randomly sampled to APs at a higher (0.6, blue) or lower (0.3, red) rate, and the inter-spike interval, based on EPSC timing, was calculated (Figure 13b). Sampling more or fewer EPSCs from the same underlying distribution caused decrease and increase in variance, due to the statistical phenomenon known as sampling variance.

Naturally, the EPSC arrival rate, which relates to vesicle release rate, is known to increase with excitation and decrease with inhibition. The probability of forming an AP is ultimately a probability of EPSCs arriving within a certain timing and holding amplitudes above a certain threshold that leads to a set of cases that produce an AP. This can be considered a sampling of a distribution of inter-EPSC intervals and EPSC amplitudes (Figure 13c). Naturally, excitation causes the inter-EPSC timing distribution to shift left, so that EPSCs are on average more likely to produce APs. Excitatory GVS causes the amplitude of EPSCs to uniformly increase, which is equivalent to shifting the threshold for EPSC amplitudes to the left (Figure 13c). Statistically, Steinhardt and Fridman (2021) showed that by the central limit theorem, there is a GVS amplitude that therefore gives an equivalent statistical probability of EPSCs producing APs to natural stimulation, resulting in the CV^* or change in CV with firing rate being preserved under GVS (Figure 13a,d).

Previously a common mechanism for spike generation was hypothesized to underlying the approximate square-root scaling between CV and ISI¹⁴³. The approximately square-root relationships between firing rate and EPSP arrival further supports this theory for the common mechanism⁹⁷. This theory from Steinhardt and Fridman (2021) suggests that the sampling would occur for any given EPSC input to an axon, and the irregularity of sampling observed in irregular afferents comes primarily from KL channel density at the point of sampling, the afferent²⁶. With these conditions, the main properties of vestibular firing under natural and GVS modulation is explainable.

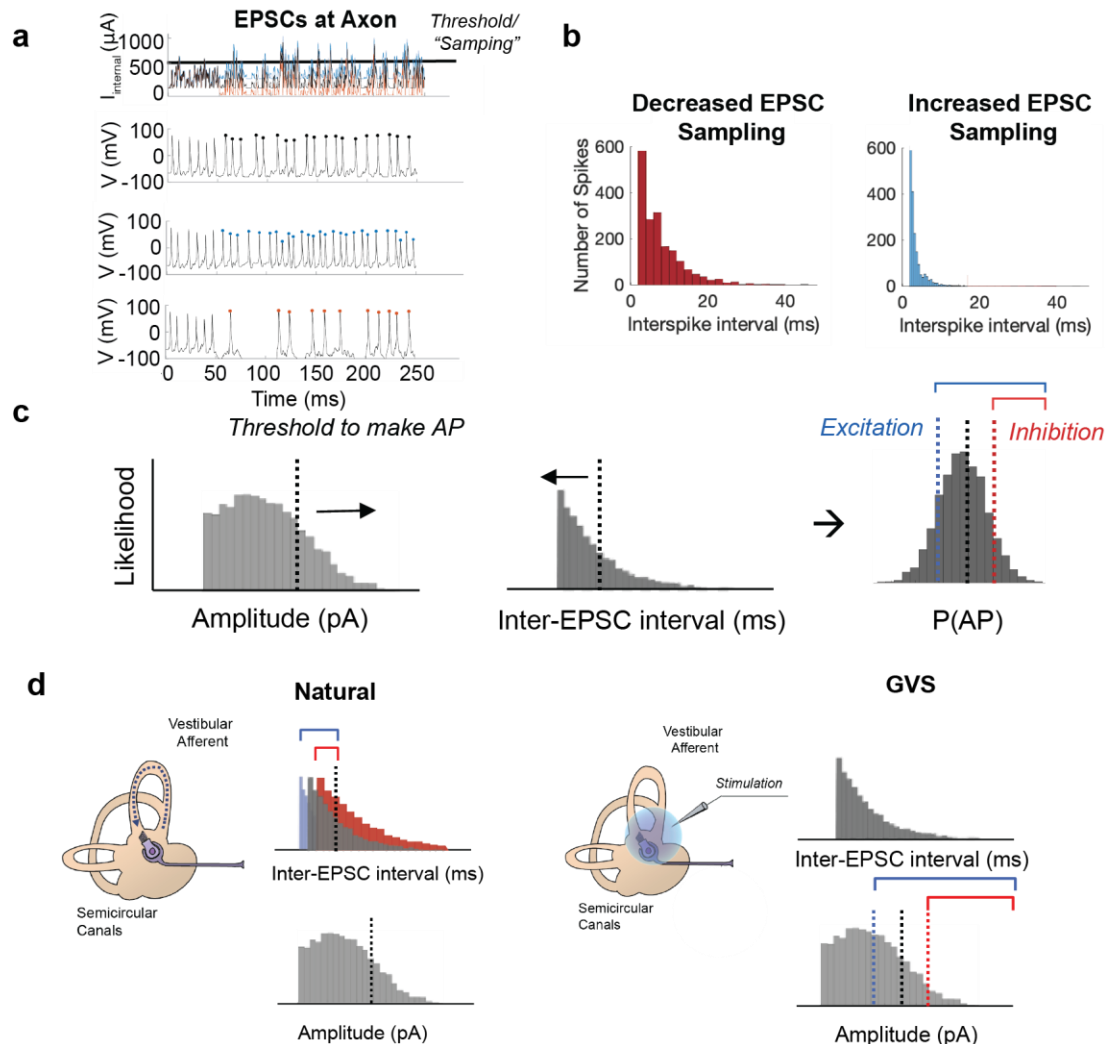


Figure 13. A theory for CV* naturally and in response to GVS.

a) Simulated EPSCs for same seed under excitatory (blue) and inhibitory (red) GVS. The induced APs are shown below with dots in respective colors for produced APs. Simulation results show the timing of APs is approximately a sampling of the timing of EPSCs when they cross a threshold current amplitude. **b**) The effect on interspike interval of randomly sampling fewer (red) or more (blue) EPSCs than 50% into APs and assume spike timing equals EPSC timing. **c**) The statistical theory that the probability of an AP is a combination of the probability that amplitude of EPSCs falls above some threshold (black dashed) and the inter-EPSC interval is less than some threshold (dashed). **d**) (left) The natural change in the number of APs produced by excitatory head movements is due to a

reduction in the mean of the inter-EPSC interval (blue) while EPSC amplitude is fixed. (right) GVS does not change EPSC interval but changes the threshold for an EPSC to create APs by shifting the EPSCs up or down by some offset proportional to current injection. Sampling these two distributions at some level statistically is shown to produce similar probabilities of excitation (blue) or inhibition (red) c).

2.5.2 Possible Sources of Conflicting Results of Galvanic Vestibular Stimulation

A topic of controversy in the Steinhardt and Fridman study²⁶ was the observation that sinusoidal GVS produces changes in firing (gain and phase of vestibular firing) that closely resembled responses to head rotations from the experimental work discussed in the publication. The observed gain and phase relationships clearly differed however from previously collected primate data^{114,144}. Our literature review suggests that different animal species may have substantially different filtering properties to GVS and natural mechanical stimulation that limit the ability to draw conclusions across studies. Certain afferents across species share a number of similarities in firing properties. However, experiments would be required to assess whether afferent responses are due to the same mechanism of parallel mechanisms that produce similar responses. Differences between species include the physical size of the vestibular system, firing properties of the afferents, and the contribution of the efferents. All three may individually or together play a role in processing differences between afferents to natural stimulation and GVS.

The physical size of the labyrinth has been shown to affect mechanical filtering properties of the labyrinth. Comparison of mammalian labyrinths showed that smaller animals have reduced bandwidth with reduced phase shift, and increased gains at lower frequencies (Figure 14a)¹⁴⁵. This trend seems to also be maintained across species in general. For example, this is seen in comparison of the filter properties of frog afferents (Figure 15b) to rat afferents (Figure 15d) to macaque monkey afferents (Figure 15f).

Another variable that factors into these comparisons is body temperature and experimental conditions across studies. Channels in the axon are known to change their dynamics with change in temperature¹⁴⁶. The measured frequency responses across species may also be affected by body and environmental temperature, because frequency responses of vestibular afferents involved in controlling afferent firing also shift with temperature (Figure 14b)⁸³. For example, frogs have lower body temperature and *ex vivo* experiments were conducted at 18°C while chinchilla and monkey body temperature is around 38°C⁷¹. This may also factor into differences between amphibian and mammal sensitivity ranges (Figure 15b vs. d-f). However, temperature differences alone do not explain differences in fiber responses across species.

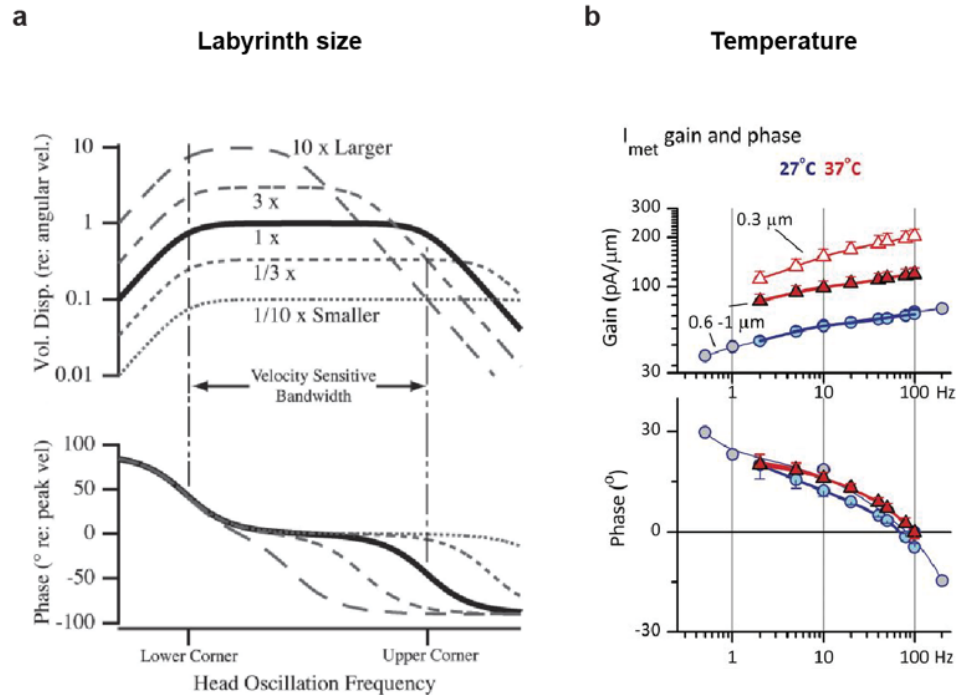


Figure 14. Physical Factors that Affect Frequency Response

a) Labyrinth size is shown to shift phase and centers of maximum gain as well, based on physiological data. Adapted from Highstein, Rabbitt, Holstein, Boyle (2004). **b)** Increased temperature increases gain and shifts the phase relationship to frequency by affecting the I_{met} hair cell channel. Adapted from Songer and Eatock (2013).

Even in animals with the same body temperature, different frequency response properties are observed across species. The toadfish, the evolutionarily oldest species, shows three distinct neuronal responses to sinusoidal GVS and mechanical stimulation of different frequencies for three distinct neuron types: low-gain, acceleration-sensitive, and high-gain in Figure 15a. Frog afferent responses seem to show not only the similar mechanical response properties to toadfish low-gain neurons, but also maintain the subtle differences between GVS and mechanical responses in a way that is similar to those of the low-gain toadfish neurons (Figure 15b red and blue; Figure 15a1 circles and triangles). Mice and rats, rodents, seem to produce nearly identical gain and phase responses to GVS and mechanical stimulation (Figure 15c and d) which mirror responses observed in acceleration-sensitive toadfish afferents (Figure 15a2). Chinchillas and squirrel monkey have irregular neurons that resemble high-gain toadfish afferents in their responses and regular neurons (Figure 15e) that more closely resemble acceleration-sensitive neurons (Figure 15a2, a3). Macaque monkeys have gain and phase relationships for regular and irregular afferents (Figure 15f) that both resemble the high-gain afferents of the toadfish (Figure 15a3).

These observations lead to the hypothesis that evolutionarily some properties of toadfish afferent firing could be relevant to higher-order animals, such as macaque monkeys.

One comparison that highlights how individual hair cell-afferent complexes may differ across organisms is the rodents (mice and rats) responses to GVS and mechanical stimulation to responses in chinchillas and squirrel monkeys (Figure 15c-d). It is likely that data from irregular afferents come from dimorphs with stronger input from Type I hair cells. However, frequency response properties (gain and phase) resemble chinchilla regular afferent responses more than irregular afferent responses (Figure 15e). This is potentially indicative of the regular fibers dominating the response characteristics of the dimorphic fibers in these animals. But more likely, irregular and regular afferents in rats versus chinchillas and squirrel monkeys have different filtering properties. These responses are also clearly different from the responses obtained from the macaques (Figure 15f) which show a rise in gain and a rise in phase response with frequency for both regular and irregular fibers when stimulated with either GVS or mechanical rotation. One potentially significant effect is the shift in phase and gain for mechanical stimulation versus GVS stimulation in the macaque studies; this may indicate there are additional mechanisms being activated mechanically that are not fully activated with GVS (Figure 15f). However, the trends in increased frequency GVS and mechanical stimulation track, which suggests similar gain and phase may be achievable with some correction.

Together the comparison of data across species indicates that animal model choice can significantly impact the effects of interventions, such as GVS. Thus, for any clinical study, animal models that approach humans as closely as possible are necessary. One promising finding in these data is that in rodents (Figure 15c-d) as well as in macaques (Figure 15f) GVS and mechanical stimulation produce changes in gain and phase of the same directionally but different magnitudes corresponding to the species. Seeing this similarity in filtering effects as animal models approach humans suggests that the naturalistic filtering of GVS may also occur in humans and may explain the advances in the clinical uses of GVS in vestibular prostheses and vestibular rehabilitation.

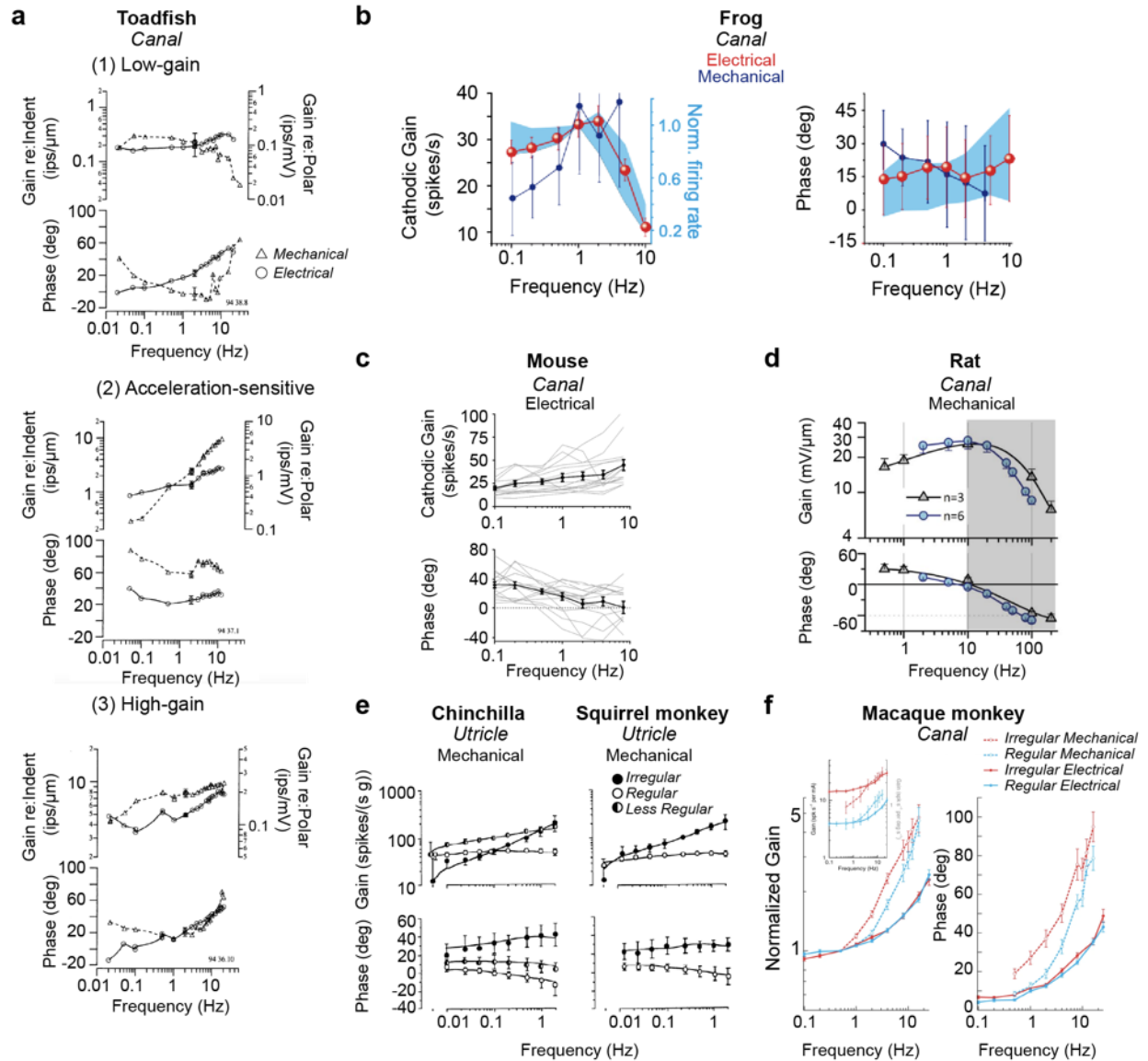


Figure 15. Cross-species comparison of Vestibular Filtering Effects to Galvanic Electrical and Mechanical Stimulation

a) Gain and phase of responses for individual low-gain (1) acceleration-sensitive (2) and high-gain (3) afferent to mechanical (triangle) or GVS (circle) stimulation of different frequencies within the toadfish. Adapted from Highstein, Rabbitt, Boyle (1996). **b)** Gain and phase of frog vestibular afferent to GVS (individual units in red with normalized standard deviation in blue) and mechanical (dark blue dots) stimulation. Adapted from Gensberger et al. (2016). **c)** Mouse canal afferent responses to electrical stimulation. Adapted from Manca et al. (2019). **d)** Rat type I hair cells at 27 ° for 3 (triangle) or 6 (circle) afferents responding to mechanical stimulation. Adapted from Songer and Eatock (2013). **e)** Chinchilla (left) and squirrel monkey (right) regular (open circle), less regular (partially filled circle), and irregular (filled circle) afferents responding to mechanical sinusoidal head rotations. Adapted from Goldberg et al. (1990a). **f)** Macaque monkey data from irregular (red) and regular (blue) afferents exposed to kinematic or mechanical rotations (dashed) versus GVS (solid). Results for otolith afferents show comparable high-gain trend with vertical shift for GVS and motion. Adapted from Kwan et al. (2019).

2.5.3 Possible Alternative Vestibular Afferents Mechanisms that May be Engaged in GVS

In Steinhardt and Fridman (2021), we suggested that GVS affects hair cell release of vesicles as well as afferent sensitivity to inputs and axonal membrane potential. This explanation satisfactorily

addressed Effects I-VI across the mouse and squirrel monkey experimental data (**Table 2-2**). However, there are alternative mechanisms that could also explain or contribute to the explanation of the experimental data examined in this publication. This discussion focuses particularly on the known effects of efferent activity that might be in some way activated by GVS.

We found that GVS affecting an axon alone could account for preservation of regularity of spike timing and change in firing rate. However, the addition of hypothetical hair-cell modulation by GVS was necessary to account for the transient changes and filtering properties (Figure 16a, b). Experimentally, there is evidence that the hair cell is contributing to afferent responses to GVS separately from the axon. A study in frogs where afferent firing rate was measured to increasing amplitudes of GVS while the synaptic transmission was blocked with glutamatergic antagonists (Figure 16d)⁷¹. After the antagonist was applied, there was an approximately linear increase in firing rate with current amplitude but a significant difference in induced firing rate that modulated non-linearly with GVS amplitude (Figure 16f blue line). Frog irregular afferents show higher sensitivity and larger size than regular afferents¹⁴⁷, and both categories of afferent show transient responses to GVS¹³⁰; however, the irregular afferent transient response is larger (Figure 16e). I_{met} (currents) in the hair cell increase with hair bundle displacement and shown to change gain and phase change with frequency of input (Figure 14b). It has gain and phase relationships like those required to model the double-exponential in Steinhardt and Fridman (2021)⁸³. One explanation then could be that the transient is caused by depolarization like that caused by I_{met} at the hair cell. This causes a change in vesicle release which is then amplified during synaptic transduction by a mechanism, like the non-quantal effect, in irregular afferent but not in non-calyx bearing regular afferents

Alternative mechanisms that were not discussed in the paper were those by which the efferents can affect the afferents and hair cells to produce some of the effects described above. Electrical stimulation of efferents seems to produce changes in firing rate at afferents that are highly similar to the effects observed under GVS. Shock or pulsatile electrical stimulation of increasing rate has been shown to produce double-exponential transients in afferent firing like those observed in response to GVS and mechanical stimulation (Figure 16c versus f)¹⁴⁸. In chinchillas, efferent stimulation has been shown to produce stronger, transient excitatory effects on irregular than regular afferents¹⁴⁹. In addition, as CV^* increased, the transient size and

sharpness grew with CV* (Figure 16g right). Both relationships resemble those of CV* affected by GVS (Figure 16c).

A complicating factor is that there are other responses to efferent stimulation that do not evoke these similar responses and the responses vary across species. Some irregular afferents show initial inhibitory followed by excitation in response to efferent stimulation¹⁵⁰. Whether efferents were inhibitory, excitatory, or showed this mixed effect was shown to relate to the location within the cristae in the turtle¹⁴⁸. In mice, efferents located ipsilaterally or near the midline were also shown to contribute a fast or slow component to the transient with times that fell close to the mean time observed for the time constants in response to mechanical stimulation (Figure 16h)¹⁵⁰. Different combinations of channel blockers were shown to block each component of this effect¹⁵⁰, and thermal inactivation of efferents was shown to reduce responses, particularly in irregular afferents¹⁵¹. Together, these results suggest that the filtering and transient effects observed during mechanical stimulation and GVS could be due at least in part to the activation of part of a natural efferent pathway that occurs across a variety of organisms.

The irregularity of an afferent, measured by its CV*, and location within the vestibular system (which is partially correlated to CV*) contribute to the differences of efferent effects and take on different relationships in different organisms. Additionally, evolutionary differences in connectivity also exist. For example, there are roughly 400 primary afferents and 50 efferents in fish, but mammals have a considerably higher ratio of afferents to efferents⁹⁵. Differences between the evolved mammalian efferent system may lead to further heterogeneity across observed efferent effects.

Based on the theory that the larger diameter axons depolarize at lower stimulation amplitudes than smaller diameter axons⁸⁸, it is unlikely that GVS directly excites efferents that are much thinner without affecting the larger diameter afferents. Thus, the working alternative hypothesis would be that depolarization of the hair cell and calyx are able to trigger mechanisms typically triggered by efferents. However, more hair cell and afferent recordings during distal efferent GVS stimulation would be required to parse out whether efferents are directly triggered by GVS in the experiments that were focused on in this study or whether the targets of efferents on afferents and hair cells being activated by GVS to produce similar effects on firing.

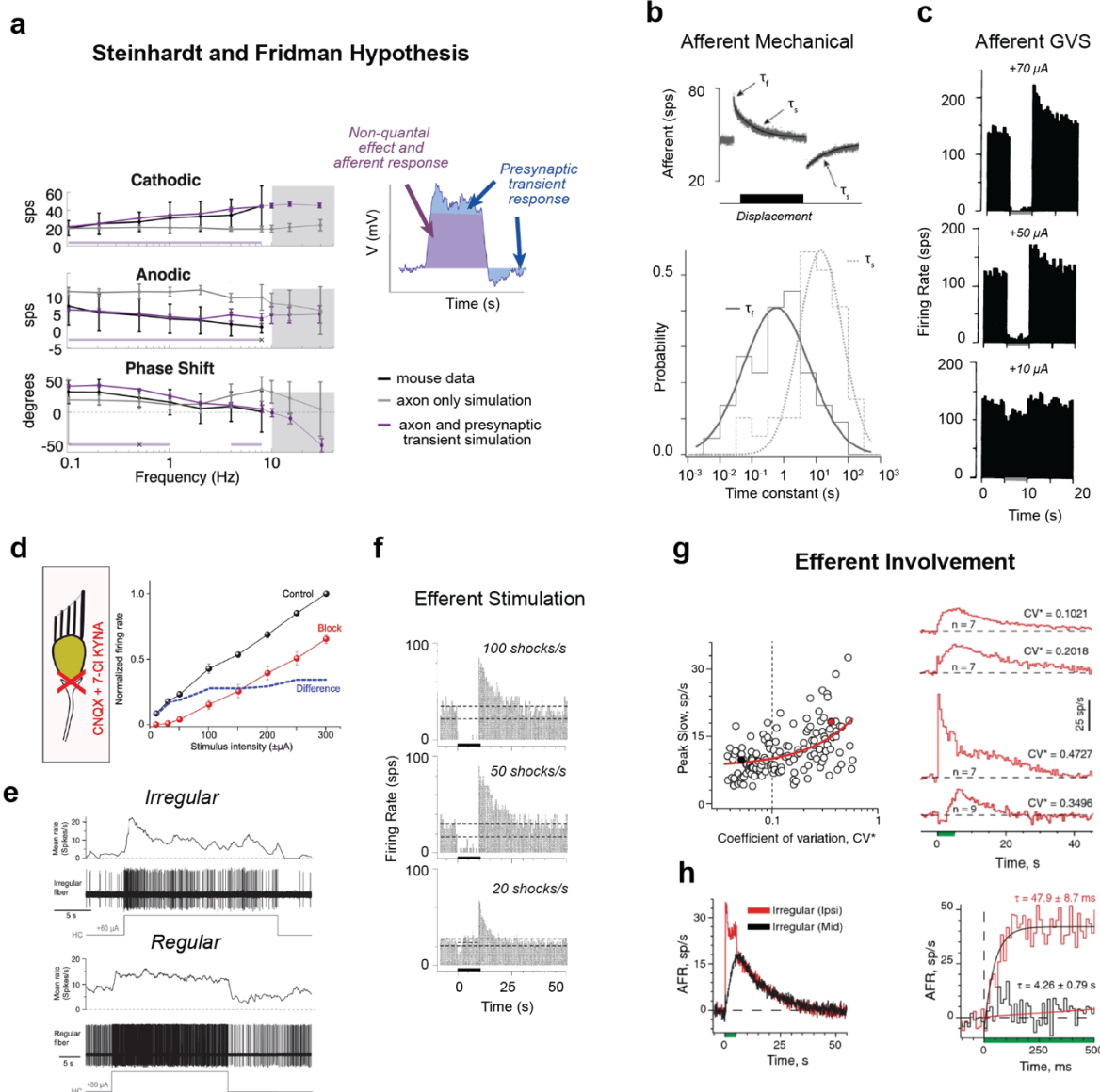


Figure 16. Contributing factors to Vestibular Processing Differences

a) Presynaptic effects have been shown to make transients in response to step inputs. Without these inputs, no filtering was observed in simulation (grey). With these effects added and amplified by GVS, filtering effects like experimental results (black) were observed (purple). Adapted from Steinhardt and Fridman (2021). **b)** Characterized double-exponential from Boyle et. al (2009) (top) and predicted fast and slow time constant range for hair cell and afferent responses (bottom). **c)** Afferents exposed to steps of GVS show a transient during GVS (grey bar) and after GVS ends that increases in size with current amplitude. Adapted from Goldberg, Smith, Fernandez (1984). **d)** CNQX and 7-Cl- KYNA were used to block synaptic transmission to the afferent while afferents were exposed to GVS. Prior to and after blocking, there was an approximately linear increase with amplitude, but there was a difference after blocking that modulate with current amplitude. Adapted from Gensberger et al. (2016). **e)** Irregular, calyx-bearing, and regular afferents were exposed to steps of GVS, and irregular afferents showed a strong transient while regular show a minimal transient. Adapted from Dlugaczky, Gensberger, and Straka (2019). **f)** Efferents exposed to shocks of different rates show similar transients as to GVS that start at onset and offset of stimulation (black bar) that increase with increased shock rate. Adapted from Brichta and Goldberg (2000). **g)** Efferent activity was shown to create a transient with a double exponential. The peak amplitude of the slow-component was shown to increase with CV^* (left). Example traces of the transient response from afferents with different irregularity. At the bottom is the case of an irregular afferent that shows inhibition then excitation. **h)** Ensemble irregular afferents responds to ipsilateral (red) and midline (black) efferent stimulation with shocks (left). Close up on first 500 ms of traces on left fit with fast time constant (τ_f) of 47.9 ± 8.7 ms and slow time constant (τ_s) of 4.26 ± 0.79 s (right). g-h adapted from Schneider et al. (2021).

2.5.4 Conclusions

Together, these findings suggest the GVS activates natural hair cell, synapses, and afferent mechanisms likely evolved to be activated by efferent input to hair cells and afferents. Whether GVS directly induces a depolarization that imitates efferent input or directly activated efferents is yet to be determined. We note that there are a number of processing differences between the frequency response characteristics of vestibular afferents across organisms, likely due to differences in size, temperature, and efferent connectivity. However, evolutionarily, analogous processing schema exist at the single neuron and population level and can be observed across vestibular afferents. Our work implies that each feature of vestibular afferent processing should be explorable with GVS across species, but it also reveals that filtering effects across species are substantially different, and, thus, when trying to draw clinical conclusions a focus should be put on primates that more closely reflect human anatomy at the cellular and physiological level.

2.6 Appendix

Table 2-3. Variables used throughout Equations for Modeling Biophysical Effects of Galvanic Stimulation

Variable	Meaning and Value in Final Model	Modification	Relevant Equation
V_m	Membrane potential	N/A	(2-1),(2-3)
C_m	Membrane capacitance. $C_m = 0.9 \text{ mF/cm}^2$	Unchanged	(2-1),(2-3)
S_m	Surface area of cell. $S_m = 1.1 \text{ e-5 cm}^2$	Unchanged	(2-1),(2-3)
I_{Na}/g_{Na}	Sodium channel current and conductance. $g_{Na} = 78 \text{ mS/cm}^2$; $g_{Na} = 7.8 \text{ mS/cm}^2$	Tuned	(2-1),(2-3),(2-5)
I_{KH}/g_{KH}	High voltage potassium channel current and conductance. $g_{KH} = 11.2 \text{ mS/cm}^2$	Tuned	(2-1),(2-3) ,(2-6)
I_{KL}/g_{KL}	Low voltage potassium channel current and conductance. $g_{KL} = 1.1 \text{ mS/cm}^2$	Unchanged	(2-1),(2-3),(2-7)
I_{leak}/g_{leak}	Leak current and conductance	Unchanged	(2-1),(2-3),(2-8)
m, h, n, p, w, z	State variables related to each of the channels and explained in relevant equations along with time constants(τ_x).	N/A	(2-6),(2-7),(2-8)
$I_h, I_{Nav1.5}$	Alternative channels not in final model. Relevant variables described in text adjacent to equations.	N/A	(2-9), (2-10)
I_{stim}	The internal current at the axon due to electrical stimulation. Some of currents in (2-1).	N/A	(2-2)
$I_{electrode}$	Current level at electrode used for external stimulation. Varied	Added	(2-2)
r	Distance from axon point source to electrode	Added	(2-2)
I_{stim}^G	The stimulation current with the NQ correction used to model the Goldberg study	Added	(2-11)
g_{NQ}, τ_{NQ}	The time constant and gain associated with the modeled NQ effect.	Added	(2-11)
i	Input stimulation (originally mechanical stimulation) used for galvanic stimulation. Same as $I_{electrode}$.	N/A	(2-12),(2-15)

$\eta_k, g_k, \tau_k, g_{\infty k}$	Original form of double-exponential state equation for k states with k=2 and are named s (slow) and f (fast) component in Eq 2-13 and 2-15 (η_s and η_f). Each has an instantaneous gain (g_k), time constant (τ_k), steady-state gain ($g_{\infty k}$). $g_{\infty k} = 0$.	N/A	(2-12)
Fadapt	The theoretical change in firing rate due to the adaptation at the hair cell. Not in final simulation but used to predict hair cell output and to create Eq. 2-14 for how vesicle release changes over time.	N/A	(2-13), (2-14), (2-16)
F	Total induced firing rate. Only used in theoretical work and predictions	N/A	(2-16)
Fo	Spontaneous firing rate. 100-120 sps; 8-15 ms. Fo is Faxon(t) under no stimulation	Added	(2-14)
$\mu(t)/\mu_o$	$\mu(t)$ is the mean inter-EPSC arrival time. μ_o is the baseline level to create the modeled spontaneous rate. $\mu_o = 0.55-0.75$ for Fo = 100-120 sps. $\mu_o = 8-15$ ms for Fo = 15- 20 sps.	Tuned	(2-14)
g_s, τ_s, g_f, τ_f	For both experimental simulation these values do not change: $g_s = 0.75, g_f = 4.5, \tau_s = 2$ s, $\tau_f = 0.15$ s. Non-quantal effects and conductance of axonal sodium channels were the only change made.	Added	(2-13),(2-15)

Values are ordered to replicate Goldberg study results then Manca study results for variables that have two values. If variables are a function or not in the final model "N/A" is put in the modification column. Existing parameters that were modified say "Tuned." Added parameters for equations such as non-quantal effects or adaptation effects say "Added."

Chapter 3 : Rules of Pulsatile Stimulation

3.1 Introduction

Electrical stimulation is ubiquitous in modern treatments for neurological disorders and studies of neural function^{42,152}. It has a longstanding and intertwined history with the field of neuroscience, starting from the first studies showing neurons could be activated by electrical stimulation^{65,153}. In the present, electrical microstimulation remains a prominent way to understand neural function and connectivity at local and interregional levels of the nervous system^{42,154,155}. Clinically, it is not only relied on for brain mapping to inform treatments¹⁵⁵; usages have expanded to neural prostheses for restoration of perception^{4,14} and treating neuropsychiatric disorders¹⁵⁶. The main driver of safety standards has been developing paradigms suitable for long-term, implantable devices, which led to the restriction of current delivery to biphasic, charged-balanced pulses that prevent electrochemical reactions at the electrode interface and neural damage¹⁴. As a result, electrical stimulation has now become synonymous with this form of pulsatile stimulation across applications.

To treat impairments including hearing¹⁵⁷, visual¹⁵⁸, and balance^{1,159} and movement disorders¹⁶⁰, implantable pulse generators have been used in neural implants since the 1950s. These devices use changes in pulse rate and amplitude to modulate local neural activity to replace natural function. While the list of clinically viable prostheses based on this technology is rapidly growing, their ability to restore encoding of the full range of information remains limited⁴. Even in the cochlear implant, which has been continually improved since the initial introduction in 1957⁴, speech perception is improved, but pitch perception, which is encoded in fine-timing of firing rates, is at a deficit, likely leading to lack of music appreciation and tonal language perception^{161,162}. Many explanations have been proposed for limitations in restored function for each sensory prosthesis, such as pathological neural rewiring of the retina¹⁵⁸, or central nervous system adaptation to vestibular stimulation²⁹. These findings imply that present stimulation paradigms do not restore the natural local responses and, in turn, raise significant questions about the validity of using either microstimulation^{152,155,163} or cortico-cortical evoked responses to understand natural local and interregional connectivity and function^{42,154}.

Here we argue that a common element associated with the inability to optimize the clinical systems may be the complexity and unpredictability of evoked neural activity in response to stimulation pulse trains. While substantial experimental evidence exists for complex interactions of pulses with neurons, a systematic theory of how pulse rate and pulse amplitude affect neurons of varying spontaneous activity has not been established. What is known, however, is that pulses produce complex effects at the axon¹⁶³⁻¹⁶⁵ (e.g., facilitation and blocking of future pulses), and spontaneous activity substantially impacts the induced firing rate in response to pulses¹²³.

In this study, we perform a systematic investigation of the relationship between the induced firing rate (F) and the pulse rate (R), pulse amplitude (I), and spontaneous rate of a neuron (S) in a biophysical model of a vestibular afferent, where baseline spontaneous firing has been shown to impact pulsatile stimulation¹²³. We use a computational model to determine the physiological underpinnings of these non-linear effects on firing rate and describe them with equations related to measurable and controllable quantities: $F = \varphi(R, I, S)$. We compare model outputs to experimental observations of vestibular afferents obtained in non-human primates in response to vestibular canal stimulation with pulse trains of different amplitudes and rates. We determine whether these observed non-linearities in the pulse rate-firing rate relationship (PFR) occur with consistency, such that they can be predicted and corrected for algorithmically in neural implants and conclude by discussing their implications for interpreting electrical stimulation studies.

3.2 Methods

3.2.1 Vestibular Afferent Experimental Paradigm

Surgical Procedures

Chronic stimulation and recording experiments were performed in three male rhesus monkeys (ages 4, 5 and 7 years old). All procedures were approved by both the McGill University Animal Care Committee and the Johns Hopkins Animal Care and Use Committee, in addition to following the guidelines of the Canadian Council on Animal Care and the National Institutes of Health.

Surgeries were performed as described in Mitchell, Della Santina & Cullen⁸⁶. An electrode array was implanted into the left labyrinth via transmastoid approach such that the strut of bone between the ampullae of the superior and horizontal semicircular canals was kept intact. This acted as a stop for the electrode

array. Reference electrodes were inserted into the common crus of the labyrinth and extracranial musculature. The animals were given a 2-week recovery time from surgery before experiments were performed. Recorded electrodes were mapped to the electrodes that delivered the evoked highest activity.

Data Acquisition

During a recording session, monkeys were seated in a primate chair. An enamel-insulated tungsten microelectrode (8-10 M Ω impedance; Frederick Haer Co., Bowdoinham, ME) was used to record single unit activity of the vestibular nuclei neurons. Single unit activity was sampled at 40 kHz. An adaptive filter (Artifact Zapper, Riverbend Instruments) was used on-line to remove stimulation artifacts in the neural recordings. If any residual artifact remained, we performed a template deletion offline in which an average waveform of the artifact was subtracted from the recording trace. Each unit was analyzed offline to ensure proper isolation. Subsequent analysis was performed using custom algorithms (Matlab, The MathWorks). After vestibular nuclei neurons and afferent fibers were characterized, all neuronal activity was recorded in complete darkness while the monkeys were head-fixed.

Experimental Stimulation Paradigms

Pulses were applied using an isolated pulse stimulator (A-M Systems), which delivered cathodic-first charge-balanced biphasic pulses with 150 μ s stimulation phases and no interphase gap. The same single unit stimulation paradigm used in the monkey physiology experiments was simulated *in silico* on the biophysical model. During each pulse block, we delivered 1 s pulse trains at rates from 25 to 300 pps (Figure 17b). These rates were chosen because they fall within the physiological range of vestibular afferent firing^{29,94}. Fixed-rate pulse blocks were delivered at a fixed pulse amplitude in order from lowest to highest pulse rate. There were typically four repetitions of each pulse rate block before increasing the pulse rate. For several there were only three repetitions. For most pulse blocks there was a 500 ms or 1 s window between blocks. The maximum current was set to 80% of the minimum value that caused visible facial muscle activation in response to pulses delivered at 300 pps. Pulse rate experiments were performed with a fixed current amplitude and repeated at amplitudes from 25%, 50%, 75%, 87.5%, and 100% of maximum amplitude (Figure 17b).

Data Analysis

Our assay of neural responses is firing rate in response to blocks of pulses. Therefore, induced firing rate was measured as the number of APs that occurred from the onset of the first stimulus pulse in a pulse block to the offset of the last pulse in the block divided by the length of that time window. There were noticeable experimental differences in spontaneous activity before and after pulse blocks. Therefore, spontaneous activity was measured as the firing rate in the window preceding a pulse train, excluding the first 50 ms, if the window occurs after another pulse block. This was done to avoid remaining effects from the previous pulse train. Many stimulation paradigms assume a linear relation between pulse rate and firing rate. To test this hypothesis, data from all repetitions of pulse rate blocks at a single current amplitude were fit with the line best fit with a y-intercept equal to the average spontaneous rate for data collected at each pulse rate (R) between 0 and 300 (S): $F = mR + S$. The slopes of best fit (m) are compared to the unity line, the slope if each pulse produced one AP (Figure 17c).

3.2.2 Data Fitting with Equation $F = \phi(R, I, S)$

Simulations revealed predictable, smooth transitions between effects of pulses with the change in pulse amplitude and spontaneous rate. These effects were captured through an equation $F = \phi(R, I, S)$ (Eq.3) explained further below that takes measurable and controllable values as inputs: pulse rate R , pulse amplitude I , and spontaneous rate S . The equation captures effects from facilitation to blocking at 0 to 350 μA as fitted to a single irregular afferent simulation. Only the magnitude of parameters changes as a function of I and S to produce these effects (Figure 18).

The experimental data were fit by using the measured values of R and S and optimizing on I_{pred} to minimize the error between the predicted induced firing rate, F_{pred} , and \bar{F} , the experimental induced firing rate. I_{pred} was chosen as the value that minimized the two-dimensional rms error between the data at 25 to 300 pps and predictions. The two-dimensional error was taken between a prediction $F_{pred} = \phi(R, I_{pred}, S)$ and the 8 experimental values, where $R \in [1: 300]$. The (x,y) error for each of the 8 sampled pulse rates (k) was taken as the minimum distance between the closest point on (R, F_{pred}) and the k th pulse rate – firing combination (\bar{R}_k, \bar{F}_k) :

$$rms_{RF} = \sum_{k=1}^8 \min_R \left\{ \sqrt{(R - \bar{R}_k)^2 + (\phi(R, I_{pred}, S) - \bar{F}_k)^2} \right\}_{R=0}^{300} \quad (3-1)$$

The total error for I_{pred} was the sum of the error at each of the 8 points.

The only restrictions on I_{pred} were the value that minimized the rms error described above and that the value was weighted by the size of I_{pred} :

$$\epsilon = rms_{RF} + 0.5 \frac{I_{pred}}{200} \quad (3-2)$$

The second rule was enforced because many R-F combinations are the same at high and low I values. Also, between 100-200 μA , the relationship is approximately static. With the sparse sampling of pulse rate, this weighting helped ensure I_{pred} was not overestimated. Note, all errors on predicting the model results reported on the figure are standard rms because there is a detailed sampling of the pulse rate firing rate relationship to compare while there may be x and y dimensional error for the comparison to experimental data .

3.2.3 Biophysical Modeling of Vestibular Afferents

Vestibular afferents were simulated using a biophysical model that has been used previously by several groups including our own to study the effects of electrical stimulation on vestibular afferents^{26,87,166}. Past work from the lab showed this model can produce experimental firing rates and changes in firing rate with pulsatile and direct current stimulation observed under the same simulated conditions^{26,166}.

We use an adapted version of the Hight and Kalluri model. More details can be found in Steinhardt and Fridman²⁶. In brief, Hight & Kalluri showed that vestibular firing can be simulated accurately by assuming cells have the same shape and size⁸⁷ Type I and Type II vestibular afferents⁸² are modeled as differing only in channel expression and EPSC magnitude (K). Spontaneous rate can be set by changing the average inter-EPSC arrival interval (μ).

The membrane potential (V) varies as:

$$\frac{dV}{dt} = \frac{1}{(C_m S)(I_{Na} + I_{KL} + I_{KH} + I_{leak} + I_{epsc} + I_{stim})} \quad (3-3)$$

where in addition to the current from each channel, membrane potential is influenced by the EPSCs arriving at axon (I_{epsc}) and the injected current (I_{stim}). The system of equations in ⁸⁷ represents each cell as a single node with overall surface area, $S = 1.1 \cdot 10^{-5} \text{ cm}^2$ and capacitance $C_m = 0.9 \text{ mF/cm}^2$. Each channel is voltage-gated and dependent on a conductance, an open state and a closed state variable: Na (g_{Na} , m , h), KH (g_{KH} , n , p), KL (g_{KL} , w , z). We simulate the electrode at 2 mm from the simulated afferent for all studies, as in previous experimental vestibular studies^{27,28}.

For this study, the simulations used to parameterize and construct our equations were performed on a single model of an irregular vestibular afferent with different pulse parameters. This canonical neuron was chosen from the experimental literature as having the mean level of responsiveness to stimulation in the experimental study ²⁹ (Figure 17e). A simulation with conductance values of $g_{Na} = 13 \text{ mS/cm}^2$, $g_{KH} = 2.8 \text{ mS/cm}^2$, and $g_{KL} = 1 \text{ mS/cm}^2$ and EPSCs with amplitude scaling factor $K = 1$ and $\mu = 1.3 \text{ ms}$ produced highly similar pulse rate firing rate relationships compared to previously published experimental findings at pulse rates from 25 to 300 pps for the canonical neuron (Figure 17e). We kept these conductance values for the main irregular afferent simulations and only changed inter-EPSC arrival times. At this level, the firing threshold was around 56 μA . We then expanded our simulations from the characterization of the effects on this neuron to other neuron cases (e.g. regular afferent, different channel conductances, etc.).

For simulations of the effects of spontaneous rates on firing, the channel conductance values were kept the same but μ was set to 0.25, 0.5, 1, 2, 4, and 8 ms. As a control, the axons were simulated without any EPSC input to assess the effects of pulses on channels alone.

Additionally, we assessed the effect of firing regularity on induced firing rate. A irregular neuron ($F = 36.6 \pm 0.9 \text{ sps}$, $CV = 0.57$, where CV is coefficient of variance), was modeled with an amplitude scaling factor $K = 1$, and $\mu = 1.65 \text{ ms}$. A conductance matched regular neuron ($F = 33.8 \pm 0.4 \text{ sps}$, $CV = 0.09$) was also modeled with $g_{Na} = 13 \text{ mS/cm}^2$, $g_{KH} = 2.8 \text{ mS/cm}^2$, and $g_{KL} = 0 \text{ mS/cm}^2$, $K = 0.025$, and $\mu = 0.09 \text{ ms}$. The irregular neuron, meant to replicate the example neuron in the Mitchell *et al.* paper was used as the main simulation for exploring pulse effects at the axon.

We simulated the effects of conductance values on the *R-F* mapping with current amplitude. We used conductance values that produced firing rates similar to those observed in a previous *in vitro* experiment with

and without exposure to DC current^{26,27}: $g_{Na} = 7.8 \text{ mS/cm}^2$, $g_{KH} = 11.2 \text{ mS/cm}^2$, and $g_{KL} = 1.1 \text{ mS/cm}^2$, $K = 1$. m was again varied from 0.25 to 8 ms.

The literature did not suggest that pulses produce action potentials by depolarizing the hair cell, so none of the hair cell related effects (adaptation, the non-quantal effect, etc.) simulated in past studies of DC stimulation²⁶ were included in this study. Without these hair cell and non-quantal effects, the experimentally observed effects of pulses we aimed to model²⁹ could be simulated, so none of these effects were considered in the simulation. The simulation is run using the Euler method to update all variables through each of the channels.

3.2.4 Simulated Pulsatile Stimulation Experiments

The experiment conducted in monkeys was simulated with finer sampling of current amplitudes and pulse rates. Electrodes were simulated as being placed 2 mm from the vestibular afferent axon. In addition to the pulse rates used experimentally, pulse rates from 1 to 300 pps in steps of 1 pps were delivered for 1 second in the simulations. Five repetitions were performed for each current amplitude, spontaneous rate, and pulse rate combination where the EPSC statistics varied between repetitions. Pulse amplitude was varied from 0 to 360 μA in steps of 12 μA and used to parameterize equations values. We interpolated between these values to create a smooth function. This function was later used to predicting induced firing rates for neurons with different spontaneous rates stimulated at any pulse rate and pulse amplitude between those mapped.

This combination of experiments was simulated for the irregular neuron, regular neuron, and low conduction/*in vitro* neuron cases (Chapter 2). It was also repeated for all values of μ to map how these effects change with different levels of spontaneous activity.

Jitter Experiment

To assess the effect of jittered pulse delivery time on induced firing rate, we performed the same simulation except that instead of delivering perfectly timed pulses we added a gaussian noise term with standard deviation of 1 ms or 2 ms to the exact pulse timing to simulate delay or advancement in the delivery of regularly scheduled pulses (Figure 21e).

Pulse Rate Modulation and Pulse Amplitude Modulation

To test how the observed effects of pulsatile stimulation discussed in this study apply to sinusoidal modulation of pulse train, as used in various prosthetic algorithms, PRM and PAM were simulated within a common range for vestibular prostheses^{15,159,167}. Pulse rates were modulated by steps of 20 or 50 pps/ μ A around values where there were predicted to be non-linearities in the PFR as pulse rate or pulse amplitude changed. They were also modulated in similar size windows where linear PFR were predicted by the biophysical fixed pulsed rate simulations (Figure 21f grey). Sinusoidal PRM (red) and PAM (blue) modulation was simulated for the same afferent with a 42 sps baseline firing rate (Figure 21f). How the predictive equations below hold were also assessed under this condition.

3.2.5 Predictive Equation

The effects characterized on the simulated irregular afferent axon were transformed into equations that depended on measurable or controllable variables: pulse amplitude (I) delivered from the electrode, pulse rate, as inter-pulse interval (ρ), and spontaneous rate (S). Equations were not optimized for real-time usage. The goal was to create equations that captured the observed effects and their mechanisms without dependence on time. Thus, they are parameterized to the model data with variables that could be fit to other neural data, fitting with respect to I and S , based on the observed behavior of the simulation. They were best fit to each I and S combination of the simulated afferent. All variables that were best fit have a * in the following equations.

3.2.6 Pulse-Pulse Interactions

Pulse-Pulse Block/Partial Block (PPB)

The most substantial effect of pulses in the absence of EPSCs is pulses blocking subsequent pulses from becoming APs. The refractory period after a pulse is driven by an underlying change in channel dynamics that leads to a temporal zone where all pulses are blocked followed by a zone of exponentially decreasing blocking effects until pulses have zero probability of being blocked (Figure 19a-c). Because the following pulses are blocked, the pulses within the block period do not extend these effects, leading to the induced firing rate contributed by pulses (F_{PP}) being a subharmonic of the pulse rate:

$$F_{PP} = \frac{\left(\frac{1}{\rho}\right)}{\text{ceil}\left(\frac{t_b}{\rho}\right) + \psi(I, \rho)} \quad (3-4)$$

where the length of the full block zone t_b changes with I (Figure 18b). t_b is large when I is small (due to channels driving the membrane towards resting state) and when I is large (due to the pulses causing large changes that push channels into unnatural states). At I around 100-200 μA *in silico*, t_b remains at approximately the same minimum values, as pulses are strong enough to consistently drive firing but not strong enough to cause extreme changes in channel states. The ratio of ρ to t_b determines what fraction of pulses are blocked, so the pulse rate at which 1/2 or 1/3 of pulses become APs is easily calculable as (n/t_b) pps, where n is the denominator of the fraction. This effect is captured with division by the $\text{ceil}()$ term.

After t_b until t_{pb} (the last time at which partial block of pulses is observed), the subsequent pulse is not blocked with certainty, but the probability of being blocked decreases toward 0. We call this zone the partial elimination (PE) zone in equations functions related to it are labeled with ψ . t_{pb} changes with I similarly to t_b (Figure 18 b-c). We implement PE with respect to the transition point between each bend (n) at which the firing rate changes from R/n to $R/(n+1)$ due to the observed changing in length of PE with each transition or bend in the pulse rate-firing rate relationship. Because transitions happen at each n/t_b pps pulse rate, the pulse rate at the start of PE for that transition can never be less than $(n-1)/t_b$. Therefore, we express the length of the PE zone as a fraction p_{pb} times t_b :

$$t_{pb}(n) = \frac{t_b}{n - \min\{1, p_{pb}\}} \quad (3-5)$$

As ρ decreases such that $n > 1$, p_{pb} becomes an increasingly larger (Figure 19c-1). This is due to a change between n and $n - 1$ at large n being equivalent to a smaller time between pulses. The length of t_{pb} does decrease as n increases.

ψ is implemented such that between $\frac{t_b}{n}$ and $t_{pb}(n)$, ψ takes values that linearly decrease from 1 to 0 as the pulse rate approaches $\frac{n}{t_{pb}}$. This term adds to the $\text{ceil}()$ term so that the transition is not abrupt from $F = R/n$ to $F = R/(n+1)$ but instead has an exponential decay from one harmonic line to the next (Figure 19c red). The strength of ψ grows with I , which could be well characterized with the scaling κ that analytically was fit with variable $\alpha(I, S)$ and took on an approximately quadratic shape:

$$\kappa = (I - \alpha^*)^4$$

$$\psi(I, \rho) = \begin{cases} \sum_{n=1}^N \min \left\{ 1, (1 + \kappa(I, S)) \left(1 - \frac{\rho - t_b/n}{(t_{pb}(n) - t_b/n)} \right) \right\}, & t_{pb}(n) < \rho < t_b/n \\ 0, & \text{else} \end{cases} \quad (3-6)$$

At midrange I , the scaling effect with I causes lower pulse rates to transition to the next subharmonic ($R/(n+1)$) but it never causes a harmonic to skip to over $n+1$. As I increases, such as at $I = 192 \mu A$, this leads to a sharper transition from one line to the next (Figure 19c-2). This effect is implemented with the *min* term such that $\psi \leq 1$. When spontaneous rate was increased, we found that κ , the scaling up of PE effects, occurs at a lower I due to the spontaneous activity distorting and expanding the timing and likelihood of pulses causing large changes along the axon for smaller changes in membrane voltage. This effect is embedded in the equation through the α which increase with S .

At very high I ($I > 204 \mu A$ in our mapping) suppression effects occurred that caused axonal firing to shut down in longer, unnatural dynamic loops. Two main effects at high amplitudes (Pulse Dynamic Loop (PDL) and Suppression of Future Pulses (SFP)) were implemented as variations of the ψ function.

Pulse Dynamic Loop (PDL)

At the transition from $n=1$ to $n=2$, with no spontaneous activity we see that the transition overshoots and returns to $n=2$ during the PE time (Figure 19e brown, 19d). We model this with a similar function to (3-6) with reverse directionality of decay:

for $t_{pb}(1) < \rho < t_b$

$$\psi_1 = \text{ceil} \left(\kappa(I, S) \left(\frac{\rho - t_b}{t_{pb}(1) - t_b} \right) \right) \quad (3-7)$$

Suppression of Future Pulses (SFP)

Additionally, instead of the pulses within the immediate refractory period being blocked, the delivery of an additional pulse pushes axonal dynamics to a state of full suppression after $n = 2$. We again see this transition is a decay to $F = 0$ as opposed to a sharp drop (Figure 19e yellow, 19d). This rule is implemented as:

for $\rho \geq t_{pb}(2)$

$$\psi_2 = (\beta^*) \left(1 - \frac{\rho - \frac{t_b}{2}}{(t_{pb}(2) - \frac{t_b}{2})} \right)^3 \quad (3-8)$$

When spontaneous activity is included, we see that, with larger spontaneous activity, the slope of this decay is exceedingly slower (Figure 18 row 3). This effect is enforced by $\beta^*(I, S)$, which increases from 0.005 to 1.25 as S increases from 0 to 130 sps.

With these terms only, the induced firing rate becomes:

$$F_{PP} = \frac{\left(\frac{1}{\rho}\right)}{\min\left[2, \text{ceil}\left(\frac{t_b}{\rho}\right) + \psi_1 + \psi_2\right]} \quad (3-9)$$

The *min* term ensures smooth transition to $F = 0$ without the bends that would typically occur at pulse rates that are multiples of $1/t_b$.

3.2.7 Pulse-Spontaneous Interactions

Pulse-Spontaneous Additive (PSA), Pulse-Spontaneous Block (PSB), and Spontaneous-Pulse Block (SPB)

Regularly timed pulses break up time into windows of length ρ in which relative effects of pulses on spontaneous activity and vice versa can be approximated. We numerically implement this effect with $\text{mod}(t_s, \rho)$. This shows that spontaneous spikes are distributed uniformly between 0 and ρ ms after a pulse for most conditions (excluding exceptions like regular spontaneous firing at the same rate as pulse rate). So, pulses affect some fraction of the evenly distributed spontaneous activity, and all pulses are affected to some level by the ongoing spontaneous activity. As R increases, the time between pulses is smaller but the probability of EPSCs capable of producing a spontaneous AP occurring is equally likely, so a greater portion of spontaneous activity is affected per pulses. We call the probability of spontaneous activity producing an AP after a pulses, p_{PS} . The probability of pulses producing an APs given proceeding spontaneous activity is p_{SP} . A simple approximation of these interactions would be:

$$p_{PS} = \min\left\{1, \frac{\rho - t_{PS}}{\rho}\right\} \quad (3-10)$$

Where t_{PS} is the time after a pulse when spontaneous APs are blocked.

Similarly, the probability of spontaneous activity being blocked by pulses is:

$$p_{SP} = \min \left\{ 1, \frac{(t_{SP}S)}{T} \right\} \quad (3-11)$$

Where t_{SP} is the time after a spontaneous AP when pulses are blocked, and T is the total length of the time window. t_{SP} and therefore p_{SP} only depends on I , as the spontaneous activity driving the baseline spontaneous rate will remain the same for a neuron. With this approximation, t_{PS} will only depend on I , and p_{PS} will increase approximately linearly with the pulse rate until reaching 1 (as pulses and the blocking zones fill the time T). To simplify fitting, we therefore fit p_{PS} and p_{SP} as directly depending on only I in our predictive rules, because spontaneous rate did not have large effects on how these variables changes with I or R in the simulation compared to other variables described in this section. However, it could be accounted for in other descriptive equations that may be used to fit the pulse-spontaneous block relationships described above.

These pulse-spontaneous interactions took two forms. At low pulse amplitudes at which a pulse would produce no APs in an axon with no EPSCs, they worked together to facilitate of pulses into APs (Figure 19). By $I = 54 \mu A$, both probabilities reach 1, representing the transition from pulses facilitating with spontaneous activity to blocking interactions (Figure 19 b,e). At very high I , the same equations taking the same shape can be used to describe pulses blocking spontaneous activity and spontaneous activity blocking pulses (Figure 19 f). These spontaneous activity effects are linked to EPSC facilitating or being facilitated by pulses into becoming APs, or pulses becoming large enough that underlying EPSC activity can quickly transition the axon to suppressed state. For facilitation, p_{PS} and p_{SP} sigmoidally increases to 1 around $50 \mu A$. In this model, the blocking effects of pulses on spontaneous activity start around $156 \mu A$ and are significantly dependent on spontaneous activity. The spontaneous activity scaling down pulse-induced firing changes rapidly around $290 \mu A$ without strong dependence on S .

Spontaneous-Pulse Full Block Effects

Between about 50 and $290 \mu A$, spontaneous activity blocks pulses to a more limited degree. These effects are likely due to spontaneous APs and not EPSCs interacting with pulses, as the number of blocked pulses directly relates to S . The largest effect is that, as S increases, the same PFR occur as in neurons with no spontaneous activity but reduced by S (Figure 20 g-h). The simulated membrane recordings indicate this is due to spontaneous activity blocking pulses (Figure 20a), and pulses are only shown to block spontaneous

activity at significantly larger amplitudes. Thus, S is subtracted from F_p . Additionally, there is another bend in the PFR around $R = S$ (Figure 20g). As described above, until $\rho = t_b$ the slope of the PFR should be 1. Prior to this bend, the slope is significantly lower, and afterwards it is 1. We find that pulses are relatively weak, such that below approximately $R = S$, pulses are often blocked by spontaneous APs, while, for $R > S$, pulses seem to alter dynamics so that multiple pulses survive between spontaneous APs (Figure 20a). We fit this non-linearity with a term (δ^*) that increases with I and depends on S because the larger the spontaneous rate the stronger the blocking effect.

Facilitation ends around 50 μA , but this threshold current varies with S , so we call it $I_{fac}(S)$. This facilitation effect combines with the other equations resulting in the following equation that encapsulates all of the pulse-driven contribution firing rate (F_p):

For $I < I_{fac}(S)$, (3-12)

$$\begin{aligned} F_p &= p_{PS}R & R < (0.8/p_{SP}) \\ &= p_{SP}F_{PP} & R \geq \left(\frac{0.8}{p_{PS}}\right) \end{aligned}$$

For $I > I_{fac}(S)$,

$$\begin{aligned} F_p &= \delta^*(I, S)R, & R < S \\ &= (\delta^*S - F_{PP}(S)) + (p_{SP}F_{PP} - S), & R \geq S \end{aligned}$$

The first term for $R \geq S$ causes the functions to meet and the second includes the remains spontaneous block effects. The contribution to the induced firing rate of spontaneous activity and spontaneously activity-induced effects (F_s) takes the form:

$$\begin{aligned} F_s &= S - p_{PS}R & I > 156 \mu A \\ &= S & \text{else} \end{aligned} \quad (3-13)$$

Together, these terms combine into the final equation that includes all the effects described. These equations were intentionally designed to separate the effects into pulse-driven contributions and spontaneous-activity driven contributions to firing rate. So, the equation takes the final form:

$$F = \max\{0, F_s\} + \max\{0, F_p\} \quad (3-14)$$

The *max* term assures each term does not go negative if blocking effects exceed S or R .

3.3 Results

To investigate the relationship between pulse parameters and induced or driven firing rate (F), we recorded neuronal activity from vestibular afferents of the semicircular canal in awake behaving primates receiving pulse train stimuli from 25 to 300 pps with amplitudes between 0 to 240 μ A (0-100% of the safe range) (Figure 17a, b; See Methods). For a typical afferent with spontaneous rate of 40 sps (Figure 17c left), F is sensitive to the pulse amplitude (I) and pulse rate (R) of a pulse train. Suprathreshold pulses are thought to produce an action potential (AP) within milliseconds of pulse delivery, regardless of spontaneous activity, yielding a relationship between R and F that would increase with slope of 1 sps/pps independent of S (Figure 17c left red line). We refer to this as a one-to-one linear and anything to the contrary as non-linear. This one-to-one relationship was not observed in this or any recorded afferent for any stimulation amplitude. Instead, slopes ranged from -0.2 to 0.5 sps/pps. This suggests that a pulse produces less than one spike per pulse over the course of a trial, can suppress activity (negative slope), and that the responses are highly variable.

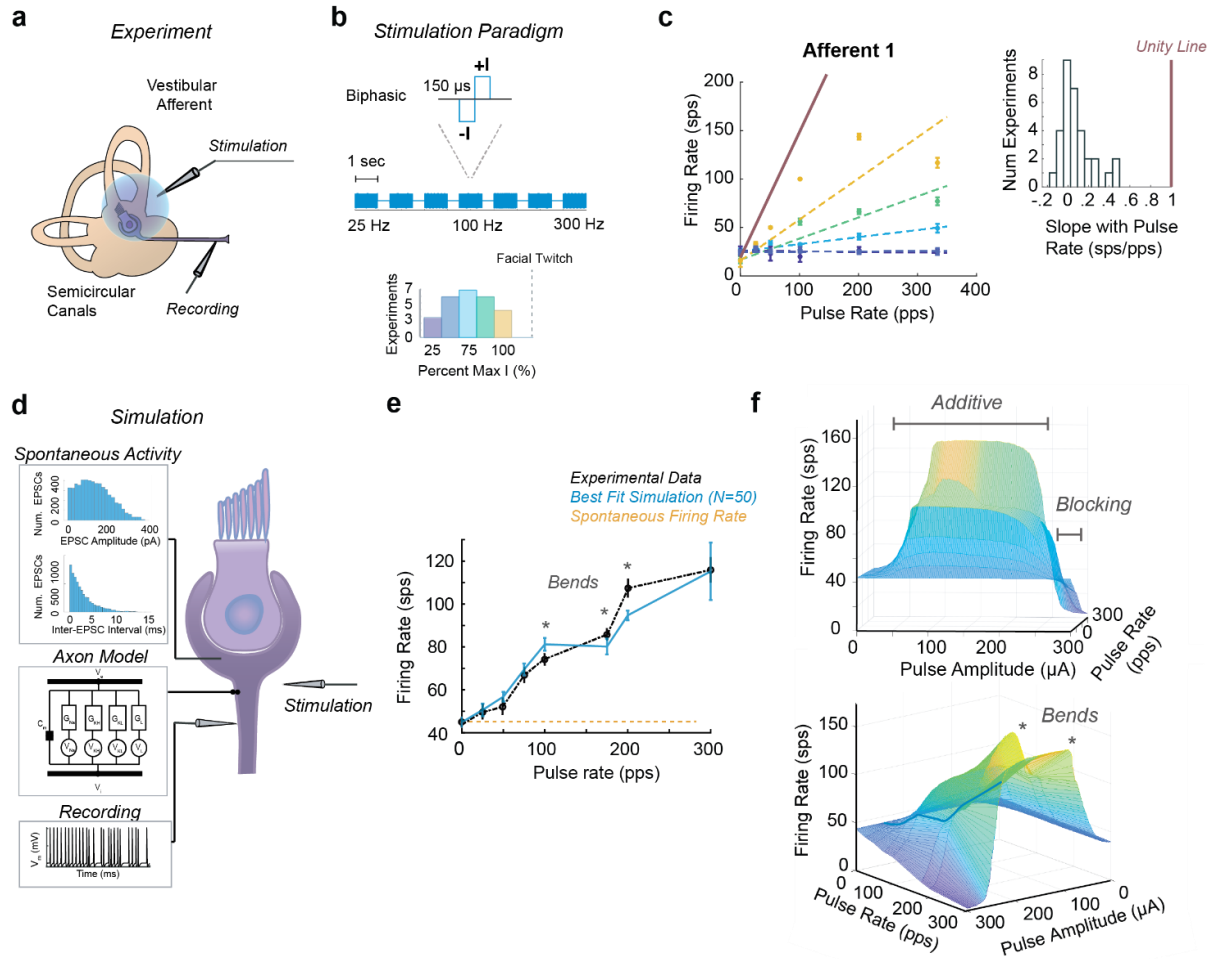


Figure 17. Paradigm for Studying Pulsatile Stimulation

a) Stimulation experiments were performed on vestibular afferent in horizontal canal of macaque monkeys. b) Afferents were stimulated with 1 second of fixed rate biphasic charge-balanced pulses (with 150 μ s stimulation phase) from 25-300 pps. Amplitudes from 25% to 100% of the amplitude of facial twitch were used across subjects. c) Example afferent recorded at amplitudes colored from low (purple) to high (yellow), showing non-linear change in firing rate with pulse rate. Histogram of average slope of linear-best fit across all afferents and amplitudes compared to expected unity slope: $\Delta F = 1 \cdot R$. d) A biophysical model of a vestibular afferent with realistic channel conductances was parameterized to replicate one of the irregular afferents with spontaneous rate of 42 sps. e) Original data (black) compared to simulation across 50 random seeds (blue). The simulation shows evidence of non-linearities observed in the original data (blue asterisks). f) Surface of relation between pulse amplitude, pulse rate and induced firing rate in simulated neuron based on 1 second trials.

We determined the factors that underlie this variability by simulating pulsatile stimulation of single vestibular afferents using a modified biophysical model developed by Hight and Kalluri and systematically analyzing which parameters contribute to observed non-linearities in the pulse rate-firing rate relationship⁸⁷ (Figure 17d, See Methods). We start by tuning the model to replicate an afferent that shows a range of responses viewed across the population of afferents from the rhesus monkey experiments (Figure 17b)²⁹. The simulation, shown for a single amplitude in Figure 17e, closely replicated experimental results - including location and direction of the bends (arrows) in the PFR ($N=50$, $rms = 11.4 \pm 4.6$ sps). We then conducted a

full sweep of pulse amplitudes (I from 0 to 300 μA) for the same pulse rates, revealing a broad range of non-linear additive and blocking effects that depend on I (Figure 17f top). The bends in the PFR are observed for all amplitudes at the same pulse rate (Figure 17f bottom). Both findings contradict standard assumptions of an activation threshold and linear PFR.

We next expanded on this simulation to explore the relationship between pulse parameters (pulse amplitude, pulse rate, pulse timing) and spontaneous activity (rate, regularity, conductance) and the observed complexities in the PFR. A complete set of responses was generated at finer sampling of combinations of each parameter (Figure 18). We found that the primary determinants of the induced firing rate are the pulse amplitude and the spontaneous rate of a neuron. In Figure 18, the PFR is shown in different panels as amplitude increases. The PFR with no excitatory post-synaptic currents (EPSCs) and therefore no spontaneous firing in the model (Figure 18, black) shows the same non-linearities observed with spontaneous activity, implying that pulses create these effects (Figure 17). Within panels, the effect of S is shown for the same I and sampling of R . Increasing spontaneous rates are shown in colors from light green (5 sps) to dark blue (131.8 sps). The same non-linearities are present as when there is no spontaneous activity (black). Spontaneous activity appears to primarily change the responsiveness of the axon to pulses, with higher S leading to smaller changes in firing rate.

Given the wide range of phenomena shown in Figure 18, the question arises: what is the underlying physiological basis and is it possible to formalize a set of rules that account for the firing rates induced by stimulation? We hypothesized that the smooth changes in phenomena that occurred could be broken into fundamental rules and approximated with mathematical equations. Thus, we developed time-invariant equations based on the underlying biophysical phenomena but represented as a function of pulse parameters and spontaneous activity. Because the prevalence of the rules are principally dependent on pulse amplitude, their relevance is shown by the thickness of color-coded lines below the panels that are labeled on the right. Pulse rate and spontaneous activity also however affect these rules as discussed in more detail below. For example, Suppression of Future Pulses (SFP), shown with a yellow line for amplitudes over 252 μA , is prevalent only for high amplitude pulses. The rules we developed successfully capture these effects. In Figure 18 and all subsequent figures, the PFR prediction is plotted with thin red traces on top of the corresponding computational model outputs.

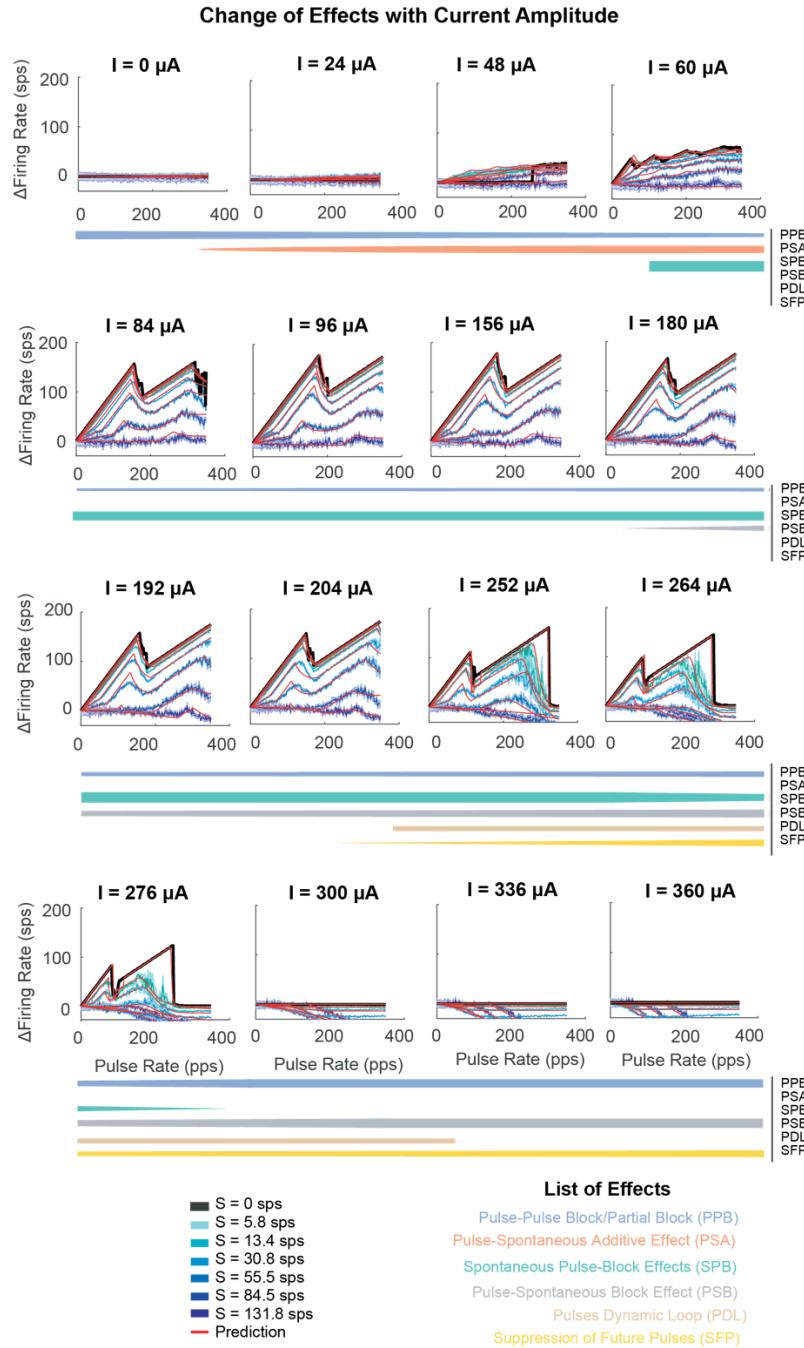


Figure 18. Map of firing rate changes in response to pulse rate trains given spontaneous activity (S) and pulse amplitude (I)

The simulation was performed at each spontaneous rate (blue-green map) and current amplitude. The change in firing rate (from the spontaneous rate) is shown with pulse rate to keep induced firing rates on the same scale. The prediction using the parameterized equations is shown for comparison (red). On the right the change in effect magnitude is shown color-coated by effect. Each row shows a transition from one effect to the next. The effects prevalent for a given range of amplitudes are shown in the left column. PPB: Pulse-pulse block/partial block, PSA: pulse-spontaneous addition, SPB: spontaneous-pulse block, PSB: pulse-spontaneous block, PDL: pulses dynamic loop, SFP: suppression of future pulses. Non-zero spontaneous rates were generated by selecting average EPSC rates from 0.25 ms (~131 sps, dark blue) to 8 ms (~5 sps, light green).

3.3.1 Effects of Pulses on Neurons with No Spontaneous Activity

To isolate the contributions of pulses to the observed non-linearities in PFR, we first investigated the effects of pulses in the absence of spontaneous activity (Figure 18 black traces). The prevalent feature of these traces is bends that occur at specific pulse rates (Figure 18 rows 2-3).

In Figure 3a, we examine these bends in more detail as a function of amplitude. The PFR starts with slope $F=R$ (i.e., one spike for each pulse) and transition from the line $F = R/(N-1)$ to $F=R/N$ where $N = 2, 3, 4, \dots$; these transitions occur at evenly spaced pulse rates. The physiological reason for this effect is that delivering a pulse, evokes an AP, but then creates an afterhyperpolarization that prevents the axon for a time t_b from evoking an AP in response to a subsequent pulse. As the R increases, the inter-pulse-interval (ρ) decreases and more pulses fall into this blocked range indicated in blue shaded area in Figure 3a, right. Meanwhile, the block window (t_b) changes only as a function of I .

t_b however describes only part of the pulse-pulse interaction dynamics. During this time, a pulse will not produce a spike, or equivalently, the probability of evoking a spike, $p_{AP} = 0$ (Figure 19a, b blue). After this initial time window, the probability of pulses being blocked from initiating spikes decreases as channel states slowly recover for time $t_{pb}(I)$ (Figure 19b, d). In this partial elimination (PE) window, p_{AP} increases gradually until it reaches 1 at $t_{pb}(I)$, after which a subsequent pulse will evoke an AP.

These effects are combined into the Pulse-Pulse Block (PPB) rule:

$$F = \frac{\left(\frac{1}{\rho}\right)}{\text{ceil}\left(\frac{t_b(I)}{\rho}\right) + \psi(I, \rho)} \quad (3-15)$$

$t_b(I)$ is a fixed value for a given I . The $\text{ceil}()$ term enforces the division by n in $F=R/n$ when ρ takes values $\frac{t_b(I)}{n} > \rho > \frac{t_b(I)}{n-1}$. At low amplitudes, $t_b(I)$ is long due to the small changes in the membrane potential being propagated by the channel dynamics such that it will block even multiple pulses. As I increases, the cathodal phase of pulses drives the axon to threshold more easily, leading to minimum $t_b(I)$ around 150 μA . At high I , delivering a pulse is more likely to produce a cathodal block, causing $t_b(I)$ to increase again. $\psi(I, \rho)$ is an increase in probability of a pulse being blocked as ρ decreases and the pulse occurs closer to $t_b(I)/n$ (Figure 19b-c red).

The contribution of these rules to the PFR can be seen in Figure 3c. As pulse rate increases for a given amplitude, a larger range of pulse rates fall into the PE zone due to smaller inter-pulse-intervals (Figure 19c Effect 1). We also note that, as I increases, recovery takes more time, leading to a longer PE zone (Figure 19c Effect 2, Figure 19d, Methods Eq. 3-4,3-5,3-6,3-14).

At high I , we see new effects: Suppression of Future Pulses (SFP, yellow) and Pulse Dynamic Loop (PDL, tan) (Figure 19e). PDL is caused by pulses being of the right size and timing to create an extended competition between the K and Na channels dynamics that prevents AP production. SFP is a more severe form of this effect. The sodium h-gate is driven to a state that it cannot recover from in time to respond to the next pulse presentation, keeping the channel inactivated and preventing all following pulses from inducing APs (Figure 19f). In sum, pulses produce additive and blocking effects in the absence of spontaneous activity, and these effects on the PFR can be reproduced with Eq. 3-4, an equation that depends on I and R (Figure 19c,e-f, Methods Eq. 3-6-14).

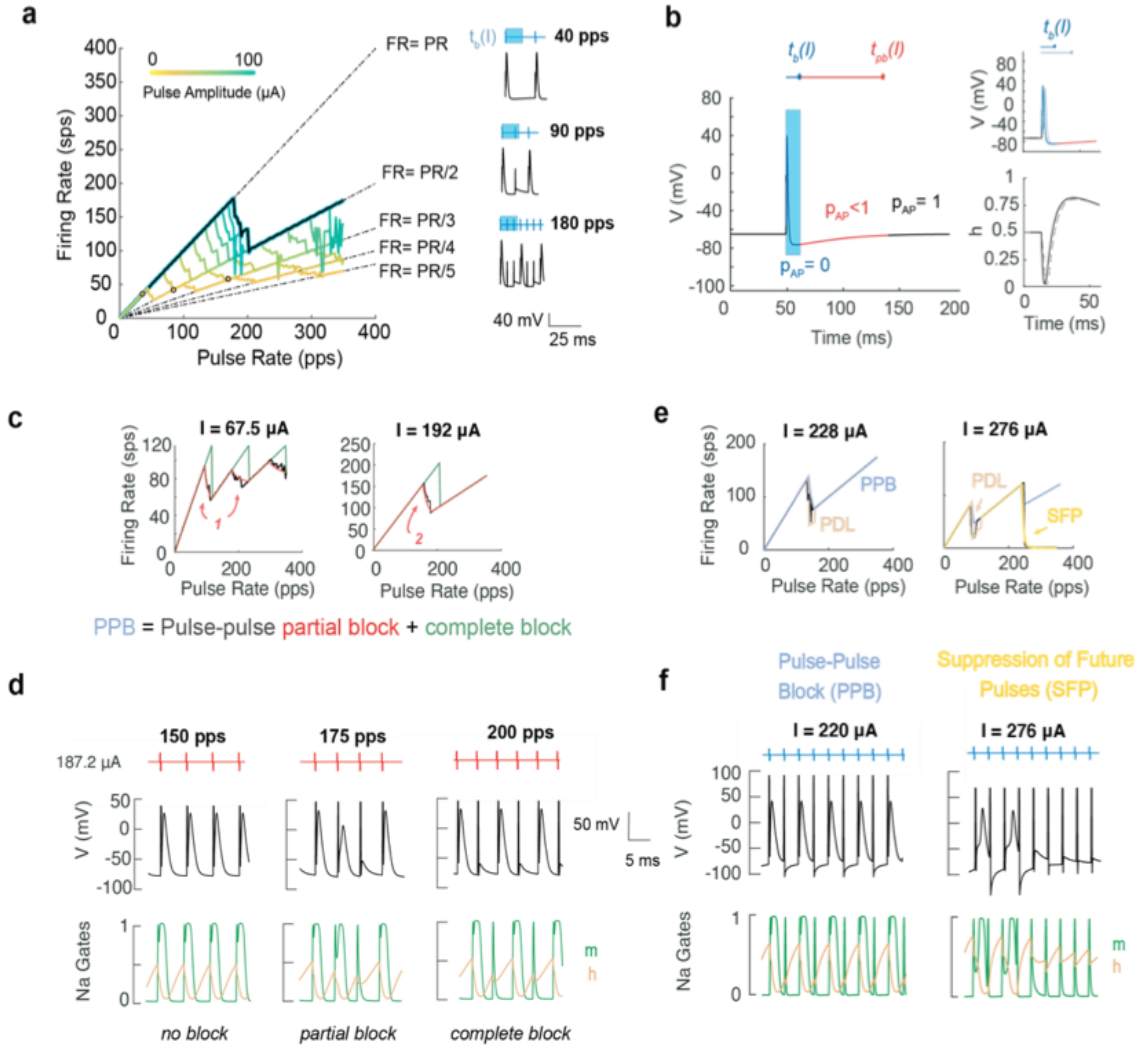


Figure 19. Effects of Pulse on a Silent Neuron

a) The length of the block zone t_b changes with I . For one I , this block window leads to the firing rate reducing to subharmonics of the pulse rate depending on the ratio of the inter-pulse-interval and t_b . This effect is shown for $I = 60 \mu A$ (yellow dots). **b)** In the after-pulse window pulses change axon channel states fully blocking pulses up to t_b ms after the pulse (blue). In the recovery period, there is a Partial Elimination (PE) zone where a subsequent pulse would be blocked with a probability that decrease to zero if pulses are t_{pb} ms after the previous pulse. As I increases from threshold levels (dash) to higher I , sodium dynamics (h) reach states for firing more quickly, changing the length of the block and PE zone. **c)** The block window (blue) and the block and partial block window (red) described by equations compared to simulated relationship (black) (see Methods). 1. PE window decreases with subharmonic jump. 2. PE window increases with I . **d)** The input pulses (red), voltage trace (black), and dynamics of the sodium channel m -gate (green) and h -gate (yellow) that drive the PPB and SFP effect. **e)** At high I , the jump from $F=R$ to $F=R/2$ creates a Pulse Dynamic Loop (PDL) that causes $1/3$ or less of pulses to produce APs until the pulse rate increases, changing the dynamic perturbation length so $F= R/2$ (left). A Suppression of Future Pulses effect occurs at pulse rates that would at lower I produce $F=R/2$ leading to $F=0$ (right). **f)** The input pulses (blue), voltage trace (black), and dynamics of the sodium channel m -gate (green) and h -gate (yellow) that drive the PPB and SFP effect.

3.3.2 Effects of Pulses on Spontaneously Firing Neurons

Most real-world systems, like the vestibular system, contain spontaneously firing neurons, with vestibular afferents containing the highest spontaneous rate neurons of up to 100 sps. To evaluate how spontaneous activity influences responses to pulses, spontaneous activity was introduced into the model. This resulted in

additional pulse-spontaneous interactions that were separable from the pulse-pulse interactions described above. At different pulse rates, spontaneous APs (green) and pulse-induced APs (black) vary in ratio of one to another (Figure 20a) shown for 30 pps and 80 pps in the example. The underlying mechanism is an extended perturbation of axonal channel dynamics in the time after a pulse-induced or spontaneous AP which results in an additive or blocking effect on the following EPSC or pulse. The extent and directionality of these interactions depends on pulse amplitude and scales differently with I than PPB.

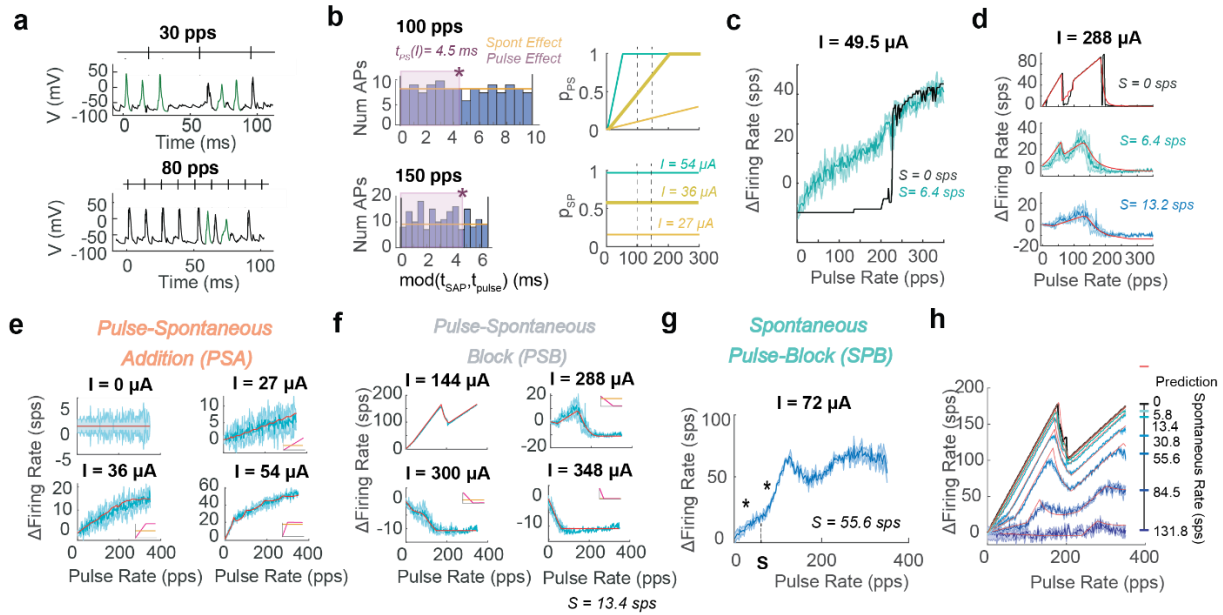


Figure 20. Interactions of Pulses with Spontaneous Firing

a) Interactions of spontaneous spikes with pulse-evoked activity at 30 pps and 80 pps. Spontaneous spikes are in green. **b)** At high and low pulse amplitudes, a pulse will interact with multiple spikes, or a spike may interact with multiple pulses. Time of spontaneous activity compared to pulses takes an approximately uniform distribution between pulses, so they have equal chance of affecting all the delivered pulses (p_{sp}). As p decreases, the after-pulse window affects a greater portion of spontaneous activity (p_{ps}), so $p_{ps}(p)$ increases. As current increases both probability of pulses affecting spikes (p_{ps}) and spikes affecting pulses (p_{sp}) increase together. **c)** Presence of even a small amount of spontaneous activity (6.4 sps) leads to smoothing of pulse-induced effects leading to facilitation even at pulse rates below the rate required for typical pulse-pulse facilitation. **d)** This also leads to reduction and eventually disappearance of PDL effects as S increases to 13.2 sps. **e)** Facilitation effects can be explained with p_{sp} and p_{ps} increasing to 1. High amplitude blocking can be explained with p_{sp} and p_{ps} returning to 0. **f)** Pulse-spontaneous block can be described with the same rules as facilitation but with induction of blocking effects with higher amplitude. See panels in corner for PPS (pink) and PSP (yellow) effects in each case. **g)** Spontaneous pulse-block was observed at middle amplitudes, causing lower rates to have lesser effects. **h)** The main spontaneous-pulse effect is blocking at mid-range I . The same pattern produced with $S=0$ is observed but with S lower firing rate and smoothed out partial elimination zones.

Fortunately, although spontaneous activity is stochastic, timing of spontaneous APs is uncorrelated to pulse timing and approximately uniformly distributed between pulses (Figure 20b), affecting all pulse-evoked APs equally independent of pulse rate (excluding if there is highly regular spiking). The probability that a pulse produces an AP after spontaneous activity, p_{sp} increases only as a function of I , because, as I

increases, pulses become large enough to break through the aftereffects of spontaneous APs; the probability of an EPSC producing an AP after a pulse, p_{ps} , depends on pulse amplitude I and pulse rate R (Methods Eq. 3-4). As R increases, the time between pulses is smaller but t_{ps} , the time after a pulse in which pulses interact with spontaneous APs remains the same (Figure 20b left). Therefore, the portion of effected spontaneous spikes increases linearly with pr until $p_{ps} = 1$, meaning that all spontaneous APs within the inter-pulse window are affected (Figure 20b right). p_{ps} and p_{sp} vary together, producing additive or blocking effects depending on I (Figure 20c-h).

With no spontaneous activity at low pulse amplitude, pulses self-facilitate, producing APs at high pulse rates (Figure 20c black). At low pulse amplitudes, Pulse-Spontaneous Addition (PSA) occurs when spontaneous activity adds to sub-threshold pulse-induced activity facilitating APs even at low pulse rates (Figure 20c, e turquoise). This effect additionally smooths the pulse-induced changes at high amplitudes and eliminates the PDL effects more as spontaneous rate increases (Figure 20d). At high pulse amplitudes, pulses begin to self-block due to the SFP rule described earlier. At these same amplitudes, the pulse-spontaneous spike interactions produce Pulse-Spontaneous Block (PSB) and block each other with the same probability as PSA (Figure 19e,f).

At intermediate pulse amplitudes, when pulses are great enough to produce APs, Spontaneous Pulse-Block (SPB) occurs (Figure 20g). Pulse-evoked APs that would be produced with no spontaneous activity are blocked. For $R > S$, S pulses are blocked, so $\max(\Delta F)$ reduces to $\Delta F_{S=0} - S$ (Figure 20g,h) but the slope is one until the first bend. For $R < S$, we observe a slope less than one, because aftereffects of spontaneous activity can block multiple pulses, but pulses self-facilitate between spontaneous APs when $R > S$. This slope increases with I until I is large enough that additive effects switch to blocking effects. Together, these effects show spontaneous activity has a significant impact on the maximum inducible firing rate. These effects are also incorporated in the prediction equation: $F = \phi(R, I, S)$ (See Methods).

We parameterized our equation for how the rules change with R , I , and S to the simulations, resulting in accurate predictions across all conditions ($\max rms = 4.0 \pm 0.41$ sps, Table 3-1) (Figure 18 red). We can then interpolate the change in parameters with I and S and predict probability of pulse-pulse interactions, pulse-spontaneous interactions, and induce firing rate for any combination of R , I , and S (See Methods).

Table 3-1. RMS across simulations of vestibular afferents with different spontaneous rates and normal conductance levels

Spontaneous rate (sps)	Average RMS (sps)
0	4.17 ± 4.70
7.1	3.92 ± 3.54
12.9	3.34 ± 2.40
29.4	3.58 ± 2.22
55.7	4.23 ± 2.39
85.8	4.42 ± 1.65
130.2	4.38 ± 1.43

The mean RMS of the rule-based prediction and simulation across 10 repetitions at various spontaneous rates. Error is reported as standard deviation.

3.3.3 Predictability of Single Neuron Responses

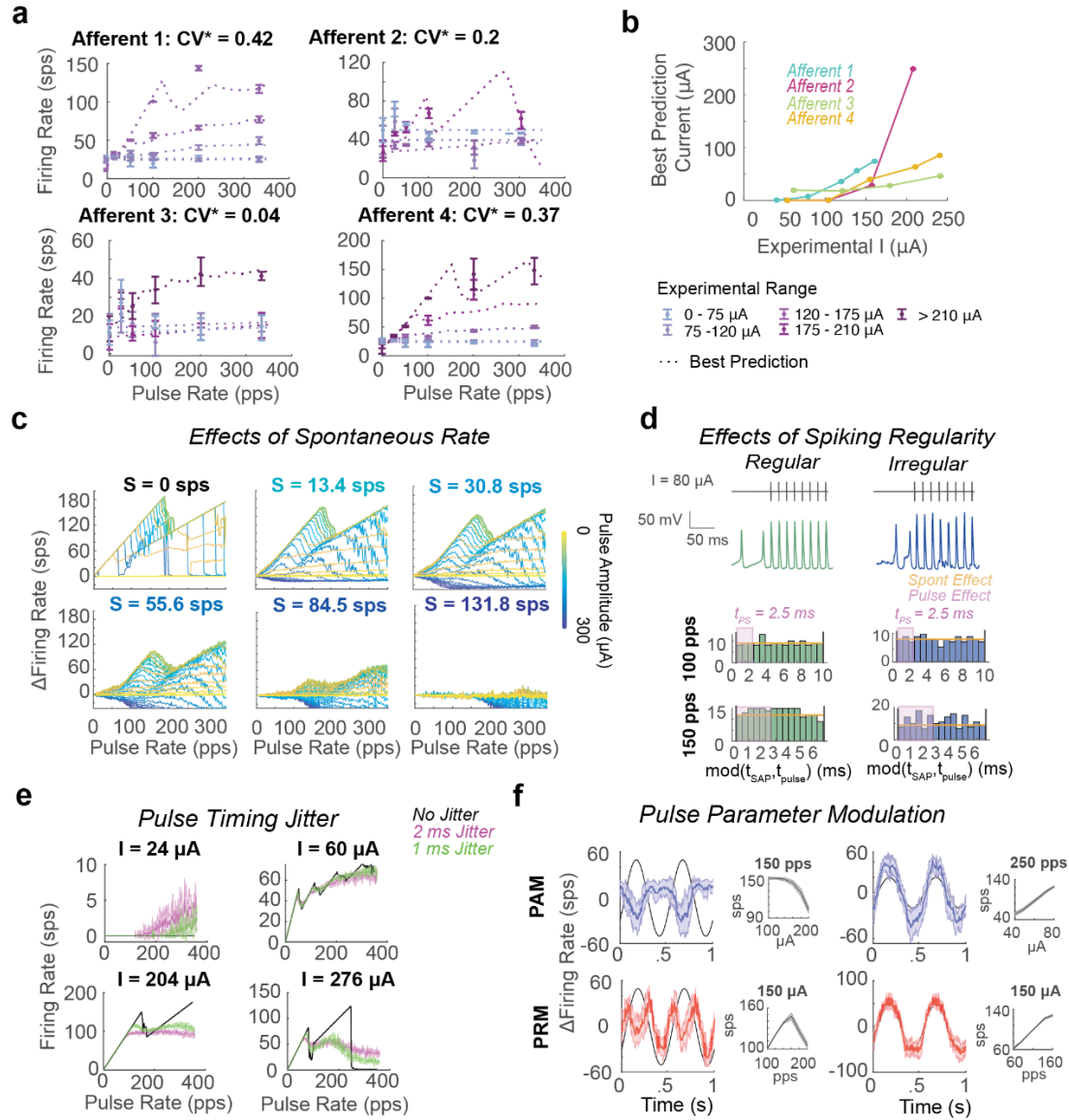


Figure 21. Prediction of Experimental Vestibular Afferent Responses

a) Four afferents varying from regular ($CV^* = 0.04$) to irregular ($CV^* = 0.42$) in response to pulsatile stimulation with 0 to 240 μA . Predictions are shown in matching color to the data (dashed). Predictions used the same parameterization with respect to I and S . S was chosen as the firing rate immediately prior to the pulse block. Only the value of I was chosen to best fit the experimental data. **b)**

The relationship between I_{pred} , the I of best fit and the experimental value delivered at the electrode for each afferent. **c)** Spontaneous activity has a massive effect on induced firing rate. The same currents (yellow-blue) lead to addition versus blocking depending on S . Each square shows the firing rate at the same amplitude with $S=0$ to $S = 131$ sps. **d)** Regularity does not substantially affect the probability of pulse-spontaneous activity interactions for $R > S$. So, we can make the simplifying assumption that regularity does not have a large influence. **e)** Pulse delivery timing often occurs with a jitter. We tested the effect of a jitter of 1ms (green) std and 2ms std (purple) compared to pulses with no jitter (black). We see the jitter smooths the partial elimination zone substantially, similarly to spontaneous activity. **f)** Pulse rate modulation (PRM) and pulse amplitude modulation (PAM) with sinusoids was simulated on the model with modulation frequency of 1 Hz. The predicted induced pulse rate for sinusoidal pulse rate (red) and pulse amplitude (blue) modulation compared to predicted changes (black). For given current range and fixed pulse rate or vice versa the prediction of our equations for change in firing rate (bottom right).

Having developed this set of time-invariant equations (Eqs. 3-4-14) that predicts all simulated conditions above, we then tested the ability of the equations to predict electrophysiological recordings of macaque vestibular afferents in response to pulse trains of different pulse amplitudes. Because the distance and tissue conductance at each recorded neuron affect the current amplitude experienced at the axon, we did not expect a one-to-one mapping between the predicted pulse amplitude (I_{pred}) and experimentally delivered pulse amplitude (I_{expt}). We determined whether this mapping is accurate by finding the I_{pred} that minimizes the *rms* error between the predicted firing rate at every pulse rate given the measured spontaneous activity and the experimentally recorded *R-F* values(See Methods). Under these conditions, the equations closely match the experimentally obtained firing rates (Table 3-2, Figure 21 a-b). The different neurons map to different ranges of the simulated pulse amplitudes. There is evidence of facilitation/PSA (Afferent #3), mid-range additive and blocking effects/PPB/SPB (Afferent #1, #4), and suppression effects/SFP/PSB (Afferent #2), providing support for each rule (Figure 21 a). Comparing Afferent #1 and #2 reveals another complexity. Both neurons receive the same R and I and have similar S but respond at different parts of the mapping (Figure 21 b). One explanation is that vestibular afferents have a large variance in conductances⁸⁷. Simulations within biophysical bounds suggest that reduced membrane conductances of neurons leads to more rapid transition in the mapping in Figure 18 from low I to high I responses with current increase (Figure 22), further explaining the I_{expt} - I_{pred} relationship for Afferents #2 and #3.

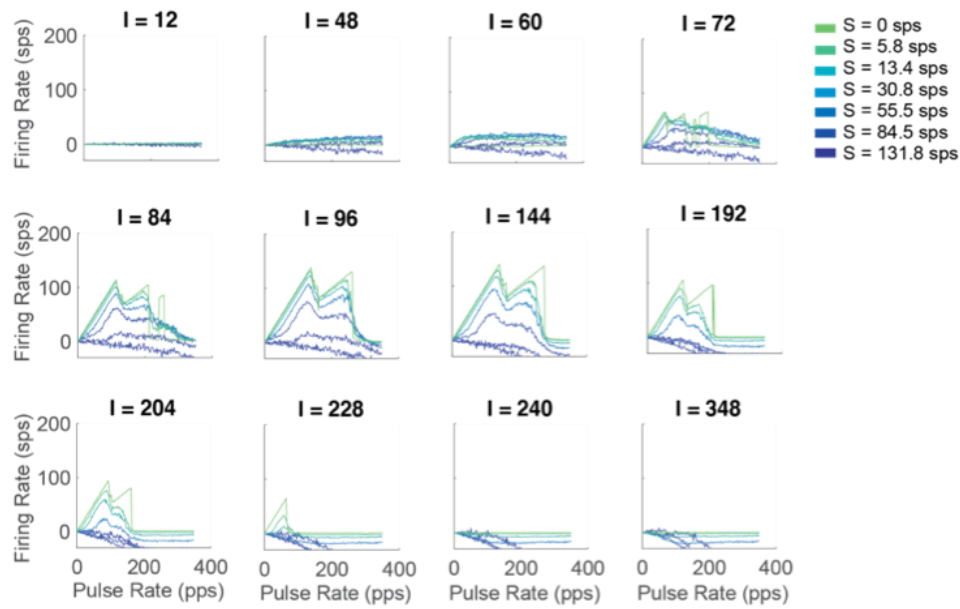


Figure 22. Effect of Conductance on Response with Current

Mapping for pulse rate and firing rate relationship for same range of baseline spontaneous rates 0 to 131 sps. We note a quick transition from facilitation to pulse-spontaneous blocking at lower current amplitudes.

Table 3-2. RMS Values and Percent Error Per Afferent

Afferent	RMS Value (sps) [%Error]				
	<i>I</i> (25%)	<i>I</i> (50%)	<i>I</i> (75%)	<i>I</i> (87.5%)	<i>I</i> (100%)
1	3.06 [1.44]	2.76 [0.93]	15.28 [3.32]	2.89 [1.96]	1.79 [1.15]
2	12.56 [4.96]	4.10 [2.05]	6.80 [2.69]	9.24 [2.57]	
3	3.99 [4.24]	6.44 [7.36]	5.18 [2.76]	7.88 [9.50]	
4	1.79 [1.16]	2.45 [1.13]	15.84 [5.78]	14.88 [3.05]	4.27 [3.11]

RMS error between recorded afferent responses and prediction using rule-based equation. Data show for current amplitude normalized to 25% to 100% of maximum safe current amplitude for each monkey for 4 afferents shown in Fig. 5a for comparison. Mean value in above and standard deviation in [] below in sps.

3.3.4 Implications for Current Usages of Pulsatile Stimulation

The rules described in this paper indicate pulses produce a variety of population responses even in neurons directly under an electrode responding to a stimulus of a fixed pulse rate and amplitude. A pulse

delivered from an implanted electrode produces an electric field that decays with distance from an electrode. Therefore, underneath a single electrode, distant neurons will experience lower stimulation currents and would respond as if they were stimulated at a lower amplitude in Figure 18. Additionally, spontaneous activity substantially impacts the magnitude and even direction of ΔF for the same stimulation amplitude, producing large additive effects for low spontaneous rates ($S < 30 \text{ sps}$) and large blocking effects for high spontaneous rate ($S = 131 \text{ sps}$) (Figure 21c). Finally, neurons with different membrane conductances respond differently to the same stimulus. Between these effects, neighboring neurons may not respond in with the same magnitude or directionality to the same stimulus.

We additionally considered whether the rules apply under realistic clinical implant scenarios that modulate pulse rates or amplitudes, and when pulses are delivered to neurons of varying spontaneous firing regularity. A potential concern would be the effect of regularity of spontaneous spike timing compared to pulse timing. For pulse rates greater than the spontaneous rate, regularity did not affect induced firing pattern substantially (Figure 21d). The largest differences are that the pulse elimination zone is substantially shorter and pulse rates below S produce no additional pulses or block spontaneous activity (Figure 23). Another question is how regularity of pulse timing affects the firing rate. Even pulses programmed with ideal regularity show some jitter in delivery due to imperfect implementation of both hardware and software. We introduced 1 and 2 ms of jitter around pulse delivery times, finding the same rules apply. The jitters extend the smoothing of the PE , similarly to spontaneous activity, but maintain the underlying mechanism and frequency of pulse-spike interaction (Figure 21e).

We assessed whether the rules (Eqs. 3-4-14) uncovered during fixed-rate pulsatile stimulation trials hold when applied in the context of pulse rate (PRM) and pulse amplitude modulation (PAM) rather than pulse trains, two standard paradigms in which pulse rates change over time. We simulated sinusoidal PRM (modulation of pr with fixed I) and PAM (modulation of I with fixed pr). The mapping from fixed pulse rate simulations (Figure 18) predicted ranges of non-linear and linear PFR (Figure 21f grey traces) for PRM and PAM. The PRM (red) and PAM (blue) simulations reflect these predictions, as shown in the grey traces to the right of each plot (Figure 21f).

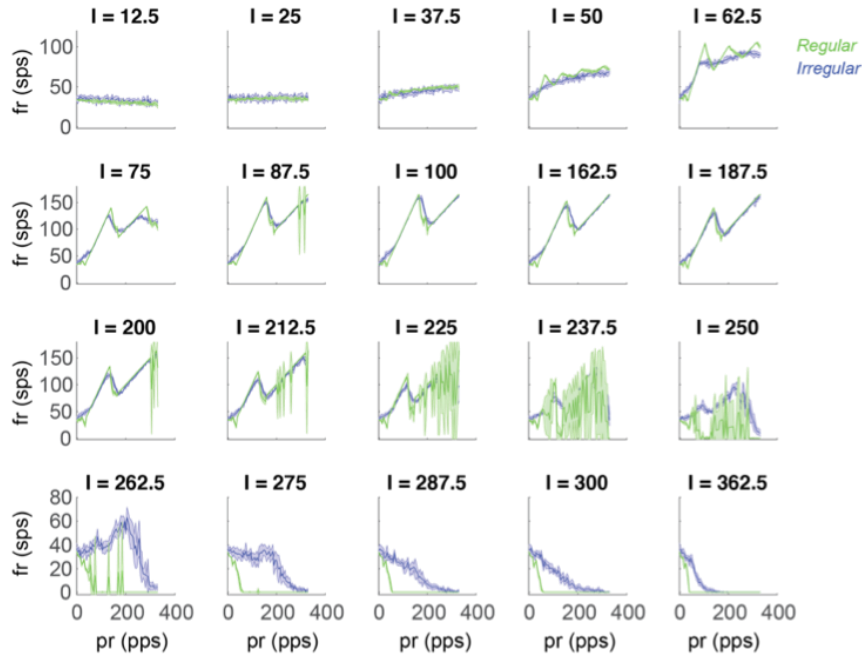


Figure 23. Effect of Regularity on Pulsatile Stimulation

Mapping of PFR for I from 0 – 362.5 μA for regular (green, $\text{CV} = 0.09$) and irregular (blue, $\text{CV} = 0.57$) neuron with similar firing rate (32-36 sps). The response at the sample current amplitude is plot for 5 repetitions, showing differences in the variance at different amplitude and the magnitude of the reduced length of the PE zone for regular neurons. The start of blocking is observed to start at lower I for regular neurons. Additionally, when $R < S$ the response dips, indicating a stronger SPB effect.

Finally, we tested how the commonly assumed mapping of a one-pulse-to-one-spike would affect the performance of a vestibular prosthetic by simulated pulse delivery at a pulse rate equivalent to natural firing rate in response to a detected head velocity^{159,168}. When we mapped the corresponding pulse rate to firing rate of the afferent, the resulting firing was severely attenuated and nonlinear as shown in purple, which could account for asymmetries in vestibular ocular reflex behavior assays and reduced sensitivity to head velocity in behavioral studies and human applications (Figure 24a)^{159,169}.

Next, we addressed whether we could improve performance by implementing the rules discussed. Specifically, the rules were used to obtain a mapping between the pulse rate and firing rate for a single neuron with a specific spontaneous activity, here 30 sps (Figure 24b). The lowest pulse rate that resulted in the desired firing rate was selected for PRM or lowest pulse amplitude for PAM. The accuracy of producing desired firing rate responses was assessed by simulating pulsatile stimulation with this strategy, the rule-based strategy (purple), and a one-to-one mapping strategy (blue) within our biophysical model of a vestibular afferent (Figure 24c). Figure 24c shows relative performance on producing single-frequency

sinusoidal modulation. The rule-based strategy shows significant improvement in producing the desired firing rates for this case and more complex cases (Figure 24e,g).

The applicability of the rule-based strategy to neurons of varying activity was assessed using neurons with the same spontaneous rates simulated previously (Figure 18). Overall, mapping pulse rate based on our set of rules led to a larger range of restored head velocities (Figure 24d left). Neurons with the lowest spontaneous rates could be driven to the largest firing rate (light green) (middle), but all neurons required a highly non-linearly mapping to produced desired firing rates (Figure 24d right). The highest spontaneous rate neurons, meanwhile, are more difficult to drive towards negative velocities in this pulse amplitude (150 μ A). Two examples of using the strategy to obtain an arbitrary target firing pattern (a combination of sinusoids) are shown - one for a neuron with spontaneous activity of 13 sps (left) and one for a neuron with spontaneous activity of 30 sps (right) (Figure 24e). The pulse modulation needed to achieve the desired firing rates is drastically different in these two cases, but the optimizing strategy produces the desired outcome in both cases. Similarly, the optimal PAM strategy can be found using the rules. Here, the strategy is applied at 250 pps to get a large firing range. The analogous strategy limitations and predictions for PAM are shown in Figure 24f, g. The mapping is also highly non-linear and shows similarly reduced firing range for high spontaneous rate neurons. Taken together, our results suggest that accounting for these rules of neurostimulation could substantially improve neuroprosthetic performance once they are verified and parameterize to the specific system being interfaced to.



3.4 Discussion

91

high frequency facilitation (row 1) have been observed in cochlear afferents⁵⁶; high amplitude block is observed in the sciatic nerve (row 4)⁵⁷; amplitude-dependent growth of firing rates has been observed in the auditory nerve (Figure 18 row 1)¹⁷¹; our experiments in the vestibular system²⁹ and hippocampal responses demonstrate pulse-spontaneous blocking effects (Figure 20)¹⁷². While such findings have previously been assumed to be system-specific issues, here we provide evidence that these non-linear interactions stem from the disruptive effects of pulses on axonal firing.

We find that the unnatural perturbation of the axonal membrane potential by biphasic pulsatile stimulation induces these effects by creating long-term loops in the dynamics of sodium and potassium channels. Given most neurons rely on these channels or channels with similar dynamics to produce action potentials, we expect pulses induce these same non-linearities in all neurons (as supported by the cases above): bends in the PFR, facilitation, and block (Figure 18). However, the pulse rates at which the first bend occurs (t_b) or the length of suppression effects will differ depending on the time constants of the channels specific to the axon.

Our present findings have several important implications for electrical stimulation-based interactions of the brain. First, suprathreshold pulse amplitudes (e.g., 100 μ A) are assumed to drive one AP per pulse and lead to increased activation as amplitude increases by recruiting more neurons. Instead, we find individual neurons are highly sensitive to pulse amplitude because it determines the perturbation of channel state and therefore length of induced dynamic loops. Thus, neurons closer to the electrode center could produce substantially different firing rates than more distal neurons within the current field. Additionally, spontaneous activity interacts with pulses, creating additive and blocking effects by priming or deactivating channels concurrent with pulse delivery. Although spontaneous activity is stochastic and channel dynamics are non-linear, the probability of interaction can be estimated with respect to pulse amplitude, pulse rate, and spontaneous rate, because of the approximately regular timing of pulses, continual EPSC activity, and orbits in channel state. We thus created equations describing these interactions. These equations were formulated to describe each of the pulse-induced effects (PPB, PDL, SFP) and pulse-spontaneous interactions (PSA, SPB, PSB); equations that captured these main effects predicted responses of real neurons to pulsatile stimulation of varying amplitudes (Figure 20a, Methods). We also found that these effects persist with jitter

in pulse delivery or when there is irregularity in firing, and they predictably distort the induced firing rate during pulse rate and amplitude modulation (Figure 21).

Based on these findings, several potential solutions for neural implants emerge from our findings. Most importantly, as discussed above (i.e., Figure 24), we can leverage our understanding of the described rules to produce corrected mappings between pulse parameters and desired firing rates and correct pulsatile stimulation trains. This strategy alone would not suffice for driving whole populations in most neural systems though, unless spontaneous activity is relatively similar across neurons due to differences observed in effect on neurons of different spontaneous activities (Figure 18, Figure 22). To increase controllability with this strategy, another potential solution indicated by our study would be to eliminate spontaneous activity or inputs from other areas. For example, in the case of a vestibular prosthesis, using gentamicin to ablate vestibular hair cells^{173,174}, or site-specific channel blockers in cortex. This would make neurons easier to drive with consistency throughout the population, because it eliminates three of the uncovered non-linear effects (PSA, SPB, PSB) and leads to a larger inducible firing range (Figure 18, Figure 24). Additionally, using a channel dynamics perspective, a novel stimulation waveform could be designed to take advantage of dynamic loops. For example, our results show that cathodic-only pulses push the channels into an unstable state. A typical anodic recovery-phase can affect the duration of the evoked spike afterhyperpolarization. The shape of the recovery-phase of a pulse could be designed to keep the channels sensitized, so that when the next pulse is delivered one-to-one AP induction occurs.

While our original intent was to develop equations that could be used to correct neural implant algorithms for non-linear effects, we also uncovered a scientifically important caveat. Neighboring neurons, for example in cortex, do not typically share the same spontaneous rate. Additionally, membrane channel densities vary between neurons and the change in extracellular potential varies with distance from the stimulation electrode. Our work shows all three of these properties can lead to differential effects of pulsatile stimulation (Figure 23). This result, which is supported by past microstimulation studies^{163,172}, implies the population responses are not predictable without characterizations of the individual neurons, which is an intractable solution for developing prostheses for patients in the clinic. This result has two scientific implications. First, it calls into question whether electrical stimulation-based mapping studies unveil natural effective connectivity and therefore function. Second, despite the fact that pulses produce seemingly unnatural and

chaotic changes in population firing rate, partial encoding of information occurs (e.g., restoration of hearing without pitch perception in cochlear implant users). Additionally, increases in pulse rate or pulse amplitude cause an increase in the local population response that is correctly interpreted by higher-level cortex (e.g., increased sound loudness). These findings support theories of population-level spatio-temporal integration of encoding¹⁷⁵ and transmission¹⁷⁶ of information and indicate that pulsatile stimulation could drive these functions, if delivered with the correct parameters.

It is worth noting that the nonlinearities identified in our study are not inherent to electrical stimulation. Some forms of electrical neuromodulation, such as galvanic stimulation, do not produce the nonlinear effects seen here²⁶. However, galvanic stimulation cannot be implemented in the standard metal electrodes used in present neural implants without producing toxic reactions at the electrodes. Meanwhile, conventional pulse generators were specifically designed to use pulses to avoid this safety concern, but, as we observe here, render electrical stimulation less effective by distorting firing patterns.

Our work takes a step towards improving neuroprosthetic algorithms in two ways. It provides a coherent explanation of the variability in neural responses to pulsatile stimulation that is observed across neural systems^{55,170,177}. Then, based on the explanations posited here, we suggest ways of overcoming the problems we identified with pulsatile stimulation to obtain desired firing patterns.

3.5 Further Support for the Effects of Pulsatile Stimulation on Neurons Across Neural Systems

Several factors contribute to the non-linearities between pulse parameters and firing rate described above not having been previously incorporated into neural prosthetics. One factor is that the driving force of clinical stimulation has been primarily clinical efforts to make neural implants to restore function; thus, functional improvements have often been used to optimize stimulation parameters⁴. In part, this focus on function has been due to restrictions on invasive human recordings. For many systems, many synapses stand between the point of stimulation and perception, which makes identifying non-linearities difficult in this way, and systems have been shown to adapt to abnormal inputs masking or changing the effect on behavior, even in the vestibular system, where there is relatively limited central processing²⁹. Additionally, many of the assumptions underlying prosthetic use of one-to-one relationships between pulse rate and firing rate in

prostheses come from a long-held understanding of how EPSCs, natural current injection into axon, produce action potentials and findings from canonical studies of single neurons that have no spontaneous firing responding to limited pulse parameters and canonical neuronal models, such as the original Hodgkin-Huxley model³⁷. Since the original Hodgkin-Huxley model was developed, much work has gone into further simplifying the dynamic equations in order to make simulations with large populations of neurons computationally efficient¹⁷⁸⁻¹⁸⁰. This goal has led the focus of much of the computational modeling community away from realistically representing the channels specific to cells. However, simultaneously, the difference in channel dynamics, even in channels for the same ion, such as sodium channels, has become clearer with further biophysical investigations of individual neurons¹¹⁸. Here, we highlight various studies where the single neuron or computational modeling confirms finding discussed in this chapter about effects of pulses on neural firing.

One of the major non-linearities of pulsatile stimulation that has been overlooked has been the how pulse rate or frequency affects the number of induced action potentials (APs). Based on the concept of a pulse being an artificial EPSC that depolarizes the axon and triggers an AP, pulses have often been considered able to induce an AP above a threshold amplitude. High-rate stimulation, stimulating with pulses at rates well above the natural firing rate, such as 1000 Hz or more, has recently become a clinical tool for deactivating axons (Figure 25a)¹⁸¹; the mechanism of inactivation has been a topic of research but points to full block of conduction across the axon¹⁸¹⁻¹⁸³. Studies support the idea that voltage-gated channels are pushed into unnatural states, creating these blocks, and particular activation of potassium channels was found to be a source of block through studies with unmyelinated axons¹⁸¹. Results of pudendal nerve stimulation show even behavior (urethral contraction) to high-frequency stimulation exhibits non-linearities depending on combinations of pulse frequency or rate and pulse amplitude that resemble those observed in the vestibular system at lower frequencies (Figure 25b).

Effects of lower rates of pulsatile stimulation have been overlooked in many systems, but studies at lower rates have implicated disruptions of channel effects in causing less than one AP to be produced per pulse. A mapping of pulse frequency and induced firing rate, (called transmitted mean frequency) was performed *in silico* for sensory skin T-cells¹⁷⁷; in this study of the sensory system, the induced firing rate was shown to vary with pulse frequency (Figure 25c). Additionally, this study further discusses the important of the

afterhyperpolarization (AHP)¹⁴⁶, an effect due to post-spike sodium and potassium channel activation that can prevent synaptic transmission, change excitability, and affect plasticity¹⁷⁷. The AHP was systematically increased by increasing amplitude of stimulation at the soma (and therefore is a correlate of pulse amplitude), and a detailed model of the segments of the T-cells was used to measure induced firing. Results show that current amplitude has a non-linear effect, like the one observed in the vestibular system (Figure 18). Cataldo and Brunelli (2005) also show change in channel conductances affect the maximal spike emitted per condition¹⁷⁷. This theory is further supported by a neocortical study of pulsatile stimulation in which channel blockers, such as apamin, 5-HT, and carbachol were systematically introduced into the system; this resulted in a change in shape of the AP and change in maximum spiking induced at a current amplitude, further supporting the role of channel conductance in controlling inducible spike range¹⁸⁴.

Cataldo and Brunelli (2005) also investigated “load ratio,” the difference in conduction as segment size changes; the study shows that transitions of segment size effect the regime of non-linearities experienced for the same current amplitude, similarly to the way that differences in conductance affected the regime of pulse relations observed in the vestibular system (Figure 22)¹⁷⁷. This effect was not considered for vestibular modeling, because there is support that the vestibular effects of electrical stimulation occur at the afferent trigger site and not having downstream axonal effects^{94,121}. However, this effect should additionally be considered for pulsatile stimulation of other neuronal types.

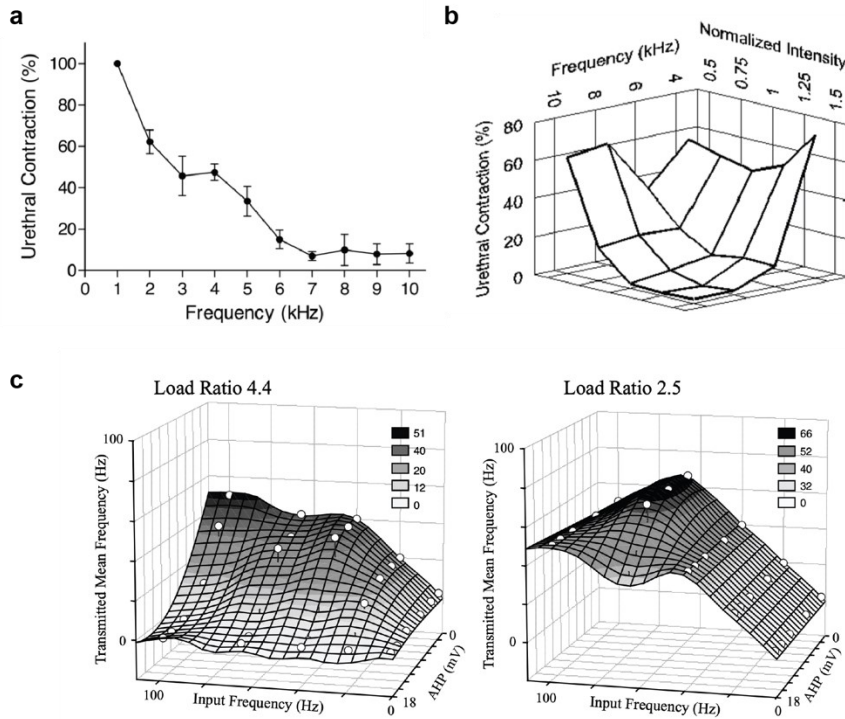


Figure 25. Evidence of Non-linear mapping of Output with Pulse Parameters

a) Evidence from urethral stimulation study that high-frequency stimulation causes urethral contraction block. b) For same study, non-linear mapping of high-rate stimulation frequency and intensity (a correlate of amplitude). Adapted from Tai, Roppolo, de Groat (2005). c) Simulated mapping of pulse frequency and afterhyperpolarization (AHP) magnitude to transmitted firing rate or firing frequency. Model represents sensory cells (T cells) of leeches. Adapted from Cataldo and Brunelli (2005).

3.5.1 Support for Non-linearities observed in Steinhardt *et al.* (2021)

Physiology data tend to be sampled at large pulse rate intervals, but across organism and system, observation of single trial firing and single neuron responses supports the pulse rate non-linearities discussed above. In a study of auditory neurons responding to pulsatile stimulation, for the same current amplitude and neuron, responses to pulse rates of 200 and 800 pps showed that at 800 pps approximately half the pulses did not produce APs (Figure 26a)¹⁷⁰. Based on the theory of pulses having a window t_b , if a window of the same size was drawn into both images, the same window size would allow one-to-one spiking at a lower pulse rate and half of pulses to be blocked at 800 pps (Figure 26a blue). At a different amplitude and for a different neuron, at 200 pps, many pulses are blocked from producing APs, supporting the concept that if the current amplitude has a stronger effect, it can shut down axonal firing for many pulses before spontaneous firing or pulses can produce APs again (Figure 26a bottom)¹⁷⁰. The interactions between pulses and spontaneous firing have also been observed in hippocampal and subthalamic neurons. In hippocampal neurons, raster plots show that baseline firing has some randomness, and, when pulses are introduced, it

causes the timing of spiking, as viewed on the PSTH to regularize (Figure 26b). The event distribution of spontaneous spiking closely reflects the distribution predicted in vestibular simulations and supports the theory that pulse-spontaneous interactions can be approximated as occurring with a fixed probability over a time window in the hippocampus, as it was in the vestibular study (Figure 20b). In a subthalamic study, spontaneous interspike intervals and regularity were measured then remeasured after exposure to pulsatile stimulation¹⁸². At a low rate of 10 pps, the different mapped pulse rate-firing rate relationships are observed at different current amplitude: at 300 μ A there is light facilitation, and some pulses produce APs; by 600 μ A a one-to-one relationship occurs, as would be expected near the far left of the pulse rate-firing rate mapping (Figure 26c; Figure 18). Garcia *et al.* (2005) study a number of subthalamic neurons of difference underlying spike timing distributions. They show at high pulse amplitude that some neural firing shuts down as observed in the vestibular system, but, exceptionally, some neurons show another period of facilitation between pulses and spontaneous firing, as shown in Figure 26c (bottom) ¹⁸². These data reflect that the underlying differences in channel conductances and other cellular properties change how neurons proceed through the mapping described in the vestibular system above and cause diversity in how individual neurons respond to pulses. This is a prediction of the simulation result of pulsatile stimulation in the vestibular system, as well (Figure 21, Figure 22, Figure 23). The equations used to describe pulse parameter and firing rate relationships should still hold and be able to capture these interactions, but the current amplitudes at which these effects occur and the exact values of t_b or t_{ps} should be adapted to individual neuron type to be able to capture the non-linearities specific to the channels of these neurons. Additionally, cochlear neurons have been repeatedly studied in response to pulses of a fixed rate and different amplitudes, because PAM is the standard for encoding loudness in cochlear implants^{185,186}. Studies of increased pulse amplitude (proportional to encoding of sound of loudness of typical talking volume show that with current increase the percent of APs generated by the system increases at different rates for different neurons, and high current amplitude suppress firing (Figure 26d) similarly to how it was shown to in the vestibular system (Figure 24f)¹⁸⁷. These trends that reflect the uncovered pulsatile effects are shown across different neurons in the same neuron type, such as across neurons throughout the auditory system in guinea pigs but at different rates of effect with change in pulse rate (Figure 26e). In simulation, these effects are not observed without realistic channel dynamics, but, if the channels are modeled accurately in rabbits (Figure 26f), leeches

(Figure 26g), or macaques (Figure 18), consistently the pulse rate as well as pulse amplitude effects occur. The pulse rate that bends in the relationship may vary, but pulses cause perfect block of every other pulse or every three⁵⁵. While current amplitude and effect sizes may vary, the principle of pulses creating unnatural rhythmic loops in channel dynamics that create temporary suppression (Figure 26f-g) or full suppression (Figure 26d-e) of axonal firing seems to be a regular occurrence for voltage-gated channels that needs to be accounted for in microstimulation experiments or prosthetic algorithm design. Thus, the work above provides an example set of equations that could be adapted by neuron type or system to address these confounding effects of pulses. Alternatively, further investigation into how to stimulate neurons without causing disruptive effects on channels may lead to better stimulation algorithms (Chapter 2). An understanding of the consistent source of non-linear effects of electricity on neuronal firing marks the first step towards improving electrical neural interfaces overall.

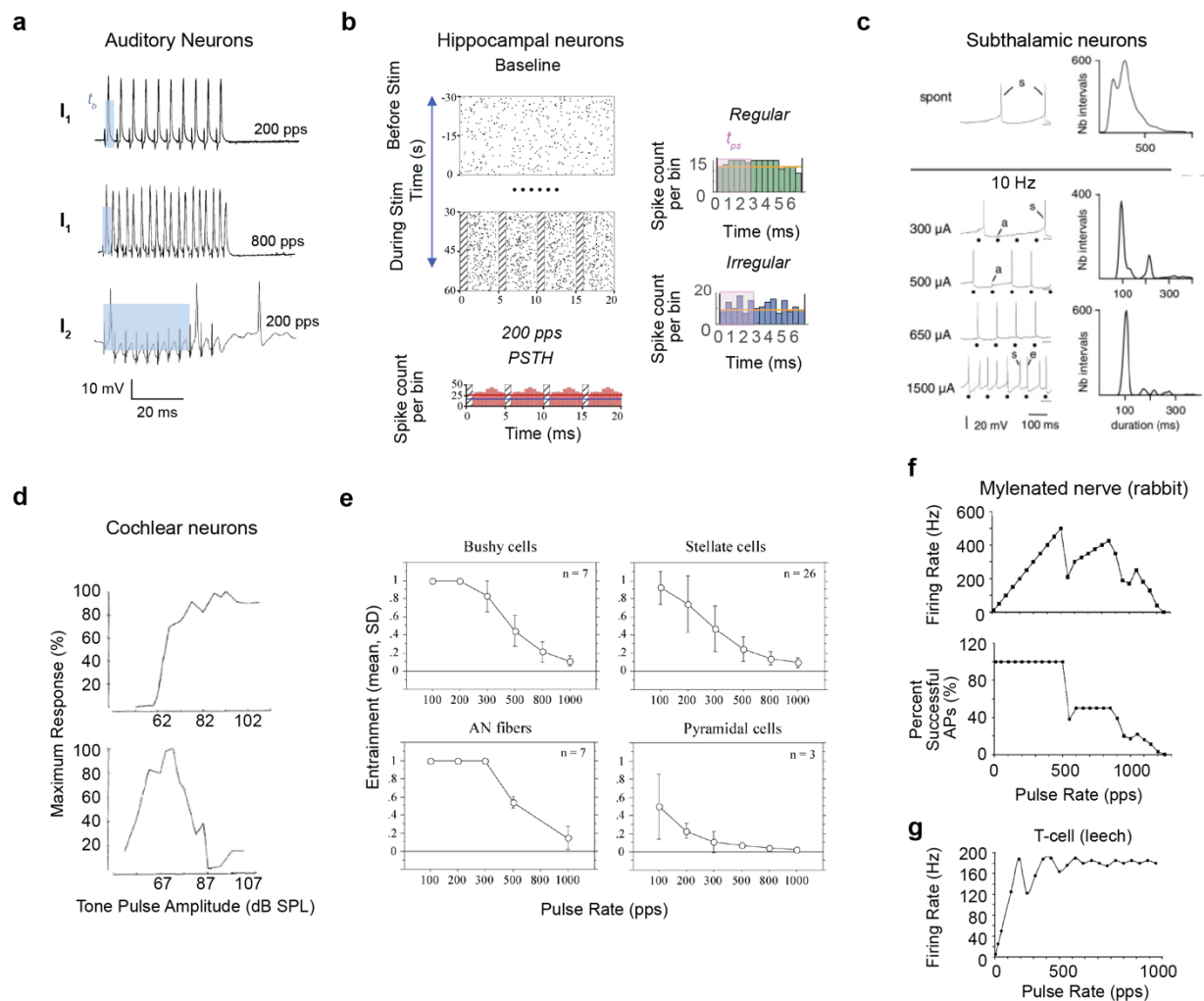


Figure 26. Evidence of Predicted Non-Monotonicities Across Systems

a) Responses of auditory neurons to pulsatile stimulation. (Top and middle) for same current (I_1) spiking to pulsatile stimulation at 200 and 800 pps. (Bottom) spiking at different current (I_2) and different neuron to pulses at 200 pps. A theoretical t_b is shown in blue of same size for current (I_1). For (I_2), t_b is longer, leading to pulse artifacts with no action potentials in bottom row. **b)** Raster of spontaneously firing hippocampal neurons at baseline (no pulses) and during pulsatile stimulation at 200 pps. Pulse times shown with hashed bars. Peristimulus time histogram shown below for same data. Adapted from Wang, Feng, Wei (2018). Simulated data from vestibular neurons stimulated at 150 pps shown on right for regularly and irregularly firing afferents. **c)** Recordings of spontaneous firing subthalamic neurons. Firing pattern is shown on left and distribution of spike intervals on the right. (Top) Spontaneous firing and spontaneous interspike interval. (Bottom) at pulse rate of 10 Hz and current amplitude of 300 to 1500 μ A. (a) artifact, (s) spontaneous spikes, and (e) evoked spikes are labeled. Pulse times are marked with *. Adapted from Garcia *et al.* (2005). **d)** Percent pulses that make APs for pulses of different amplitudes proportional to tone loudness in cochlear neurons. Adapted from Phillips and Kelly (1989). **e)** Entrainment, or ratio of APs to pulses, for to rates from 0 to 1000 pps across various auditory neurons. **a** and **f** adapted from Babalian, Ryugo, Rouiller (2003). **f)** Simulated myelinated rabbit nerve responding to pulses from 0 to 1000 pps, showing bends in pulse rate-firing rate relationship (top) and percent successful APs (bottom). **g)** Simulate for T-cell of leech. **f-g)** adapted from Krauthamer and Croscheck (2002).

3.6 Appendix

Table 3-3. Variables used in Equations for Modeling Pulsatile Interactions.

Variable	Meaning	Relevant Equations
F	Induced firing rate (in presence of spontaneous firing, pulses, etc.)	(3-14),(3-15)
R	Pulse rate	(3-1),(3-12),(3-13)
I	Pulse amplitude	Drives many variables. Shown as bold in equations
S	Spontaneous firing rate of neuron under no stimulation	(3-11),(3-13) Drives many variables. Indicated throughout equations
I_{pred}/ F_{pred}	Predicted pulse amplitude estimated by minimizing the error between data and model prediction for induced firing rate at a given current amplitude. F_{pred} – corresponding firing rate for a prediction	(3-2)
F_{PP}	Firing rate induced by pulse-pulse interactions	(3-4),(3-9)
t_b	Time of block after a pulse where another pulse is blocked from evoking an action potential	(3-4),(3-5),(3-6),(3-7),(3-9)
ρ	The inter-pulse interval (1/R) in ms	(3-4),(3-5),(3-6),(3-7),(3-9)
t_{pb}	The time after t_b until less than pulses produce action potentials with less than probability of 1.	(3-5)
PE(I, ρ)	Partial elimination factor and estimate of with what probability pulses are blocked after t_b and before t_{pb} . Takes values between 0 and 1.	(3-4),(3-6)
n	The number of the bend in the pulse-rate firing rate relationship being considered.	(3-6)
PE₁	Condition on first bend with partial elimination under extreme pulse amplitudes. (Pulse dynamic loop Rule where there is exponential decay between t_{pb} and t_b .)	(3-7),(3-9)
PE₂	Condition on second bend with partial elimination under extreme pulse amplitudes. (Suppression of Future Pulses where there is exponential decay toward zero action potentials being produced.).	(3-8),(3-9)

α, β, δ	Parameterized scaling variables that changes depending on spontaneous rate and pulse amplitude	(3-7),(3-8),(3-12)
p_{PS}	Probability of a pulse blocking spontaneous action potentials.	(3-10),(3-12)
p_{SP}	Probability of spontaneous activity blocking a pulse	(3-11),(3-12)
t_{PS}/t_{SP}	Timing after a pulse when spontaneous activity is blocked/ opposite. Note this relation can be used but p_{PS} and p_{SP} were fit directly for simplicity.	(3-10),(3-11)
T	The total length of the time window being considered	(3-10),(3-11)
I_{fac}	Pulse amplitude at which facilitation effects switch to blocking effects	(3-12)
F_P	Contribution to induced firing rate of spontaneous activity induced effects	(3-12),(3-14)
F_S	Contribution to induced firing rate of pulse induced effects	(3-13),(3-14)

Chapter 4 : Using Electrical Stimulation to Create More Naturalistic Neural Implants

4.1 A General Approach for a Novel Neural Implant Algorithm

Neural implants have become an increasingly common method for treating neurological disorders in the last several decades. Neural implants offer a number of advantages over alternative treatments: they are more targeted than many pharmaceutical treatments and provide a non-addictive and removable treatment, which has led, for example, to the increased popularity of spinal cord stimulators in the treatment of chronic pain¹⁸⁸. Additionally, the ability to activate neurons with partial damage provides restoration of abilities unattainable through other means. For example, neural implants can activate axons directly via electrical stimulation and restore lost sensations, such as touch, hearing, and seeing. Alternatively, implanted recording technology can be used to process firing from large populations of neurons and use the firing as a control signal to drive devices, such as computers or robotic limbs. These implants allow amputees and paraplegics to interact virtually and physically with the world¹⁸⁹. For this later case, machine learning and signal processing techniques have extensively contributed to better abilities to “decode” desired actions from the brain¹⁹⁰. However, for interacting with the brain through neural stimulation implants, there are consistent limitations in the ability to elicit naturalistic percepts.

Across systems, this style of device leads to a similar level of functional restoration. For example, in the cochlear implant, which has been continually improved since the initial introduction in 1957⁴, speech perception is restored, but pitch perception, which is encoded in fine-timing of firing rates, is lacking, likely leading to issues with music appreciation and tonal language perception^{161,162}. Whether the issue has been related to noise reduction in the front-end processing in cochlear implants¹⁹¹, pathological neural rewiring of the retina¹⁵⁸, or central nervous system adaptation to vestibular stimulation²⁹. These findings imply that present stimulation paradigms do not restore the natural local responses.

One reason that neural implants may share limitations in restoration of function is that they share a common architecture⁴. Figure 27 shows common neural implants, including cochlear implants for restoration of hearing and spinal cord stimulators for suppression of pain. These devices are highly similar to the original pacemaker and rely on an implanted pulse generator, a device for delivering pulses of current, and

electrodes in target tissue associated with the impairment being treated to restore sensation⁴. Additionally, devices are designed for real-time transformation of inputs, such as sound, into stimulation parameters at a rate at which implant users can respond. As such, clinical implants use simplified transformation of inputs into modulation of pulse rate or pulse amplitude proportional to a recorded inputs (i.e., sound with a microphone, images with a camera, movements with a gyroscope). The stimulation parameters such as pulse amplitude, pulses rate, and even electrode location are primarily empirically chosen to fit individual patients or become canonical to the paradigm, as opposed to being optimized or based on a scientific understanding^{4,192-194}.

The two main classes of algorithms being developed are learning-based and biomimetic approaches¹⁸⁸. In learning-based approaches, the user is expected to learn the meaning of different patterns of stimulation and relate them to information such as hand movement or object texture^{195,196}. Biomimetic approaches aim to create stimulation patterns that mimic the natural inputs to a system. Within this class of approach, there are both model-based algorithms, stimulation based on a fixed model of neural responses, and model-free approaches in which machine learning has been increasingly used to learn the stimulation patterns that work best within a specific neural population of a specific brain¹⁹⁷. Present clinical algorithms with pulse amplitude and pulse rate modulation likely sit between a model-based biomimetic category and a learning-based approach.

Recent research has continued to push towards a biomimetic approach with the hypothesize that increased realism should improve stimulation-induced neural responses. However, within these approaches there are several issues. A general problem with biomimetic algorithms, which often rely on machine learning or optimization to find ideal parameters and transformations, is the requirement of a large training dataset¹⁹⁸. Even then, in many systems the networks do not learn the full range of non-linearities and therefore cannot extrapolate beyond their training set or capture non-linearities of neural transformations^{63,197}. Model-free approaches are highly adaptable to drift or noise of neural responses and well-suited to learn to treat an individual brain and any damage that has transformed neural computations; however, they have the disadvantage of requiring independent learning of how to create each desired stimulus. This would not be conducive to usage in real-time device receiving an on-going stream of inputs, as would be the case in sensory prosthetics (e.g. touch, vision, hearing¹⁹⁷). Thus, at the moment, an improved model-based approach

appears to be the better strategy for improving real-time prosthetics. A trade-off of model-based approaches is that the less detailed they are, the less likely they will capture all cases of inputs to a system and the complexities of neural encoding. Additionally, model-based approaches likely do not account for changes to neural circuits in a post-damage brain. On the contrary, as model-based approaches rely on more complex models of the brain, for example, models that include thousands of neurons in an accurate hypercolumn architectures⁶⁰, they become extremely computationally intensive. This is arguably the most severe issue with more naturalistic algorithms – an inability to create accurate target firing patterns in real-time, using microcontrollers that are standard in neural implants.

In this chapter, work is outlined for creating a novel algorithm that could run in real-time on an implanted microcontroller and approaches more naturalistic firing. The work outlined here suggests a way forward for finding a balance between highly accurate models of neural architecture and algorithms that are capable of usage in real-time devices. This algorithm has two parts, a front-end for predicting the natural response of the system faster than real-time, and a back-end that can find the optimal stimulation parameters to produce a desired firing rate in target neurons. Together, these components would transform a senses input into a stimulation pattern for a given set of neurons. This approach is tested in the context of a cochlear implant. However, it is generalizable to other neural implant usage, due to similarity of stimulation strategies across implants. This work differs from the approaches described previously, because it emphasizes how complex model-based prediction algorithms could be sped up to run in real-time on neural implants. This provides the potential for us to create smarter neural implants that run at real-time speeds and function from initial implantation, without requiring further learning online or offline.

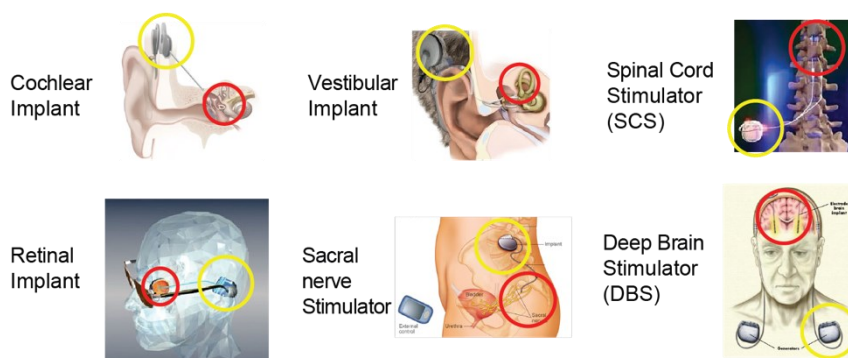


Figure 27. General Architecture of Neural Implant

Diagram of six common neural implants, showing the two standard components: an implanted pulse generator (yellow) and electrodes in target tissue delivering electrical stimulation (red).

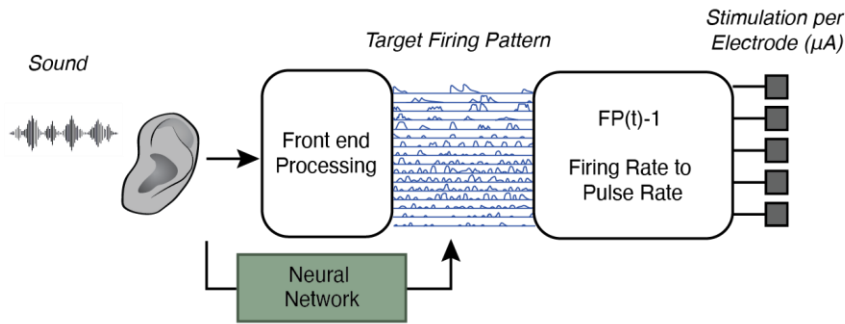
4.2 A Novel Neural Implant Front-end Focusing on Cochlear Implant Usages

Cochlear implants (CIs) are arguably the most successful neural implant with nearly 40 years of innovation and over 736,900 devices implanted as of December 2019^{2,199}. CIs significantly improve speech recognition and comprehension in children and adult users^{2,200,201}. However, they are considerably less successful at restoring pitch of sound. This poses major issue for CI users who speak tonal languages, such as Mandarin, as it results in difficulties with speech comprehension¹⁶¹. It also creates a lesser but significant quality of life deficiency by limiting music appreciation²⁰².

Until recently, the focus of improving cochlear implants has been on preventing current spread from distorting perceived sound. Hardware innovations were implemented to minimize electrode distance from the modiolar wall to more directly target spiral ganglion neurons, and algorithms were modified to avoid electrical interference by ensuring no electrodes delivered current simultaneously^{200,203}; these improvements led to significant gains in fidelity of targeting neurons for spatial encoding of sound to give the percept in sound of a certain frequency. These improvements paired with the continuous interleaved sampling (CIS) strategy, modulation of amplitude of fixed-rate pulsatile stimulation to the envelope of sound, have led to highly accurate English speech comprehension in CI users.

Studies indicate that the inability to correctly convey pitch is the result of unrealistic CI-evoked timing of neural responses²⁰⁴. For example, when normal hearing subjects listened to computer generated tones that deliver pulses with timing reflecting fine timing information of sound, they show improved perception of tonal language (Mandarin)²⁰⁵⁻²⁰⁷. Thirty-years of detailed studies produced a phenomenological model that reflects the full process of sound processing, including mechanical transduction and outer hair cell connectivity; this model produces accurate fine-timing for a single frequency of cochlear neuron²⁰⁸. However, even on a powerful desktop processor, this algorithm requires considerably more time to process the sound than the duration of the sound itself. This problem worsens when considering the reduced processing power on an implanted device.

SPEECH PROCESSING ALGORITHM



SIMPLIFIED PROBLEM

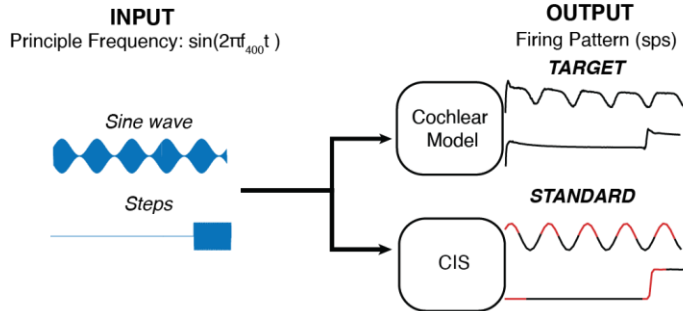


Figure 28. Front-end Processor Experiment Design

We aim to create a front-end sound processing algorithm for a cochlear implant to transform natural sound into a target population firing pattern for the cochlea. This pattern could then be transformed into a stimulation pattern that induces a response with naturalistic fine timing. A neural network will be used to learn the relationship between sound and firing rate from a realistic phenomenological model of the cochlea (top). In this paper, we test algorithm performance on a simplified problem, producing single auditory fiber responses to sine wave and step stimuli, because the CIS algorithm does not replicate firing for these inputs (red), but the cochlear model does.

While replicating exact timing of natural spiking has not been attempted per se, high-rate pulsatile stimulation was popularized as an improvement to CIS because it leads to more desynchronized, naturalistic neural responses and in turn improved speech perception in noisy environments¹⁶. However, a recent study showed that reducing the number of high-rate pulses by half while considering natural firing principles improves speech perception²⁰⁹; this further supports the idea that reducing the number of pulses but more accurately replicating fine timing would improve perception.

Simulations were performed using a highly accurate model of the frequency-specific cochlear neuron responses to sound to understand whether there is a significant difference in induced neural responses using CIS, compared to natural sensation of sound. When pure 200 Hz and 2000 Hz tones were simulated at 65 dB, speaking volume, there was place coding, primarily a localization of neural responses to neurons tonotopically mapping along the cochlea and close to 200 and 2000 Hz in frequency (Figure 29b); this

response closely matches the activity that would be evoked by fixed-amplitude, fixed-rate stimulation with the CIS algorithm (Figure 29a). However, when neural responses were simulated to the same pure tones at a higher loudness, neural responses were shown to spread across the cochlea and take on complex patterns outside the range that would be stimulated using CIS (Figure 29c). These simulations provide evidence that the CIS algorithm does not imitate the complexity of natural responses across the cochlea to a variety of sound inputs. Thus, improvements in inducing naturalistic responses across populations of neurons became a focus of this work.

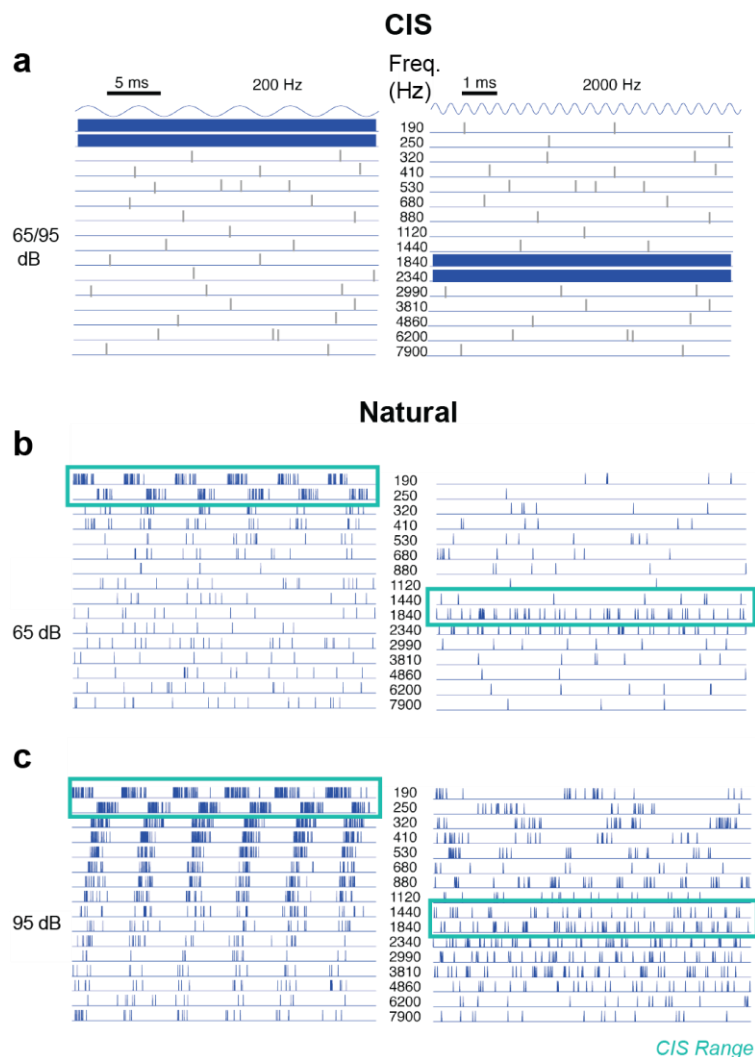


Figure 29. Comparison of CIS to Natural Sound Encoding in Cochlea

Simulated cochlear neurons tuned to sounds at 190 to 7900 Hz. **a)** Responses to Continuous Interleaved Sampling (CIS) based electrical stimulation to encode a pure 200 Hz tone (left) and pure 2000 Hz tone (right). Spontaneous spikes are in grey and high frequency, single amplitude stimulation is in blue. It would be identical but of different amplitude for 65 or 95 dB. Cochlear response to pure tone of 200 Hz or 2000 Hz at cochlear neurons with tuning from 190 to 7900 Hz, according to Zilany model. **b)** At 65 dB. **c)** At 95 dB. The same range of neural firing shown to be activated by CIS is marked with a turquoise rectangle for comparison of activation.

To do this, we create a prototype of a front-end algorithm for cochlear implants that can transform any sound into the naturalistic fine timing of spikes for a fiber at real-time processing speeds using a machine learning (ML) approach (Figure 28). Our approach is to train a recurrent neural network (RNN) to learn the sound-wave-to-spiking relationship captured in the validated Zilany 2014 version of the phenomenological model of the cochlea²⁰⁸. We will first evaluate the performance of the RNN in producing natural responses to sine waves and steps. We choose this simplified problem because the CIS algorithm fails to capture the complexity of the natural encoding of these stimuli (Figure 28 red). This front-end could then be included in a CI processing algorithm that (1) breaks sound into the power in spectral bands, (2) converts power to firing rate over time with a machine learning algorithm, and (3) converts induced firing rate into a pulse rate stimulation pattern, using equations relating pulse rates to induced firing rates²⁰⁹ (Figure 28). Here we focus on optimizing part (2) of this signal processing chain using an ML technique.

4.2 Methods

4.2.1 Generation of Training and Test Waveforms

The data used to train and test the model were synthetically generated sine waves and steps in power of a 400 Hz sinusoid (Figure 28). All inputs were generated with signal of volume V_{stim} in dB, which was converted to A_{mod} sound pressure level (SPL) with Eq. 4-1.

$$A_{mod}(V_{stim}) = \sqrt{2} \left(20^{-6} \left(10^{\frac{V_{stim}}{20}} \right) \right) \quad (4-1)$$

All inputs modulated a 400 Hz wave of the form:

$$s_{base} = \sin(2\pi f_{princ}t), f_{princ} = 400 \text{ Hz} \quad (4-2)$$

Sinusoidal modulation was performed with Equation 4-3:

$$s_{sine} = A_{mod}(0.95(1 - d_{mod}) \sin(2\pi f_{mod}t + \phi_{mod}) + d_{mod})s_{base} \quad (4-3)$$

, where depth of modulation, d_{mod} , determined the portion of modulation compared to A_{mod} , reaching up to 0.95. d_{mod} , frequency of modulation f_{mod} , phase of modulation ϕ_{mod} and A_{stim} were varied as shown in Table 4-1:

Table 4-1. Parameters for Sinusoidal Input Generation

	d_{mod}	$f_{mod}(Hz)$	ϕ_{mod} (radians)	V_{stim} (dB)
Min	0.5	2	0	45
Max	0.9	40	2π	95
Steps	8	10	5	10

Step modulation was performed with Equation 4-4, where V_{stim1} and V_{stim2} , the volume in dB of the first and second half of each step, and the shift, t_{mod} , were varied in the range of Table 4-2:

Table 4-2. Parameters for Step Input Generation

	V_{stim1} (dB)	V_{stim2} (dB)	t_{mod}
Min	0	45	0.2
Max	60	95	0.8
Steps	10	20	20

V_{stim1} and V_{stim2} were converted to A_{mod1} and A_{mod2} , using Eq. 4-1, and step inputs were calculated as:

$$s_{step} = (A_{mod1} + (A_{mod2} - A_{mod1})u(t - t_{mod}T))s_{base} \quad (4-4)$$

, where $u(t)$ is the unit step, and t_{mod} is the fraction of the trial length, T .

Additionally, performance of the model was tested on individual spoken word recordings from the training set of the Speech Command dataset²¹⁰. Recordings were filtered in the 400 Hz band to be equivalent to synthetic inputs.

The waveforms were converted into power by using the *spectrogram* function in MATLAB with a hamming window of length 512 (Figure 30a). This produced 6.4 ms bins.

The Zilany 2014 model was used to generate the natural firing rate over time in responses to these stimuli. The power was used as the input for the neural network, and the firing rate over time generated by the model was used as the target for training and evaluation (Figure 30b & c). The Zilany model produced data every 0.2 ms for each 6.4ms sound sample. This different bin size was addressed when designing the neural network.

For training, 100 synthetic waveforms were randomly sample from the data set, half sine waves and half steps. For testing performance on natural stimuli, 100 words from the Speech Command dataset were randomly selected.

4.2.2 Modeling Cochlear Neuron Response

A phenomenological model that we refer to as the Zilany model of the human auditory periphery was developed over the last 30 years to replicate healthy auditory response to perception of any sound^{208,211}. This model accounts for outer hair cell and inner hair cell contributions to firing, filtering effects, and nonlinearities related to synaptic and axonal activation. The model transforms sound pressure level (SPL) into spiking and firing rate over time for an auditory nerve fiber with low, medium, or high spontaneous firing (Figure 30b). Our model consisted of 50 ganglion cells in the physiologically observed ratio of low and high spontaneous activity fibers located at the 400 Hz position along the membrane²¹². The neural responses (spikes/second over the duration of the sound stimulus) were used to create a dataset for testing and training the neural network.

4.2.3 Recurrent Neural Network (RNN) Model

Although machine learning has been used for a variety of speech processing problems, we found no evidence of it being used for optimization of calculation or for generation of neural population spiking²¹³. Because this is an inherently “forwards-only” problem due to signal processing progressing from the eardrum to the ganglion cell firing pattern, we chose to use a gated recurrent unit (GRU) which incorporates the memory of past network states to generate new inputs as the core of the network design for the task. This should account for effects of history, such as past spikes affecting proceeding spikes due to refractoriness. There were 32 firing rate values for every spectrogram time bin, so a fully connected layer was used to transform the outputs of the GRU layer into 32 outputs. This also allowed additional calculations to be made to adjust firing rate predictions within several milliseconds of one another that occur within one spectral bin. During this study, we assessed model size and used GRUs with 25, 50, 100, 200, 500, and 1000 nodes. We then used a fully connected layer that reduced the GRU nodes to 32 outputs (Figure 30c).

The model was created using the Python Pytorch package. To train this model, the mean squared error (MSE) was used for backpropagation, using the “MSELoss” criteria.

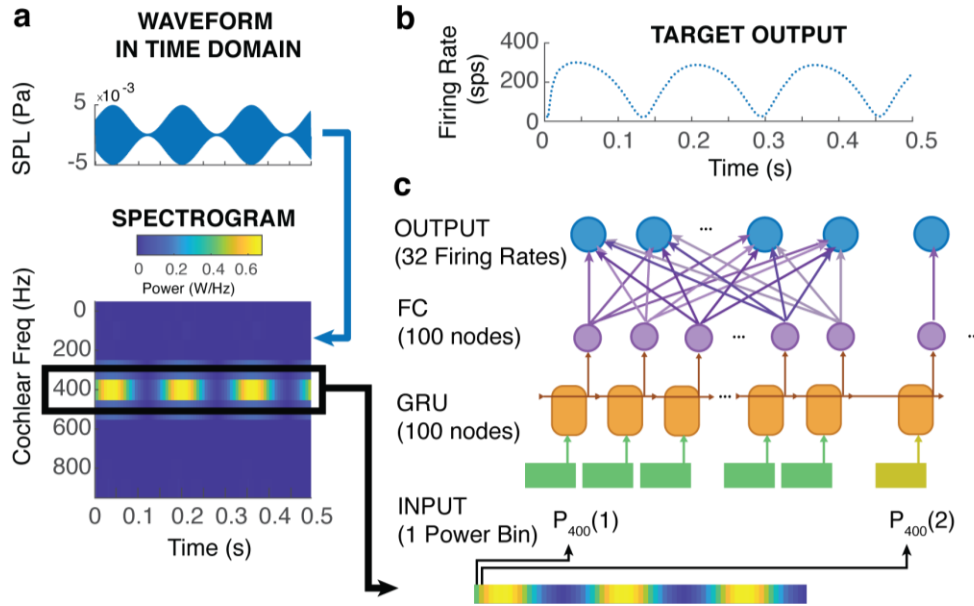


Figure 30. Network architecture for this study

a) Waveforms are transformed in spectrograms in MATLAB and each bin of the 400 Hz power band is run through the neural network to generate induced firing rate over time. **b)** Target outputs are generated by the Zilany model with smaller time bins. **c)** A recurrent neural network is used to turn each time bin into thirty-two firing rate predictions over time.

4.2.4 Performance Metrics

To assess performance on the test and training data, the rms between the target firing rate in spikes per second (sps) of the Zilany model and the output of the RNN was used as a measure of error. During testing, the model was assessed on 100 waveforms (49 sinewaves). Transfer learning as also evaluated on 100 speech command recordings in the 400 Hz frequency. The rms between 10 predictions of the same response to sound with the Zilany model was used as a measure of the variance in natural responses to sound. The rms was transformed into percent error by dividing by the rms of the firing rate over time.

Statistical testing between models and performance was computed with a paired t-test for comparing model size performance and a two-sided t-test when comparing performance on sinusoidal versus step modulation.

This study is attempting to understand whether a machine learning based front-end could be implemented in real-time in a cochlear implant. Thus, in addition to determining the minimum number of nodes necessary to predict responses to sinusoidal and step modulation, the computation time for the model was also assessed compared to the computation time of running the Zilany 2014. Run-time was evaluated on one CPU from a 2.4 GHz 8-Core Intel Core i9 Processor on a 2019 15-inch MacBook Pro when the trained RNN

and Zilany model perform a prediction in response to the same 0.5 second sound 10 times. We used the ratio of speed as a metric in the results.

Additionally, we created RNNs of different sizes to determine the minimum number of nodes necessary to reach an acceptable loss value. We also assessed whether better trained networks involved more calculations and therefore led to significantly slower run times by comparing performance between RNNs trained with 500 and 250,000 epochs.

4.3 Results

Studies indicate restoration of pitch perception requires fine timing of cochlear neuron firing. Standard cochlear implant algorithms, such as the CIS algorithm do not attempt to replicate this fine timing because it is computationally intensive. In this study, we attempt to perform the same computation as in the phenomenological model of cochlear response from Zilany 2014 in real-time by training a neural network to learn the computations performed in Zilany 2014. We assess performance of our RNN first on predicting responses to sinusoidal and step modulation of a 400 Hz sound, a simplified task with observable transformations compared to natural sound. We then determine whether learned transformations apply to natural sounds in the 400 Hz frequency and produce neural responses to natural inputs that are not captured by the existing CIS algorithm.

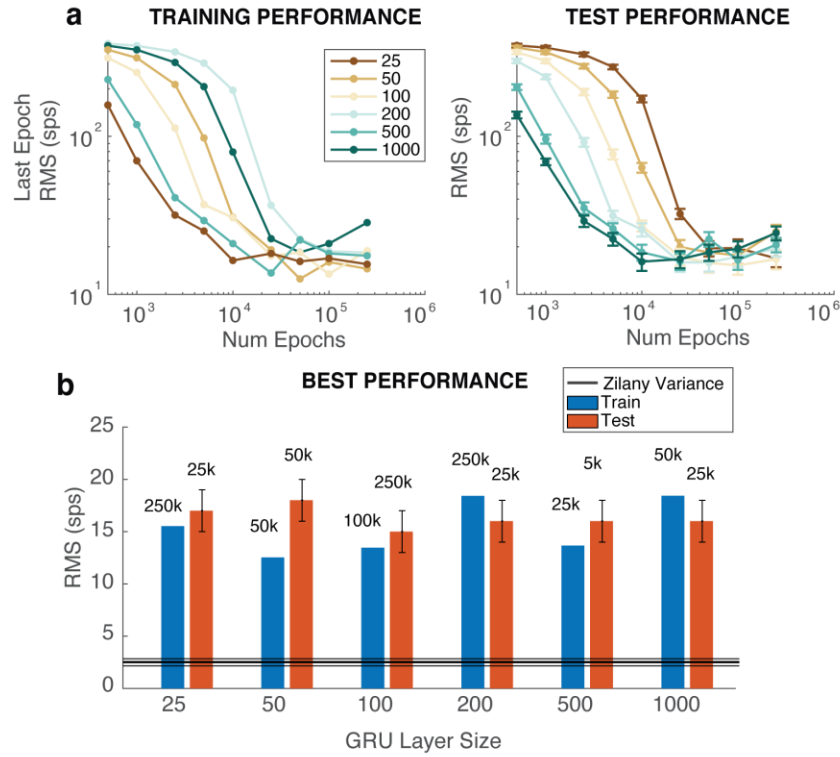


Figure 31. Loss/Performance with Epochs

a) Left. The rms by the last epoch of training on networks with 25 to 1000 GRU nodes. Right. Test performance of each of the trained models on 100 novel sine and step modulated waveforms. **b)** The best performance of each size network on the training (blue) and test (red) data with the number of training epochs at which it best performed written above. Error bars are SEM.

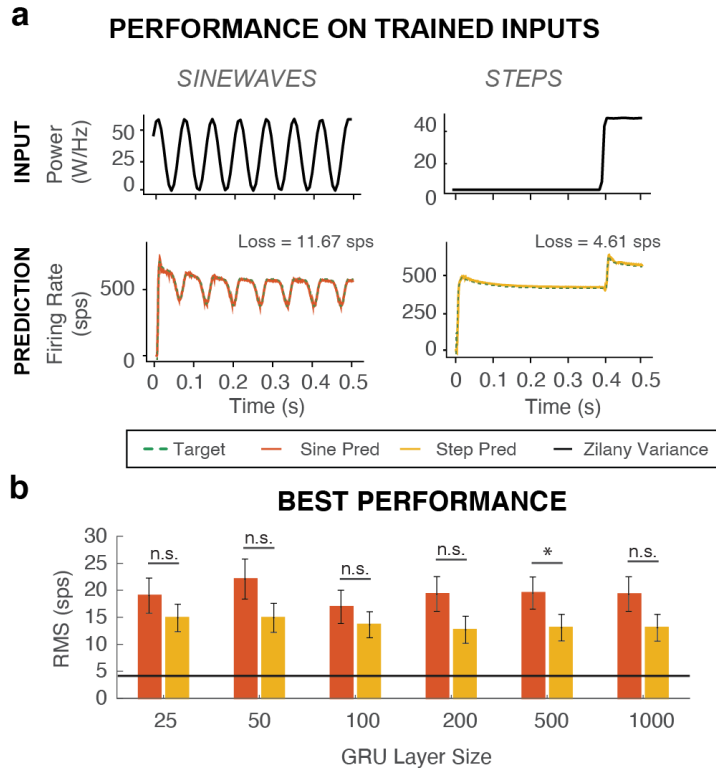


Figure 32. Relative Performance on Sine and Step Waveforms

a) Input power signal (top) and prediction (red/yellow) and target firing response generate by Zilany model (green dash). **b)** Test performance across models on predicting responses to sinusoidal (red) versus step (yellow) inputs with networks trained for number of epochs of best overall performance. Statistics are two-sample t-test. *, $p < 0.1$.

4.3.1 Performance on Synthetic Sounds

We first examined the training time and network size required to create an RNN that can perform this task. The RNN contains a GRU layer and fully connected layer. We attempted to train networks with as few as 25 GRU nodes and as many as 1000 GRU nodes for up to 250,000 epochs. The smaller models trained and reached the lowest training errors after fewer epochs (Figure 31a left). However, all models converged to approximately the same performance by 250,000 training epochs. Larger models reached lower test error more quickly. However, by 250,000 training epochs, all model size performances were approximately the same (Figure 31a right). We speculate that there are fewer weights to adjust so these models converge more quickly to an optimization minimum. However, ultimately, even a 25-node GRU layer learned this transformation after a reasonable number of training epochs. Although the best performance occurred after different numbers of training epochs, depending on model size, all models had test performance comparable to training performance of approximately a rms of 10 sps (Figure 31b).

We compared this to the minimum achievable error, the rms between multiple simulations of the natural response to a sound with the Zilany model, which reaches a minimum of 3.0 ± 0.2 (SEM) sps. Compared to the rms of the signal, the models on average have a test error of 4.20 ± 0.03 %.

The models were trained to infer responses to both sinusoidal (red) and step (yellow) modulation (Figure 32a). The RNN was able to generate both types of responses with high fidelity to the outputs generated by the Zilany model (green dash) (Figure 32a). The model appeared to predict step input responses more accurately. However, differences in performance were not statistically significant except for the 500 node GRU model (Figure 32b). We expect performance to converge with a larger number of training epochs and more training data.

4.3.2 Performance on Natural Sounds

We then evaluated the relative difficulty of learning responses to natural sounds and consistency of cochlear neuron transformations by using the same models (Figure 32) without retraining to predict responses to recorded speech in the same 400 Hz auditory fiber bundle. Audio recordings from the Speech

Command dataset of male and female subjects saying individual words were inputted into the RNN. The amount of transfer learning was again measured with the rms between the prediction of the RNN and the output of the Zilany model for these natural inputs (Figure 33a).

Without retraining, the model is capable of transfer learning and capturing complex structure in the response not captured using the CIS algorithm (Figure 33a). The error primarily comes from offsets in predicted firing rate not inability to capture complexity. This leads to rms increases of up to 80 sps across models, and the minimum percent error across models averaged $46.1 \pm 0.76 \%$ (Figure 33a-b). Model size shows some significant effect. The 50-node RNN significantly outperforms all models except for the 500-node RNN (Figure 33b). However, we speculated that the large models had not converged and learned the rules as accurately as the smaller models did with fewer weights and biases to train. Plotting the minimum loss achieved for each network size when the network was trained for up to 250,000 epochs supported this idea, as the rms still showed higher loss values and high variance than when the model was trained on sine and step inputs (Figure 31a). Longer training epochs are therefore required to determine the ideal network size, but this implies a network larger than 50-100 nodes is not necessary to learn cochlear responses to natural stimuli.

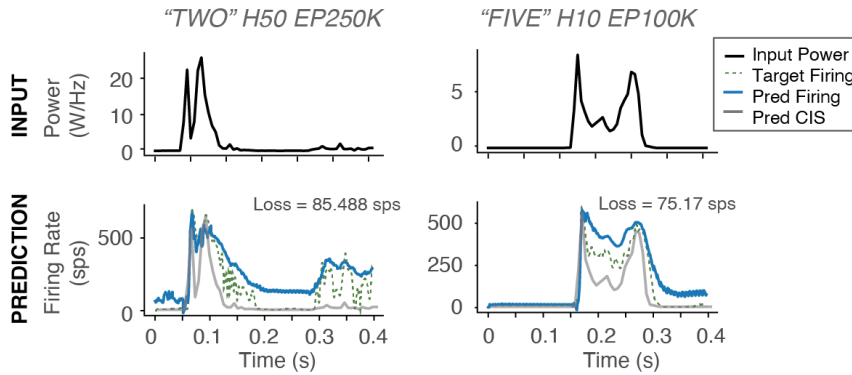
Observing differences between the inferred response by the RNN (blue) and target response (green dash), we find the model captured non-linear transformations of the sound into firing rate (Figure 33a left .05-1.5 s & .3-.5 s, right .15-.3 s). The model appeared to accumulate the most error for portions of response that were not scaled accurately. However, it captured complexities in shape that would not be captured with a CIS model (grey), which linearly maps the sound amplitude envelope to pulse amplitude. These results suggest that essential transformations were learned from sine and step inputs alone. Additionally, because the models have not yet converged, with more training epochs, the RNN will likely capture both shape transformation and scaling accurately, as it was able to learn offsets in the step response (Figure 32a right). How significantly the present differences in scaling influence pitch perception is yet to be determined.

4.3.3 Real-time Applicability

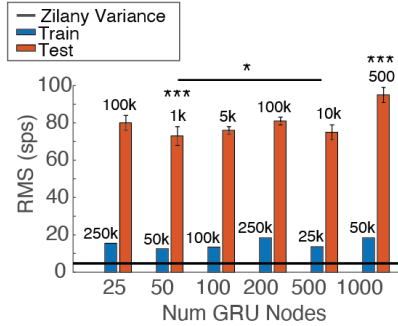
We evaluated the potential of these RNNs to be used in a real-time implementation on the same 0.5 second sound. The Zilany model required 1.47 ± 0.01 seconds to predict the neural response of a single

fiber. The 25-node network required 4.73 ± 0.02 milliseconds. We plotted this improvement as a ratio of time to perform the task with the Zilany model over the time to perform the task with the RNN (Figure 34). The RNN was 335.4 ± 4.54 times faster with a 25-node network trained with 50,000 epochs. We chose to evaluate performance with a minimum 50,000 epochs, because the performance of the RNNs converged by 50,000 epochs across models on the synthetic data (Figure 31a). So, models of these size produced reasonable predictions of responses.

a PERFORMANCE ON NATURAL INPUTS (400 Hz)



b BEST PERFORMANCE



c TEST PERFORMANCE

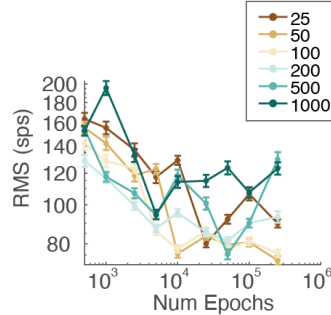


Figure 33. Performance on Natural Sounds

a) Example natural inputs with word, GRU size and number of training epochs written above. Target response (green dash) and inferred response (blue) of RNN. **b)** Best training performance on synthetic sounds (blue) of each model and test performance (red) on natural sounds for each network size. Best model training epochs written above. *, p < 0.1; ***, p < 0.01 with paired t-test. If there is no bar (as for the 50 node GRU), stars indicate t-test compared to all models. **c)** Test performance across models for predicting responses to natural inputs.

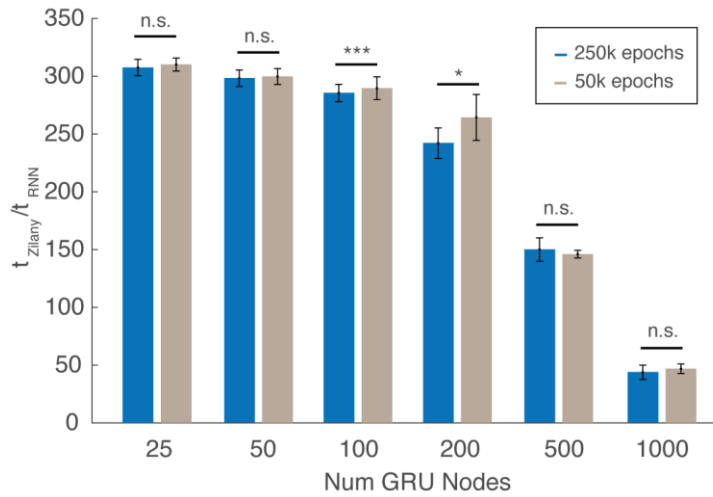


Figure 34. Run-time Evaluation of RNN

The ratio of run-time for calculating the response to a 0.5 second synthetic sound was measures across 10 runs with the Zilany model and the trained RNN one 1 CPU from a 2.4 GHz 8-Core Intel Core i9 Processor on a 2019 15-inch MacBook Pro.

The number of training epochs did not significantly influence run-time for most models (Figure 34 grey v. blue). For models with a GRU layer with less than 200 nodes, run-time was approximately the same. As the model approached 100 nodes, the relative gain in computation speed was significantly reduced (Figure 34). As performance was consistently low when the RNN has less than 200 nodes (Figure 33b), we do not anticipate requiring a network that is less than 200 times faster than the Zilany model. At these speeds, the model can perform a computation in approximately 1/100 of the length of the stimulus. If we assume this processing speed scales with sound size, because the GRU steps are an iterative process, we anticipate these computation speeds to be within the range of real-time.

The computation speed was evaluated on a 2019 MacBook Pro with an Intel Core i9 with 2.4GHz Processor (I909980HK). These processors are clocked at 478 GFLOPS.

If we implement the RNN using fundamental blocks rather than the ones provided by Python libraries, we can calculate the number of operations for each sound sample. This calculation yields the following number of operations for each sound sample: (One GRU node calculation = 48 operation) + (32 Linear operations, one for each output node: $32(2N)$, where N is the number of GRU nodes). For a 25 node RNN, we expect only $48 + 25 \times 2 \times 32 = 1648$ operations. If these operations are to be completed in 6.4ms, the processor must be able to execute $1648 / 0.0064 = 250,000$ operations per second. Assuming the typical average 4 cycles/operation, the clock speed of this processor must be $250K \times 4 = 1\text{MHz}$. If we assume there are 20

channels that must execute at the same time, one for each electrode, we will need a 20MHz microprocessor. While many highly powerful microcontrollers exist that function at 40 or 80 MHz, this is a comfortable execution speed for even a common modern microcontroller, such as MSP430 which executes at 24 MHz²¹⁴. At 142 $\mu\text{A}/\text{MHz}$, a typical cochlear implant battery with 126mAh would have a $126\text{mAh}/(20\text{ MHz}\cdot 142\text{ }\mu\text{A}/\text{MHz}) = 44\text{ hour battery life}$ ²¹⁵.

With these results, we feel this is a promising approach for creating a real-time front-end for a cochlear implant that can generate realistic target responses. To use this novel front-end to the benefit of patients, algorithms also require accurate transformation of a predicted firing pattern to a stimulation pattern that can evoke this firing pattern in actual neurons. These algorithms also need to be able to incorporate complexities of how stimulation parameters, such as pulse amplitude and rate affect induced firing rate; however, recent studies have begun to explore these exact issues¹²³. Ultimately, efficacy of these approaches will require clinical evaluation of speech and pitch perception using the novel CI processing algorithm.

4.4 Utilizing Electrical Stimulation for a Better Neural Implant Back-End

The front-end processing strategy that is described in Section 4.3 is the first stage in a neural implant algorithm for turning an input, such as sound, into stimulation from a set of implanted electrodes in target tissue (i.e., the cochlea). The back-end would require an optimization of the stimulation parameters from the electrodes closest to a target location. This involves two sets of computations. The first is finite-volume modeling of what level of stimulation reaches neurons in three-dimensional space, and the second is a conversion of target neural activation (firing rate, spike-timing, etc.) into stimulation parameters. Finite-volume modeling has been used to model electrical stimulation, the focus of this thesis, from external and internal electrodes across neural systems^{216,217}, including the cochlea²¹⁸. Additionally, similar strategies have been used for other paradigms, such as optical stimulation²¹⁹ or ultrasound²²⁰. Calculating the current that arrives at a target set of neurons would therefore be achievable with existing methods.

Where the front-end work described above interfaces with the other parts of the dissertation is through the use of the scientific findings from Chapters 2 and Chapters 3 to improve the back-end of this novel device. Chapter 2 uses biophysical modeling to create a theory for where galvanic stimulation interacts with neurons

and how current amplitude affects induced firing regularity and rate. Evidence from this work indicates an approximately linear change in firing rate with galvanic stimulation amplitude, such that, for example, a galvanic sinusoidal waveform produces a sinusoidal change in firing in local neurons (Figure 3). Additionally, frequency-dependent effects were uncovered and implicated as deriving from the hair cell (Figure 10). Equations were made that capture both of these effects and could be incorporated into a back-end for a galvanic stimulation device (Eq. 2-14). In Chapter 3, complexities of the non-monotonic relationship between pulse parameters (pulse rate and pulse amplitude) and induced firing rate were uncovered and transformed into equations, as well. These equations, that were derived from simulations of fixed rate pulsatile stimulation, were shown to hold for pulse rate and pulse amplitude modulation and frequencies of up to 10 Hz, and the equations were used to produce optimal pulse rate or pulse amplitude modulation parameters for neurons with different firing properties (Figure 24). The equations described in each of these sections could be adapted into a neural implant, following the front-end described in Section 4.2, to complex a neural prosthetic that transforms sound into target cochlear neuron firing rates over time into stimulation parameters from a neighboring electrode.

4.5 Discussion

The novel neural implant design discussed in this section is a contribution to an increasing amount of work on biomimetic algorithms for neural implants with the hope that inducing more naturalistic firing rates from neurons will produce increased restoration of function. Although a number of model-based approaches have been tried already across systems, no attempt to create a cochlear implant algorithm with a focus on fine-timing of individual cochlear neurons was found. Additionally, arguably the more significant advance of this work was on creating a strategy for making complex models of neural firing implementable in real-time. In this section, a front-end was created for a cochlear implant, because fine-timing of neural firing is known to be important to cochlear encoding and not captured by CIS and standard cochlear algorithms, so it was thought to be a use case in which significant improvements may be observed with an improved biomimetic algorithm. However, the same strategy could be applied for other neural system, if data was collected or model could be created and used to train an RNN-based front-end.

An approach like this has been recently attempted that combined a model-based and model-free approach: a biophysical model of the connections between tens of thousands of neurons in hypercolumns of cortex were used to model pools of neurons responding to electrical stimulation, and a recurrent neural network (RNN) was trained to learn the optimal stimulation pattern for creating a simulated neural pattern that produced simulated neural firing that resembled recorded monkey electrophysiology responses to reaches and touch⁶⁰. The approach from Kumaravelu requires a number of assumptions to relate neural recording and stimulation to simulated neural firing and recording, which may have impacted how accurately the trained RNN could produce optimal stimulation patterns. However, this technique offers another approach to training a front-end to learn the transformation of a population of neurons. Whether an approach of training on simulation of complex models of neural networks^{60,221} is advantageous over collecting data from individual patients to create patient-specific treatments is the better strategy^{197,222,223}, is yet to be determined.

The machine learning-based approach proposed in this section offers two additional suggestions for future work in biomimetic design. First, it offers an opportunity to create more efficiently algorithms both for choosing stimulation parameters and for performing the calculations for finite-volume modeling. Applying this concept to both parts of the neural implant algorithm may allow overall more complex algorithms to be run in real-time, which could be advantageous for continuing to add more complexity into neural implant algorithms. Second, we show that the algorithm which started by being trained on simple sine and step-inputs learned essential non-linearities in the transformation of sound into cochlear neuron firing that were also observed in response to natural sounds (Figure 33). This work suggests that a multi-stage training, starting from a simplified problem, may allow even a small network to learn more complex transformations of a system more quickly. Using this strategy, perhaps a multi-stage training could be used to first learn a simpler model-based approach and then have additional training sections to make the algorithm patient-specific.

Chapter 5 : From Single Neurons to Population-Level Effects

5.1 Introduction

The findings from Chapters 2 and 3 give insight on how pulsatile and galvanic stimulation affect individual neurons with a focus on effects in vestibular afferents. However, as pointed out in Section 3.5, the phenomena observed with electrical stimulation in vestibular afferents, down to the complex interactions with pulses are observed across neural systems. Additionally, *in vitro* studies of galvanic stimulation in pyramidal cells from hippocampus and the motor cortex further support that presynaptic and post-synaptic effects uncovered in Chapter 2 apply in other neuron types^{72,76,224}. This section discusses some of the broader implications of these single neuron effects in the context of what is known about network neuroscience.

5.1.1 Viewing the Brain as a Network of Neurons

Starting from the studies of Fritsch in the nineteenth century, there was an awareness of connectivity across brain regions that support behavior³¹. Electrical stimulation was an integral part of the first understanding of the structure and function of regions across the brain. However, the focus of the field turned to understanding the computations of the brain as sums of the functions of single neuron after the Hubel and Wiesel experiments famously uncovered the function of individual primary cortex neurons – for the first time linking individual neural functions and neural processing to behavior²²⁵. From there the field of neuroscience progressed, centered around primarily visual perception as a means of understanding other cognitive functions, such as decision making^{41,226}, with the perspective of there being functions localized to individual neurons. Famously, this ideology became so foundational that it was extended to the idea of “gnostic units,” individual neurons with very complex tuning properties, such as “grandmother cells” with such specific tuning that they responded only to the face of one’s grandmother²²⁷.

Tracing and histology studies had provided evidence of long-range structural connections between distant parts of the brain for some time, but an interest in viewing the brain as a network only started in the last several decades. There were several major factors that co-evolved during that time: the development of function magnetic resonance imaging (fMRI) and use diffusion tensor imaging (DTI) to trace connections across the human brain during behavior²²⁸; the increasing computational power for using connectomics to

map the brain or simulate thousands of neurons; developments in the fields of complex systems; and better technology for recording from hundreds of neurons at once²²⁸⁻²³⁰. These circumstances have led to new ways of interpreting neuronal signaling as an “ensemble” that works together to process information. In this framework, structural connectivity is not as important as neurons with functional connectivity, dynamics that are statistically dependent on one another, or effective connectivity, have causal influence in one direction of information flow in networks⁴². In these cases, neurons must be understood in the context of other neural activations to understand how the brain processes information.

5.1.2 The Role of Electrical Stimulation in Network Neuroscience

Electrical stimulation is also important to studies in network neuroscience. Functional connectivity has been studied with electrical stimulation by using current to activate neurons and observe how network activity or behavior changes. In invasive animal physiology studies, this takes the form of microstimulation studies, to understand activity within cortical columns and local neural connectivity (Figure 35a)^{41,226}. Most commonly in the epilepsy clinic, cortico-cortical evoked potential (CCEP) studies are used to understand interregional connectivity through stimulation at one or a bipolar pair of surface electrodes and recording the latency and magnitude of evoked potentials across the brain (Figure 35b). These studies attempt to address causality of connections from one region to another at the millisecond scale and how networks contribute to behavior^{42,44,154}. Finally, non-invasive, alternatives, such as transcranial magnetic stimulation have been introduced so that non-invasive electrical interventions can be made during EEG or fMRI recording. While these electric fields are less targeted, they increase the human population that can be studied with electrical stimulation technologies (Figure 35c)⁴². Thus, electrical stimulation continues to be an integral part of the study of human and animal network neuroscience research.

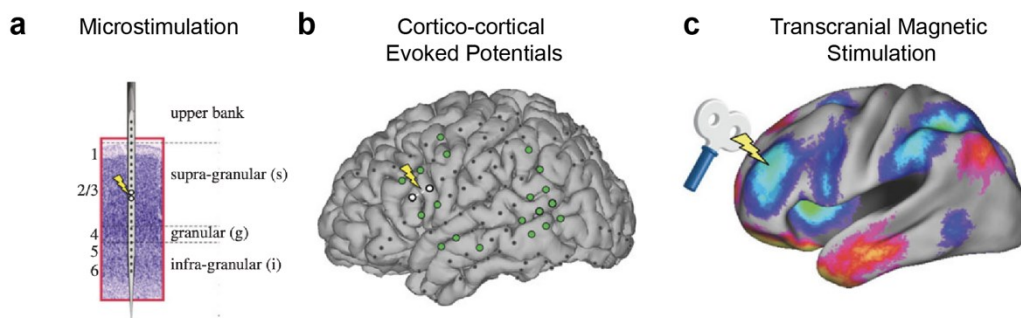


Figure 35. Uses of Electrical Stimulation to interact with Networks of Neurons

Electrical stimulation techniques for measuring connectivity include: **a)** microstimulation: stimulating and measuring neural activity within the same cortical column. **b)** cortico-cortical evoked potentials: current is injected between pairs of electrodes on the cortical surface and activity is measure on electrodes through the cortex. Example activation shown in green. **c)** Transcranial magnetic stimulation: generating magnetic fields outside the skull induces electrical currents within while neural activity can be monitored with scalp EEG or fMRI. Adapted from Keller *et al.* (2014).

Here these findings connect to the findings from Chapters 2 and 3. In Chapter 3, evidence is found that pulsatile stimulation does not affect neurons in proportion to pulse rate or pulse amplitude. Instead, pulses are predicted to have different effects on depending on the spontaneous activity of a neuron, pulse amplitude and pulse rate, so even at the same distance from the electrode, neurons may respond differently. Meanwhile, Chapter 2 studies an alternative form of electrical stimulation, galvanic stimulation, which is predicted to smooth increase excitation proportional to current amplitude. Whether consistent activation across a population is a helpful feature for neural networks and behavior likely depends on the neural network but has yet to be addressed. The work from each chapter leads to a prediction as to what the complexity of population firing may look like under each condition (Figure 36). Specifically, galvanic stimulation is predicted to excite all neurons with a decreased effect as distance from the electrode increases (Figure 36 right). Pulsatile stimulation is expected to have excitatory and inhibitory effects, depending on the existing activity of a neuron, and a decreased effect with distance from the electrode (Figure 36 left). How these effects will be amplified in connected networks of neurons with on-going computationally relevant firing will be important for understanding the relative advantages and weakness of each of these paradigms for improving neural interfaces.

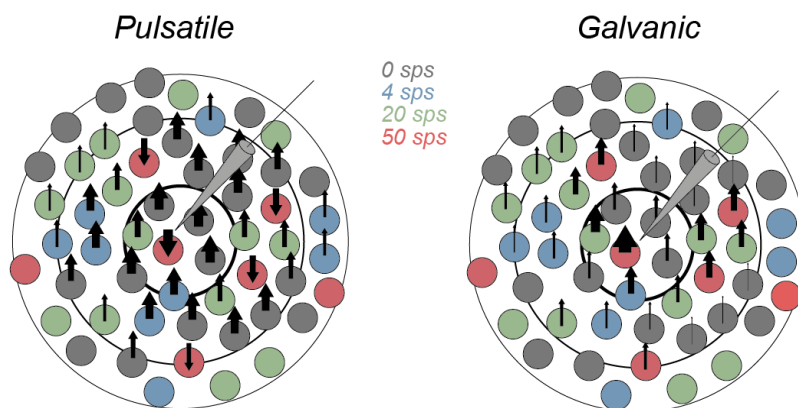


Figure 36. Predicted Effects of Electrical Stimulation on a Population of Neurons

Population of neurons with spontaneous firing rate or on-going firing rate of 0 sps (grey), 4 sps (blue), 20 sps (green), or 50 sps (red). Predicted magnitude and directionality of change in firing rate with pulsatile stimulation (left) and galvanic stimulation (right).

5.1.3 Studying Differences between Pulsatile and Electrical Stimulation in a Decision-Making Network

Biphasic pulsatile stimulation (PS) is the present standard for safe long-term electrical stimulation of the brain. As a result, single sub-millisecond pulses or sequences of pulses are commonly used to excite areas of the brain to understand connectivity and functionality of the brain, through brain mapping studies⁴²⁻⁴⁴. Additionally, clinically, pulses are used for stimulation in neural prosthetic treatments⁴, or pre-resection surgeries for drug-resistant epilepsy³. While pulses are clearly capable of inducing sensations (as relied on for sensory neural prosthetics)⁴ and have been experimentally used to bias decision making⁴¹ or trigger arm movements²³¹, there are numerous observed limitations to their ability to drive perception with the same spectrum of experience as natural sensation¹⁶¹ or to induce movements with the precision and control observed naturally²³².

Investigations of the source of these deficits seem to point to a lack of naturalistic firing induction throughout processing networks being interacted with electrically. In the case of the cochlear implants, deficits include a lack of ability to distinguish hearing in noise, which points to an inability to trigger top-down network effects²³³. Additionally, in the vestibular system, pulsatile stimulation has been found to drive neural firing with unnatural regularity (timing closely aligned to the timing of pulse delivery) across thousands of neurons in the population; this unnatural synchrony has been hypothesized to cause adaptation of higher order areas and reduced effectiveness of electrical stimulation at behavior over time²⁹. These effects have not been thoroughly investigated *in vivo* or *in silico*.

Galvanic stimulation (GS), extended periods of current delivery with no restriction to balance negative or positive charge, has re-emerged as an alternative form of stimulation, due to the recent development of novel, implantable galvanic stimulation devices^{23,24,234}. GS causes larger, more naturalistic vestibulo-ocular reflex (VOR) eye responses to vestibular stimulation²⁵, and it modulates single neuron firing rates up and down while preserving natural firing statistics and without producing unnatural synchrony^{26,28}. Detailed biophysical modeling predicts that GS has these effects because it modulates axonal sensitivity to incoming inputs²⁶. As a result, GS is predicted to cause any neuron within the field to experience the same directional modulation, so neurons will modulate firing rate up or down together, with modulation proportional to the distance from the electrode²⁶.

In contrast, recent investigations of the single neuron effects of pulsatile stimulation reveal that the source of limited recovery of function for neural prosthetics could be non-linear relationships between pulse parameters (pulse rate and pulse amplitude) and the induced firing rate of neurons^{123,166}. Pulses were shown to produce unnatural activations of voltage-gated channels that result in facilitation or inhibition of firing, depending on pulse parameters and the level of natural activity (i.e., EPSCs arriving at the axon). These findings suggest that neighboring neurons with on-going activity will not experience the same induced firing rate and that as distance from the electrode increases mixed effects will be observed throughout the population¹⁶⁶. Importantly, GS has been shown to produce more naturalistic behavioral responses than PS²⁵, suggesting that these differences in single neuron stimulation may lead to differences in network effects of the two paradigms.

The effects on single neurons described above lead to strong predictions about how populations of neurons and therefore network activity may be altered by PS versus GS. However, existing models have not included these recently uncovered effects of pulses on single neurons¹⁶⁶. Typically, the leaky-integrate-and-fire (LIF) model, a simplified channel model, has been used to create simulations with hundreds of neurons for computational efficiency. Thus, past models of electrical stimulation of a behavioral network have not accounted for the complexities of PS mentioned above^{68,235,236}. This study aims to answer the question of how pulses induce coherent behavior in networks of neurons, while producing complex population-level firing patterns that are different from the natural ones. Additionally, this study investigates whether GS has different network-level firing behaviors compared to natural and pulsatile. We also observe how these differences in firing patterns in response to each stimulus type may lead to differences in experimentally testable behavioral responses.

To study these different response patterns, we introduced both forms of stimulation *in silico* to a winner-take-all (WTA) decision-making network²³⁶ and compared the effects on individual neuron spiking, mean firing rates of motion-selective populations, and network-level decisions (Figure 1). The experimental paradigm was based on a classic decision making experiment in which pulsatile microstimulation of a population of neurons associated with one choice was shown to shift the accuracy versus coherence curve^{41,237}. To ensure equivalence in stimulation amplitude, PS and GS were parameterized to change the average firing rate of the biased population (P1) by 3 spikes per second (spk/s) across ten simulated “brains”

with different sensitivities to electrical stimulation. Despite the apparent equivalence in electrical stimulation inputs, we observed that PS directly affected more neurons than GS and induced highly regular synchronous firing that quickly propagated through the network. At the population level, pulses maintained unnaturally elevated firing rates in the stimulated population, even when the stimulated population lost the trial. This resulted in PS inducing a greater bias in decision making than GS for the same population-level firing rate change in this firing-rate-dependent network. Together, these effects show several ways in which both paradigms interact with networks of neurons that should cause differences at the behavioral and neural computation levels.

5.2 Materials and Methods

5.2.1 Perceptual Decision-making Task

A Random-Dot-Motion task was simulated at coherence levels from fully leftward (+100%) to fully rightward (-100%) coherence (Figure 37a circles). 36 trials were run at each coherence level under three conditions: pulsatile, galvanic, and control. Throughout the 4-second trial, all modeled neurons received 2400 Hz background Poisson inputs that triggered AMPA EPSCs. This caused neurons in the network to fire spontaneously at 2-3 spk/s (Figure 37b). At $t = 1$ s, neurons in populations P1 (blue) and P2 (red) received task-related input proportional to coherence (c):

$$I_{\text{task}} = 40c + 40 \quad (5-1)$$

where if motion is in the opposite direction c is negative²³⁶ (Figure 37 a-b, magenta). To bias the network, all neurons in P1 also received electrical stimulation (black) concurrent with task input (Figure 37). At $t = 3$ s, task-related inputs and stimulation ceased, and P1 or P2 kept a high firing rate if a decision was made favoring that population. Decision making experiments show a sigmoidal relationship between coherence and accuracy. To capture this relationship, coherences were sampled logarithmically (in 5 steps) around the empirically determined center of the sigmoid for each stimulation condition. For control stimulation, this was 0%^{236,237}. For pulsatile and galvanic stimulation, the center coherences were estimated as -72.4% and -36.2% respectively.

5.2.2 Biophysical Attractor Model

The biophysical model used was based on a well-established decision-making network described in ²³⁶. The model simulates a two alternative forced choice task with P1 (blue) and P2 (red) encoding task input (strength of moving dot leftward versus rightward motion). A non-selective (NS) population (yellow) and inhibitory interneuron (Int) population (purple) are also included for a winner-take-all network construction (Figure 37a). The network model consisted of N neurons (80% pyramidal neurons and 20% inhibitory interneurons), connected with weights $w_s = 1.7$, $w_m = 1$, $w_w = 0.8765$ for strong, medium, and weak connections respectively (Figure 37 strength shown with line thickness). Importantly, all neurons in this model were connected with one of these three weights. The model simulated neurons with leaky-integrate-and-fire (LIF) dynamics and synaptic currents from AMPA, NMDA, and GABA receptors. For our simulations, $N = 1000$ neurons and a time step of $dt = 0.05\text{ms}$ were used. The model was modified to include more accurate effects of pulsatile stimulation.

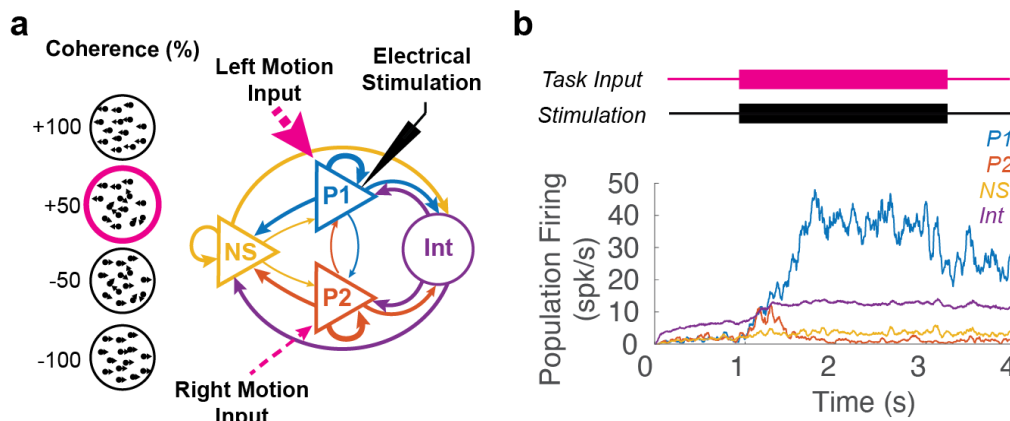


Figure 37. Decision Making Experiment Design and Simulated Implementation

a) Model consists of two subpopulations (P1 and P2) responsive to leftward and rightward motion, non-selective pyramidal neurons (NS) and inhibitory interneurons (Int). Neurons are connected with strong, medium, and weak connections (thickness proportional to strength). During a trial, all neurons receive background input. From 1-3s, P1 receives input proportional to coherence of left versus rightward motion. Stronger input to P1 shown for +50% leftward coherence in magenta. P1 also receives electrical stimulation from 1-3s (black) to bias the network. **b)** Mean population firing rates of P1 (blue), P2 (red), NS (yellow) and Int (purple) in a representative pulsatile stimulation trial. Stimulation and task input timing shown above.

5.2.3 Realistic Intracortical Microstimulation

Three electrical stimulation conditions were simulated in the model: pulsatile, galvanic, and control.

Pulsatile stimulation parameters were selected based on ²³⁷: $10\ \mu\text{A}$, $300\ \mu\text{s}/\text{phase}$, $200\ \text{pulse/s}$. Because the decision network relied on population firing rate, galvanic stimulation amplitude ($28\ \text{nA}$) was chosen such that the average firing rate increase in P1 matched that of pulsatile stimulation for disconnected neurons (~ 3

spk/s, Figure 39c). In the control condition, no electrical stimulation was delivered. In all three conditions, the background and task-related inputs and neuron-electrode distances were the same, allowing a control counterfactual comparison.

Current was assumed to spread through a uniform resistivity medium from the electrode to the neuron. This resulted in an internal current inversely dependent on the square of the distance:

$$I_{internal} = -\frac{I_{electrode} \times A_{axon}}{4\pi r^2} \quad (5-2)$$

where A_{axon} is the surface area of a typical axon segment ($100 \mu m^2$). Our recent simulation work¹⁶⁶ showed that when biphasic pulsatile stimulation (PS) is introduced to neurons exhibiting spontaneous firing, a variety of interactions can occur that deviate from the classical assumption that every pulse produces an action potential (AP). For example, pulses can block subsequent spontaneous APs, spontaneous APs can block subsequent pulses, and pulses can block subsequent pulses. These refractory effects are amplitude-dependent, with higher-amplitude pulses causing longer blocking periods. Here, we adapted these effects¹⁶⁶ to the neural dynamics of LIF neurons in our decision-making network²³⁶. Using the blocking times from Steinhardt et al.¹⁶⁶ (0-132 ms) scaled to the range of pulse amplitudes relevant for LIF dynamics (0-278 nA), we reproduced the non-monotonic, amplitude dependent relationship between pulse rate and firing rate.

5.2.4 Simulating Distinct Virtual Subjects

In physical pulsatile microstimulation experiments, monkeys show high variability in their responsiveness to the pulse input^{41,237,238}, likely due to variability in the placement of the stimulation electrode relative to target neurons. To simulate this effect, for each subject, neurons in P1 were placed randomly from $10 \mu m$ to 2 mm away from the stimulation electrode based on geometry of the putative decision-making microcircuit^{239,240}. This gave each virtual subject a slightly different sensitivity to electrical stimulation inputs.

5.2.5 Decision Data Analyses

Instantaneous neuron firing rates were calculated in 5 ms bins, followed by a 50 ms moving average. Population firing rates were then taken as the average instantaneous firing rate of all the neurons in a given subpopulation. Decisions were recorded at the end of the 4-second trial, if the final average firing rate of

one of the two neural subpopulations (P1 or P2) exceeded 15 spk/s, while the other did not. In such cases, the subpopulation whose firing rate exceeded 15 spk/s was deemed the “winner” of the trial. This threshold was chosen based on ²³⁶. Decision data were then analyzed using logistic regression as in ²³⁷. The time at which the winning subpopulation exceeded 15 spk/s after the start of task stimulation ($t = 1\text{ s}$) was considered the decision time.

Comparisons of decision-making metrics between the three stimulation conditions were assessed for significance by 1-way ANOVA. Activation of neurons was determined by whether stimulation caused a change in firing rate three standard deviations from control levels. Phase-locking of neurons to the pulse stimuli was assessed by measuring the percentage of APs occurring during pulse presentations for each neuron. If the percentage differed from control levels by three standard deviations or more, that neuron was determined to be significantly phase-locked to the pulses. Regularity of spiking was assessed using coefficient of variation (CV). Comparisons of changes in end-of-task and start-of-task firing rates between galvanic and pulsatile stimulation were assessed for significance by unpaired t-tests. Distributions of single-neuron firing rates were also investigated, and comparisons were assessed for significance by Kolmogorov-Smirnov tests.

5.3 Results

The effects of pulsatile and galvanic electrical stimulation were assessed on networks of neurons in this study by exposing a well-established attractor model²³⁶ of decision making to both paradigms. To ensure a fair comparison between the two stimulation modalities, we selected stimulation amplitudes such that both produced the same average increase in firing rates in the stimulated population ($+2.78 \pm 0.18\text{ spk/s}$ for galvanic, $+2.83 \pm 0.04\text{ spk/s}$ for pulsatile). Since network-level decisions in the model only depend on population-averaged firing rates, we expected this to equalize the effects of galvanic and pulsatile stimulation. Despite this apparent equivalence, differences in behavioral, neuron-level, and population-level effects were observed.

5.3.1 Behavioral Differences

The behavioral effects of PS and GS were measured by the change in the percentage of trials the stimulated population (P1) won and the decision time. Although both paradigms changed the firing rate of

disconnected neurons by only ~3 spk/s, they significantly biased the decision making of the network toward choosing P1 ($p < 0.00001$ by 1-way ANOVA). PS caused a significantly larger shift in the coherence curve ($p < 0.00001$ by 1-way ANOVA), shifting the curve by 66.44% (red), while GS shifted it by 38.31% (Figure 38a green).

Both stimulation paradigms also significantly reduced decision times ($p < 0.00001$ by 1-way ANOVA) and shifted the coherence curve left so that peak decision time was at a more negative coherence (Figure 38b, $p < 0.00001$ by 1-way ANOVA). PS reduced overall decision-time by 0.3528 s and shifted peak decision time by 75.92% (Figure 38b red), while GS reduced overall decision times by 0.2452 s and shifted peak decision time by 39.74% (Figure 38b green).

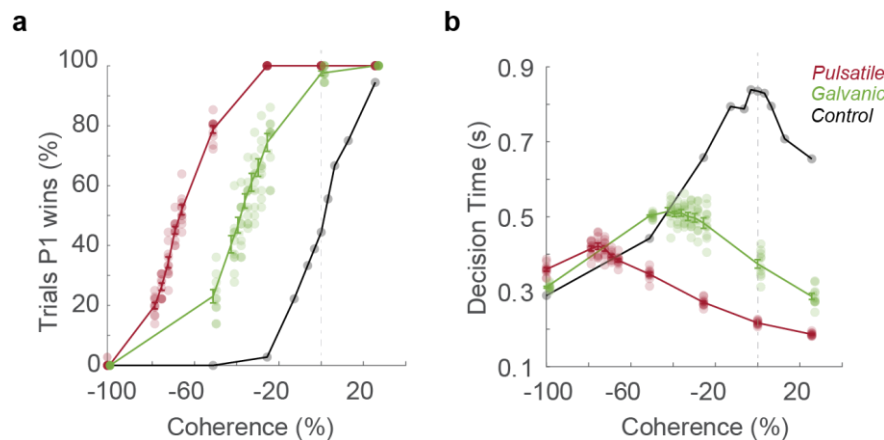


Figure 38. Effects of Pulsatile and Galvanic Stimulation on Decision Making and Decision Time

The decision metrics across simulated brains at the same coherence levels for pulsatile (red), galvanic (green) and control (black) conditions. **a)** The percentage of trials in which the stimulated population (P1) wins the decision-making process. **b)** The time it takes for the winning population to clear the decision threshold (15 spk/s). Bold error bars depict mean and standard error at each coherence level.

The changes in decision making elicited by PS in our model are consistent with those observed in behavioral studies²³⁷: coherence vs. accuracy curves are shifted such that stronger task-related input is required to make decisions against the stimulated population (P1); decision times decreased when task-related input and stimulation both favor P1 (e.g. at +25.6% coherence) but increased when task-related input and stimulation battle over control of the network (e.g. at -100% coherence) (Figure 38). GS showed these same interactions. However, for the same change in firing rate, the magnitude of shift and reduction in decision time were less. These behavioral differences suggested differences in how both forms of stimulation interact with networks of neurons.

5.3.2 Differences in Spatial Spread of Neuronal Activation during Pulsatile and Galvanic Stimulation

We observed a variety of differences between the effect of PS and GS on the distributions of neural firing rates, the regularity and synchrony of spike timing, and their interactions with networks of connected neurons.

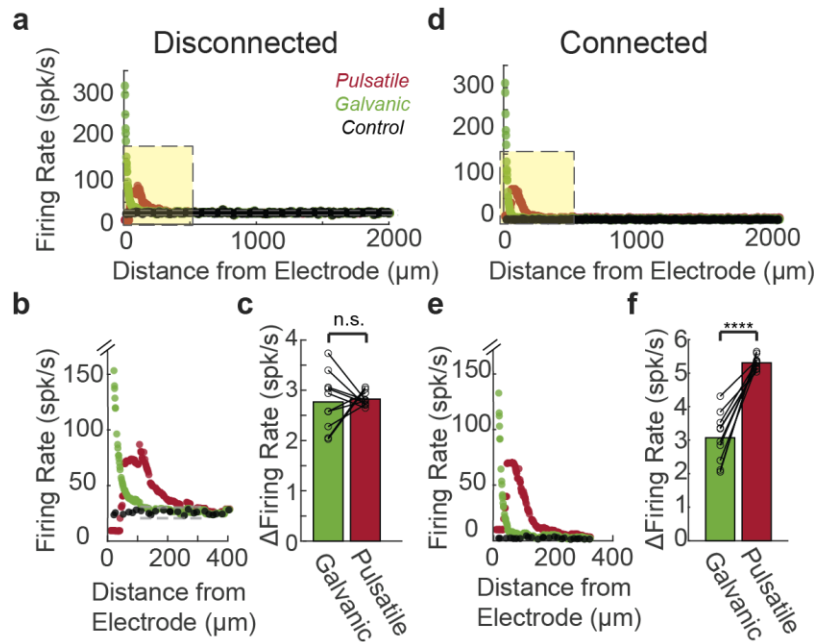


Figure 39. Effects of Pulsatile and Galvanic Stimulation in Connected Network

Effects of pulsatile (red), galvanic (green) and control (black) stimulation on individual neural firing rates across subjects with disconnected (a-c) and connected (d-f) neurons. Each neuron's start-of-task firing rate ($t=1.0-1.1\text{s}$) is shown as a function of its distance to the stimulation electrode (a: full P1, b: closest 20% of P1). Bar graphs (c and f) depict each brain's population-averaged change in firing rate relative to control. For all trials, task-related input was equal for P1 and P2 (coherence = 0%). The effect of pulses on change in start-of-task firing rate was significantly stronger than galvanic ($p<0.00001$, ****).

As expected from single neuron studies, in the disconnected network, in which the average population firing rate was equalized for GS and PS, the distributions of firing rates are significantly different ($p=0.0363$ by Kolmogorov-Smirnov test, Figure 39a). Due to the refractory effects of high-amplitude pulses, the neurons closest to the pulsatile stimulation electrode ($<40\ \mu\text{m}$) are blocked, producing firing rates below baseline. The neurons farther away ($40-250\ \mu\text{m}$) get excited, but because of pulse-pulse blocking effects, they never achieve firing rates over $100\ \text{spk/s}$ (Figure 39a-b red). In contrast, the neurons closest to the galvanic stimulation electrode ($<100\ \mu\text{m}$) are strongly excited with firing rates up to $300\ \text{spk/s}$, and none are blocked (Figure 39b green). As a result, for the same change in population firing rate in the disconnected network (Figure 39c), pulses activated more neurons (14.00%) than galvanic stimulation (5.83%, Figure 39a-b

dashed line). Only 40.5% of the neurons affected by pulses were affected by GS. In this network, where average firing rate is important and all neurons are connected, this was not a detriment, but in a sparser network, this difference could also cause significant differences in network effects.

When the neurons were connected, they became subject to feedback inhibition, which decreased spontaneous neural firing rates from ~25 spk/s to 2-3 spk/s (Figure 39d-e black). Neurons directly affected by electrical stimulation, however, are largely resistant to feedback inhibition. The neurons closest to the GS electrode still achieve firing rates up to 300 spk/s (Figure 39d green) and the neurons a moderate distance away from the PS electrode (55-85 μ m) still fire at ~70 spk/s (Figure 39d-e red). Since PS directly affects more neurons than GS, its effects are more resistant to the balancing effect of feedback inhibition. As a result, not only do pulses and GS have significantly different distributions of activation ($p < 0.00001$ by Kolmogorov-Smirnov test, Figure 39d-e), but also they induce significantly different increases of average firing rate in connected neurons ($p < 0.00001$ by unpaired t-test). Compared to control conditions in the connected network, pulses increased firing rates by 5.31 ± 0.06 spk/s. Meanwhile, GS only increased firing rates by 3.07 ± 0.24 spk/s (Figure 39f). The relatively larger effect of pulses in the connected network is likely one cause of the downstream differences in behavioral outcomes.

5.3.3 Differences in Spike-timing

Single neuron studies also predict differences in spike timing in response to PS and GS^{26,166}. PS transiently depolarizes neuron membrane potentials at a fixed interval, and, if the membrane potential is sufficiently depolarized, they induce action potentials (APs). Even if they do not elicit APs, pulses generate brief amplitude-dependent refractory periods, which prevent natural EPSCs from triggering APs immediately after pulses. As a result, neurons directly affected by PS have highly regular spike trains with APs phase-locked to the timing of the pulse. This phenomenon is visible in raster plots of individual spike trains (Figure 40a red). On the other hand, GS provides a constant current input that effectively sets the resting membrane potential closer to the AP threshold, so neurons fire for more of the incoming EPSCs. This essentially increases the likelihood of firing with timing dependent on natural inputs¹⁶⁶. We also see these effects in the raster, with corresponding GS neurons firing in a desynchronized, irregular fashion, similar to control (Figure 40a green).

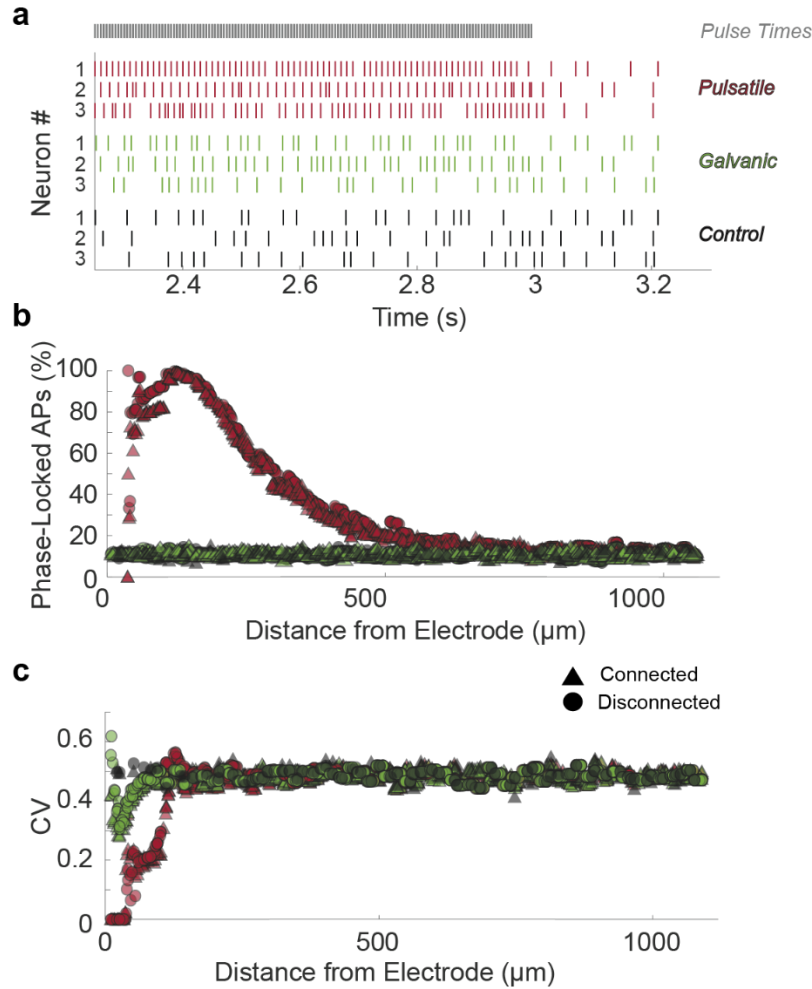


Figure 40. Differences in Induced Spike Timing between Pulsatile and Galvanic Stimulation

a) Raster plots for the three neurons with highest firing rates in the pulsatile condition, along with the times of each pulse (grey). Corresponding neurons receiving identical natural inputs are plotted for galvanic and control conditions. (Pulsatile, red; Galvanic, green; and Control, black). **b)** The percent of each neuron's action potentials that occur during a pulse presentation for the end-of-task ($t=2.5-3\text{s}$) period is shown as a function of its distance to the stimulation electrode for connected (triangles) and disconnected (circles) cases. **c)** Each neuron's end-of-task coefficient of variation (CV) is shown as a function of its distance to the stimulation electrode for connected (triangles) and disconnected (circles) cases. For all trials, task-related input was equal for P1 and P2 (coherence = 0%). For connected simulations, only trials in which P1 won were included.

Phase-locking and regularity of firing were quantified across trials by analyzing responses at the end of the stimulation window when effects would likely be maximized (2.5-3 s). Once the neurons were connected the effects of pulsatile stimulation were reassessed. Phase-locking was compared to levels in galvanic and control conditions and showed that 26.8% of neurons up to 671 μm away from the electrode were significantly phase-locked in P1 to pulses. The maximum phase-locking was found to be 100%. When the network was connected, there was no significant difference in phase-locking compared to when it was disconnected ($p=0.1623$ by unpaired t-test, Figure 40b). This suggests that the unnatural synchrony

produced by pulses can overcome the network connections and the naturally irregular timing that would typically occur (Figure 40a black). Whether artificial regularity was larger with pulses than control or galvanic conditions was assessed using coefficient of variation (CV) in the same window. Neurons receiving PS were significantly more regular than control or galvanic stimulation ($p < 0.00001$ by 1-way ANOVA), but galvanic stimulation also induced more regular firing than control ($p < 0.00001$ by 1-way ANOVA, Figure 40c). The unnatural phase-locking which appears to override the natural spike timing of the network likely contributes to the resistance of P1 to feedback inhibition and excitation under pulsatile stimulation.

5.3.4 Population-level Differences

In addition to differences in spatial spread of activation and spike timing, PS and GS also had different effects at the population level, depending on the decision outcome of the network. When the population receiving the stimulation (P1) won the trial, the population firing rate of P1 was greater in response to GS ($+4.21 \pm 0.27$ spk/s) than PS ($+2.18 \pm 0.08$ spk/s) relative to control ($p < 0.00001$ by unpaired t-test, Figure 41a-c). However, when the population not receiving stimulation (P2) won the trial, the average firing rate of P1 remained more elevated in the pulsatile condition ($+2.09 \pm 0.06$ spk/s) than galvanic ($+0.93 \pm 0.04$ spk/s) compared to control ($p < 0.00001$ by unpaired t-test, Figure 41d-f). This suggests that neurons undergoing PS are less sensitive to network-level effects (feedback inhibition and recurrent excitation) than neurons undergoing GS. For PS, neurons in P1 were less excited when P1 wins and less suppressed when P1 loses. As discussed earlier, this effect may derive from two sources. One is that PS directly affects more neurons, and, in consequence, PS has a greater effect on decision making than GS. The other may be that during pulse delivery, the refractory effects may be blocking incoming input from other neurons.

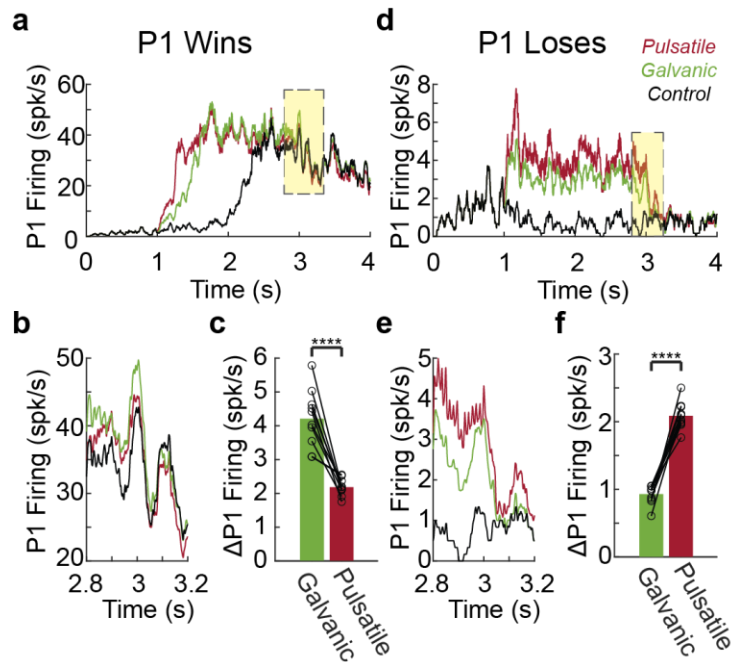


Figure 41. Effects of Pulsatile and Galvanic Stimulation on P1 Firing Rate during Wins and Losses

Trials in which (a-c) P1 wins (coherence=+25.6%) and (d-f) P1 losses (coherence=-100%). Average P1 firing rates for all 3 stimulation conditions (Pulsatile, red; Galvanic, green; and Control, black) are shown for the full trial (a and d) and during the end of task period (b and e, t=2.9-3s highlighted yellow in a and d). Bar graphs (c and f) depict each brain's population-averaged change in end-of-task firing rate relative to control in all trials in which P1 wins (c) and P1 losses (f). Significance of effect ($p < 0.00001$) is indicated by ****.

5.4 Discussion

The central finding of this work is that when the non-linear stimulation effects of biphasic pulses are applied to a decision-making network, they affect the network more dramatically than GS, even when both are parameterized to elicit the same effects on average neural firing rates. This difference occurs because pulses affect more neurons than GS and the pulse effect is synchronized across the network. As a result, neurons experiencing pulse inputs are less sensitive to network effects, such as feedback inhibition. Feedback inhibition is a crucial component of the decision-making network, and disruptions to its operation have been shown to impair the decision-making process²⁴¹. Similarly, synchrony effects are important in a variety of cognitive processes²⁴² and disease states such as epilepsy²⁴³. Therefore, although electrical pulses are clearly an effective way to alter decision-making circuits and, more broadly, to interface with the nervous system at large, they may struggle to replicate nuanced interactions that depend on precise spike timing or on-going network activity. GS may preserve neural spike timing and respect feedback inhibition, but it has its own set of challenges, including safe implementation in implanted devices. Additionally, it remains an open question whether preserving the feature of unsynchronized spike timing across neurons

while the population of neurons simultaneous increase their firing rate is beneficial. This study shows this effect to occur even in the presence of network connectivity, but it remains open whether this simultaneous modulation is also pathological, particularly in cortical networks where large network activity causes pathologies such as epilepsy²⁴³.

5.4.1 Future Directions

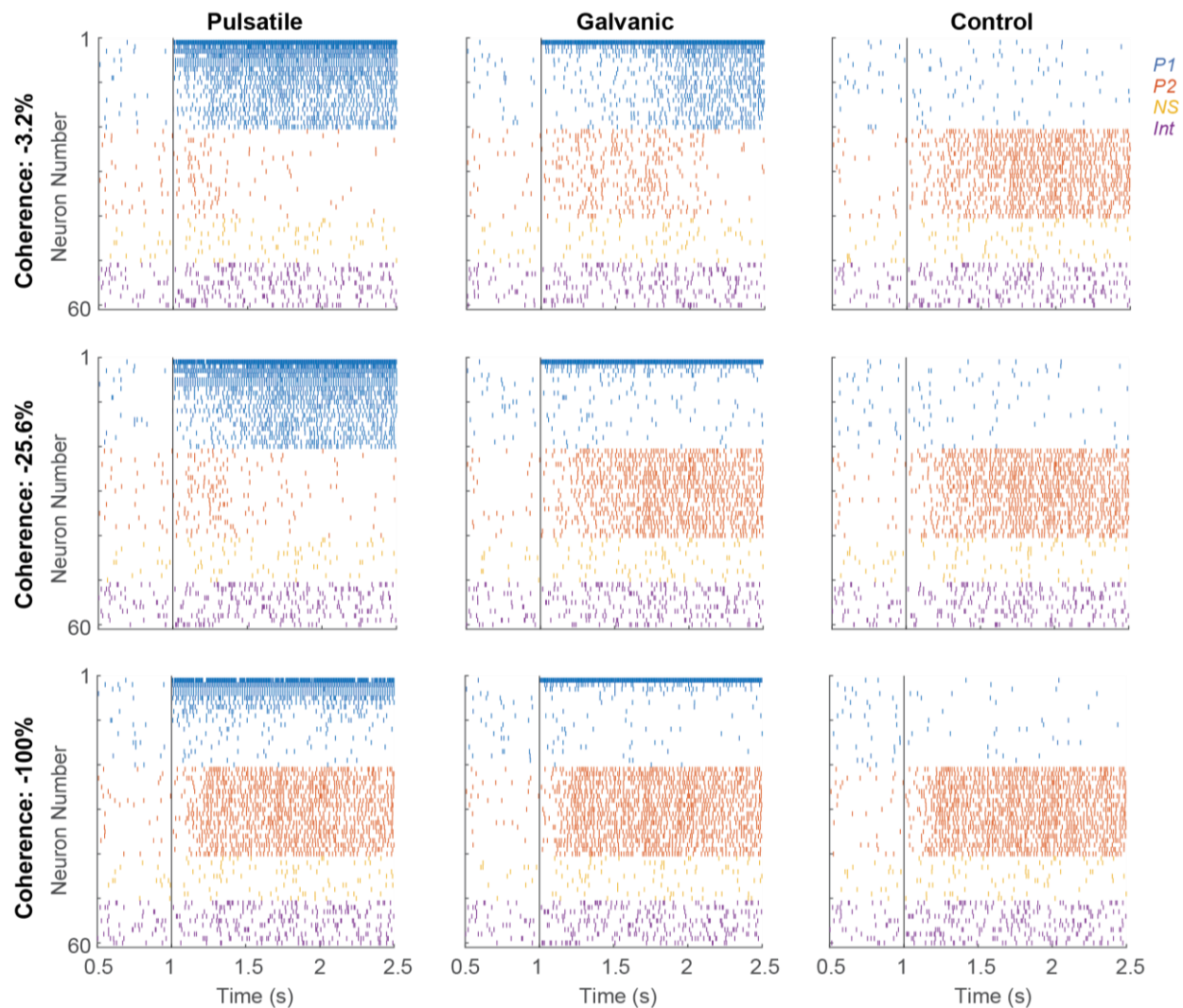


Figure 42. Raster Plots across Different Stimulus Coherences and Stimulation Paradigms

Response of maximally responsive neurons in each population P1 (blue), P2 (red), NS (yellow), and Int (purple) under different coherence intensities and stimulation paradigms (pulsatile, galvanic, and control) when stimulation biases towards P1 for a decision P2 should win. (Row 1) Case where pulsatile and galvanic stimulation cause P1 to win ($c = -3.2\%$). (Row 2) Case where only pulsatile stimulation causes P1 to win ($c = -25.6\%$). (Row 3) Case where neither pulsatile nor galvanic stimulation causes P1 to win ($c = -100\%$).

The work described above can be expanded on in a number of ways to assess the differences between pulsatile and galvanic stimulation on networks. The most important question to address next will be to expand

this work beyond the analysis of P1 alone and assess how other parts of the network are affected by PS and GS.

Figure 42 shows that PS and GS are both capable of biasing the network of neurons as a whole when stimulus inputs should cause P2 to win (row 1-2). However, PS clearly induces biases more quickly than GS for equivalent stimulus inputs (row 1) and can overtake the network in situations where GS cannot (row 2). Analyses above show that P1 which is stimulated directly with PS shows an unnatural synchrony that overrides network connections within P1; this effect is also present in P1 when P2 wins the takes (row 3) Figure 42. Future work should address whether PS also produces unnatural spike timing through the network, or the local change is sufficient to significantly bias behavior.

Additionally, in this work, we only considered one type of equivalence between pulsatile and galvanic stimulation: equivalent average firing rate increase. However, many other types of equivalence exist, such as equivalent proportion of neurons affected. Other types of equivalence need to be explored, in order to better way the pros and cons of each paradigm alone or potentially together.

Another drive for future work would be to use more accurate models of the neural circuit and individual neurons. To be able to have a network with thousands of neurons, a LIF neuron model was selected and modified to account for other effects of PS. This introduced assumptions that may have allowed for unrealistic conditions. For example, in this study, the effect of PS on decision making in the model is much larger than the effect *in vivo* with the same stimulation parameters²³⁷, but similar studies with lower pulse amplitude (5 μ A) can achieve an equivalent effect on decision making^{87,166,238}. Also due to a lack of blocking effects, GS can drive firign rates very high (>200 spk/s) for a few neurons very close to the electrode. Instead, using a model with realistic channel dynamics, like the one used to uncover these effects of pulsatile stimulation, although computationally intensive, might be accurate for revealing more of the differences in spike timing and network-level effects. At the network level, this model did not account for plasticity, which is known to be influenced by GS⁷⁵, and only the average population firing rate between two regions was used to determine the decision made. A more accurate modeling of network connectivity, one that includes spike timing, would likely be crucial to understanding the intricacies of both paradigms and how they interact with neural computation.

Chapter 6 : Conclusions

The work represented in this thesis provides insights into the ability to use electrical stimulation in novel ways in order to improve interactions between neural implants in healthy and impaired systems. However, there are a number of limitations that stand between the science described above and real-world changes in current neural implant systems.

6.1 Limitations of Biophysical Modeling

The conclusions drawn about electrical stimulation are generalized towards uses of electrical stimulation across neural systems. However, the work in this thesis is based on detailed biophysical modeling of interactions of electrical stimulation with the vestibular hair cell, calyx, and afferent. The model is brought toward being more realistic by incorporating detailed models of the ion channels specific to the neuron and including nonquantal effects that are known to be important to vestibular processing. However, a number of details of vestibular afferent processing had not been previously modeled, and the origins of effects, such as the non-quantal effect, are still undergoing investigation. As such, detailed modeling of these effects and how they may be triggered, particularly by galvanic stimulation, could not be accurately modeled in this work. This work assumes the EPSC input to the afferent could be considered to derive from a single underlying distribution, which likely ignores complexities in EPSCs inputs that occur in the vestibular system, due to inputs from multiple hair cells. Additionally, efferent activity, which is likely highly important for effects such as modulating vesicle release, non-quantal effects, and afferent sensitivity, was not modeled in this study. Understanding how smaller fibers, such as efferents could be activated by galvanic stimulation is important to expanding on this work.

There is always a tradeoff between accuracy of modeling and runtime when simulating neurons. For example, there is a trade-off between modeling a neuron and electrode as a point source in space and creating a detailed model of the membrane at one location versus simulating activation of channels along a full axon, cell body, and dendrites. Neuron-specific dendritic arborizations or orientations and differences in the external medium have been shown to change how current affects firing. Thus, some of these assumptions likely build on top of the issues of electrical stimulation discussed in this paper, further complicating the story of how electrical stimulation could be optimized for better neuron control. At the

network modeling level, as simulated in 0, there are further abstractions to be capable of simulating thousands of neurons at once. Particularly, using the leaky integrate-and-fire model of neurons does not take into account of complex channel dynamics, so the pulsatile rules from Chapter 3 were incorporating, which assumes identical effects to those observed in vestibular afferents. More likely, different neurons have different channel dynamic loops and time constants, but this work provides some insights into how networks of neurons would behave differently with the types of non-linearities produced by pulses versus galvanic stimulation. More accurate characterization of these effects as well as accounting for known plasticity effects of galvanic stimulation⁷⁶ would be essential to further understanding network-level effects of both paradigms. Additionally, detailed modeling of network using spike-timing as well as firing rate as metrics for behavior and networks with more complex constructions would bring further insights on to how these forms of electrical stimulation differentially modify behavior and neural computation.

6.2 Future Directions

This work advanced our understanding of galvanic and pulsatile stimulation through theoretical and computational work alone. Although experimental data was heavily relied upon to draw conclusions about the effects of pulsatile and galvanic stimulation, experimental work is required to test whether the single neuron or network effects discussed above hold true under experimental conditions.

The major step that needs to be taken before expanding on this work is to undergo experiments to test experimental predictions of Chapters 2 and 3. For Chapter 2, these effects involve isolating hair cell and afferent activity through channel blockers and assessing the effects of galvanic stimulation on the hair cell channels and vesicle release. Afferent-only recordings under galvanic stimulation and with hair cell input being suppressed would also be important for axon-specific predictions. For predictions from Chapter 3 to be tested, single neuron electrophysiology experiments should be conducted in which individual vestibular afferents with different firing regularities and firing ranges are exposed to pulses of different amplitudes and pulse rates while individual firing rates are recorded. This could determine whether the non-linearities modeled in the final equations from Chapter 3 are observed across vestibular afferents. For Chapter 4, using the front-end and back-end transformation algorithm together within a cochlear implant and performing clinical trials in which improvements in pitch perception are studied would be an important behavioral

measure of whether our predictions about pulses and about how naturalistic spike timing relates to behavior hold. An intermediate step could also be to attempt to deliver pulses with the corrections of pulsatile stimulation in patterns suggested by the front-end from Chapter 4 and assessing whether they could be induced accurately in single neurons. Finally, for Chapter 5, behavioral testing during local pulsatile and galvanic stimulation could be performed in an awake behaving animal, such as a rat, during a two-alternative forced choice task. The behavioral predictions could be tested by assessing change in decision making under the influence of electrical bias. Individual neurons could be recorded with a tetrode to provide an estimate location as well as record firing rate, and local population firing could be analyzed to test predictions about how populations of neurons respond to both forms of electrical stimulation.

Additionally, a number of modeling steps could be made toward expanding this work. One step could be to further extrapolate the biophysical single neuron model so that it captures even more of the vestibular afferent physiology and geometry. Another could be to work toward simulations of population of vestibular afferents under electrical stimulation and to assess whether effects observed at the vestibular afferent population level explain central responses recorded to electrical stimulation and or behavioral readouts, such as vestibular ocular reflexes. As discussed above, a number of steps could be taken to improve modeling of networks of neurons in more detail. Also, the machine learning algorithm could be trained to include neurons with multiple tuning frequencies more efficiently into the cochlear implant algorithm described in Chapter 4.

6.3 Implications and Impact

The work presented in this thesis indicates that there are a number of ways that we can improve our electrical stimulation paradigms to better control individual neurons and coherently change populations of neurons. The approach was to start from a detailed biophysical understanding of how electrical stimulation interacts with various features of single neurons and build from this understanding toward theories for how electricity should interact with populations and networks, ultimately shaping behavior. To do this a computational modeling approach was used to simulate existing experimental results using both paradigms. Then, through perturbation studies, new theories were formed for why electrical stimulation has a variety of previously unexplained effects on neuronal firing. These simulations led to several new theories for how

pulses versus galvanic current interact with neurons and therefore should have different effects on populations of neurons and behavior. Within this manuscript, algorithms are also developed to take advantage of this new understanding of electrical stimulation and correct neural prosthetic algorithms so that they may be able to better produce intended neural firing patterns and match a desired firing pattern in real-time. These improvements all open the door to more effective prosthetic treatments.

The implications of the work with pulsatile stimulation are that there are a number of challenges to driving neural firing with pulsatile stimulation and correctly predicting the induced firing of neurons. This work shows that pulse amplitude and pulse rate have non-linear effects on induced firing, depending on the channel dynamics of a neurons. The dependence on channel dynamics adds additional diversity to the neuronal responses, due to natural variance in channel densities within cells. Thus, this work indicates that populations of neurons that are activated by pulsatile stimulation should have a large diversity of local responses, as observed before¹⁶³. But also, this work indicates that these non-linearities are predictable at the level of single neurons and thus could be predictable at larger scales with more understanding of the spatial distribution of neurons with different firing properties. These findings also have important implications for existing electrical stimulation studies with pulsatile stimulation. At high current amplitude (which are often used in stimulation studies and neural implants), these results show that previously highly activity neurons will be suppressed while previously non-firing neurons will be highly activated by pulses. This implies that previously active parts of a population that may be important to neural network calculations may be suppressed while inactive or uninvolved neurons could be activated. This brings into question whether, when pulses are used for brain mapping of connectivity and behavior, we are truly understanding natural function or something about passing connections in the area.

Additionally, this work indicates that local populations experience a combination of excitation and inhibition, even though we see consistent behavioral effects in response to electrical stimulation. For example, cochlear implant users experience increased perception of loudness with increased stimulation amplitude. At the same time, cochlear implant users are also known to have hearing deficits, such as difficulty with efferent feedback or pitch perception, which are considered finer details of cochlear encoding. Thus, this work suggests that there are different hierarchies to neural processing in which at some basic level of neural computation (for example hearing sound) may take place at the level of spatial integration. For

example, a majority increase in population firing within an area of the cochlea gives sound perception, but that some system functions are encoded in other aspects of the neural encoding schema. Present electrical stimulation paradigms tap into these basic features of neural processing, if that is the case, but it also brings into question how many other properties of neuronal encoding may be accessible by changing how electrical stimulation is delivered.

The work on galvanic stimulation suggests that, by changing the waveform of electrical stimulation delivery, axonal ion channels will be affected differently and smaller features of neuronal physiology, such as hair cells, may be activatable. Both differences in effects of galvanic stimulation are shown in this manuscript to allow neurons to be locally excited together, unlikely the mixed effects that are predicted to occur with pulsatile stimulation. Additionally, induced synchrony observed with pulsatile stimulation is shown not to occur with galvanic stimulation, and this work provides a theory for why this should be the case in any neuron and leads to more naturalistic activation or inhibition of neurons. These findings suggest that some of the issues uncovered with pulsatile stimulation can be overcome with galvanic stimulation, providing smoother modulation of local neuronal firing rate. However, an open question then became whether and how this difference in driving a local population of neurons might lead to improvements at the network or behavioral level.

Chapter 5 works to begin to address these questions by comparing the effects of pulsatile and galvanic stimulation on a well-established network decision making model²³⁶. Although the model used still has simplifications in neuronal channel dynamics and connectivity, the work in this manuscript already provides clear predictions for how both electrical stimulation paradigms should affect networks differently. It is predicted that pulses need to be of an approximately 100 times higher current amplitude to create an equivalent effect to direct current galvanic stimulation. Additionally, pulses are predicted to activate a different portion of the local population of neurons and different neurons within the population for an equivalent change in firing rate. In the simulation of a connected network of neurons receiving natural implants, pulses had the predicted mixture of effects at different distances, while galvanic stimulation produced a change in firing rate that falls off smoothly with distance from the electrode. Pulses also were shown to cause the network to come to a decision significantly faster than galvanic stimulation and natural stimulation and be able to break network dynamics for making a decision. The level of galvanic stimulation modeled in this example also

shifts towards a faster decision time than is observed in the natural network, suggesting the effects of both forms of stimulation may still be unnatural. Findings indicate that properties of pulse-induced firing rate disrupt feedback inhibition that is essential in these networks. Further, work would be to assess how other networks in which spike-timing is more essential or local field potentials²⁴⁴ may be important are affected by these forms of stimulation as well.

The last contribution of this work is attempting to use these novel theories and models of electrical stimulation to develop improved neural prosthetic algorithms. This work focuses on attempting to improve neural control at the level of producing more naturalistic firing patterns in terms of firing rates over time. From this perspective, an issue with most neural implants is a focus on efficiently transforming a perceived input (e.g., sound) into pulse parameter modulation (e.g., pulse amplitude modulation). This work uses machine learning to create a schema for transforming complex models of neural firing in a local population, in this case the Zilany-Carney model²⁰⁸, into real-time algorithms that could be used at the front-end of a neural prosthetic. This front-end was designed with the intent to then use a back-end to optimally transform that target firing pattern into stimulation parameters based on electrode location. In this work, the focus would be to use algorithms like those discussed in Chapters 2 and 3 to better optimize electrical stimulation. However, a front-end of this type could also be used for other ultrasound, optogenetic stimulation, or any alternative approach.

The work discussed in this dissertation takes a number of steps towards a better scientific understanding of electrical stimulation and improved algorithm design for neural prosthetics. It is very much a stepping-stone toward improved usage of electrical stimulation to interact with neurons overall and, if anything, opens the door to more computational experiments, animal experiments, and translational work to in fact test whether the suggested changes to the electrical stimulation paradigm could improve neural interfacing more generally.

References

- 1 Chow, M. R. *et al.* Posture, Gait, Quality of Life, and Hearing with a Vestibular Implant. *N Engl J Med* **384**, 521-532, doi:10.1056/NEJMoa2020457 (2021).
- 2 Semenov, Y. R., Martinez-Monedero, R. & Niparko, J. K. Cochlear implants: clinical and societal outcomes. *Otolaryngol Clin North Am* **45**, 959-981, doi:10.1016/j.otc.2012.06.003 (2012).

- 3 Zangiabadi, N. *et al.* Deep Brain Stimulation and Drug-Resistant Epilepsy: A Review of the Literature. *Front Neurol* **10**, 601, doi:10.3389/fneur.2019.00601 (2019).
- 4 Loeb, G. E. Neural Prosthetics: A Review of Empirical vs. Systems Engineering Strategies. *Appl Bionics Biomech* **2018**, 1435030, doi:10.1155/2018/1435030 (2018).
- 5 Jebari, K. Brain Machine Interface and Human Enhancement - An Ethical Review. *Neuroethics-Neth* **6**, 617-625, doi:10.1007/s12152-012-9176-2 (2013).
- 6 Richardson, J. K. & Ashton-Miller, J. A. Peripheral neuropathy - An often-overlooked cause of falls in the elderly. *Postgraduate Medicine* **99**, 161-168, doi:10.1080/00325481.1996.11946142 (1996).
- 7 Bertucci, C., Koppes, R., Dumont, C. & Koppes, A. Neural responses to electrical stimulation in 2D and 3D in vitro environments. *Brain Research Bulletin* **152**, 265-284, doi:10.1016/j.brainresbull.2019.07.016 (2019).
- 8 Parisier, S. C., Elexiades, G., Hoffman, R. & Jr, M. Cochlear implants: obstacles limiting application. *Int Congr Ser* **1273**, 255-258, doi:10.1016/j.ics.2004.07.008 (2004).
- 9 Epstein, L. J. & Palmieri, M. Managing Chronic Pain With Spinal Cord Stimulation. *Mt Sinai J Med* **79**, 123-132, doi:10.1002/msj.21289 (2012).
- 10 Mazurek, K. A. & Schieber, M. H. Injecting Information into the Mammalian Cortex: Progress, Challenges, and Promise. *Neuroscientist* **27**, 129-142, doi:10.1177/1073858420936253 (2021).
- 11 Cameron, T. *et al.* Micromodular implants to provide electrical stimulation of paralyzed muscles and limbs. *Ieee Transactions on Biomedical Engineering* **44**, 781-790, doi:10.1109/10.623047 (1997).
- 12 Ferlauto, L. *et al.* Development and Characterization of PEDOT:PSS/Alginate Soft Microelectrodes for Application in Neuroprosthetics. *Front Neurosci* **12**, 648, doi:10.3389/fnins.2018.00648 (2018).
- 13 Lacour, S. P. *et al.* Flexible and stretchable micro-electrodes for in vitro and in vivo neural interfaces. *Medical & Biological Engineering & Computing* **48**, 945-954, doi:10.1007/s11517-010-0644-8 (2010).
- 14 Merrill, D. R., Bikson, M. & Jefferys, J. G. R. Electrical stimulation of excitable tissue: design of efficacious and safe protocols. *Journal of Neuroscience Methods* **141**, 171-198, doi:10.1016/j.jneumeth.2004.10.020 (2005).
- 15 Davidovics, N. S., Fridman, G. Y., Chiang, B. & Della Santina, C. C. Effects of biphasic current pulse frequency, amplitude, duration, and interphase gap on eye movement responses to prosthetic electrical stimulation of the vestibular nerve. *IEEE Trans Neural Syst Rehabil Eng* **19**, 84-94, doi:10.1109/TNSRE.2010.2065241 (2011).
- 16 Runge, C. L., Du, F. & Hu, Y. Improved Speech Perception in Cochlear Implant Users With Interleaved High-Rate Pulse Trains. *Otology & Neurotology* **39**, E319-E324, doi:10.1097/Mao.0000000000001790 (2018).
- 17 Gong, W. S., Haburcakova, C. & Merfeld, D. M. Vestibulo-Ocular Responses Evoked Via Bilateral Electrical Stimulation of the Lateral Semicircular Canals. *Ieee Transactions on Biomedical Engineering* **55**, 2608-2619, doi:10.1109/Tbme.2008.2001294 (2008).
- 18 DeVries, L. & Arenberg, J. G. Current Focusing to Reduce Channel Interaction for Distant Electrodes in Cochlear Implant Programs. *Trends Hear* **22**, 2331216518813811, doi:10.1177/2331216518813811 (2018).
- 19 Padilla, M. & Landsberger, D. M. Reduction in spread of excitation from current focusing at multiple cochlear locations in cochlear implant users. *Hearing Research* **333**, 98-107, doi:10.1016/j.heares.2016.01.002 (2016).
- 20 Friesen, L. M., Shannon, R. V., Baskent, D. & Wang, X. Speech recognition in noise as a function of the number of spectral channels: comparison of acoustic hearing and cochlear implants. *J Acoust Soc Am* **110**, 1150-1163, doi:10.1121/1.1381538 (2001).
- 21 Bikson, M. *et al.* Effects of uniform extracellular DC electric fields on excitability in rat hippocampal slices in vitro. *J Physiol-London* **557**, 175-190, doi:10.1113/jphysiol.2003.055772 (2004).
- 22 Fridman, G. Safe Direct Current Stimulator Design for Reduced Power Consumption and Increased Reliability. *P Ann Int Ieee Embs*, 1082-1085 (2017).
- 23 Fridman, G. Y. & Della Santina, C. C. Safe direct current stimulator 2: concept and design. *Annu Int Conf IEEE Eng Med Biol Soc* **2013**, 3126-3129, doi:10.1109/EMBC.2013.6610203 (2013).
- 24 Fridman, G. Y. & Della Santina, C. C. Safe direct current stimulation to expand capabilities of neural prostheses. *IEEE Trans Neural Syst Rehabil Eng* **21**, 319-328, doi:10.1109/TNSRE.2013.2245423 (2013).
- 25 Aplin, F. P., Singh, D., Santina, C. C. D. & Fridman, G. Y. Ionic Direct Current Modulation for Combined Inhibition/Excitation of the Vestibular System. *IEEE Trans Biomed Eng* **66**, 775-783, doi:10.1109/TBME.2018.2856698 (2019).
- 26 Steinhardt, C. R. & Fridman, G. Y. Direct current effects on afferent and hair cell to elicit natural firing patterns. *iScience* **24**, 102205, doi:10.1016/j.isci.2021.102205 (2021).

- 27 Manca, M., Glowatzki, E., Roberts, D. C., Fridman, G. Y. & Aplin, F. P. Ionic direct current modulation evokes spike-rate adaptation in the vestibular periphery. *Scientific Reports* **9**, doi:ARTN 18924 10.1038/s41598-019-55045-6 (2019).
- 28 Goldberg, J. M., Smith, C. E. & Fernandez, C. Relation between Discharge Regularity and Responses to Externally Applied Galvanic Currents in Vestibular Nerve Afferents of the Squirrel-Monkey. *Journal of Neurophysiology* **51**, 1236-1256, doi:DOI 10.1152/jn.1984.51.6.1236 (1984).
- 29 Mitchell, D. E., Della Santina, C. C. & Cullen, K. E. Plasticity within non-cerebellar pathways rapidly shapes motor performance in vivo. *Nat Commun* **7**, 11238, doi:10.1038/ncomms11238 (2016).
- 30 Geddes, L. A. & Hoff, H. E. Discovery of Bioelectricity and Current Electricity - Galvani-Volta Controversy. *Ieee Spectrum* **8**, 38-&, doi:Doi 10.1109/Mspec.1971.5217888 (1971).
- 31 Fritsch, B. Über die elektrische Erregbarkeit des Grosshirns. *Arch, anat Physiol Wiss Med.* (1870).
- 32 Krause, F. Die operative Behandlung der Epilepsie. *Med. Klin*, 1418-1422 (1909).
- 33 Cushing, H. A note upon the faradic stimulation of the postcentral gyrus in conscious patients. *Brain* **32**, 44-53, doi:DOI 10.1093/brain/32.1.44 (1909).
- 34 Foerster, O. & Altenburger, H. Elektrobiologische Vorgänge an der menschlichen Hirnrinde. *Deutsche Zeitschrift für Nervenheilkunde* (1935).
- 35 Penfield, W. & Perot, P. Brains Record of Auditory and Visual Experience - a Final Summary and Discussion. *Brain* **86**, 595-&, doi:DOI 10.1093/brain/86.4.595 (1963).
- 36 Schuetze, S. M. The Discovery of the Action-Potential. *Trends in Neurosciences* **6**, 164-168, doi:Doi 10.1016/0166-2236(83)90078-4 (1983).
- 37 Hodgkin, A. L. & Huxley, A. F. The components of membrane conductance in the giant axon of Loligo. *J Physiol* **116**, 473-496, doi:10.1113/jphysiol.1952.sp004718 (1952).
- 38 Hodgkin, A. L. & Katz, B. The effect of temperature on the electrical activity of the giant axon of the squid. *J Physiol* **109**, 240-249, doi:10.1113/jphysiol.1949.sp004388 (1949).
- 39 Purpura, D. P., Pool, J. L., Ransohoff, J., Frumin, M. J. & Housepian, E. M. Observations on Evoked Dendritic Potentials of Human Cortex. *Electroencephalography and Clinical Neurophysiology* **9**, 453-459, doi:Doi 10.1016/0013-4694(57)90034-2 (1957).
- 40 Kanwisher, N., McDermott, J. & Chun, M. M. The fusiform face area: A module in human extrastriate cortex specialized for face perception. *Journal of Neuroscience* **17**, 4302-4311 (1997).
- 41 Salzman, C. D., Britten, K. H. & Newsome, W. T. Cortical Microstimulation Influences Perceptual Judgments of Motion Direction. *Nature* **346**, 174-177, doi:DOI 10.1038/346174a0 (1990).
- 42 Keller, C. J. *et al.* Mapping human brain networks with cortico-cortical evoked potentials. *Philos T R Soc B* **369**, doi:ARTN 20130528 10.1098/rstb.2013.0528 (2014).
- 43 Yamao, Y. *et al.* Intraoperative Dorsal Language Network Mapping by Using Single-Pulse Electrical Stimulation. *Human Brain Mapping* **35**, 4345-4361, doi:10.1002/hbm.22479 (2014).
- 44 Matsumoto, R. *et al.* Parieto-frontal network in humans studied by cortico-cortical evoked potential. *Human Brain Mapping* **33**, 2856-2872, doi:10.1002/hbm.21407 (2012).
- 45 DeForge, W. F. Cardiac pacemakers: a basic review of the history and current technology. *J Vet Cardiol* **22**, 40-50, doi:10.1016/j.jvc.2019.01.001 (2019).
- 46 Stefan, H. & da Silva, F. H. L. Epileptic neuronal networks: methods of identification and clinical relevance. *Frontiers in Neurology* **4**, doi:ARTN 8 10.3389/fneur.2013.00008 (2013).
- 47 van Elswijk, G. *et al.* Corticospinal Beta-Band Synchronization Entails Rhythmic Gain Modulation. *Journal of Neuroscience* **30**, 4481-4488, doi:10.1523/Jneurosci.2794-09.2010 (2010).
- 48 PrevotEAU, C., Chen, S. Y. & Lalwani, A. K. Music enjoyment with cochlear implantation. *Auris Nasus Larynx* **45**, 895-902, doi:10.1016/j.anl.2017.11.008 (2018).
- 49 Sun, X. A., Huang, S. & Wang, N. Y. Neural Interface: Frontiers and Applications Cochlear Implants. *Adv Exp Med Biol* **1101**, 167-206, doi:10.1007/978-981-13-2050-7_7 (2019).
- 50 Haider, N. *et al.* Spinal Cord Stimulation (SCS) Trial Outcomes After Conversion to a Multiple Waveform SCS System. *Neuromodulation* **21**, 504-507, doi:10.1111/ner.12783 (2018).
- 51 Jiman, A. A. *et al.* Multi-channel intraneural vagus nerve recordings with a novel high-density carbon fiber microelectrode array. *Scientific Reports* **10**, doi:ARTN 15501 10.1038/s41598-020-72512-7 (2020).
- 52 Beebe, X. & Rose, T. L. Charge Injection Limits of Activated Iridium Oxide Electrodes with 0.2ms Pulses in Bicarbonate Buffered Saline. *Ieee Transactions on Biomedical Engineering* **35**, 494-495, doi:Doi 10.1109/10.2122 (1988).
- 53 Rose, T. L. & Robblee, L. S. Electrical-Stimulation with Pt Electrodes .8. Electrochemically Safe Charge Injection Limits with 0.2 Ms Pulses. *Ieee Transactions on Biomedical Engineering* **37**, 1118-1120, doi:Doi 10.1109/10.61038 (1990).
- 54 van Wieringen, A., Carlyon, R. P., Laneau, J. & Wouters, J. Effects of waveform shape on human sensitivity to electrical stimulation of the inner ear. *Hearing Research* **200**, 73-86, doi:10.1016/j.heares.2004.08.006 (2005).

- 55 Krauthamer, V. & Crosheck, T. Effects of high-rate electrical stimulation upon firing in modelled and real neurons. *Medical & Biological Engineering & Computing* **40**, 360-366, doi:10.1007/Bf02344220 (2002).
- 56 Litvak, L. M., Delgutte, B. & Eddington, D. K. Improved temporal coding of sinusoids in electric stimulation of the auditory nerve using desynchronizing pulse trains. *Journal of the Acoustical Society of America* **114**, 2079-2098, doi:10.1121/1.1612493 (2003).
- 57 Bhadra, N. & Kilgore, K. L. High-frequency electrical conduction block of mammalian peripheral motor nerve. *Muscle Nerve* **32**, 782-790, doi:10.1002/mus.20428 (2005).
- 58 Joseph, L. & Butera, R. J. High-Frequency Stimulation Selectively Blocks Different Types of Fibers in Frog Sciatic Nerve. *Ieee Transactions on Neural Systems and Rehabilitation Engineering* **19**, 550-557, doi:10.1109/Tnsre.2011.2163082 (2011).
- 59 Simon, D. T. *et al.* An organic electronic biomimetic neuron enables auto-regulated neuromodulation. *Biosens Bioelectron* **71**, 359-364, doi:10.1016/j.bios.2015.04.058 (2015).
- 60 Kumaravelu, K. *et al.* A comprehensive model-based framework for optimal design of biomimetic patterns of electrical stimulation for prosthetic sensation. *Journal of Neural Engineering* **17**, doi:ARTN 046045 10.1088/1741-2552/abacd8 (2020).
- 61 Maheshwari, A., Pope, J. E., Deer, T. R. & Falowski, S. Advanced methods of spinal stimulation in the treatment of chronic pain: pulse trains, waveforms, frequencies, targets, and feedback loops. *Expert Review of Medical Devices* **16**, 95-106, doi:10.1080/17434440.2019.1567325 (2019).
- 62 Tafazoli, S. *et al.* Learning to control the brain through adaptive closed-loop patterned stimulation. *Journal of Neural Engineering* **17**, doi:ARTN 056007 10.1088/1741-2552/abb860 (2020).
- 63 Hasson, U., Nastase, S. A. & Goldstein, A. Direct Fit to Nature: An Evolutionary Perspective on Biological and Artificial Neural Networks. *Neuron* **105**, 416-434, doi:10.1016/j.neuron.2019.12.002 (2020).
- 64 Schier, P. *et al.* Model-Based Vestibular Afferent Stimulation: Evaluating Selective Electrode Locations and Stimulation Waveform Shapes. *Frontiers in Neuroscience* **12**, doi:ARTN 588 10.3389/fnins.2018.00588 (2018).
- 65 Finger, S., Piccolino, M. & Stahnisch, F. W. Alexander von Humboldt: galvanism, animal electricity, and self-experimentation part 1: formative years, naturphilosophie, and galvanism. *J Hist Neurosci* **22**, 225-260, doi:10.1080/0964704X.2012.732727 (2013).
- 66 Brunoni, A. R. *et al.* Clinical research with transcranial direct current stimulation (tDCS): challenges and future directions. *Brain Stimul* **5**, 175-195, doi:10.1016/j.brs.2011.03.002 (2012).
- 67 Guleyupoglu, B., Schestatsky, P., Edwards, D., Fregni, F. & Bikson, M. Classification of methods in transcranial Electrical Stimulation (tES) and evolving strategy from historical approaches to contemporary innovations. *Journal of Neuroscience Methods* **219**, 297-311, doi:10.1016/j.jneumeth.2013.07.016 (2013).
- 68 Hammerer, D., Bonaiuto, J., Klein-Flugge, M., Bikson, M. & Bestmann, S. Selective alteration of human value decisions with medial frontal tDCS is predicted by changes in attractor dynamics. *Sci Rep* **6**, 25160, doi:10.1038/srep25160 (2016).
- 69 Jackson, M. P. *et al.* Animal models of transcranial direct current stimulation: Methods and mechanisms. *Clinical Neurophysiology* **127**, 3425-3454, doi:10.1016/j.clinph.2016.08.016 (2016).
- 70 Fitzpatrick, R. C. & Day, B. L. Probing the human vestibular system with galvanic stimulation. *J Appl Physiol* (1985) **96**, 2301-2316, doi:10.1152/japplphysiol.00008.2004 (2004).
- 71 Gensberger, K. D. *et al.* Galvanic Vestibular Stimulation: Cellular Substrates and Response Patterns of Neurons in the Vestibulo-Ocular Network. *Journal of Neuroscience* **36**, 9097-9110, doi:10.1523/Jneurosci.4239-15.2016 (2016).
- 72 Bikson, M., Rahman, A. & Datta, A. Computational Models of Transcranial Direct Current Stimulation. *Clinical Eeg and Neuroscience* **43**, 176-183, doi:10.1177/1550059412445138 (2012).
- 73 Reato, D., Rahman, A., Bikson, M. & Parra, L. C. Effects of weak transcranial alternating current stimulation on brain activity-a review of known mechanisms from animal studies. *Frontiers in Human Neuroscience* **7**, doi:ARTN 687 10.3389/fnhum.2013.00687 (2013).
- 74 Spelman, F., Johnson, T., Corbett, S. & Clopton, B. Apparatus and method for treating strial hearing loss (U.S. Patent No. 6,694,190.). (2002).
- 75 Aplin, F. P. & Fridman, G. Y. Implantable Direct Current Neural Modulation: Theory, Feasibility, and Efficacy. *Front Neurosci* **13**, 379, doi:10.3389/fnins.2019.00379 (2019).
- 76 Kronberg, G., Rahman, A., Sharma, M., Bikson, M. & Parra, L. C. Direct current stimulation boosts hebbian plasticity in vitro. *Brain Stimulation* **13**, 287-301, doi:10.1016/j.brs.2019.10.014 (2020).
- 77 Yamashita, M. Weak electric fields serve as guidance cues that direct retinal ganglion cell axons in vitro. *Biochem Biophys Rep* **4**, 83-88, doi:10.1016/j.bbrep.2015.08.022 (2015).
- 78 Goldberg, J. M., Fernandez, C. & Smith, C. E. Responses of vestibular-nerve afferents in the squirrel monkey to externally applied galvanic currents. *Brain Res* **252**, 156-160, doi:10.1016/0006-8993(82)90990-8 (1982).

79 Buzsaki, G., Anastassiou, C. A. & Koch, C. The origin of extracellular fields and currents--EEG, ECoG, LFP and spikes. *Nat Rev Neurosci* **13**, 407-420, doi:10.1038/nrn3241 (2012).

80 Kostyuk, P. G. Diversity of Calcium-Ion Channels in Cellular Membranes. *Neuroscience* **28**, 253-261, doi:10.1016/0306-4522(89)90177-2 (1989).

81 Sohl, G., Maxeiner, S. & Willecke, K. Expression and functions of neuronal gap junctions. *Nature Reviews Neuroscience* **6**, 191-200, doi:10.1038/nrn1627 (2005).

82 Eatock, R. A. & Songer, J. E. Vestibular Hair Cells and Afferents: Two Channels for Head Motion Signals. *Annual Review of Neuroscience* **34**, 501-534, doi:10.1146/annurev-neuro-061010-113710 (2011).

83 Songer, J. E. & Eatock, R. A. Tuning and timing in mammalian type I hair cells and calyceal synapses. *J Neurosci* **33**, 3706-3724, doi:10.1523/JNEUROSCI.4067-12.2013 (2013).

84 Goldberg, J. M. The vestibular end organs: morphological and physiological diversity of afferents. *Curr Opin Neurobiol* **1**, 229-235, doi:10.1016/0959-4388(91)90083-j (1991).

85 Kalluri, R., Xue, J. B. & Eatock, R. A. Ion Channels Set Spike Timing Regularity of Mammalian Vestibular Afferent Neurons. *Journal of Neurophysiology* **104**, 2034-2051, doi:10.1152/jn.00396.2010 (2010).

86 Mitchell, D. E., Della Santina, C. C. & Cullen, K. E. Plasticity within excitatory and inhibitory pathways of the vestibulo-spinal circuitry guides changes in motor performance. *Sci Rep* **7**, 853, doi:10.1038/s41598-017-00956-5 (2017).

87 Hight, A. E. & Kalluri, R. A biophysical model examining the role of low-voltage-activated potassium currents in shaping the responses of vestibular ganglion neurons. *J Neurophysiol* **116**, 503-521, doi:10.1152/jn.00107.2016 (2016).

88 Bhadra, N. & Kilgore, K. L. Direct current electrical conduction block of peripheral nerve. *IEEE Trans Neural Syst Rehabil Eng* **12**, 313-324, doi:10.1109/TNSRE.2004.834205 (2004).

89 Yang, F. *et al.* Differential expression of voltage-gated sodium channels in afferent neurons renders selective neural block by ionic direct current. *Sci Adv* **4**, eaaq1438, doi:10.1126/sciadv.aaq1438 (2018).

90 Radman, T., Su, Y., An, J. H., Parra, L. C. & Bikson, M. Spike timing amplifies the effect of electric fields on neurons: implications for endogenous field effects. *J Neurosci* **27**, 3030-3036, doi:10.1523/JNEUROSCI.0095-07.2007 (2007).

91 Cheng, C., Thakur, R., Nair, A. R., Sterrett, S. & Fridman, G. Miniature Elastomeric Valve Design for Safe Direct Current Stimulator. *IEEE Biomed Circuits Syst Conf* **2017**, 1-4, doi:10.1109/BIOCAS.2017.8325194 (2017).

92 Ou, P. & Fridman, G. Electronics for a Safe Direct Current Stimulator. *IEEE Biomed Circuits Syst Conf* **2017**, doi:10.1109/BIOCAS.2017.8325191 (2017).

93 Aplin, F. P., Singh, D., Della Santina, C. C. & Fridman, G. Y. Combined ionic direct current and pulse frequency modulation improves the dynamic range of vestibular canal stimulation. *J Vestib Res* **29**, 89-96, doi:10.3233/VES-190651 (2019).

94 Goldberg, J. M. Afferent diversity and the organization of central vestibular pathways. *Experimental Brain Research* **130**, 277-297, doi:10.1007/s002210050033 (2000).

95 Highstein, S. M. & Holstein, G. R. The anatomical and physiological framework for vestibular prostheses. *Anat Rec (Hoboken)* **295**, 2000-2009, doi:10.1002/ar.22582 (2012).

96 Matthews, G. & Fuchs, P. The diverse roles of ribbon synapses in sensory neurotransmission. *Nat Rev Neurosci* **11**, 812-822, doi:10.1038/nrn2924 (2010).

97 Holmes, W. R., Huwe, J. A., Williams, B., Rowe, M. H. & Peterson, E. H. Models of utricular bouton afferents: role of afferent-hair cell connectivity in determining spike train regularity. *J Neurophysiol* **117**, 1969-1986, doi:10.1152/jn.00895.2016 (2017).

98 Baird, R. A., Desmadryl, G., Fernandez, C. & Goldberg, J. M. The vestibular nerve of the chinchilla. II. Relation between afferent response properties and peripheral innervation patterns in the semicircular canals. *J Neurophysiol* **60**, 182-203, doi:10.1152/jn.1988.60.1.182 (1988).

99 Fernandez, C., Baird, R. A. & Goldberg, J. M. The vestibular nerve of the chinchilla. I. Peripheral innervation patterns in the horizontal and superior semicircular canals. *J Neurophysiol* **60**, 167-181, doi:10.1152/jn.1988.60.1.167 (1988).

100 Eatock, R. A. Specializations for Fast Signaling in the Amniote Vestibular Inner Ear. *Integrative and Comparative Biology* **58**, 341-350, doi:10.1093/icb/icy069 (2018).

101 Govindaraju, A. C., Lysakowski, A., Eatock, R. A. & Raphael, R. M. Computational Model of Ephaptic Coupling and Potassium Modulation at the Vestibular Hair Cell Calyx Synapse. *Biophysical Journal* **120**, 353a-353a (2021).

102 Govindaraju, A. C., Quraishi, I., Lysakowski, A., Eatock, R. A. & Raphael, R. M. Biophysical Model of the Vestibular Hair Cell CALYX Synapse. *Biophysical Journal* **118**, 28a-28a (2020).

103 Holt, J. C., Chatlani, S., Lysakowski, A. & Goldberg, J. M. Quantal and nonquantal transmission in
calyx-bearing fibers of the turtle posterior crista. *J Neurophysiol* **98**, 1083-1101,
doi:10.1152/jn.00332.2007 (2007).

104 Contini, D., Price, S. D. & Art, J. J. Accumulation of K(+) in the synaptic cleft modulates activity by
influencing both vestibular hair cell and calyx afferent in the turtle. *J Physiol* **595**, 777-803,
doi:10.1113/JP273060 (2017).

105 Manca, M. *et al.* Current Response in Ca V 1.3(-/-) Mouse Vestibular and Cochlear Hair Cells. *Front*
Neurosci **15**, 749483, doi:10.3389/fnins.2021.749483 (2021).

106 Sadeghi, S. G., Goldberg, J. M., Minor, L. B. & Cullen, K. E. Effects of canal plugging on the
vestibuloocular reflex and vestibular nerve discharge during passive and active head rotations. *J*
Neurophysiol **102**, 2693-2703, doi:10.1152/jn.00710.2009 (2009).

107 Lim, S. B. *et al.* Postural threat influences vestibular-evoked muscular responses. *J Neurophysiol*
117, 604-611, doi:10.1152/jn.00712.2016 (2017).

108 Mathews, M. A., Camp, A. J. & Murray, A. J. Reviewing the Role of the Efferent Vestibular System in
Motor and Vestibular Circuits. *Frontiers in Physiology* **8**, doi:ARTN 552 10.3389/fphys.2017.00552
(2017).

109 Rabbitt, R. D., Boyle, R. & Highstein, S. M. Mechanical amplification by hair cells in the semicircular
canals. *Proceedings of the National Academy of Sciences of the United States of America* **107**,
3864-3869, doi:10.1073/pnas.0906765107 (2010).

110 Sadeghi, S. G., Goldberg, J. M., Minor, L. B. & Cullen, K. E. Efferent-Mediated Responses in
Vestibular Nerve Afferents of the Alert Macaque. *Journal of Neurophysiology* **101**, 988-1001,
doi:10.1152/jn.91112.2008 (2009).

111 Goldberg, J. M., Lysakowski, A. & Fernandez, C. Morphophysiological and Ultrastructural Studies in
the Mammalian Cristae-Ampullares. *Hearing Research* **49**, 89-102, doi:Doi 10.1016/0378-
5955(90)90097-9 (1990).

112 Castellano-Munoz, M., Israel, S. H. & Hudspeth, A. J. Efferent Control of the Electrical and
Mechanical Properties of Hair Cells in the Bullfrog's Sacculus. *Plos One* **5**, doi:ARTN e13777
10.1371/journal.pone.0013777 (2010).

113 Rabbitt, R. D., Boyle, R., Holstein, G. R. & Highstein, S. M. Hair-cell versus afferent adaptation in the
semicircular canals. *J Neurophysiol* **93**, 424-436, doi:10.1152/jn.00426.2004 (2005).

114 Kwan, A., Forbes, P. A., Mitchell, D. E., Blouin, J. S. & Cullen, K. E. Neural substrates, dynamics
and thresholds of galvanic vestibular stimulation in the behaving primate. *Nat Commun* **10**, 1904,
doi:10.1038/s41467-019-09738-1 (2019).

115 Iwasaki, S., Chihara, Y., Komuta, Y., Ito, K. & Sahara, Y. Low-voltage-activated potassium channels
underlie the regulation of intrinsic firing properties of rat vestibular ganglion cells. *J Neurophysiol*
100, 2192-2204, doi:10.1152/jn.01240.2007 (2008).

116 Kalluri, R., Xue, J. & Eatock, R. A. Ion channels set spike timing regularity of mammalian vestibular
afferent neurons. *J Neurophysiol* **104**, 2034-2051, doi:10.1152/jn.00396.2010 (2010).

117 Sadeghi, S. G., Pyott, S. J., Yu, Z. & Glowatzki, E. Glutamatergic signaling at the vestibular hair cell
calyx synapse. *J Neurosci* **34**, 14536-14550, doi:10.1523/JNEUROSCI.0369-13.2014 (2014).

118 Balbi, P., Massobrio, P. & Hellgren Kotaleski, J. A single Markov-type kinetic model accounting for
the macroscopic currents of all human voltage-gated sodium channel isoforms. *PLoS Comput Biol*
13, e1005737, doi:10.1371/journal.pcbi.1005737 (2017).

119 Boyle, R., Rabbitt, R. D. & Highstein, S. M. Efferent Control of Hair Cell and Afferent Responses in
the Semicircular Canals. *Journal of Neurophysiology* **102**, 1513-1525, doi:10.1152/jn.91367.2008
(2009).

120 Dulon, D., Safieddine, S., Jones, S. M. & Petit, C. Otoferlin Is Critical for a Highly Sensitive and
Linear Calcium-Dependent Exocytosis at Vestibular Hair Cell Ribbon Synapses. *Journal of*
Neuroscience **29**, 10474-10487, doi:10.1523/Jneurosci.1009-09.2009 (2009).

121 Smith, C. E. & Goldberg, J. M. A stochastic afterhyperpolarization model of repetitive activity in
vestibular afferents. *Biol Cybern* **54**, 41-51, doi:10.1007/BF00337114 (1986).

122 Rattay, F. The basic mechanism for the electrical stimulation of the nervous system. *Neuroscience*
89, 335-346, doi:10.1016/s0306-4522(98)00330-3 (1999).

123 Steinhardt, C. R. & Fridman, G. Y. Predicting Response of Spontaneously Firing Afferents to
Prosthetic Pulsatile Stimulation. *Annu Int Conf IEEE Eng Med Biol Soc* **2020**, 2929-2933,
doi:10.1109/EMBC44109.2020.9175282 (2020).

124 Grant, P. F. & Lowery, M. M. Effect of Dispersive Conductivity and Permittivity in Volume Conductor
Models of Deep Brain Stimulation. *Ieee Transactions on Biomedical Engineering* **57**, 2386-2393,
doi:10.1109/Tbme.2010.2055054 (2010).

125 Eatock, R. A., Xue, J. B. & Kalluri, R. Ion channels in mammalian vestibular afferents may set
regularity of firing. *Journal of Experimental Biology* **211**, 1764-1774, doi:10.1242/jeb.017350 (2008).

- 126 Yamashita, M. & Ohmori, H. Synaptic responses to mechanical stimulation in calyceal and bouton
type vestibular afferents studied in an isolated preparation of semicircular canal ampullae of chicken.
Exp Brain Res **80**, 475-488, doi:10.1007/BF00227989 (1990).
- 127 Fuchs, P. A. Vestibular calyx, potassium: Kalium in Calyx Regnat. *J Physiol* **595**, 623,
doi:10.1113/JP273432 (2017).
- 128 Hurley, K. M. *et al.* M-like K⁺ currents in type I hair cells and calyx afferent endings of the developing
rat utricle. *J Neurosci* **26**, 10253-10269, doi:10.1523/JNEUROSCI.2596-06.2006 (2006).
- 129 Contini, D., Holstein, G. R. & Art, J. J. Synaptic cleft microenvironment influences potassium
permeation and synaptic transmission in hair cells surrounded by calyx afferents in the turtle. *J*
Physiol **598**, 853-889, doi:10.1113/JP278680 (2020).
- 130 Dlugacz, J., Gensberger, K. D. & Straka, H. Galvanic vestibular stimulation: from basic concepts
to clinical applications. *Journal of Neurophysiology* **121**, 2237-2255, doi:10.1152/jn.00035.2019
(2019).
- 131 Cole, K. S. Permeability and Impermeability of Cell Membranes for Ions. *Cold Spring Harbor*
Symposia on Quantitative Biology **8**, 110-122 (1940).
- 132 Rattay, F., Paredes, L. P. & Leao, R. N. Strength-duration relationship for intra- versus extracellular
stimulation with microelectrodes. *Neuroscience* **214**, 1-13, doi:10.1016/j.neuroscience.2012.04.004
(2012).
- 133 Sadeghi, S. G., Chacron, M. J., Taylor, M. C. & Cullen, K. E. Neural variability, detection thresholds,
and information transmission in the vestibular system. *J Neurosci* **27**, 771-781,
doi:10.1523/JNEUROSCI.4690-06.2007 (2007).
- 134 Flynn, G. E. & Zagotta, W. N. Insights into the molecular mechanism for hyperpolarization-dependent
activation of HCN channels. *Proceedings of the National Academy of Sciences of the United States*
of America **115**, E8086-E8095, doi:10.1073/pnas.1805596115 (2018).
- 135 Ramakrishna, Y., Manca, M., Glowatzki, E. & Sadeghi, S. G. Cholinergic Modulation of Membrane
Properties of Calyx Terminals in the Vestibular Periphery. *Neuroscience* **452**, 98-110,
doi:10.1016/j.neuroscience.2020.10.035 (2021).
- 136 Hirvonen, T. P., Minor, L. B., Hullar, T. E. & Carey, J. P. Effects of intratympanic gentamicin on
vestibular afferents and hair cells in the chinchilla. *J Neurophysiol* **93**, 643-655,
doi:10.1152/jn.00160.2004 (2005).
- 137 Sultemeier, D. R. & Hoffman, L. F. Partial Aminoglycoside Lesions in Vestibular Epithelia Reveal
Broad Sensory Dysfunction Associated with Modest Hair Cell Loss and Afferent Calyx Retraction.
Front Cell Neurosci **11**, 331, doi:10.3389/fncel.2017.00331 (2017).
- 138 Aw, S. T., Todd, M. J., Aw, G. E., Weber, K. P. & Halmagyi, G. M. Gentamicin vestibulotoxicity
impairs human electrically evoked vestibulo-ocular reflex. *Neurology* **71**, 1776-1782,
doi:10.1212/01.wnl.0000335971.43443.d9 (2008).
- 139 McElvain, L. E., Bagnall, M. W., Sakatos, A. & du Lac, S. Bidirectional plasticity gated by
hyperpolarization controls the gain of postsynaptic firing responses at central vestibular nerve
synapses. *Neuron* **68**, 763-775, doi:10.1016/j.neuron.2010.09.025 (2010).
- 140 Meredith, F. L., Benke, T. A. & Rennie, K. J. Hyperpolarization-activated current (I_h) in vestibular
calyx terminals: characterization and role in shaping postsynaptic events. *J Assoc Res Otolaryngol*
13, 745-758, doi:10.1007/s10162-012-0342-3 (2012).
- 141 Yi, E., Roux, I. & Glowatzki, E. Dendritic HCN channels shape excitatory postsynaptic potentials at
the inner hair cell afferent synapse in the mammalian cochlea. *J Neurophysiol* **103**, 2532-2543,
doi:10.1152/jn.00506.2009 (2010).
- 142 Ventura, C. M. & Kalluri, R. Enhanced Activation of HCN Channels Reduces Excitability and Spike-
Timing Regularity in Maturing Vestibular Afferent Neurons. *J Neurosci* **39**, 2860-2876,
doi:10.1523/JNEUROSCI.1811-18.2019 (2019).
- 143 Paulin, M. G. & Hoffman, L. F. Models of vestibular semicircular canal afferent neuron firing activity.
J Neurophysiol **122**, 2548-2567, doi:10.1152/jn.00087.2019 (2019).
- 144 Forbes, P. A. *et al.* Neural Mechanisms Underlying High-Frequency Vestibulocollic Reflexes In
Humans And Monkeys. *J Neurosci* **40**, 1874-1887, doi:10.1523/JNEUROSCI.1463-19.2020 (2020).
- 145 Highstein, S. M., Rabbitt, R. D., Holstein, G. R. & Boyle, R. D. Determinants of spatial and temporal
coding by semicircular canal afferents. *J Neurophysiol* **93**, 2359-2370, doi:10.1152/jn.00533.2004
(2005).
- 146 Frankenhaeuser, B. & Huxley, A. F. The Action Potential in the Myelinated Nerve Fiber of *Xenopus*
laevis as Computed on the Basis of Voltage Clamp Data. *J Physiol* **171**, 302-315,
doi:10.1113/jphysiol.1964.sp007378 (1964).
- 147 Goldberg, J. M. & Brichta, A. M. Evolutionary trends in the organization of the vertebrate crista
ampullaris. *Otolaryng Head Neck* **119**, 165-171, doi:10.1016/S0194-5998(98)70051-8 (1998).

148 Brichta, A. M. & Goldberg, J. M. Responses to efferent activation and excitatory response-intensity
relations of turtle posterior-crista afferents. *Journal of Neurophysiology* **83**, 1224-1242, doi:DOI
10.1152/jn.2000.83.3.1224 (2000).

149 Marlinski, V., Plotnik, M. & Goldberg, J. M. Efferent actions in the chinchilla vestibular labyrinth.
Jaro-J Assoc Res Oto **5**, 126-143, doi:10.1007/s10162-003-4029-7 (2004).

150 Schneider, G. T., Lee, C., Sinha, A. K., Jordan, P. M. & Holt, J. C. The mammalian efferent
vestibular system utilizes cholinergic mechanisms to excite primary vestibular afferents. *Sci Rep* **11**,
1231, doi:10.1038/s41598-020-80367-1 (2021).

151 Raghu, V., Salvi, R. & Sadeghi, S. G. Efferent Inputs Are Required for Normal Function of Vestibular
Nerve Afferents. *J Neurosci* **39**, 6922-6935, doi:10.1523/JNEUROSCI.0237-19.2019 (2019).

152 Urdaneta, M. E., Kunigk, N. G., Delgado, F., Fried, S. I. & Otto, K. J. Layer-specific parameters of
intracortical microstimulation of the somatosensory cortex. *J Neural Eng* **18**, doi:10.1088/1741-
2552/abedde (2021).

153 Piccolino, M. Animal electricity and the birth of electrophysiology: the legacy of Luigi Galvani. *Brain
Res Bull* **46**, 381-407, doi:10.1016/s0361-9230(98)00026-4 (1998).

154 Steinhardt, C. R. *et al.* Characterizing and predicting cortical evoked responses to direct electrical
stimulation of the human brain. *Brain Stimul* **13**, 1218-1225, doi:10.1016/j.brs.2020.05.001 (2020).

155 Vincent, M. *et al.* The difference between electrical microstimulation and direct electrical stimulation -
towards new opportunities for innovative functional brain mapping? *Rev Neurosci* **27**, 231-258,
doi:10.1515/revneuro-2015-0029 (2016).

156 Khairuddin, S. *et al.* A Decade of Progress in Deep Brain Stimulation of the Subcallosal Cingulate for
the Treatment of Depression. *J Clin Med* **9**, doi:10.3390/jcm9103260 (2020).

157 Cosetti, M. K. & Waltzman, S. B. Cochlear implants: current status and future potential. *Expert
Review of Medical Devices* **8**, 389-401, doi:10.1586/Erd.11.12 (2011).

158 Nowik, K., Langwinska-Wosko, E., Skopinski, P., Nowik, K. E. & Szaflik, J. P. Bionic eye review - An
update. *J Clin Neurosci* **78**, 8-19, doi:10.1016/j.jocn.2020.05.041 (2020).

159 Boutros, P. J. *et al.* Nonhuman primate vestibuloocular reflex responses to prosthetic vestibular
stimulation are robust to pulse timing errors caused by temporal discretization. *Journal of
Neurophysiology* **121**, 2256-2266, doi:10.1152/jn.00887.2018 (2019).

160 Kolaya, E. & Firestein, B. L. Deep brain stimulation: Challenges at the tissue-electrode interface and
current solutions. *Biotechnol Prog* **37**, e3179, doi:10.1002/btpr.3179 (2021).

161 Wei, C. G., Cao, K. L. & Zeng, F. G. Mandarin tone recognition in cochlear-implant subjects. *Hearing
Research* **197**, 87-95, doi:10.1016/j.heares.2004.06.002 (2004).

162 Zeng, F. G. Challenges in Improving Cochlear Implant Performance and Accessibility. *IEEE Trans
Biomed Eng* **64**, 1662-1664, doi:10.1109/TBME.2017.2718939 (2017).

163 Histed, M. H., Bonin, V. & Reid, R. C. Direct activation of sparse, distributed populations of cortical
neurons by electrical microstimulation. *Neuron* **63**, 508-522, doi:10.1016/j.neuron.2009.07.016
(2009).

164 Boulet, J., White, M. & Bruce, I. C. Temporal Considerations for Stimulating Spiral Ganglion Neurons
with Cochlear Implants. *Jaro-J Assoc Res Oto* **17**, 1-17, doi:10.1007/s10162-015-0545-5 (2016).

165 Hey, M., Muller-Deile, J., Hessel, H. & Killian, M. Facilitation and refractoriness of the electrically
evoked compound action potential. *Hear Res* **355**, 14-22, doi:10.1016/j.heares.2017.09.001 (2017).

166 Steinhardt, C. R., Mitchell, D. E., Cullen, K. E. & Fridman, G. Y. The Rules of Pulsatile
Neurostimulation. *bioRxiv* (2021).

167 Fridman, G. Y. & Della Santina, C. C. Progress toward development of a multichannel vestibular
prosthesis for treatment of bilateral vestibular deficiency. *Anat Rec (Hoboken)* **295**, 2010-2029,
doi:10.1002/ar.22581 (2012).

168 Della Santina, C. C., Migliaccio, A. A. & Patel, A. H. A multichannel semicircular canal neural
prosthesis using electrical stimulation to restore 3-d vestibular sensation. *IEEE Trans Biomed Eng*
54, 1016-1030, doi:10.1109/TBME.2007.894629 (2007).

169 Golub, J. S. *et al.* Prosthetic Implantation of the Human Vestibular System. *Otology & Neurotology*
35, 136-147, doi:DOI 10.1097/Mao.0000000000000003 (2014).

170 Babalian, A. L., Ryugo, D. K. & Rouiller, E. M. Discharge properties of identified cochlear nucleus
neurons and auditory nerve fibers in response to repetitive electrical stimulation of the auditory
nerve. *Exp Brain Res* **153**, 452-460, doi:10.1007/s00221-003-1619-x (2003).

171 Shepherd, R. K. & Javel, E. Electrical stimulation of the auditory nerve: II. Effect of stimulus
wave shape on single fibre response properties. *Hear Res* **130**, 171-188, doi:10.1016/s0378-
5955(99)00011-8 (1999).

172 Wang, Z., Feng, Z. & Wei, X. Axonal Stimulations With a Higher Frequency Generate More
Randomness in Neuronal Firing Rather Than Increase Firing Rates in Rat Hippocampus. *Front
Neurosci* **12**, 783, doi:10.3389/fnins.2018.00783 (2018).

- 173 Carey, J. P. *et al.* Changes in the three-dimensional angular vestibulo-ocular reflex following
intratympanic gentamicin for Meniere's disease. *J Assoc Res Otolaryngol* **3**, 430-443,
doi:10.1007/s101620010053 (2002).
- 174 Sun, D. Q. *et al.* Histopathologic Changes of the Inner ear in Rhesus Monkeys After Intratympanic
Gentamicin Injection and Vestibular Prosthesis Electrode Array Implantation. *J Assoc Res*
Otolaryngol **16**, 373-387, doi:10.1007/s10162-015-0515-y (2015).
- 175 Fridman, G. Y., Blair, H. T., Blaisdell, A. P. & Judy, J. W. Perceived intensity of somatosensory
cortical electrical stimulation. *Exp Brain Res* **203**, 499-515, doi:10.1007/s00221-010-2254-y (2010).
- 176 Fries, P. Rhythms for Cognition: Communication through Coherence. *Neuron* **88**, 220-235,
doi:10.1016/j.neuron.2015.09.034 (2015).
- 177 Cataldo, E. *et al.* Computational model of touch sensory cells (T Cells) of the leech: role of the
afterhyperpolarization (AHP) in activity-dependent conduction failure. *J Comput Neurosci* **18**, 5-24,
doi:10.1007/s10827-005-5477-3 (2005).
- 178 Hedjoudje, A. *et al.* Virtual Rhesus Labyrinth Model Predicts Responses to Electrical Stimulation
Delivered by a Vestibular Prosthesis. *J Assoc Res Otolaryngol* **20**, 313-339, doi:10.1007/s10162-
019-00725-3 (2019).
- 179 Lansky, P., Sanda, P. & He, J. The parameters of the stochastic leaky integrate-and-fire neuronal
model. *J Comput Neurosci* **21**, 211-223, doi:10.1007/s10827-006-8527-6 (2006).
- 180 Sherfey, J., Ardid, S., Miller, E. K., Hasselmo, M. E. & Kopell, N. J. Prefrontal oscillations modulate
the propagation of neuronal activity required for working memory. *Neurobiol Learn Mem* **173**,
107228, doi:10.1016/j.nlm.2020.107228 (2020).
- 181 Tai, C., Roppolo, J. R. & de Groat, W. C. Response of external urethral sphincter to high frequency
biphasic electrical stimulation of pudendal nerve. *J Urol* **174**, 782-786,
doi:10.1097/01.ju.0000164728.25074.36 (2005).
- 182 Garcia, L., D'Alessandro, G., Fernagut, P. O., Bioulac, B. & Hammond, C. Impact of high-frequency
stimulation parameters on the pattern of discharge of subthalamic neurons. *J Neurophysiol* **94**, 3662-
3669, doi:10.1152/jn.00496.2005 (2005).
- 183 Lempka, S. F., McIntyre, C. C., Kilgore, K. L. & Machado, A. G. Computational analysis of kilohertz
frequency spinal cord stimulation for chronic pain management. *Anesthesiology* **122**, 1362-1376,
doi:10.1097/ALN.0000000000000649 (2015).
- 184 Lorenzon, N. M. & Foehring, R. C. Relationship between Repetitive Firing and
Afterhyperpolarizations in Human Neocortical Neurons. *Journal of Neurophysiology* **67**, 350-363,
doi:DOI 10.1152/jn.1992.67.2.350 (1992).
- 185 de Jong, M. A. M., Briaire, J. J. & Frijns, J. H. M. Dynamic Current Focusing: A Novel Approach to
Loudness Coding in Cochlear Implants. *Ear Hear* **40**, 34-44, doi:10.1097/AUD.0000000000000593
(2019).
- 186 Green, T., Faulkner, A. & Rosen, S. Enhancing temporal cues to voice pitch in continuous
interleaved sampling cochlear implants. *Journal of the Acoustical Society of America* **116**, 2298-
2310, doi:10.1121/1.1785611 (2004).
- 187 Phillips, D. P. & Kelly, J. B. Coding of Tone-Pulse Amplitude by Single Neurons in Auditory-Cortex of
Albino-Rats (*Rattus Norvegicus*). *Hearing Research* **37**, 269-279, doi:Doi 10.1016/0378-
5955(89)90027-0 (1989).
- 188 Gupta, M., Abd-Elseyed, A. & Knezevic, N. N. Improving care of chronic pain patients with spinal
cord stimulator therapy amidst the opioid epidemic. *Neurological Sciences* **41**, 2703-2710,
doi:10.1007/s10072-020-04435-0 (2020).
- 189 Willett, F. R., Avansino, D. T., Hochberg, L. R., Henderson, J. M. & Shenoy, K. V. High-performance
brain-to-text communication via handwriting. *Nature* **593**, 249-+, doi:10.1038/s41586-021-03506-2
(2021).
- 190 Glaser, J. I. *et al.* Machine Learning for Neural Decoding. *eNeuro* **7**, doi:10.1523/ENEURO.0506-
19.2020 (2020).
- 191 Henry, F., Glavin, M. & Jones, E. Noise Reduction in Cochlear Implant Signal Processing: A Review
and Recent Developments. *IEEE Rev Biomed Eng* **PP**, doi:10.1109/RBME.2021.3095428 (2021).
- 192 Grill, W. M. Temporal Pattern of Electrical Stimulation is a New Dimension of Therapeutic Innovation.
Curr Opin Biomed Eng **8**, 1-6, doi:10.1016/j.cobme.2018.08.007 (2018).
- 193 McIntyre, C. C., Chaturvedi, A., Shamir, R. R. & Lempka, S. F. Engineering the next generation of
clinical deep brain stimulation technology. *Brain Stimul* **8**, 21-26, doi:10.1016/j.brs.2014.07.039
(2015).
- 194 Miller, J. P. *et al.* Parameters of Spinal Cord Stimulation and Their Role in Electrical Charge
Delivery: A Review. *Neuromodulation* **19**, 373-384, doi:10.1111/ner.12438 (2016).
- 195 O'Doherty, J. E. *et al.* Active tactile exploration using a brain-machine-brain interface. *Nature* **479**,
228-231, doi:10.1038/nature10489 (2011).

196 Dadarlat, M. C., O'Doherty, J. E. & Sabes, P. N. A learning-based approach to artificial sensory
feedback leads to optimal integration. *Nat Neurosci* **18**, 138-144, doi:10.1038/nn.3883 (2015).

197 Tafazoli, S. *et al.* Learning to control the brain through adaptive closed-loop patterned stimulation. *J*
Neural Eng **17**, 056007, doi:10.1088/1741-2552/abb860 (2020).

198 Choi, J. S. *et al.* Eliciting naturalistic cortical responses with a sensory prosthesis via optimized
microstimulation. *J Neural Eng* **13**, 056007, doi:10.1088/1741-2560/13/5/056007 (2016).

199 Disorders, N. I. o. D. a. O. C. *What are Cochlear Implants for Hearing?*,
<[https://www.nidcd.nih.gov/health/cochlear-
implants#:~:text=A%20cochlear%20implant%20is%20a,the%20skin%20\(see%20figure\).](https://www.nidcd.nih.gov/health/cochlear-implants#:~:text=A%20cochlear%20implant%20is%20a,the%20skin%20(see%20figure).)> (2021).

200 Wilson, B. S. & Dorman, M. F. Cochlear implants: current designs and future possibilities. *J Rehabil*
Res Dev **45**, 695-730, doi:10.1682/jrrd.2007.10.0173 (2008).

201 Wilson, B. S. & Dorman, M. F. Cochlear implants: a remarkable past and a brilliant future. *Hear Res*
242, 3-21, doi:10.1016/j.heares.2008.06.005 (2008).

202 Riley, P. E., Ruhl, D. S., Camacho, M. & Tolisano, A. M. Music Appreciation after Cochlear
Implantation in Adult Patients: A Systematic Review. *Otolaryngol Head Neck Surg* **158**, 1002-1010,
doi:10.1177/0194599818760559 (2018).

203 Sit, J. J., Simonson, A. M., Oxenham, A. J., Faltys, M. A. & Sarpeshkar, R. A low-power
asynchronous interleaved sampling algorithm for cochlear implants that encodes envelope and
phase information. *IEEE Trans Biomed Eng* **54**, 138-149, doi:10.1109/TBME.2006.883819 (2007).

204 Mehta, A. H. & Oxenham, A. J. Vocoder Simulations Explain Complex Pitch Perception Limitations
Experienced by Cochlear Implant Users. *J Assoc Res Otolaryngol* **18**, 789-802, doi:10.1007/s10162-
017-0632-x (2017).

205 Chen, F. & Zhang, Y. T. A novel temporal fine structure-based speech synthesis model for cochlear
implant. *Signal Processing* **88**, 2693-2699, doi:10.1016/j.sigpro.2008.05.011 (2008).

206 Lan, N., Nie, K. B., Gao, S. K. & Zeng, F. G. A novel speech-processing strategy incorporating tonal
information for cochlear implants. *Ieee Transactions on Biomedical Engineering* **51**, 752-760,
doi:10.1109/Tbme.2004.826597 (2004).

207 Li, Y., Wang, S., Su, Q., Galvin, J. J. & Fu, Q. J. Validation of list equivalency for Mandarin speech
materials to use with cochlear implant listeners. *International journal of audiology* **56**, S31-S40
(2017).

208 Zilany, M. S., Bruce, I. C. & Carney, L. H. Updated parameters and expanded simulation options for
a model of the auditory periphery. *J Acoust Soc Am* **135**, 283-286, doi:10.1121/1.4837815 (2014).

209 Lamping, W., Goehring, T., Marozeau, J. & Carlyon, R. P. The effect of a coding strategy that
removes temporally masked pulses on speech perception by cochlear implant users. *Hear Res* **391**,
107969, doi:10.1016/j.heares.2020.107969 (2020).

210 Warden, P. Speech commands: A dataset for limited-vocabulary speech recognition.
arXiv:1804.03209 (2018).

211 Carney, L. H., Zilany, M. S., Huang, N. J., Abrams, K. S. & Idrobo, F. Suboptimal use of neural
information in a mammalian auditory system. *J Neurosci* **34**, 1306-1313,
doi:10.1523/JNEUROSCI.3031-13.2014 (2014).

212 Wirtzfeld, M. R., Pourmand, N., Parsa, V. & Bruce, I. C. Predicting the quality of enhanced wideband
speech with a cochlear model. *J Acoust Soc Am* **142**, EL319, doi:10.1121/1.5003785 (2017).

213 Bianco, M. J. *et al.* Machine learning in acoustics: Theory and applications. *J Acoust Soc Am* **146**,
3590, doi:10.1121/1.5133944 (2019).

214 Instruments, T. (2018).

215 Medqor. *What's the State of Rechargeable Batteries for Hearing Aids?*,
<[https://hearingreview.com/hearing-products/hearing-aids/whats-state-rechargeable-batteries-
hearing-aids](https://hearingreview.com/hearing-products/hearing-aids/whats-state-rechargeable-batteries-hearing-aids)> (2021).

216 Grant, P. F. & Lowery, M. M. Electric field distribution in a finite-volume head model of deep brain
stimulation. *Medical Engineering & Physics* **31**, 1095-1103, doi:10.1016/j.medengphy.2009.07.006
(2009).

217 Bai, S., Loo, C. & Dokos, S. A review of computational models of transcranial electrical stimulation.
Critical Reviews™ in Biomedical Engineering **41** (2013).

218 Potrusil, T. *et al.* Finite element analysis and three-dimensional reconstruction of tonotopically
aligned human auditory fiber pathways: A computational environment for modeling electrical
stimulation by a cochlear implant based on micro-CT. *Hear Res* **393**, 108001,
doi:10.1016/j.heares.2020.108001 (2020).

219 Yona, G., Meitav, N., Kahn, I. & Shoham, S. Realistic Numerical and Analytical Modeling of Light
Scattering in Brain Tissue for Optogenetic Applications(1,2,3). *eNeuro* **3**,
doi:10.1523/ENEURO.0059-15.2015 (2016).

- 220 Salahshoor, H., Shapiro, M. G. & Ortiz, M. Transcranial focused ultrasound generates skull-conducted shear waves: Computational model and implications for neuromodulation. *Appl Phys Lett* **117**, 033702, doi:10.1063/5.0011837 (2020).
- 221 Steinhardt, C. R. & Fridman, G. Y. A Machine Learning-based Neural Implant Front End for Inducing Naturalistic Firing. *Annu Int Conf IEEE Eng Med Biol Soc* **2021**, 5713-5718, doi:10.1109/EMBC46164.2021.9630548 (2021).
- 222 Chaturvedi, A., Butson, C. R., Lempka, S. F., Cooper, S. E. & McIntyre, C. C. Patient-specific models of deep brain stimulation: influence of field model complexity on neural activation predictions. *Brain Stimul* **3**, 65-67, doi:10.1016/j.brs.2010.01.003 (2010).
- 223 Liu, Z., Cakir, A. & Noble, J. H. Auditory Nerve Fiber Health Estimation Using Patient Specific Cochlear Implant Stimulation Models. *Simul Synth Med Imaging* **12417**, 184-194, doi:10.1007/978-3-030-59520-3_19 (2020).
- 224 Chakraborty, D., Truong, D. Q., Bikson, M. & Kaphzan, H. Neuromodulation of Axon Terminals. *Cereb Cortex* **28**, 2786-2794, doi:10.1093/cercor/bhx158 (2018).
- 225 Wurtz, R. H. Recounting the impact of Hubel and Wiesel. *J Physiol* **587**, 2817-2823, doi:10.1113/jphysiol.2009.170209 (2009).
- 226 Newsome, W. T., Britten, K. H. & Movshon, J. A. Neuronal correlates of a perceptual decision. *Nature* **341**, 52-54, doi:10.1038/341052a0 (1989).
- 227 Gross, C. G. Genealogy of the "grandmother cell". *Neuroscientist* **8**, 512-518, doi:10.1177/107385802237175 (2002).
- 228 Sporns, O. Structure and function of complex brain networks. *Dialogues Clin Neurosci* **15**, 247-262 (2013).
- 229 Wallis, J. D. Decoding Cognitive Processes from Neural Ensembles. *Trends Cogn Sci* **22**, 1091-1102, doi:10.1016/j.tics.2018.09.002 (2018).
- 230 Vyas, S., Golub, M. D., Sussillo, D. & Shenoy, K. V. Computation Through Neural Population Dynamics. *Annu Rev Neurosci* **43**, 249-275, doi:10.1146/annurev-neuro-092619-094115 (2020).
- 231 Philipp, R. & Hoffmann, K. P. Arm movements induced by electrical microstimulation in the superior colliculus of the macaque monkey. *J Neurosci* **34**, 3350-3363, doi:10.1523/JNEUROSCI.0443-13.2014 (2014).
- 232 Churchland, M. M. & Shenoy, K. V. Delay of movement caused by disruption of cortical preparatory activity. *J Neurophysiol* **97**, 348-359, doi:10.1152/jn.00808.2006 (2007).
- 233 Bidelman, G. M., Price, C. N., Shen, D. W., Arnott, S. R. & Alain, C. Afferent-efferent connectivity between auditory brainstem and cortex accounts for poorer speech-in-noise comprehension in older adults. *Hearing Research* **382**, doi:ARTN 107795 10.1016/j.heares.2019.107795 (2019).
- 234 Fridman, G. Safe Direct Current Stimulator design for reduced power consumption and increased reliability. *Annu Int Conf IEEE Eng Med Biol Soc* **2017**, 1082-1085, doi:10.1109/EMBC.2017.8037015 (2017).
- 235 Bonaiuto, J. J. & Bestmann, S. Understanding the nonlinear physiological and behavioral effects of tDCS through computational neurostimulation. *Computational Neurostimulation* **222**, 75-103, doi:10.1016/bs.pbr.2015.06.013 (2015).
- 236 Wang, X. J. Probabilistic decision making by slow reverberation in cortical circuits. *Neuron* **36**, 955-968, doi:10.1016/s0896-6273(02)01092-9 (2002).
- 237 Hanks, T. D., Ditterich, J. & Shadlen, M. N. Microstimulation of macaque area LIP affects decision-making in a motion discrimination task. *Nat Neurosci* **9**, 682-689, doi:10.1038/nn1683 (2006).
- 238 Ditterich, J., Mazurek, M. E. & Shadlen, M. N. Microstimulation of visual cortex affects the speed of perceptual decisions. *Nat Neurosci* **6**, 891-898, doi:10.1038/nn1094 (2003).
- 239 Curtis, C. E. & Sprague, T. C. Persistent Activity During Working Memory From Front to Back. *Front Neural Circuits* **15**, 696060, doi:10.3389/fncir.2021.696060 (2021).
- 240 Levitt, J. B., Lewis, D. A., Yoshioka, T. & Lund, J. S. Topography of pyramidal neuron intrinsic connections in macaque monkey prefrontal cortex (areas 9 and 46). *J Comp Neurol* **338**, 360-376, doi:10.1002/cne.903380304 (1993).
- 241 Murray, J. D. & Wang, X. J. Cortical Circuit Models in Psychiatry: Linking Disrupted Excitation-Inhibition Balance to Cognitive Deficits Associated With Schizophrenia. *Computational Psychiatry: Mathematical Modeling of Mental Illness*, 3-25, doi:10.1016/B978-0-12-809825-7.00001-8 (2018).
- 242 Ward, L. M. Synchronous neural oscillations and cognitive processes. *Trends in Cognitive Sciences* **7**, 553-559, doi:10.1016/j.tics.2003.10.012 (2003).
- 243 Truccolo, W. *et al.* Neuronal Ensemble Synchrony during Human Focal Seizures. *Journal of Neuroscience* **34**, 9927-9944, doi:10.1523/Jneurosci.4567-13.2014 (2014).
- 244 Bastos, A. M., Loonis, R., Kornblith, S., Lundqvist, M. & Miller, E. K. Laminar recordings in frontal cortex suggest distinct layers for maintenance and control of working memory. *Proc Natl Acad Sci U S A* **115**, 1117-1122, doi:10.1073/pnas.1710323115 (2018).

Curriculum Vitae

Cynthia R. Steinhardt

Education

Johns Hopkins School of Medicine	Ph.D. Biomedical Engineering	2016-2022
Princeton University	B.A. Neuroscience	2012-2016

Ph.D. Thesis

Title: A Modeling Perspective on Developing Naturalistic Neuroprosthetics Using Electrical Stimulation

Advisor: Gene Y. Fridman

Description: Using biophysical and computational modeling of interactions between pulsatile and direct current electrical stimulation and vestibular afferents to characterize their capabilities to induce firing patterns. Leveraging this understanding to create new stimulation algorithm for cochlear implants.

Awards

- 2022:** Simons Society of Fellows Junior Fellowship
- 2021:** Nomination for International Phase of Schmidt Science Fellowship
- 2020:** Professional Development Innovation Initiative Award, Johns Hopkins University
- 2017:** Fellowship in Computational Medicine, Johns Hopkins University
- 2016-2021:** National Science Foundation Graduate Research Fellowship (GRFP)
- 2015:** Dean's Fellowship, Princeton University
- 2014:** Lambert Award for Neuroscience, Princeton University

Patents

Steinhardt, C.R. and Fridman, G.Y. (2020). Method and System for Processing Input Signals Using Machine Learning for Neural Activation (U.S. Provisional Patent No. 63/150,829). U.S. Patent and Trademark Office. Filed February 18, 2021

Other Research Experience

- 2020–2021:** Medtronic: 3D modeling of spinal cord and spinal cord stimulator
- 2017-2019:** Zaghloul Lab, NIH: applying linear systems techniques to predict induced response to biphasic current stimulation
- 2016:** Nielsen-Connor Lab, Mind Brain Institute, JHU: analyzing electrode recordings from monkeys; two-photon vision experiment in ferrets
- 2015-6:** Buschman Lab, Princeton: modeling of neural functionality; experience with craniotomies, virus injection surgeries, histologies, electrophysiology surgery, building electrodes and 3D-printing
- 2014:** Benucci Lab, RIKEN Brain Science Institute (Japan),: Harvard Summer Research Program: studied functional connectivity of the visual system in vivo in transgenic mice
- 2011-2:** Gregor Lab, Princeton: morphogenetic study of left-right and inter-individual precision of bilaterally symmetric fly wings in *Drosophila* across a range of genetic and environmental conditions

Publications

Adkisson, P., Fridman, G.Y., **Steinhardt, C.R.**, (*in review*) Difference in Network Effects of Pulsatile and Galvanic Stimulation. 2022 43rd Annual International Conference of the IEEE Engineering in Medicine & Biology Society (EMBC) (*in review*)

Steinhardt, C.R., D.E. Mitchell, K.E. Cullen and Fridman, G. Y. (2021). The Rules of Pulsatile Neurostimulation. *bioRxiv*

Steinhardt, C.R. and Fridman, G. Y. (2021). Cochlear Implant Front-End Processing Using Machine Learning. 2021 42nd Annual International Conference of the IEEE Engineering in Medicine & Biology Society (EMBC) (*in press*)

Steinhardt, C.R. and Fridman, G. Y. (2021). Direct current effects on afferent and hair cell to elicit natural firing patterns. *iScience*, 24(3), 102205.

Tafazoli, S., MacDowell, C. J., Che, Z., Letai, K. C., **Steinhardt, C.R.**, and Buschman, T. J. (2020). Learning to control the brain through adaptive closed-loop patterned stimulation. *Journal of Neural Engineering*, 17(5), 056007.

Steinhardt, C.R., and Fridman, G. Y. (2020, July). Predicting Response of Spontaneously Firing Afferents to Prosthetic Pulsatile Stimulation. In 2020 42nd Annual International Conference of the IEEE Engineering in Medicine & Biology Society (EMBC) (pp. 2929-2933). IEEE.

Taylor, C., Greene, P., D'Aleo, R., Breault, M. S., **Steinhardt, C.R.**, Gonzalez-Martinez, J., and Sarma, S. V. (2020, July). Correlates of Attention in the Cingulate Cortex During Gambling in Humans. In 2020 42nd Annual International Conference of the IEEE Engineering in Medicine & Biology Society (EMBC) (pp. 2548-2551). IEEE.

Steinhardt, C.R., Sacré, P., Sheehan, T. C., Wittig, J. H., Inati, S. K., Sarma, S., and Zaghloul, K. A. (2020). Characterizing and predicting cortical evoked responses to direct electrical stimulation of the human brain. *Brain Stimulation*, 13(5), 1218-1225.

Steinhardt, C.R., Sacré, P., Inati, S. K., Sarma, S. V., and Zaghloul, K. A. (2019, July). Investigation of Architectures for Models of Neural Responses to Electrical Brain Stimulation. In 2019 41st Annual International Conference of the IEEE Engineering in Medicine and Biology Society (EMBC) (pp. 6892-6895). IEEE.

Steinhardt, C.R., Betthausen, J., Hunt, C., and Thakor, N. (2018, October). Registration of EMG Electrodes to Reduce Classification Errors due to Electrode Shift. In 2018 IEEE Biomedical Circuits and Systems Conference (BioCAS) (pp. 1-4). IEEE.

Abouchar, L., Petkova, M. D., **Steinhardt, C.R.**, and Gregor, T. (2014). Fly wing vein patterns have spatial reproducibility of a single cell. *Journal of The Royal Society Interface*, 11 (97), 20140443.

Selected Invited Talks & Conference Presentations

Steinhardt, C.R. and Fridman, G. Y. (2021, November) A Machine Learning-based Neural Implant Front End for Induce Naturalistic Firing. 2021 42nd Annual International Conference of the IEEE Engineering in Medicine & Biology Society (EMBC) (Virtual Talk)

Steinhardt, C.R. (2021, July). Galvanic Stimulation: A New World of Possibilities for Driving Neural Populations, Invited Talk for Pinotsis Lab, University College London, London WC1E 6BT, UK

Steinhardt, C.R. (2021, June). Galvanic Stimulation: A New World of Possibilities for Driving Neural Populations, Invited Talk for Churchland Lab, Columbia University, New York, NY 10027

Steinhardt, C.R. (2021, June). Galvanic Stimulation: A New World of Possibilities for Driving Neural Populations, Invited Talk for Miller Lab, MIT, Cambridge, MA 02139

Steinhardt, C.R. (2021, March). Designing a Neural Implant that Writes in Neural Code, Invited Talk for Buschman Lab, Princeton University, Princeton, NJ 08544

Steinhardt, C.R. (2021, February). Designing a Neural Implant that Speaks the Neural Language, Invited Talk for Grill Lab, Duke University, Durham, NC 27708

Steinhardt, C.R. (2020, December). Understanding Differences Between DC and Pulsatile Stimulation Through Vestibular Afferent Studies, Invited Talk for CCNY Neural Engineering group, The City College of New York, New York, NY 10031

Steinhardt, C.R. (2020, September). The Mechanism of Direct Current Stimulation in Vestibular Afferents. Center for Hearing and Balance Seminar, Johns Hopkins University, Baltimore, MD (Talk)

Steinhardt, C.R. (2020, August). Biomedical Engineering: Improving the Cochlear Implant. Neils Bohr Institute, Copenhagen, Denmark (Talk)

Steinhardt, C.R. and Fridman G. Y. (2020, July). Predicting Response of Spontaneously Firing Afferents to Prosthetic Pulsatile Stimulation. 2020 42nd Annual International Conference of the IEEE Engineering in Medicine and Biology Society (EMBC) (Montreal, Canada) (Virtual Talk)

Steinhardt, C.R., Sacré, P., Inati, S. K., Sarma, S. V., and Zaghloul, K. A. (2019, July). Investigation of Architectures for Models of Neural Responses to Electrical Brain Stimulation. (Talk) University of Copenhagen Health Talk Lecture Series

Steinhardt, C.R., Sacré, P., Inati, S. K., Sarma, S. V., and Zaghloul, K. A. (2019, July). Investigation of Architectures for Models of Neural Responses to Electrical Brain Stimulation. 2019 41st Annual International Conference of the IEEE Engineering in Medicine and Biology Society (EMBC) (Berlin, Germany) (Talk)

Steinhardt, C.R., Betthausen, J., Hunt, C., and Thakor, N. (2018, October). Registration of EMG Electrodes to Reduce Classification Errors due to Electrode Shift. Poster session at the 2018 IEEE Biomedical Circuits and Systems Conference (BioCAS), Cleveland, Ohio. (Poster)

Steinhardt, C.R., Hung C.C., and Connor, C.E. (2017, May). Overrepresentation of vertical limbs in primate inferotemporal cortex. Poster session at the meeting of the Vision Sciences Society, St. Pete Beach, Florida. (Poster)

Steinhardt, C.R., Sheehan, T., Inati, S.K., Zaghloul, K.A. (2017, Nov). Characterizing neural responses to single pulse direct cortical stimulation in the human. Society for Neuroscience. Washington D.C. (Talk)

Leadership & Teaching

2020–2021: President of Translational Neuroengineering Technologies (TNT) Networks, JHU

2020: Ad hoc review for *Brain Stimulation*

2020: Co-founding member of Translational Neuroengineering Technologies (TNT) Networks, JHU

2019: Mentoring high school and college students in summer research projects, JHU

Spring 2019: Foundations of Computational Biology and Bioinformatics, JHU

Spring 2018: Systems and Controls, JHU

Skills & Languages

MATLAB, Simulink, Python, R, LABVIEW, Adobe Photoshop, Adobe Illustrator & InDesign English (native), French (working), Japanese (working), Italian (basic), Hebrew (basic)